Bioinspired fluid-structure interaction problems: gusts, load mitigation and resonance

by

CAYETANO MARTÍNEZ MURIEL

in partial fulfillment of the requirements for the degree of Doctor in
Fluid Mechanics Interuniversity PhD Program

Universidad Carlos III de Madrid

Advisor 1:
Oscar Flores
Universidad Carlos III de Madrid

Advisor 2:
Manuel García-Villalba
TU Wien

Tutor:
Oscar Flores

Leganés, February 2023

Vulnerant omnes,
ultima necat

ACKNOWLEDGEMENTS

This thesis has been carried out in the Aerospace Engineering Department at Universidad Carlos III de Madrid. The financial support has been provided by the Universidad Carlos III de Madrid through a PIPF scholarship awarded on a competitive basis, and by the Spanish Ministry of Economy and Competitiveness through grant DPI2016-76151-C2-2-R (AEI/FEDER, UE).

PUBLISHED AND SUBMITTED CONTENT

Paper 1. Martínez-Muriel, C., & Flores, O. (2020). Analysis of vortical gust impact on airfoils at low Reynolds number. *J. Fluids Struct.*, **99**, 103138. doi: 10.1016/j.jfluidstructs.2020.103138. Wholly included in Chapter 3.

Paper 2. Martínez-Muriel, C., Arranz, G., García-Villalba, M. & Flores, O. (2023). Fluid-structure resonance in spanwise-flexible flapping wings. *J. Fluid Mech., Under review*. Wholly included in Chapter 5.

Paper 3. Martínez-Muriel, C., García-Villalba, M. & Flores, O. (2023). On the role of wake-capture and resonance in tandem flapping wings. *J. Fluid Mech., Submitted*. Wholly included in Chapter 6.

Whenever material from these sources is included in this thesis, it is singled out with typographic means and an explicit reference.

Division of work between authors

Paper 1. The simulations and the analysis were performed by CMM. The first version of the manuscript was written by CMM. The final version of the manuscript included corrections and contributions from OF. The planning of the research was carried out by OF.

Paper 2. The simulations and the analysis were performed by CMM. The model was developed by CMM. The software was developed by GA. The first version of the manuscript was written by CMM. The final version of the manuscript included corrections and contributions from GA, OF and MGV. The planning of the research was carried out by OF and MGV.

Paper 3. The simulations and the analysis were performed by CMM. The first version of the manuscript was written by CMM. The final version of the manuscript included corrections and contributions from OF and MGV. The planning of the research was carried out by OF and MGV.

Acronyms correspond to:

CMM Cayetano **Martínez Muriel**. Universidad Carlos III de Madrid.

OF Oscar **Flores**. Universidad Carlos III de Madrid.

MGV Manuel **García-Villalba**. TU Wien.

GA Gonzalo **Arranz**. Massachusetts Institute of Technology.

OTHER RESEARCH MERITS

Publications

Arranz, G., Martínez-Muriel, C., García-Villalba, M. & Flores, O. (2022). Fluid-structure interaction of multi-body systems: Methodology and applications. *J. Fluids Struct.*, **110**, 103519.
doi: 10.1016/j.jfluidstructs.2022.103519

Conferences

The presenting author is underlined:

Martínez-Muriel, C., Arranz, G., García-Villalba, M. & Flores, O. Direct Numerical Simulation of flow around spanwise-flexible, flapping wings in horizontal tandem configuration. *DLES13*, Udine, Italy, 2022.

Martínez-Muriel, C., Arranz, G., García-Villalba, M. & Flores, O. Numerical simulation of bioinspired fluid-structure interaction problems using a multi-body structural model. *8th ECCOMAS*, Oslo, Norway, 2022.

Martínez-Muriel, C., Cavallaro, R., Bombardieri, R., García-Villalba, M. & Flores, O.. Comparison of numerical methods for three-dimensional Fluid-Structure Interaction problems at low Reynolds numbers. *APS Division of Fluid Dynamics Annual Meeting*. Chicago, USA, 2020.

Martínez-Muriel, C., Cavallaro, R., Bombardieri, R., García-Villalba, M. & Flores, O. Towards the implementation of an aeroelastic solver for unsteady aerodynamics at low Reynolds number. *Workshop on Fluid Mechanics*, Granada, Spain, 2019.

ABSTRACT

Nature often serves as a reference for the design and development of sustainable solutions in numerous different fields. The recent development of small-scale robotic vehicles, as Micro-Air Vehicles (MAVs), is not an exception, and has had an increasingly important impact on society, proposing new alternatives in areas as surveillance or planetary exploration. Trying to mimic the flight of insects and small birds, these devices try to offer more efficient designs and with higher manoeuvrability abilities than the already existing designs. It happens similar with robotic swimmers, with many different existing prototypes. Indeed, it is even possible to find designs of bioinspired small-scale wind turbines based on auto-rotating seeds looking for a more efficient energy harvesting. Besides, in order to develop sustainable designs, increasing their lifetime and reducing the maintenance costs are crucial factors. Depending on the device to design, different methodologies may be followed in order to achieve these two goals while meeting the design requirements. One clear example can be found in the development of wind turbines. Their blades must be designed to withstand not only maximum loads and stresses but also the fatigue caused by the fluctuations around the load required to operate correctly. Reducing fatigue issues by limiting the amplitude of those fluctuations using passive or active control is a viable option to improve their lifetime.

The aim of this dissertation is to contribute to the understanding of the underlying physics in biolocomotion. To this end, direct numerical simulations of different examples and problems at low Reynolds number, Re, have been performed using an existing fluid-structure interaction (FSI) solver. This FSI solver relies on the coupling of an incompressible-flow solver with robotic algorithms for the computation of the dynamics of a system of connected rigid bodies. The particularities of this solver are detailed in the thesis.

The second part of the thesis includes the analysis of these examples and problems mentioned above. More in detail, the aerodynamic and aeroelastic behaviour of airfoils and wings at $Re = 1000$ in various conditions and environments has been analysed.

Natural flyers and swimmers are immersed in turbulent and gusty environments which affect their aerodynamic behaviour. The first problem that has been studied is that of the unsteady response of airfoils impacted by vortical gusts. This first example focuses on how the impact of viscous vortices of different size and intensity on two-dimensional airfoils modify their response. Although in a simplified framework, this analysis allows to gather relevant information about the aerodynamic performance of the airfoils. This aerodynamic response is seen to be self-similar, and the work proposes a semi-empirical model to determine the temporal evolution of the lifting forces based on

an integral definition of the vertical velocity induced by the gust, which can be known *a priori*.

The target of the second problem is to analyse the load that can be mitigated in airfoils undergoing oscillations in the angle of attack using passive-pitching trailing edge flaps. This corresponds, for example, to a simplification of the problem of load mitigation in small-scale wind turbines. The use of passive-pitching trailing edge flaps is a strategy that has recently been recently proposed for large-scale wind turbines. Here, we investigate the validity of this strategy on a completely different scenario. Contrary to what happens in experiments at higher Reynolds numbers, whose results match the predictions of a quasi-steady linear model when the kinematics are within the range of applicability of this model, the load mitigation obtained in this work differs from the values of this theory. The load mitigated is larger or smaller than the predicted values depending on the amplitude of the oscillations in the angle of attack. However, the results of this work show that an increase in the length of the flap while the chord of the airfoil is kept constant leads to an equal change in the reduction of load, in line with the predictions of the quasi-steady model. The development of vortical structures is clearly affected by the flap when it is sufficiently large, which also involves changes in the dynamics of the flap and the forces seen by the airfoil. The repercussion that several of the variables defining the parametric space have on the aerodynamic behaviour of the foil and the dynamics of the flap are analysed. This allows to gather more information for an appropriate selection of those variables.

Finally, the third and fourth problems involve the study of the effects of spanwise flexibility on both isolated wings and pairs of wings arranged in horizontal tandem undergoing flapping motions. The wings are considered to be rectangular flat plates, and the spanwise flexibility is modelled discretizing these flat plates in a finite number of rigid sub-bodies that are connected using torsional springs. The wings are considered to be rigid in the chordwise direction. Isolated spanwise-flexible wings find an optimal propulsive performance when a fluid-structural resonance occurs. At this flexibility, the time-averaged thrust is maximum and twice the value yielded by the rigid case, and the increment in efficiency is around a 15%. Flexibility and the generation of forces are coupled, such that the structural response modifies the development of the vortical structures generated by the motion of the wing, and vice versa. The optimal performance comes from a combination of larger effective angles of attack, properly timed with the pitching motion such that the projection of the forces is maximum, with a delayed development of the vortical structures. Besides, while aspect ratio effects are important for rigid wings, this effect becomes small when compared to flexibility effects when the wings become flexible enough. In fact, while the increase in thrust coefficient for rigid wings with aspect ratio 4 is 1.2 times larger than that provided by rigid wings with aspect ratio equal to 2, the value of this coefficient for resonant wings is twice the value yielded by rigid wings of aspect ratio 4. While forewings of the tandem systems are found to behave similarly to isolated wings, the aeroelastic response of the hindwings is substantially affected by the interaction with the vortices developed and shed by the forewings. This wake capture effect modifies the flexibility at which an optimal propulsive behaviour is obtained. This wake capture effect is analysed through

an estimation of the effective angle of attack seen by both forewings and hindwings, linking the optimal behaviour with the maximisation of the effective angle of attack at the right instants. Based on the obtained results, a proof-of-concept study has been carried out analysing the aerodynamic performance of tandem systems made of wings with different flexibility, which suggests that the latter could outperform systems of equally flexible wings.

Key words: Unsteady aerodynamics, fluid-structure interaction, biolocomotion, gusts, load mitigation, resonance, flexible wings, aeroelasticity, low Reynolds number, direct numerical simulations

RESUMEN

La naturaleza sirve habitualmente de referencia para el diseño y desarrollo de soluciones sostenibles en numerosos campos diferentes. El reciente desarrollo de vehículos robóticos de pequeña escala, como Micro Vehículos Aéreos (MAVs, en inglés), no es una excepción y ha tenido un impacto cada vez más importante en la sociedad, proponiendo nuevas alternativas en áreas cómo vigilancia o exploración planetaria. Tratando de imitar el vuelo de insectos y pequeños pájaros, estos dispositivos pretenden ofrecer diseños más eficientes y con mayor maniobrabilidad que los diseños ya existentes. Ocurre de manera similar con robots nadadores, contando con muchos prototipos diferentes. Incluso existen, por ejemplo, diseños de turbinas eólicas de pequeña escala bioinspiradas en semillas auto-rotantes, buscando una extracción de energía más eficiente. Además, para desarrollar diseños sostenibles, incrementar su tiempo de vida y reducir sus costes de mantenimiento son ideas clave. Dependiendo del dispositivo a diseñar, se pueden seguir diferentes metodologías para alcanzar estas dos metas a la par que se cumplen con los requisitos de diseño. Un claro ejemplo puede encontrarse en el desarrollo de turbinas eólicas. Sus palas deben ser diseñadas para soportar no solo cargas y tensiones máximas sino también la fatiga causada por las fluctuaciones alrededor de la carga requerida para operar correctamente. Reducir los problemas asociados a fatiga limitando la amplitud de estas fluctuaciones usando control activo o pasivo es una manera de incrementar su vida útil.

El objetivo de esta disertación es contribuir al entendimiento de la física bajo la locomoción de vehículos inspirados en la naturaleza. Con este fin, se han realizado simulaciones numéricas directas de diferentes ejemplos y problemas a bajo número de Reynolds, Re, utilizando un solver de interacción fluido-estructura (FSI). El solver FSI se basa en el acople de un solver fluido para flujo incompresible ya existente con algoritmos robóticos para el cómputo de la dinámica de sistemas de cuerpos rígidos conectados. Las particularidades de este solver se detallan en la tesis.

La segunda parte de la tesis incluye el análisis de estos ejemplos y problemas mencionados anteriormente. Más en detalle, se ha analizado el comportamiento aerodinámico y aeroelástico de perfiles y alas a $Re = 1000$ en varias condiciones y ambientes.

Animales que vuelan y nadan están inmersos en ambientes turbulentos y racheados que afectan a su comportamiento aerodinámico. El primer problema que ha sido estudiado es el de la respuesta no estacionaria de perfiles que son impactados por ráfagas tipo vórtice. Este primer ejemplo se centra en cómo el impacto de vórtices viscosos de diferente tamaño e intensidad en perfiles bidimensionales modifican su respuesta. Aunque en un marco simplificado, este análisis permite extraer información relevante sobre el comportamiento aerodinámico de estos perfiles. Esta respuesta aerodinámica

se ha visto que es semejante, y se propone un modelo semi-empírico para determinar la evolución temporal de las fuerzas de sustentación basándose en una definición integral de la velocidad vertical inducida por la ráfaga, la cuál puede ser conocida a priori.

El objetivo del segundo problema es analizar la carga que es posible mitigar en perfiles utilizando flaps pasivos-rotantes de borde de salida en perfiles que experimentan oscilaciones en el ángulo de ataque. Esto se corresponde con una simplificación del problema de mitigación de cargas en turbinas eólicas de pequeña escala. El uso de flaps pasivos-rotantes de borde de salida es análoga a la estrategia que se ha propuesto recientemente para turbinas eólicas de gran escala. Aquí se investiga la validez de esta estrategia en un escenario completamente diferente. Al contrario de lo que ocurre en experimentos a mayor número de Reynolds, cuyos resultados coinciden con las predicciones de un modelo lineal cuasi-estacionario cuando la cinemática del problema está bajo el rango de aplicabilidad del modelo, la mitigación de carga obtenida en este trabajo difiere de los valores proporcionados por esta teoría. La carga mitigada es mayor o menor que los valores predichos dependiendo de la amplitud de las oscilaciones en el ángulo de ataque. Sin embargo, los resultados de este trabajo muestran que un incremento en la longitud del flap manteniendo fija la cuerda del perfil lleva a un incremento igual en la reducción de carga, en línea con las predicciones del modelo cuasi-estacionario. El desarrollo de estructuras vorticales se ve claramente afectadas por el flap cuando es suficientemente grande, lo cual implica cambios en la dinámica del flap y en las fuerzas vistas por el perfil. Se analiza también la repercusión que tienen varias de las variables que definen el espacio paramétrico en el comportamiento aerodinámico del perfil y en la dinámica del flap. Esto permite obtener información relevante de cara a una selección apropiada de estas variables.

Finalmente, el tercer y cuarto problema estudian los efectos de la flexibilidad en la dirección de la envergadura tanto en alas aisladas como en pares de alas dispuestas en tandem horizontal mientras realizan movimientos de batida. Las alas se consideran placas planas rectangulares, y la flexibilidad en la dirección de la envergadura se modela discretizando estas placas planas en un número finito de sub-cuerpos rígidos que se conectan a través de muelles de torsión. Las alas se consideran rígidas en la dirección de la cuerda. Alas aisladas flexibles en la dirección de la envergadura encuentran un óptimo en el comportamiento propulsivo cuando ocurre una resonancia fluido-estructural. A esta flexibilidad, el promedio temporal del empuje es máximo, siendo el doble que el valor dado por alas rígidas, y el incremento de la eficiencia es de alrededor del 15%. La flexibilidad y la generación de fuerzas están acopladas, de tal forma que la respuesta estructural modifica el desarrollo de estructuras vorticales generadas por el movimiento del ala, y viceversa. El comportamiento óptimo proviene de una combinación de mayores ángulos de ataque efectivos, sincronizados convenientemente con el movimiento de rotación de tal forma que la proyección de fuerzas es máxima, con un desarrollo retrasado de estas estructuras vorticales. Además, mientras que los efectos de relación de aspecto son importantes para alas rígidas, estos efectos son pequeños comparados con los efectos de flexibilidad cuando las alas son suficientemente flexibles. De hecho, mientras que el incremento en el coeficiente de empuje para alas rígidas con relación de aspecto 4 es 1.2 veces mayor que aquel dado por alas

rígidas con relación de aspecto 2, el valor de este coeficiente de empuje para alas resonantes es dos veces superior al proporcionado por alas rígidas de relación de aspecto 4. Mientras se ha visto que las alas delanteras de los sistemas de alas en tandem se comportan de manera similar a las aisladas, la respuesta aeroelástica de las alas traseras se ve sustancialmente afectada por la interacción con los vórtices desarrollados y desprendidos por el ala delantera. Este efecto de captura de estela modifica la flexibilidad a la cual se obtiene un comportamiento propulsivo óptimo. Este efecto de captura de estela se analiza a través de una estimación del ángulo de ataque efectivo visto tanto por alas delanteras como traseras, conectando el comportamiento óptimo con la maximización del ángulo de ataque efectivo en los instantes requeridos. Dados estos resultados, se ha llevado a cabo un estudio preliminar analizando el comportamiento aerodinámico de sistemas en tandem compuestos por alas con diferente flexibilidad, los cuales sugieren que éstos podrían mejorar el comportamiento aerodinámico de sistemas hechos por alas igualmente flexibles.

Palabras clave: Aerodinámica no estacionaria, interacción fluido-estructura, biolocomoción, ráfagas, mitigación de cargas, resonancia, alas flexibles, aeroelasticidad, bajo número de Reynolds, simulaciones numéricas directas

TABLE OF CONTENTS

CHAPTER 1

INTRODUCTION

Animal kingdom has fascinated the human being for hundreds, thousands or even millions of years for many different reasons. Evolution has lead all organisms to change through natural selection, making them suitable to survive in and adapt to the changing environment they are immersed in. These changes have also affected animal locomotion, as most animals rely on it for survival (Hosoi & Lauga, 2010), shaping them in a way such that they are able to perform efficiently the needed tasks to survive. Many examples can be easily found. Regarding fish, in particular those that depend on their agility to survive, they are able to reverse direction without slowing down and using a turning radius up to 30% of their body length, in striking contrast with ships, which need to reduce their speed by a 50% with a turning radius 10 times larger than those of fish (Triantafyllou & Triantafyllou, 1995). In sustained swimming mode, the swimming time of fish can long at least 200 min without any sign of fatigue (Nikora et al., 2003). Other examples of astonishing figures in locomotion are those shown by many flying animals. Compared to a Lookheed YF-12, which is one of the few aircraft that is able to exceed Mach 3.0 and travels approximately 34 body lengths per second, a European Starling is capable of flying at 120 body lengths per second. Another example is that of a Barn Swallow, which has a roll rate of about 5,000°/s, compared to that of aerobatic aircraft, which is around 720°/s (Shyy et al., 2013).

Based on their excellent performance, numerous animals have been selected in the last decades to be the reference for the design of many robotic devices, whose goal is to improve the efficiency and develop more sustainable vehicles while still being to perform the duties they are devoted to. Starting with *RoboTuna* (Triantafyllou & Triantafyllou, 1995), which was probably the first functional swimming robot, many different examples of robotic fish (J. Liu et al., 2005; Katzschmann et al., 2016; Raj & Thakur, 2016) or amphibious (Crespi & Ijspeert, 2008; Manfredi et al., 2013) can be found in the literature.

In a similar fashion, flapping wing Micro Air Vehicles (FWMAVs) can also be found, resembling the flight of insects and birds. Contrary to fixed wing or rotary wing MAVs, which find their aerodynamic performance degraded at low Reynolds numbers (Pines & Bohorquez, 2006), the flight of FWMAVs rely on the same unconventional lifting mechanisms as insects and birds, namely delayed stall with Leading Edge Vortex (LEV) generation, rapid pitch up, wake recapture and clap and fling (Sane, 2003), which allow them to enhance their efficiency and performance. Examples of robotic fliers include, among many others, the *DelFly* (De Croon et al., 2009), the *Nano Hummingbird* (Keennon et al., 2012), the *Colibri* (Roshanbin et al., 2017) or the *Robird* (Folkertsma et al., 2017), which have evolved or presented different designs with time to achieve either a better performance or to perform different missions.

Yet, the efficiency and performance of these robotic devices are far from those reached by the animals (Haider et al., 2021). The main reason explaining this fact is the lack of knowledge of reliable models for the force generation covering the vast parametric space in terms of geometry and material properties of the devices or the kinematics to be followed in order to perform a given manoeuver, among others. For example, there are qualitative explanations to ensure that attached LEVs increase the force generation providing additional normal force (Dickinson et al., 1999). However, these LEVs are three-dimensional structures that interact with the devices in different ways depending on their location, intensity and shape, which are complex to be predict *a priori*, leading to the absence of robust models to quantify the increase in additional lift.

Looking for reliable models, if the focus is put on a particular geometry or kinematics, the results might be difficult to be extended to other configurations. Conversely, the analysis of the fundamental effects of the material properties might apply generally. In fact, it is well known that flexibility, if properly selected, may enhance the aero-hydrodynamic performance of these devices. There are many works in the last two decades addressing the effects of flexibility on the propulsive performance and the aero-hydroelastic response of the wings or fins (Hamamoto et al. (2007), Heathcote et al. (2008), Alben (2012), Quinn et al. (2014), Moore (2015), Yeh & Alexeev (2016), Arora et al. (2018), Shahzad et al. (2018), and K. Liu et al. (2022) among many others). Despite the advances in the understanding of chordwise, spanwise and isotropic flexibility, the knowledge of the mechanisms playing a role on the aero-hydroelastic response is still limited. The state of the flow and the structural response are coupled, resulting in a complex configuration whose behaviour is very difficult to compute accurately with cost-effective tools. Further understanding of the relevance of the different mechanisms on the optimal performance may eventually lead to robust reduced-order models applicable to general configurations.

Additional complexity and uncertainty may be linked to the gusty and turbulent environments where the animals and robotic vehicles move through, which also alter their aero-hydrodynamic behaviour. Differently to large-scale aircraft, the size and intensity of the disturbances in the flow are of the order of magnitude of the size of the devices and the travelling speed, usually resulting in massive flow separation, changing completely their response and making the available tools based on

potential flow invalid for these configurations. Active or passive control techniques are then needed to meet the aero-hydrodynamic requirements and mitigate the loads that can affect the structure, similar to fish and birds that change their shape through muscular activity or through passive flow control as for example that provided by feathers in owls and others (van Oorschot et al., 2020).

On the other hand, individuals can also enhance its performance by properly interacting with the perturbed environment. Numerous examples can be found in nature, as the flock of birds (Hummel, 1983) or the school of fish (Weihs, 1973), where the individuals interact with the surrounding fluid that is perturbed by the rest of individuals. Another particular example can be seen on the wing-wing interaction found in dragonflies (Bomphrey et al., 2016).

Finally, the technological limitations in the manufacturing of the devices might also hinder the achievement of the expected efficiency.

All the aforementioned problems may be summed up in fluid-structure interaction (FSI) problems. Experiments can provide results at a relatively low cost, but are not able to provide the state of the flow, i.e. flow velocity and pressure, at each time instant. This can be overcome performing numerical simulations, where the amount of data that can be acquired from these numerical simulations is high in both time and space. However, as the dynamics of the bodies and the fluid are coupled, leading to highly non-linear problems, they are complex to solve numerically and they come at the expense of high computational cost.

With the work presented in this thesis, we aim to contribute to the current understanding of the underlying physics in different FSI problems, in order to pave the way for future work.

1.1 Objectives

The main objective of this dissertation is to contribute to the understanding of the underlying physics of flying and swimming animals in both laminar and gusty environments following simplified configurations, which eventually will aid in the development of more sustainable and long-lasting efficient vehicles. To achieve this aim, three objectives are defined.

- The first objective is to analyse the response of travelling bodies to isolated vortical gusts, in order to better understand the aero-hydrodynamic performance of these bodies when they are immersed in perturbed environments.

- The second objective is to study the load that can be mitigated in airfoils using passive trailing-edge flaps, characterising the fluid-structure interaction problem and, in particular, the aerodynamic performance of those airfoils.

- The third and last objective is to analyse numerically the role of spanwise flexibility, resonance and wake capture on the optimal propulsive performance of both isolated wings and pairs of flapping wings arranged in tandem configuration.

1.2 Thesis structure

The present document is divided in chapters. In chapters 1 and 2, the thesis is introduced and the numerical methodology used to carry out the studies in this dissertation is presented. Chapter 3 investigates the aerodynamic behaviour of airfoils when impacted by vortical gusts. The load mitigation on heaving airfoils using passive pitching trailing-edge flaps is addressed in chapter 4. Chapters 5 and 6 involve the analysis of the relevance of fluid-structure resonance on optimal performance of spanwise flexible wings when they are both isolated and arranged in horizontal tandem configuration. Lastly, the main contributions and highlights of the thesis, together with future lines of work are described in chapter 7.

REFERENCES

Alben, S. 2012. Flapping propulsion using a fin ray. *J. Fluid Mech.* 705:149–164.

Arora, N., Kang, C.-K., Shyy, W. & Gupta, A. 2018. Analysis of passive flexion in propelling a plunging plate using a torsion spring model. *J. Fluid Mech.* 857:562–604.

Bomphrey, R. J., Nakata, T., Henningsson, P. & Lin, H. T. 2016. Flight of the dragonflies and damselflies. *Philosophical Transactions of the Royal Society B: Biological Sciences* 371 (1704): 20150389.

Crespi, A. & Ijspeert, A. J. 2008. Online optimization of swimming and crawling in an amphibious snake robot. *IEEE Transactions on robotics* 24 (1): 75–87.

De Croon, G. C. H. E. et al. 2009. Design, aerodynamics, and vision-based control of the DelFly. *Int. J. Micro Air Veh.* 1 (2): 71–97.

Dickinson, M. H., Lehmann, F.O. & Sane, S. P. 1999. Wing rotation and the aerodynamic basis of insect flight. *Science* 284 (5422): 1954–1960.

Folkertsma, G. A. et al. 2017. Robird: a robotic bird of prey. *IEEE robotics & automation magazine* 24 (3): 22–29.

Haider, N., Shahzad, A., Mumtaz Q., Muhammad N. & A. S., Syed I. 2021. Recent progress in flapping wings for micro aerial vehicle applications. *Proc. Inst. Mech. Eng., Part C* 235 (2): 245–264.

Hamamoto, M., Ohta, Y., Hara, K. & Hisada, T. 2007. Application of fluid–structure interaction analysis to flapping flight of insects with deformable wings. *Adv. Robotics* 21 (1-2): 1–21.

Heathcote, S., Wang, Z. & Gursul, I. 2008. Effect of spanwise flexibility on flapping wing propulsion. *J. Fluids Struct.* 24 (2): 183–199.

Hosoi, A. E. & Lauga, E. 2010. Mechanical aspects of biological locomotion. *Exp. Mech.* 50 (9): 1259–1261.

Hummel, D. 1983. Aerodynamic aspects of formation flight in birds. *J. Theor. Biol.* 104 (3): 321–347.

Katzschmann, R. K., Marchese, A. D. & Rus, D. 2016. Hydraulic autonomous soft robotic fish for 3D swimming. In *Experimental Robotics,* 405–420. Springer.

Keennon, M., Klingebiel, K. & Won, H. 2012. Development of the nano hummingbird: A tailless flapping wing micro air vehicle. In *50th AIAA aerospace sciences meeting including the new horizons forum and aerospace exposition*, 588.

Liu, J., Dukes, I. & Hu, H. 2005. Novel mechatronics design for a robotic fish. In *2005 IEEE/RSJ International Conference on Intelligent Robots and Systems*, 807–812. IEEE.

Liu, K., Liu, X. & Huang, H. 2022. Scaling the self-propulsive performance of pitching and heaving flexible plates. *J. Fluid Mech.* 936.

Manfredi, L. et al. 2013. A bioinspired autonomous swimming robot as a tool for studying goal-directed locomotion. *Biol. Cybern.* 107 (5): 513–527.

Moore, M. N. J. 2015. Torsional spring is the optimal flexibility arrangement for thrust production of a flapping wing. *Phys. Fluids* 27 (9): 091701.

Nikora, V. I. et al. 2003. Effects of fish size, time-to-fatigue and turbulence on swimming performance: a case study of Galaxias maculatus. *J. Fish Biol.* 63 (6): 1365–1382.

Pines, D. J. & Bohorquez, F. 2006. Challenges facing future micro-air-vehicle development. *J. Aircr.* 43 (2): 290–305.

Quinn, D. B., Lauder, G. V. & Smits, A. J. 2014. Scaling the propulsive performance of heaving flexible panels. *J. Fluid Mech.* 738:250–267.

Raj, A. & Thakur, A. 2016. Fish-inspired robots: design, sensing, actuation, and autonomya review of research. *Bioinspir. Biomim.* 11 (3): 031001.

Roshanbin, A., Altartouri, H., Karásek, M. & Preumont, A. 2017. COLIBRI: A hovering flapping twin-wing robot. *Int. J. Micro Air Veh.* 9 (4): 270–282.

Sane, S. P. 2003. The aerodynamics of insect flight. *J. Exp. Biol.* 206 (23): 4191–4208.

Shahzad, A., Tian, F. B., Young, J. & Lai, J. C. S. 2018. Effects of flexibility on the hovering performance of flapping wings with different shapes and aspect ratios. *J. Fluids Struct.* 81:69–96.

Shyy, W., Aono, H., Kang, C. K. & Liu, H. 2013. *An introduction to flapping wing aerodynamics*. Vol. 37. Cambridge University Press.

Triantafyllou, M. S. & Triantafyllou, G. S. 1995. An efficient swimming machine. *Scientific American* 272 (3): 64–70.

van Oorschot, B. K., Choroszucha, R. & Tobalske, B. W. 2020. Passive aeroelastic deflection of avian primary feathers. *Bioinsp. & Biomim.* 15 (5): 056008.

Weihs, D. 1973. Hydromechanics of fish schooling. *Nature* 241 (5387): 290–291.

Yeh, P. D. & Alexeev, A. 2016. Effect of aspect ratio in free-swimming plunging flexible plates. *Comput. Fluids* 124:220–225.

CHAPTER 2

NUMERICAL METHODOLOGY

This chapter is devoted to introduce and describe the general numerical methods used to solve the problems considered in chapters 3 to 6, which will include a section describing its own numerical set-up. First, the general equations that govern the motion of bodies immersed in a flow are stated. Then, the methodology to model the presence of these bodies in the fluid is introduced. Afterwards, the approach followed to account for the interaction between multi-body systems and the fluid is presented. Finally, the in-house fluid-structure interaction (FSI) solver used to analyse the problems considered in this dissertation is described.

2.1 Governing equations

Let us consider the general problem of several rigid bodies immersed in a fluid, as depicted in figure 2.1. Under the assumptions of incompressible and Newtonian fluid, suitable for the problems considered in the following chapters,the flow is governed by the Navier-Stokes equations:

$$\nabla \cdot \mathbf{u} = 0, \tag{2.1a}$$

$$\frac{\partial \mathbf{u}}{\partial t} + (\mathbf{u} \cdot \nabla)\,\mathbf{u} = -\frac{1}{\rho}\nabla p + \nu \nabla^2 \mathbf{u}, \tag{2.1b}$$

where $\mathbf{u}$ is the velocity of the flow, p is the pressure, and ρ, ν are the density and the kinematic viscosity of the fluid, respectively. As the Navier-Stokes equations are being solved for a viscous fluid, a no-slip boundary condition needs to be imposed at the surface of the bodies:

$$\mathbf{u} = \mathbf{U}_{\partial\Gamma_i}(\mathbf{x}) \quad \forall \mathbf{x} \in \partial\Gamma_i, \quad \forall i \in B, \tag{2.2}$$

where $\mathbf{U}_{\partial\Gamma_i}(\mathbf{x})$ is the velocity at a point $\mathbf{x}$ of the interface $\partial\Gamma_i$ between the fluid and a body Γ_i, and $B = \{1, ..., N_B\}$ is the set of bodies, where N_B is the total number of bodies. The value of $\mathbf{U}_{\partial\Gamma_i}(\mathbf{x})$ can be

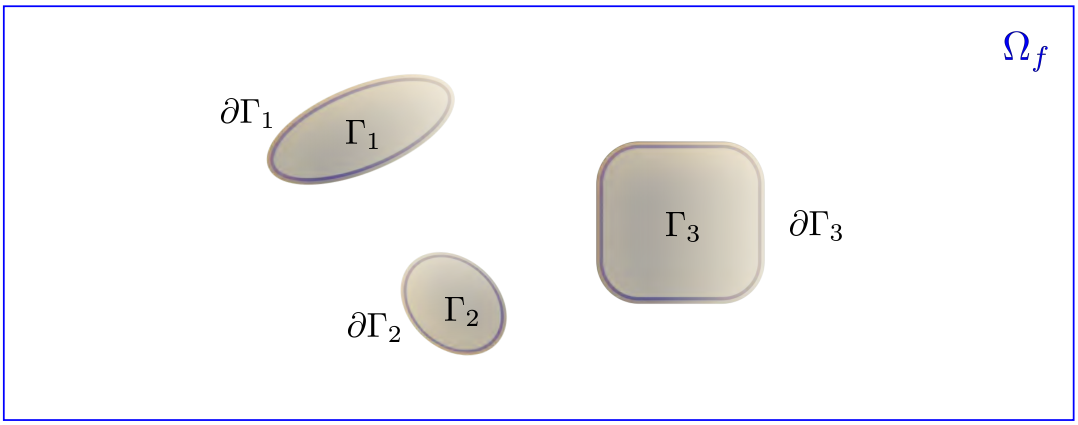

Figure 2.1: Sketch of a set of bodies, Γ_i, immersed in a surrounding fluid whose domain is Ω_f, describing the general problem.

either prescribed or given by the dynamics of the body due to the interaction with the fluid and the rest of the bodies immersed in it.

In the latter scenario, together with equations (2.1), other *structural* equations linking the motion of the bodies with the forces acting have to be solved. To model the fluid-structure interaction of solid bodies immersed in a fluid, two main approaches can be followed depending on the formulation used: *monolithic* and *partitioned* (non-monolithic) approaches (Kim & Choi, 2019). Monolithic formulations combine fluid and structural equations in a single mathematical framework. This leads to a single system of equations that solves the entire problem. While the accuracy of these solvers is often higher than those following non-monolithic partitioned formulations, it usually requires the use of iterative solvers, which may lead to a large increase in the needed computational resources. Contrary, partitioned formulations are such that fluid and structure are solved separately, with the boundary condition (2.2) acting as a mean to ensure compatibility at the interface of both fluid and structural problems. They are usually better conditioned than monolithic formulations, although in certain scenarios, as those where the ratio between the density of fluid and solid is very close to 1, may present very poor convergence. In this work, a partitioned non-monolithic formulation is used to solve the problems described in chapters 3 to 6. Section 2.4 provides further details about its implementation.

2.2 Modelling the presence of bodies in fluid: the Immersed Boundary Method

A common fact among the problems presented in the following chapters is the presence of moving bodies immersed in a surrounding fluid. In order to consider the presence of these bodies immersed in the fluid, different approaches available in the literature can be followed to impose fluid-solid interfaces. One of the proposed ways to tackle the problem is to solve the Navier-Stokes equations

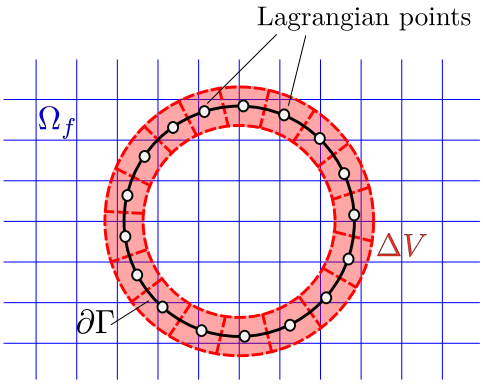

Figure 2.2: Sketch of the discretization used in the immersed boundary method for the fluid, Ω_f, and solid, $\partial\Gamma$, domains.

in the fluid domain, which is discretized such that the fluid mesh fits the bodies, imposing directly the boundary condition of no-slip at the fluid-solid interface. This requires re-meshing to the new position of the moving bodies, increasing substantially the cost of the computations. These are the so-called body-conformal mesh methods (Haeri & Shrimpton, 2012). An example of this technique is the Arbitrary Lagrangian-Eulerian (ALE) formulation (Hirt et al., 1974; Takashi & Hughes, 1992; Hu et al., 2001; Souli & Benson, 2013).

On the other hand, the other available approach is to solve the Navier-Stokes equations on a fixed grid, adding the contribution of the presence of the bodies through source terms. Methods following this approach are known as fixed-mesh methods, and within them, we can find the Immersed Boundary Method (IBM), avoiding the need of re-meshing the fluid domain. Numerous examples can be found in the literature (Mittal & Iaccarino, 2005; Uhlmann, 2005; Pinelli et al., 2010), suggesting the feasibility of this technique to reproduce the presence and motion of solids in a fluid.

The idea of the IBMs is to discretize the fluid domain, denoted with Ω_f, using a Cartesian grid where equation (2.1) is solved. On the other hand, the surface $\partial\Gamma_i$ of a solid is discretized in an arbitrary number of *Lagrangian force points* $L_i = \{1, \ldots, n_i\}$. Each Lagrangian point has an associated volume $\Delta_{i,j}$. This idea is sketched in figure 2.2. The main idea of the IBM is then to add a forcing term $\mathbf{f}_{\text{IBM}}$ to the right-hand side of equation (2.1*b*), such that the no-slip boundary condition (eq. 2.2) can be satisfied at the Lagrangian force points.

2.3 Interaction of a multi-body system of rigid bodies

When imposing the boundary condition at the interface of the bodies using equation (2.2), the velocity $\mathbf{U}_{\partial\Gamma_i}$ might not be prescribed, as mentioned in section 2.1. Instead, for a general problem where the motion of the bodies is given by the fluid-structure interaction, the value of $\mathbf{U}_{\partial\Gamma_i}$ is unknown *a priori*.

Let us consider the problem of many rigid bodies forming the multi-body system (MBS) connected among them using kinematic constraints -joints-, and subject to hydrodynamic forces and torques exerted by the surrounding fluid where they are immersed. To exemplify the problem, a

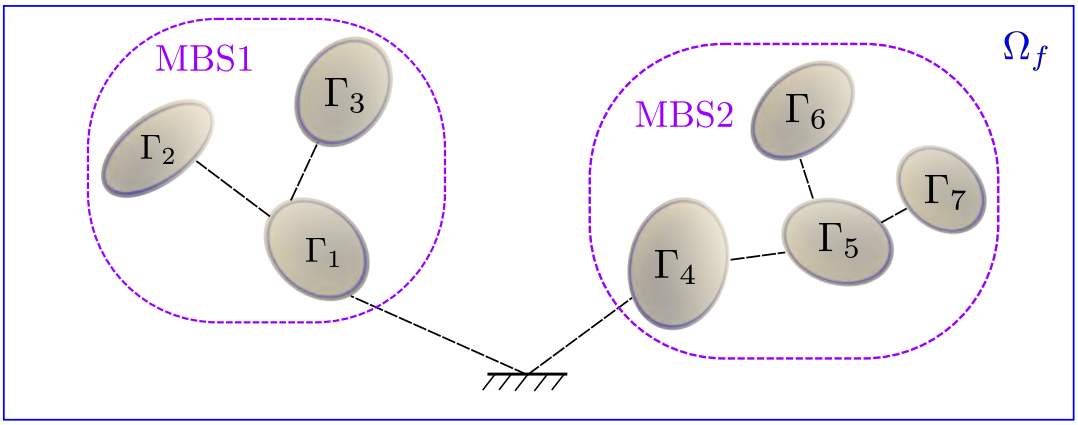

Figure 2.3: Sketch of the problem of two multi-body systems (MBS1 and MBS2), each conformed by several rigid bodies connected among themselves arbitrarily.

sketch of a pair of multi-body systems is shown in figure 2.3, where bodies $\Gamma_1, \Gamma_2, \Gamma_3$ conform MBS1 and $\Gamma_4, \Gamma_5, \Gamma_6, \Gamma_7$ conform MBS2. Both MBS are linked to a reference fixed inertial base.

To describe the dynamics of a single body in three dimensions (3D), the so-called Newton-Euler equations are needed, which are six scalar equations:

$$m\dot{\mathbf{U}}_G = \mathbf{F}_{ext} \tag{2.3a}$$

$$I_G\dot{\Omega} + \Omega \times I_G\Omega = \mathbf{M}_{G,ext} \tag{2.3b}$$

where m and I_G represent the mass and the inertia tensor of the body, the linear and angular velocities of the body are $\mathbf{U}_G$ and Ω, respectively, and $\mathbf{F}_{ext}$ and $\mathbf{M}_{G,ext}$ are the external force and moment acting on the body. The magnitudes that are computed with respect to the center of mass of the body are denoted with the subscript G. Equation (2.3*b*) is only valid if it is expressed in a body-fixed reference frame.

To fully describe the dynamics of a given MBS, a total of $6 \times N_B$ equations are needed. Nevertheless, the joints connecting the bodies act as constraints for their relative motion. Hence, the number of degrees of freedom (N_{dof}) is reduced, and so the number of equations required to model the MBS. This results in a system of ordinary differential equations (ODEs). To find these equations, different approaches can be used (Greenwood, 2003). In this work, the system of ODEs for a MBS are written following the approach in Featherstone (2014):

$$H(\mathbf{q})\ddot{\mathbf{q}} + \mathbf{c}(\mathbf{q}, \dot{\mathbf{q}}) = \boldsymbol{\xi} + \boldsymbol{\xi}_h, \tag{2.4}$$

where $\mathbf{q}$ is the vector of generalized coordinates, describing the instantaneous configuration of the MBS in the N_{dof}-dimensional space, H is the joint space or generalized inertia matrix, $\mathbf{c}$ is the generalized bias force, that accounts for Coriolis, centripetal and gravity forces, $\boldsymbol{\xi}$ is the vector of generalized forces and torques, considering, for example, for springs and/or dampers in the joints,

and $\boldsymbol{\xi}_h$ is the vector of generalized hydrodynamic forces and torques due to the surrounding fluid. Although omitted, both H and $\mathbf{c}$ also depend on the inertia properties of the bodies.

2.4 In-house FSI solver: TUCANMB

The in-house FSI code TUCANMB used to solve the problems in this thesis was first introduced and developed as TUCAN by Moriche (2017), only as a flow solver, with improvements shown in Gonzalo (2018). Afterwards, the implementation of the multi-body solver module and the coupling to the fluid solver was performed in Arranz et al. (2022b), giving rise to TUCANMB. Therefore, only a brief and overall description of the code is provided here. This way, the reader is referred to the previously mentioned works for a more detailed picture.

2.4.1 Flow solver

The approach to solve equation (2.1) in TUCAN/TUCANMB is based on the numerical method proposed in Uhlmann (2005). It uses an IBM to model the presence of the bodies in the fluid, and relies on a projection method to enforce continuity. Time integration is performed using a three-stage, low-storage Runge-Kutta method. The linear terms are treated implicitly while non-linear terms are treated explicitly. A staggered grid is used for the spatial discretization. The spatial derivatives are computed using second-order, centered finite differences. The discretized equations at a kth Runge-Kutta sub-step are:

$$\tilde{\mathbf{u}} = \mathbf{u}^{k-1} + \Delta t \left(2\alpha_k \nu \nabla^2 \mathbf{u}^{k-1} - 2\alpha_k \rho^{-1} \nabla p^{k-1} - \gamma_k [(\mathbf{u}\cdot\nabla)\mathbf{u}]^{k-1} - \zeta_k [(\mathbf{u}\cdot\nabla)\mathbf{u}]^{k-2} \right), \tag{2.5a}$$

$$\tilde{\mathbf{U}}\left(\mathbf{X}_{i,j}\right) = \sum_{i\in B} \sum_{j\in L_i} \tilde{\mathbf{u}}(\mathbf{x}) \delta_h \left(\mathbf{x} - \mathbf{X}_{i,j}\right) \Delta_{\mathrm{eu}}^3, \tag{2.5b}$$

$$\mathbf{F}_{\mathrm{IBM}}^k \left(\mathbf{X}_{i,j}\right) = \frac{\mathbf{U}_{\partial\Gamma_i}^d \left(\mathbf{X}_{i,j}\right) - \tilde{\mathbf{U}}\left(\mathbf{X}_{i,j}\right)}{\Delta t}, \tag{2.5c}$$

$$\mathbf{f}_{\mathrm{IBM}}^k = \sum_{i\in B} \sum_{j\in L_i} \mathbf{F}_{\mathrm{IBM}}^k \left(\mathbf{X}_{i,j}\right) \delta_h \left(\mathbf{x} - \mathbf{X}_{i,j}\right) \Delta V_{i,j}, \tag{2.5d}$$

$$\nabla^2 \mathbf{u}^* - \frac{\mathbf{u}^*}{\alpha_k \nu \Delta t} = -\frac{1}{\nu \alpha_k} \left(\frac{\tilde{u}}{\Delta t} + \mathbf{f}_{\mathrm{IBM}}^k \right) + \nabla^2 \mathbf{u}^{k-1}, \tag{2.5e}$$

$$\nabla^2 \phi^k = \frac{\nabla \cdot \mathbf{u}^*}{2\alpha_k \Delta t}, \tag{2.5f}$$

$$\mathbf{u}^k = \mathbf{u}^* - 2\alpha_k \Delta t \nabla \phi^k, \tag{2.5g}$$

$$p^k = p^{k-1} + \rho \left(\phi^k - \alpha_k \nu \Delta t \nabla^2 \phi^k \right). \tag{2.5h}$$

The value of the coefficients $\alpha_k, \gamma_k, \zeta_k$ of the k sub-step are selected to be those given in Rai & Moin (1991). $\tilde{\mathbf{u}}$ is an estimate of the velocity used to compute the forcing term $\mathbf{f}_{\mathrm{IBM}}$ that appears in equations (2.5$b-d$), while $\mathbf{u}^*$ is an intermediate velocity. The variable Δ_{eu} is the spacing of the eulerian grid. On the other hand, ϕ is the pseudo-pressure, and has no physical meaning.

The forcing term $\mathbf{f}_{\text{IBM}}$ needs of several steps to be computed. Once the estimate of the velocity, $\tilde{\mathbf{u}}$, is obtained, it is interpolated to the Lagrangian forcing points $\mathbf{X}_{i,j}$ in equation (2.5*b*). In combination with the desired velocity at each Lagrangian point, $U^d_{\partial\Gamma_i}$, a Lagrangian forcing term in this set of Lagrangian points is computed using equation (2.5*c*). The forcing term $\mathbf{f}_{\text{IBM}}$ in the Eulerian grid is then obtained after the spreading operation in equation (2.5*d*). The interpolations performed in equations (2.5*b*, *d*) are performed using δ_h, the regularized delta function proposed in Peskin (2002).

2.4.2 Multi-body solver

Multi body systems were introduced in section 2.3, where the dynamics of a MBS can be expressed with equation (2.4). The time integration of this equation yields the generalized velocities $\dot{\mathbf{q}}$ of the degrees of freedom of the MBS. Integrating again, it is possible to obtain the generalized coordinates $\mathbf{q}$ at a time t.

In a general sense, it is reasonable to assume that the kinematics of certain degrees of freedom will be prescribed, while others will be unknown. This way, it is possible to express the generalized coordinates as $\mathbf{q} = [\mathbf{q}_u^T \ \mathbf{q}_p^T]^T$, where the kinematics of the prescribed degrees of freedom are introduced through $\mathbf{q}_p$. In a similar fashion, it is possible to introduce

$$H = \begin{bmatrix} H_u & H_{up} \\ H_{pu} & H_p \end{bmatrix}, \quad \mathbf{c} = \begin{bmatrix} \mathbf{c}_u \\ \mathbf{c}_p \end{bmatrix}, \quad \boldsymbol{\xi} = \begin{bmatrix} \boldsymbol{\xi}_u \\ \boldsymbol{\xi}_p \end{bmatrix}, \quad \boldsymbol{\xi}_h = \begin{bmatrix} \boldsymbol{\xi}_{h,u} \\ \boldsymbol{\xi}_{h,p} \end{bmatrix}. \tag{2.6}$$

This way, it is possible to obtain a reduced system for the generalized accelerations only of the unknown degrees of freedom that has the form

$$H_u(\mathbf{q})\ddot{\mathbf{q}}_u = \boldsymbol{\xi}_u + \boldsymbol{\xi}_{u,h} - \mathbf{c}^*_u(\mathbf{q}, \dot{\mathbf{q}}), \tag{2.7}$$

where $\mathbf{c}^*_u(\mathbf{q}, \dot{\mathbf{q}}) = \mathbf{c}_u - H_{up}\ddot{\mathbf{q}}_p$ depends on all the degrees of freedom, both prescribed and unknown. The time discretization of equation (2.7) uses the same scheme used for the convective terms of equation (2.1),

$$\dot{\mathbf{q}}^k_u = \dot{\mathbf{q}}^{k-1}_u + \Delta t\left(\gamma_k\left[H_u^{-1}\left(\boldsymbol{\xi}_u - \mathbf{c}^*_u\right)\right]^{k-1} + \zeta_k\left[H_u^{-1}\left(\boldsymbol{\xi}_u - \mathbf{c}^*_u\right)\right]^{k-2} + \left[H_u^{-1}\right]^{k-1}\boldsymbol{\xi}^k_{h,u}\right). \tag{2.8}$$

The computation of the generalized coordinates is performed implicitly as

$$\mathbf{q}^k_u = \mathbf{q}^{k-1}_u + \Delta t\alpha_k\left(\dot{\mathbf{q}}^k_u - \dot{\mathbf{q}}^{k-1}_u\right), \tag{2.9}$$

in a similar fashion as done for the viscous terms of equation (2.5).

To compute the matrices H and $\mathbf{c}$, the Rigid Body Dynamics Library (RBDL) developed by Felis (2017) has been used. In particular, the matrix H has been computed using the Composite Rigid-Body Algorithm (CRBA), while the generalized bias force $\mathbf{c}$ has been computed using the Recursive Newton-Euler Algorithm (RNEA) (Featherstone, 2014; Felis, 2017).

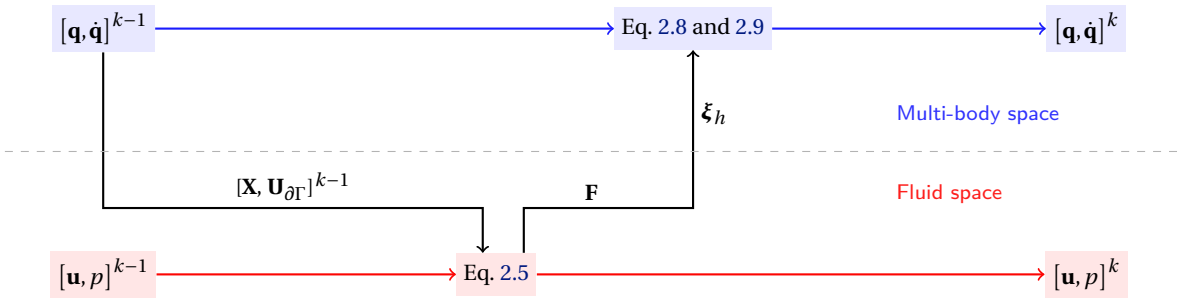

Figure 2.4: Diagram sketching the coupling between the fluid and multi-body solvers for a Runge Kutta substep k.

2.4.3 Coupling

The coupling between the fluid and the multi-body solvers is sketched in figure 2.4. To advance from a state known at a Runge-Kutta substep $k-1$ to a substep k, the algorithm followed is described hereafter:

1. The position and velocity of the Lagrangian points $\mathbf{X}_{i,j}^{k-1}$ and $\mathbf{U}_{\partial\Gamma_i}^{k-1}\left(\mathbf{X}_{i,j}\right)$ are computed using the generalized coordinates and velocities $\mathbf{q}^{k-1},\dot{\mathbf{q}}^{k-1}$.

2. Using the position and velocity of the Lagrangian points, equation (2.5c) is used to compute the lagrangian forcing term $\mathbf{F}_{\text{IBM}}^{k}$. After the spreading operation, equation (2.5d), the forcing term at the Eulerian grid, $\mathbf{f}_{\text{IBM}}^{k}$, is obtained.

3. Using $\mathbf{f}_{\text{IBM}}^{k}$, the state of the fluid can be advanced to substep k solving the remaining steps of equation (2.5), i.e., the velocity, $\mathbf{u}^{k}$, and pressure, p^{k}, fields are obtained.

4. The generalized external forces, $\boldsymbol{\xi}_h$, are obtained mapping the hydrodynamic forces and moments acting on the bodies, $\mathscr{F}$ and $\mathscr{M}$ respectively, which are computed from $\mathbf{F}_{\text{IBM}}^{k}$ as shown below. With $\boldsymbol{\xi}_h$, equation (2.8) is solved to obtain $\dot{\mathbf{q}}^{k}$.

5. Finally, $\mathbf{q}^{k}$ is obtained using equation (2.9). After solving this equation, the state of the MBS is determined for the RK substep k.

The terms $\mathbf{X}_{i,j}^{k-1}$ and $\mathbf{U}_{\partial\Gamma_i}^{k-1}\left(\mathbf{X}_{i,j}\right)$ are treated explicitly, while, on the other hand, the generalized external forces $\boldsymbol{\xi}_h$ represents an integrated state between $k-1$ and k. These two considerations lead to a *weak coupling* between fluid and structural systems. This means that fluid and structural states at the end of a substep k might not be fully compatible (Uhlmann, 2005).

The hydrodynamic forces and moments acting on the bodies, $\mathscr{F}_i$ and $\mathscr{M}_i$, are computed as in Uhlmann (2005):

$$\mathscr{F}_i = \underbrace{-\rho \sum_{j\in L_i} \mathbf{F}_{\mathrm{IBM}}\left(\mathbf{X}_{i,j}\right)\Delta V_j}_{P_i} + \frac{\rho}{\rho_i} m_i \ddot{\mathbf{x}}_{G,i}, \tag{2.10a}$$

$$\mathscr{M}_i = \underbrace{-\rho \sum_{j\in L_i} \left(\mathbf{X}_{i,j}-\mathbf{x}_i\right)\times \mathbf{F}\left(\mathbf{X}_{i,j}\right)\Delta V_j}_{Q_i} + \rho \int_{\partial\Gamma_1} (\mathbf{x}-\mathbf{x}_i)\times \mathbf{u}\,\mathrm{d}\mathbf{x}, \tag{2.10b}$$

where $m_i, \rho_i, \ddot{\mathbf{x}}_{G,i}$ are the mass, density and acceleration of the centre of gravity of the body Γ_i. The last term of equation (2.10b) is the angular momentum of the fluid inside Γ_i, and should be integrated numerically. However, this term has been approximated in this work assuming rigid-body motion of the fluid inside the body Γ_i for efficiency reasons. Then, the contribution of the last term in each of the equations 2.10(a, b) can be directly included in H and $\mathbf{c}$ building them using an effective density $\left(\rho_i - \rho\right)$ (Uhlmann, 2005; Arranz et al., 2022b). This way, a limit on the density ratio exists when using the present approach, approximately $\rho_i/\rho \leq 1.2$, making the study of buoyant bodies impossible. The terms P, Q are those constituting $\boldsymbol{\xi}_h$ after performing the mapping mentioned in step 4.

2.4.4 Main features and details of TUCAN/TUCANMB

As said before, TUCAN and TUCANMB have been previously developed. Here we highlight the main details and features of the solvers. The reader is referred to Moriche (2017) and Gonzalo (2018) for a more detailed overview of TUCAN, and to Arranz et al. (2022b) for TUCANMB.

TUCAN/TUCANMB can be used to perform both two- and three-dimensional simulations. The discretization of the staggered grid can be performed in a non-uniform way, controlled using a stretch factor. While 2D simulations are performed in a rectangular computational domain, 3D ones are performed in a rectangular prism. Dirichlet, Neumann and periodic boundary conditions can be imposed in any of the boundaries of the computational domain. Additionally, in simulations where an inflow is imposed at any of the boundaries, an advective boundary condition given by

$$\partial_t \mathbf{u} + u_c \partial_x \mathbf{u} = 0, \tag{2.11}$$

can be imposed at the opposite boundary, allowing the fluid to leave the computational domain avoiding reflections, where u_c is a convective velocity.

TUCAN/TUCANMB can operate in both single-processor and parallel processing. Parallelization is performed using a block domain decomposition. The grid corresponding to the Eulerian space, i.e., flow domain, is split into a number N_P of smaller blocks that are assigned to an equal number of processors, where the size of the blocks is comparable such that the workload on each processor is similar. The processors only have information about the flow sub-domain assigned to them. This way, the blocks communicate among themselves using Message Passing Interface (MPI).

In TUCAN, there are three/four linear systems to be solved at each substep, namely a Helmholtz problem (equation 2.5*e*) for each velocity component, and a Poisson problem (equation 2.5*f*) for the pseudo-pressure. In order to solve these linear systems in parallel, the library used is HYPRE, which provides a number of preconditioners for high performance computing. A biconjugate gradient stabilized solver (BiCGSTAB) preconditioned with a parallel semicoarsening multigrid solver (PFMG) is used to solve the Poisson equation. On the other hand, a preconditioned conjugate solver (PCG) is used to solve each Helmholtz equation for each of the velocity components.

TUCAN/TUCANMB uses the HDF5 library, Hierarchical Data Format version 5, for Input/Output (I/O) tasks. HDF5 is designed for parallel, collective I/O handling the MPI standard, allowing for a efficient performance for complex data management.

TUCAN and TUCANMB have both been extensively validated. For TUCAN, validation cases can be found in 2D in (Moriche, 2017), while for 3D, they can be found in (Gonzalo, 2018), for fixed and moving bodies. Besides, it has been employed in many different configurations, for external aerodynamic problems (Gonzalo et al., 2018; Arranz et al., 2018b; Jurado et al., 2022) and cardiac flows (García-Villalba et al., 2021), among others. TUCANMB presents validation cases in Arranz et al. (2022b), and has been employed in other works as Arranz et al. (2022a).

REFERENCES

Arranz, G., Flores, O. & García-Villalba, M. 2022a. Flow interaction of three-dimensional self-propelled flexible plates in tandem. *J. Fluid Mech.* 931.

Arranz, G., Martínez-Muriel, C., Flores, O. & García-Villalba, M. 2022b. Fluid-structure interaction of multi-body systems: Methodology and applications. *J. Fluid Struct.* 110:103519.

Arranz, G. et al. 2018b. Kinematics and dynamics of the auto-rotation of a model winged seed. *Bioinspir. Biomim.* 13 (3): 036011.

Featherstone, R. 2014. *Rigid body dynamics algorithms.* Springer.

Felis, M. L. 2017. RBDL: an efficient rigid-body dynamics library using recursive algorithms. *Auton. Robots* 41 (2): 495–511.

García-Villalba, M. et al. 2021. Demonstration of patient-specific simulations to assess left atrial appendage thrombogenesis risk. *Frontiers Physiol.* 12:596596.

Gonzalo, A. 2018. "Aerodynamic forces and vortex structures of flapping wings in forward flight." PhD diss., Universidad Carlos III Madrid.

Gonzalo, A. et al. 2018. From flapping to heaving: A numerical study of wings in forward flight. *J. Fluid. Struct* 83:293–309.

Greenwood, D. 2003. *Advanced dynamics.* Cambridge University Press, Cambridge.

Haeri, S. & Shrimpton, J. S. 2012. On the application of immersed boundary, fictitious domain and body-conformal mesh methods to many particle multiphase flows. *Int. J. Multiph. Flow* 40:38–55.

Hirt, C. W., Amsden, A. A. & Cook, J. L. 1974. An arbitrary Lagrangian-Eulerian computing method for all flow speeds. *J. Comp. Phys.* 14 (3): 227–253.

Hu, H. H., Patankar, N. A. & Zhu, M. 2001. Direct numerical simulations of fluid–solid systems using the arbitrary Lagrangian–Eulerian technique. *J. Comp. Phys.* 169 (2): 427–462.

Jurado, R., Arranz, G., Flores, O. & García-Villalba, M. 2022. Numerical simulation of flow over flapping wings in tandem: Wingspan effects. *Phys. Fluids* 34 (1): 017114.

Kim, W. & Choi, H. 2019. Immersed boundary methods for fluid-structure interaction: A review. *Int. J. Heat Fluid Flow*. 75:301–309.

Mittal, R. & Iaccarino, G. 2005. Immersed boundary methods. *Annu. Rev. Fluid Mech*. 37:239–261.

Moriche, M. 2017. "A numerical study on the aerodynamic forces and the wake stability of flapping flight at low Reynolds number." PhD diss., Universidad Carlos III Madrid.

Peskin, C. S. 2002. The immersed boundary method. *Acta Numer*. 11:479–517.

Pinelli, A., Naqavi, I. Z., Piomelli, U. & Favier, J. 2010. Immersed-boundary methods for general finite-difference and finite-volume Navier–Stokes solvers. *J. Comput. Phys*. 229 (24): 9073–9091.

Rai, M. & Moin, P. 1991. Direct simulations of turbulent flow using finite-difference schemes. *J. Comp. Phys*. 96 (1): 15–53.

Souli, M. & Benson, D. J. 2013. *Arbitrary Lagrangian Eulerian and fluid-structure interaction: numerical simulation*. John Wiley & Sons.

Takashi, N. & Hughes, T. J. R. 1992. An arbitrary Lagrangian-Eulerian finite element method for interaction of fluid and a rigid body. *Comput. Methods Appl. Mech. Eng*. 95 (1): 115–138.

Uhlmann, M. 2005. An immersed boundary method with direct forcing for the simulation of particulate flows. *J. Comput. Phys*. 209 (2): 448–476.

CHAPTER 3

ANALYSIS OF VORTICAL GUST IMPACT ON AIRFOILS AT LOW REYNOLDS NUMBER

The contents of this chapter are fully included in:
Journal of Fluids and Structures (2020), vol. ***99****, 103138.*

Abstract

The response of a NACA0012 airfoil impacted by vortical gusts is investigated performing Direct Numerical Simulations of the two-dimensional incompressible flow. Taylor vortices of different diameter and intensity located at different vertical separations with respect to the airfoil are deployed in the free stream. These vortices, which are characterized by its compact distribution of vorticity, are advected downstream to interact with the airfoil, set at a fixed angle of attack. For the low Reynolds number used in these simulations ($Re = 1000$), the effect of the different parameters defining the vortical gust and the impact is characterized. It is found that the change in the time evolution of the variation of the lift coefficient with respect to the steady state, $\Delta C_l(t)$, is fairly independent on the angle of attack, at least in the range of α considered in this study. Furthermore, it is found that the time at which the peak in ΔC_l is produced scales with the diameter of the viscous core of the vortex and the free-stream velocity, D/U_∞. On the other hand, the maximum value of ΔC_l is roughly proportional to the non-dimensional vortex circulation, but varies non-linearly with the vertical distance between the vortex and the airfoil. This dependency can be captured by scaling ΔC_l with the relative intensity of the vertical velocity induced over the airfoil and the free-stream velocity (w_h/U_∞), where the former is defined as a integral of the vortex velocity profile over the chord of the airfoil. Using this scaling, the profiles of $\Delta C_l(tU_\infty/D)/(w_h/U_\infty)$ collapse over a single curve for the different

vortex intensities, sizes and vertical separations considered in the present study, specially during the initial evolution of the vortical gust impact. The self-similar profile of $\Delta C_l(tU_\infty/D)/(w_h/U_\infty)$ is found to depend on the velocity profile of the vortex (i.e., Taylor vortices versus Lamb-Oseen vortices). However, the peak aerodynamic force and the time to peak aerodynamic force seem to scale with D/U_∞ and w_h/U_∞ irrespective of the velocity profile of the vortex, suggesting that our definition of w_h is sufficiently robust.

3.1 Introduction

Unsteady aerodynamics, and in particular the unsteady response of airfoils to gusts, has been thoroughly studied in the frame of potential flow. The literature in the topic is vast, including classical (Küssner, 1936; Press & Mazelsky, 1954; Horlock, 1968) and more recent works (Tang & Dowell, 2002; Raveh & Zaide, 2006; Corkery & Babinsky, 2019), among many others. In general, the applications of potential theory to the gust response of an airfoil is a simplification of the problem that requires several assumptions, including a sufficiently high Reynolds number, attached flow over the airfoil and considering the gust as a small perturbation compared to the free stream. The conditions that allow these assumptions are easily satisfied in most conventional aircraft, but they are not easily satisfied for Micro Air Vehicles (MAVs).

According to Mueller & DeLaurier (2003), MAVs are small aerial vehicles with characteristic wing span of the order of 15 cm and cruise speeds of 1-10 m/s. Using Kolmogorov's scaling for an equilibrium turbulent flow, it is easy to show that in a typical atmospheric boundary layer the velocity fluctuations associated with a length scale of the order of $O(0.1)$ m are of the order of $O(1)$ m/s. This results in a gust velocity comparable to the cruise speed of the MAV, invalidating the small perturbation hypothesis and often resulting in massive separated flow over the wing of the MAV. Moreover, the typical Reynolds number of conventional aircraft is $Re = U_\infty c/\nu \sim 10^6 - 10^8$ (where c is the characteristic chord of the wing, U_∞ is the free-stream velocity and ν is the kinematic viscosity of air), while the Reynolds numbers for MAVs are usually much smaller, $Re \sim 10^3 - 10^5$.

The difference in the velocity and length ratios (i.e, between the gust and the vehicle) of conventional aircraft and MAVs has consequences in terms of the applicability of the different gust models that can be found in the literature. For a conventional aircraft a typical gust consists of a small velocity perturbation (longitudinal or transverse) occurring over a length scale much larger than the airfoil chord. These gusts can be modelled by an appropriate surge, plunge or pitching motion of the airfoil, since the velocity perturbation is felt (roughly) at the same time over the whole airfoil. Examples of recent studies of this type of gust at moderate to low Reynolds numbers include Perrotta & Jones (2018) and Moriche et al. (2019), among others. The results show that the gust produces a transient increase in the aerodynamic forces associated to the changes in the effective angle of attack of the plate, followed by an opposite sign extremum of smaller amplitude associated to the deceleration of the flow displaced by the plunge motion of the airfoil.

For MAVs, the small size of the vehicle results in a localized gust, where the characteristic length of the velocity perturbation is of the same order of magnitude (or even smaller) than the chord of the airfoil. Most experimental and numerical realization of these types of gusts are based on either airfoils/wings passing over a vertical jet (i.e, localized transverse gusts as in Perrotta & Jones, 2017; Biler et al., 2019; Leung et al., 2018; Corkery et al., 2018), or airfoils/wings encountering a localized vortex in the free-stream (i.e., vortical gusts as in Hufstedler & McKeon, 2019; Barnes & Visbal, 2018a; Zehner et al., 2018; Alaminos-Quesada & Fernández-Feria, 2017; Peng & Gregory, 2015; Nguyen et al., 2018; Barnes & Visbal, 2018b; Chen & Jaworski, 2020). The results of the localized transverse gusts are very similar to the plunge maneouvers discussed earlier when the jet width is sufficiently large (Leung et al., 2018; Corkery et al., 2018). For narrower jets, the initial evolution and the maximum lift coefficient are still similar to those observed in the plunge maneouvers, but the interaction of the leading edge vortex with the trailing shear layer of the jet results in a different recovery of the aerodynamic forces.

Note that plunge maneouvers and localized transverse gusts (jets) are inherently different to the vortical gusts, since in the latter the vortex intensity is modified by the interaction with the airfoil. Also, the vertical velocity induced by the vortex on the airfoil changes sign as the vortex moves downstream, resulting in two extrema of opposite sign on the lift coefficient with comparable intensities. The results of Barnes & Visbal (2018a), Peng & Gregory (2015), and Nguyen et al. (2018) at moderate Reynolds numbers ($Re \sim 10^3 - 10^4$) show that the times and intensities of these extrema depend on the intensity, size and vertical displacement of the vortex with respect to the airfoil. Similar conclusions are offered by Alaminos-Quesada & Fernández-Feria (2017), who propose a potential model to predict the lift force produced by a vortical gust. The model shows a moderately good agreement with the experimental results when the vertical distance between the vortex and the airfoil is sufficiently large, failing to predict head-on collisions. The potential model predicts that the enhancement of the aerodynamic forces is proportional to the vortex circulation and to the relative velocity between the vortex and the airfoil, producing a maximum force when the vortex trajectory bifurcates from passing above to below the airfoil.

It should be noted that the vortices generated in the experiment of Alaminos-Quesada & Fernández-Feria (2017) have viscous cores much smaller than the airfoil chord, so that the non-linear interactions between the airfoil and the incoming vortex are restricted to the trajectory of the vortex. On the other hand, the experiments of Hufstedler & McKeon (2019) and Peng & Gregory (2015) and the numerical simulations of Barnes & Visbal (2018a), Zehner et al. (2018), and Nguyen et al. (2018) have larger viscous cores, of the order of 0.1 - 0.5 chords. Larger viscous cores allow for stronger non-linear interactions between the vortex and the airfoil, specially for near head-on collisions, where the airfoil splits the vortex, disturbing the upper and lower boundary layer over the airfoil (Barnes & Visbal, 2018a).

A second important difference between the aforementioned studies is the velocity profile of the vortical gust. While Alaminos-Quesada & Fernández-Feria (2017) and Zehner et al. (2018) report

vortical gusts with potential-like vortices (i.e., with circumferential velocities decaying as the inverse of the distance to the vortical core), Nguyen et al. (2018) and Barnes & Visbal (2018a, 2018b) use Taylor vortices. The slower decay of the circumferential velocity of the former allow larger-scale interaction between the vortical gust and the airfoil, which potentially can affect the trajectory of the vortex and the maximum aerodynamic forces produced during the interaction.

The purpose of the present study is to analyze the aerodynamic performance of airfoils in the presence of large vortical gusts at low Reynolds numbers, of the order of $Re \sim 10^3$. The vortex sizes and characteristic velocities considered in this study are of the order of the free-stream velocity and the airfoil chord, respectively. As a consequence, the study corresponds to the flight regime of the smaller MAVs, which has not been covered in previous studies. The effect of the vortex size, intensity and vertical displacements will be analyzed, as well as the effect of decay rate of the circumferential velocity of the vortex. To that end, Taylor vortices and Lamb-Oseen vortices will be used to model vortical gusts. These two type of vortex models have very different profiles of circumferential velocity, and both have been used in the literature to model numerically vortical gusts (i.e., Lamb-Oseen vortices in Zehner et al., 2018, Taylor vortices in Nguyen et al., 2018; Barnes & Visbal, 2018a, 2018b).

The paper is organized as follows. The details of the numerical method are described in section 3.2. In section 3.3, the results for Taylor-vortex gusts impact on a NACA0012 are presented, where the response of the airfoil is characterized in terms of flow and forces. We extend the analysis to the rest of the cases in the database (Taylor and Lamb-Oseen vortices) and compare the obtained results with those provided by the potential theory. To end with the section, a semi-empiric model for the aerodynamic response of the airfoil is developed. Finally, conclusions are presented in section 3.4.

3.2 Numerical Method

The two-dimensional Navier-Stokes equations for an incompressible flow are solved using Direct Numerical Simulation (DNS) to evaluate the performance of a NACA0012 airfoil at angle of attack α when it encounters a vortical gust. The Reynolds number based on the airfoil chord c and the free stream velocity U_∞ is $Re = cU_\infty/\nu = 1000$, where ν is the kinematic viscosity of the fluid. Different velocities and sizes are considered for the vortical gust, which is modeled with a viscous vortex as discussed below.

The DNS is performed using TUCAN, a finite differences code with an immersed boundary method. For the temporal discretization, TUCAN uses a three-stages semi-implicit low-storage Runge-Kutta scheme. The spatial derivatives are approximated by centered finite differences in a staggered grid. The implementation of the immersed boundary method is the direct forcing proposed by Uhlmann (2005), using a regularized delta with a 3-point stencil. TUCAN has already been extensively validated, both for 2D (Moriche et al., 2016, 2017) and 3D (Gonzalo et al., 2018; Arranz et al., 2018a; Arranz et al., 2018b) configurations. More details about the implementation of TUCAN in 2D can be found in Moriche (2017).

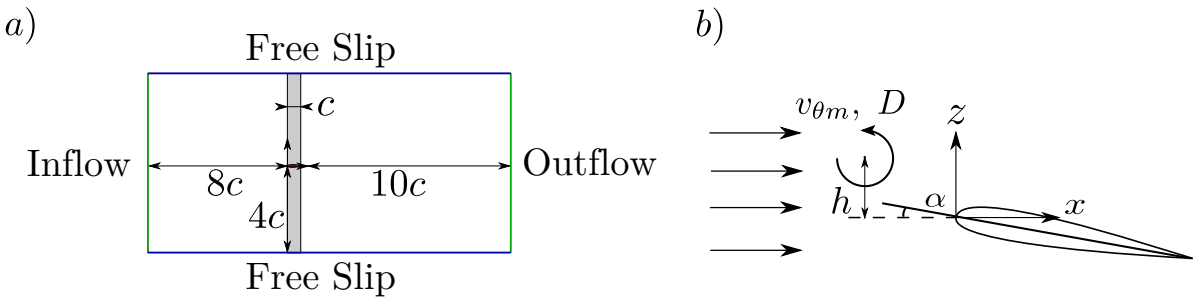

Figure 3.1: (*a*) Sketch of the computational domain. Grey zone represents the location of the airfoil in the x direction. (*b*) Sketch for the initial condition with the vortical gust.

The simulations have been performed in the computational domain sketched in figure 3.1(*a*), with dimensions $19c \times 8c$ in the streamwise and vertical directions, respectively. As shown in the figure, the airfoil is located roughly in the middle of the computational domain, leaving enough space upstream to place the viscous vortex that models the gust, and enough space downstream to properly develop the wake. The origin of the reference system is located at the leading edge of the airfoil. The free stream condition is modeled with an inflow velocity at the inlet boundary (left), while the outflow has been modeled with an advective boundary condition ($\partial\mathbf{u}/\partial t + U_\infty \partial\mathbf{u}/\partial x = 0$) at the outlet (right). Free slip boundary conditions are imposed in the horizontal boundaries (top and bottom).

The spatial resolution used for this study is 128 points per chord, which was selected after a grid refinement study. This spatial resolution yields a total of 2432×1024 grid points in the streamwise and vertical directions, respectively. The temporal resolution is chosen such that $CFL \leq 0.25$.

The vortical gust is modelled as viscous vortex, initially placed in the free stream at $x_0 = -4c$ (i.e. 4 chords upstream of the leading edge) and $z_0 = h$, as shown in figure 3.1(*b*). Two different vortex models are considered in the present study. Most cases presented here use finite Taylor vortices, like the ones used in Barnes & Visbal (2018a) and Nguyen et al. (2018). They have a characteristic diameter D, a characteristic circumferential velocity $v_{\theta m}$, and a circumferential velocity distribution given by

$$v_\theta = -v_{\theta m} \frac{2r}{D} \exp\left(\frac{-2r^2}{D^2}\right), \tag{3.1}$$

$$r = \sqrt{(x-x_0)^2 + (z-z_0)^2}. \tag{3.2}$$

This velocity profile is plotted in figure 3.2, together with the corresponding distribution of vorticity. It can be observed that the circumferential velocity is maximum at $r/D = 1/2$, where the circulation becomes $\Gamma = \Gamma_{v_{\theta max}} = \pi \exp\{-1/2\} v_{\theta m} D$. Besides, the vorticity distribution changes sign at $r/D = 1/\sqrt{2}$. At this radius the circulation of the viscous vortex is maximum, and equal to $\Gamma_{\max} = 2\pi \exp\{-1\} v_{\theta m} D$.

The present study also includes a few cases with Lamb-Oseen vortices. The rationale for this is to evaluate the effect that the vortex velocity profile has on the aerodynamic forces developed in the

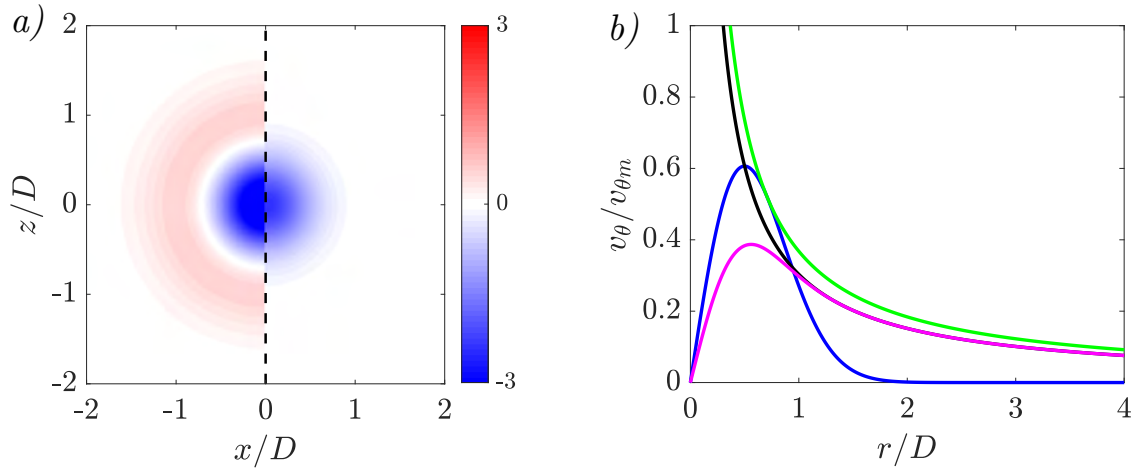

Figure 3.2: (*a*) Normalized vorticity, $\omega D/v_{\theta m}$, for viscous vortices: Taylor vortex (eq. 3.2) at the left, Lamb-Oseen vortex (eq. 3.3) with $\Gamma = \Gamma_{v_{\theta max}} = \pi \exp\{-1/2\} v_{\theta m} D$ at the right. (*b*) Normalized circumferential velocity profiles of viscous and potential vortices. ——: Taylor vortex. ——: Lamb-Oseen vortex with $\Gamma = \Gamma_{v_{\theta max}}$. ——: Potential vortex with $\Gamma = \Gamma_{v_{\theta max}}$. ——: Potential vortex with $\Gamma = \Gamma_{\max} = 2\pi \exp\{-1\} v_{\theta m} D$.

airfoil. Lamb-Oseen vortices have

$$v_\theta = \frac{\Gamma}{2\pi r}\left[1 - \exp\frac{-4r^2}{D^2}\right], \tag{3.3}$$

whose center will be initially located at $x_0 = -6c$. These simulations are run in a larger computational domain, with the inlet plane located at $-12c$. The vorticity and velocity profiles of this vortices are compared to Taylor vortices in figure 3.2, showing a similar viscous core but a much slower decay of the circumferential velocity. Indeed, at $r \gtrsim D$ the velocity of the Lamb-Oseen vortices is indistinguishable from that of potential vortices with comparable circulation, as shown in the figure.

3.3 Results

The effect that a vortical gust (with a given v_θ profile) has on the aerodynamic forces on a given airfoil depends on 4 parameters: the angle of attack of the airfoil (α), the size (D) and intensity ($v_{\theta m}$) of the vortex, and its vertical location (h) with respect to the leading edge of the airfoil. The influence of these parameters is analyzed with a parametric study, considering all combinations of 3 values for each parameter:

$$v_{\theta m}/U_\infty = 0.1,\ 0.3,\ 1.0 \tag{3.4}$$

$$D/c = 0.5,\ 1.0,\ 2.0 \tag{3.5}$$

$$h/c = 0.0,\ 0.5,\ 1.0 \tag{3.6}$$

$$\alpha = 0^\circ,\ 8^\circ,\ -8^\circ. \tag{3.7}$$

This results in a database of 81 simulations, for Taylor vortices, with a few additional cases using Lamb-Oseen vortices, available at http://aero.uc3m.es/cfd.html. In the following, these cases are labeled as AaZzDdVv, where a represents the angle of attack α, z is the nondimensional initial vertical position of the vortical gust h/c, d stands for the diameter of the core of the vortex normalized with the chord D/c, and v is the circumferential velocity of the vortex normalized with the freestream velocity $v_{\theta m}/U_\infty$. For example, A0Z0D1V1 stands the case were the airfoil with angle of attack $\alpha = 0°$ is impacted by a vortex with intensity $v_{\theta m}/U_\infty = 1$ and size $D/c = 1$, initially located at a vertical distance $h/c = 0$ with respect to the leading edge of the airfoil.

Note that, unless explicitly stated, the results presented in this section correspond to Taylor vortices.

3.3.1 Effects on C_l and C_d

We first describe the evolution of the flow around the airfoil during the impact of the vortical gust, prior to analyze the effect on the aerodynamic forces (i.e, lift and drag coefficients). Figure 3.3 shows the instantaneous vorticity field around the airfoil at several times. The time reference ($t = 0$) is taken as the time when the center of the vortical gust would have reached the leading edge of the airfoil ($x = 0$) if the airfoil were not present. Positive/negative vorticity (i.e., clockwise/counterclockwise) is represented in red/blue colors in the figure. The green line upstream of the airfoil shows an instantaneous streamline arriving to a point located $0.1c$ upstream of the leading edge of the airfoil, and serves as an indicator for the effective angle of attack of the airfoil. The figure also includes contours of the Lambda-2 vortex identification method of Jeong & Hussain (1995), using a threshold $\lambda_2 = -0.25U_\infty^2/c^2 \approx -4 \times 10^{-4}\omega_{\max}^2$.

Figures 3.3(a) and (b) show that as the vortical gust approaches the airfoil, it induces a positive effective angle of attack. This increase in the effective angle of attack results in the formation of a Leading Edge Vortex (LEV) in the upper surface of the airfoil, which travels downstream over the surface of the airfoil (figure 3.3c, d and e). At the same time, the boundary layer in the lower surface of the airfoil becomes thinner, and the stagnation point at the leading edge of the airfoil moves towards the lower surface. As the vortical gust moves around the airfoil, the effective angle of attack changes sign, the stagnation point in the leading edge shifts towards the upper surface, and the boundary layer in the lower surface becomes thicker. By the time the vortical gust leaves the airfoil (figure 3.3f), the LEVs formed in the upper surface and vortices generated in the separation of the lower-surface boundary layer are being shed into the wake, straining the remains of the vortical gust. It is interesting to note that the flow evolution depicted in figure 3.3 is qualitatively similar to that shown in Nguyen et al. (2018) and Peng & Gregory (2017) and Barnes & Visbal (2018a) at much higher Reynolds numbers. Also, similar flow structures are observed in the cases run with Lamb-Oseen vortices, as discussed later in section 3.3.2 (see figure 3.13).

The vorticity fields and effective angle of attack shown in figure 3.3 is consistent with the expected time evolution of the aerodynamic forces on the airfoil. This is confirmed in figure 3.4, which shows

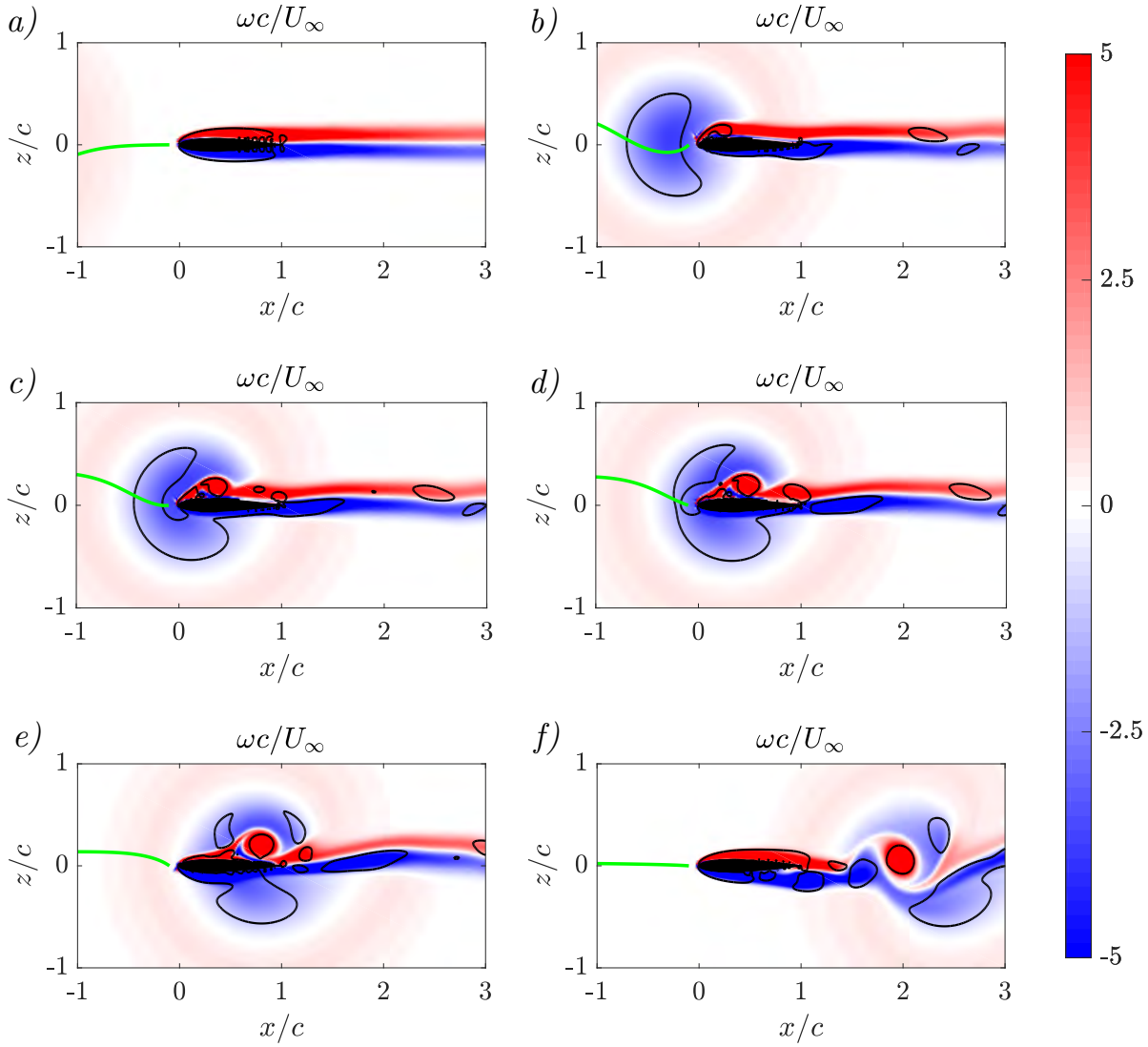

Figure 3.3: Vorticity contours for A0Z0D1V1 at (*a*) $tU_\infty/c = -2$, (*b*) $tU_\infty/c = -0.3$, (*c*) $tU_\infty/c = 0$, (*d*) $tU_\infty/c = 0.2$, (*e*) $tU_\infty/c = 0.7$, (*f*) $tU_\infty/c = 2.2$. The green line corresponds to the streamline arriving at $(x,z) = (-0.1c, 0)$. The black line corresponds to $\lambda_2 = -0.25U_\infty^2/c^2$.

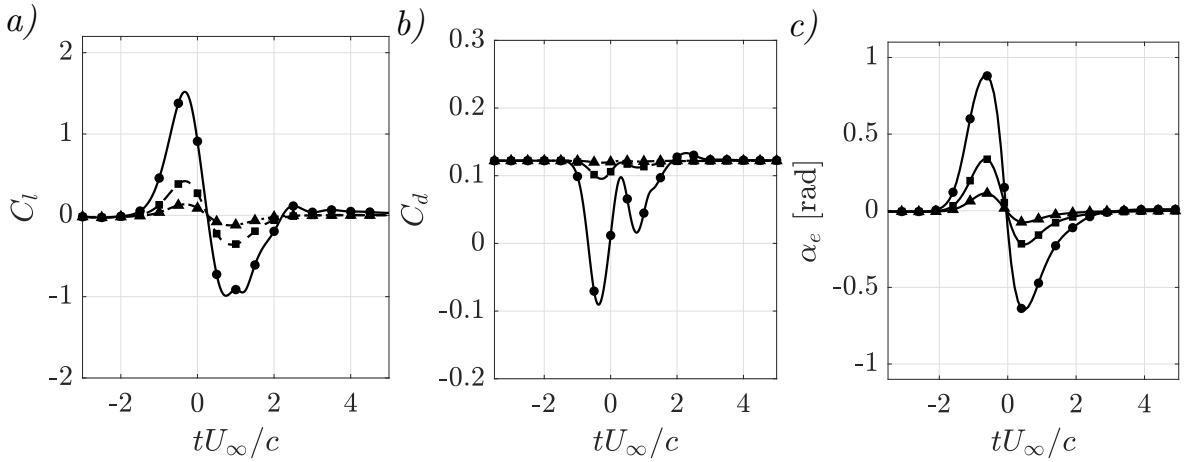

Figure 3.4: Temporal evolution of (*a*) lift and (*b*) drag forces, and (*c*) effective angle of attack for A0Z0D1. Symbols correspond to: ▲: $v_{\theta m}/U_\infty = 0.1$. ■: $v_{\theta m}/U_\infty = 0.3$. •: $v_{\theta m}/U_\infty = 1.0$.

the time evolution of the lift coefficient C_l, the drag coefficient C_d and the effective angle of attack α_e for case A0Z0D1V1. The effective angle of attack is defined somewhat arbitrarily as the angle between the chord of the airfoil and the direction of the velocity vector at a position $0.1c$ upstream of its leading edge (i.e., same point used to defined the green streamlines shown in figure 3.3). Note that α_e only represents the local orientation of the flow with respect to the airfoil in the vicinity of the leading edge.

The time evolution of C_l and α_e (figure 3.4*a* and *c*) shows positive peaks for $t < 0$ as the vortical gust approaches the leading edge, and a negative peaks for $t > 0$ as the gust sweeps the airfoil.

Note that the positive peak of C_l is larger in absolute value than the negative peak, consistent with the intensity of the peaks in the α_e and the absence of a strong LEV in the lower surface of the airfoil, as discussed in the previous paragraph. This weaker $C_{l,min}$ can be partly explained by the additional suction force produced by the LEV in the upper surface (observable in the pressure fields, not shown here), which partially counteracts the expected negative lift while it remains over the airfoil (i.e., for $0 < t \lesssim c/U_\infty$).

This counteracting effect is absent during the initial interaction between the vortical gust and the airfoil (i.e., $t < 0$), when the boundary layer on the lower surface of the airfoil has not developed an LEV.

The evolution of the drag coefficient is shown in figure 3.4(*b*), with two minima for C_d occurring nearly at the time instants where C_l is either maximum or minimum. Inspection of the pressure fields (not shown here) suggests that these drag-reduction events are due to the suction peaks generated at the leading edge when the effective angle of attack is either maximum or minimum (see α_e in figure 3.4(*c*) and flow visualizations in figures 3.3*b* and *e*). Similar reductions in drag have been reported in pitching-heaving motion (Moriche et al., 2017), and flapping motion (Gonzalo et al., 2018).

Figure 3.4 also includes the time histories of C_l, C_d and α_e for cases with decreasing intensity of the vortical gust (i.e, decreasing $v_{\theta m}$). The corresponding vorticity visualizations are provided in the

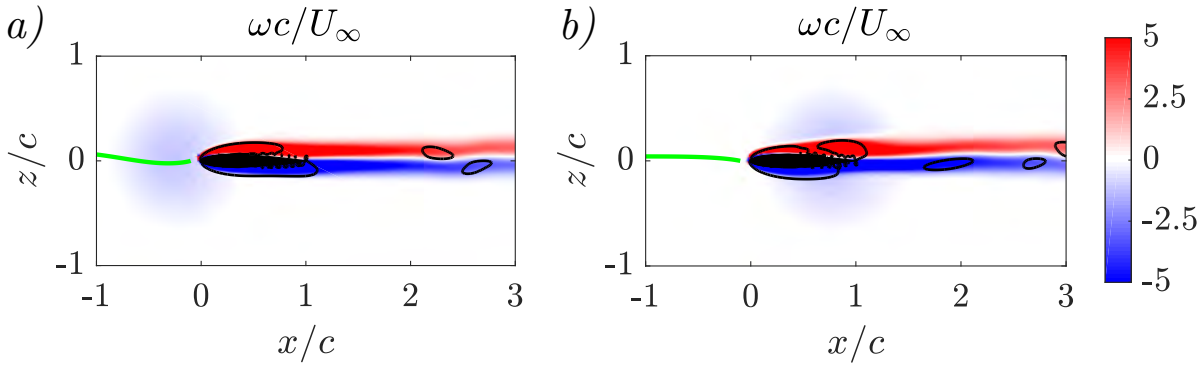

Figure 3.5: Vorticity contours for A0Z0D1V03 at (*a*) $tU_\infty/c = -0.3$, (*b*) $tU_\infty/c = 0.7$. The green line corresponds to the streamline arriving at $(x,z) = (-0.1c, 0)$. The black line corresponds to $\lambda_2 = -0.25U_\infty^2/c^2$.

Supplementary Material S1, S2 and S3. It can be observed that the behaviour is qualitatively the same irrespective of $v_{\theta m}$: maximum (C_l, α_e) and minimum C_d around $tU_\infty/c = -0.3$, minimum (C_l, α_e) and a second minimum C_d around $tU_\infty/c = 0.7$, slow recovery afterwards. From a quantitative point of view, the absolute value of the peaks of C_l, C_d and α_e increases monotonically with $v_{\theta m}$, suggesting that stronger vortical gusts results in larger effective angles of attack, and consequently larger aerodynamic forces. The changes in α_e and in the force coefficients also have a footprint in the vortical structures of the flow. Figure 3.3 shows that the vortical gust with $v_{\theta m} = 0.3U_\infty$ yields weaker vorticity perturbations in the boundary layers around the airfoil, and a strongly reduced vortex shedding into the wake.

The absence of strong LEVs could explain the similar amplitude of the maximum and minimum values of C_l and α_e for case A0Z0D1V03. Recall the previous discussion about the effect of the upper surface LEV on the negative peak of C_l for $t > 0$. Applied to case A0Z0D1V03, it would imply that C_l depends on the instantaneous angle of attack induced by the vortical gust, and not on the instantaneous positions of the LEVs (which are too weak to have an impact on C_l). From this point of view, the response of case A0Z0D1V03 is more *linear*, or *quasi-steady*.

The effect of the size of the vortical gust on the histories of C_l, C_d and α_e is evaluated in figure 3.6, where cases with $\alpha = 0°$, $h/c = 0$, $v_{\theta m}/U_\infty = 1$ and $D/c = 0.5$, 1 and 2 are shown. The corresponding vorticity visualizations are provided in the Supplementary Material S4, S1 and S5. It can be observed that the size of the vortical gust has an impact on both the temporal extent and the intensity of the interaction. For the largest vortical gust, the effect on the aerodynamic forces and effective angle of attack is felt earlier and last longer, the intensity of the resulting aerodynamic forces is larger (specially for the C_l), and the relaxation to the steady state is more complex, with alternating peaks of small amplitude in C_l for $t \gtrsim 3$.

The fact that the absolute value of the peaks of C_l and C_d increase monotonically with D, together with the effect of $v_{\theta m}$ discussed in figure 3.4, suggests that the important parameter in terms of predicting the intensity of these peaks is the circulation of the vortical gust, as suggested by the

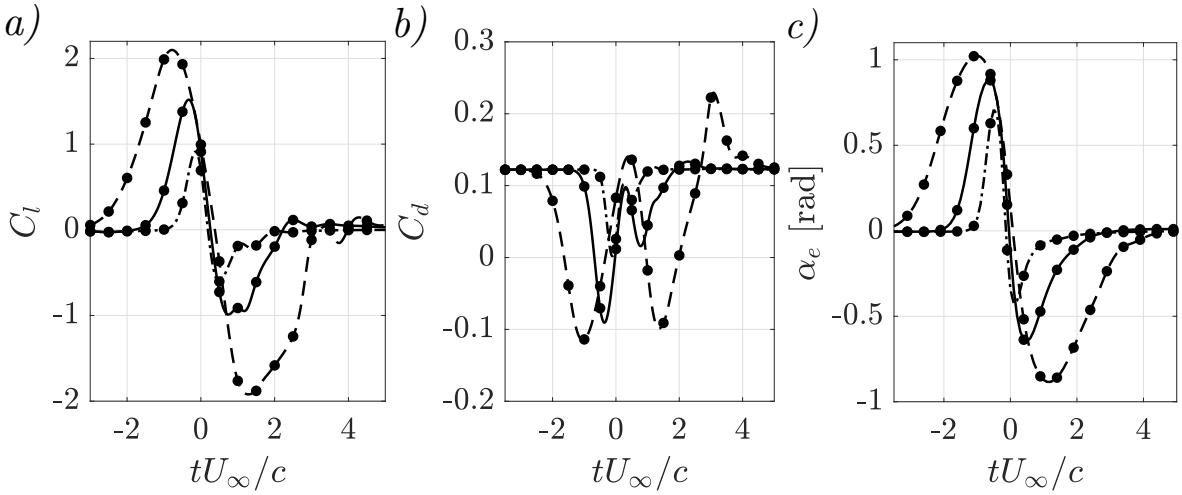

Figure 3.6: Temporal evolution of (*a*) lift and (*b*) drag forces, and (*c*) effective angle of attack for A0Z0V1. Linetypes correspond to: —·—·—: $D/c = 0.5$. ——: $D/c = 1.0$. — — —: $D/c = 2.0$.

potential theory model developed by Alaminos-Quesada & Fernández-Feria (2017). The results in figures 3.4 and 3.6 also suggests that the relationship between C_l and α_e might not be independent on the gust intensity: increasing $v_{\theta m}/U_\infty$ from 0.1 to 0.3 yields a 2-fold increase in $C_{l,\max}$ and $\alpha_{e,\max}$ (figure 3.4), but increasing D/c from 0.5 to 2 yields a 2-fold increase in $C_{l,\max}$ and a 1.5-fold increase in $\alpha_{e,\max}$ (figure 3.6). These issues will be investigated further in sections 3.3.2 and 3.3.3.

Next, the effect of the vertical distance (h) between the airfoil and the vortical gust is analyzed, keeping the size and intensity of the latter constant. The corresponding histories of C_l, C_d and α_e are shown in figure 3.7. The corresponding vorticity visualizations are provided in the Supplementary Material S1, S6 and S7. As h increases, the maximum values of C_l and α_e decreases monotonically, with essentially no variation on the time of the peaks. It is interesting to note that, while the negative peaks of α_e vary monotonously with h the same is not true for the negative peaks of C_l. Indeed, the strongest negative C_l is observed for the case with $h/c = 0.5$.

The non-monotonous behaviour of the negative peak of C_l with h can be explained comparing the flow visualizations of cases A0Z0D1V1 and A0Z05D1V1, shown in figures 3.3 and 3.8, respectively. The most striking difference between the vorticity fields of both cases at $tU_\infty/c = 0.7$ (figures 3.3*e* and 3.8*b*) is the position of the LEV developed on the upper surface of the airfoil, which is still over the airfoil for the case with $h = 0$ but downstream of the trailing edge for the case with $h/c = 0.5$. This difference is caused by the streamwise velocities induced by the vortical gust on the upper surface of the airfoil when $h/c = 0.5$, which advect the LEV faster downstream. As it can be observed in the pressure fields shown in figure 3.9(*a*), the low pressure region associated to the LEV in case A0Z0D1V1 is producing a positive contribution to C_l, and hence reducing the absolute value of the negative C_l peak at $tU_\infty/c = 0.7$. For case A0Z05D1V1 (figure 3.9*b*), the LEV and its associated low pressure region are downstream of the airfoil, and do not affect much the aerodynamic forces.

In terms of the effect of h on the drag of the airfoil, figure 3.7(*b*) shows that increasing h results

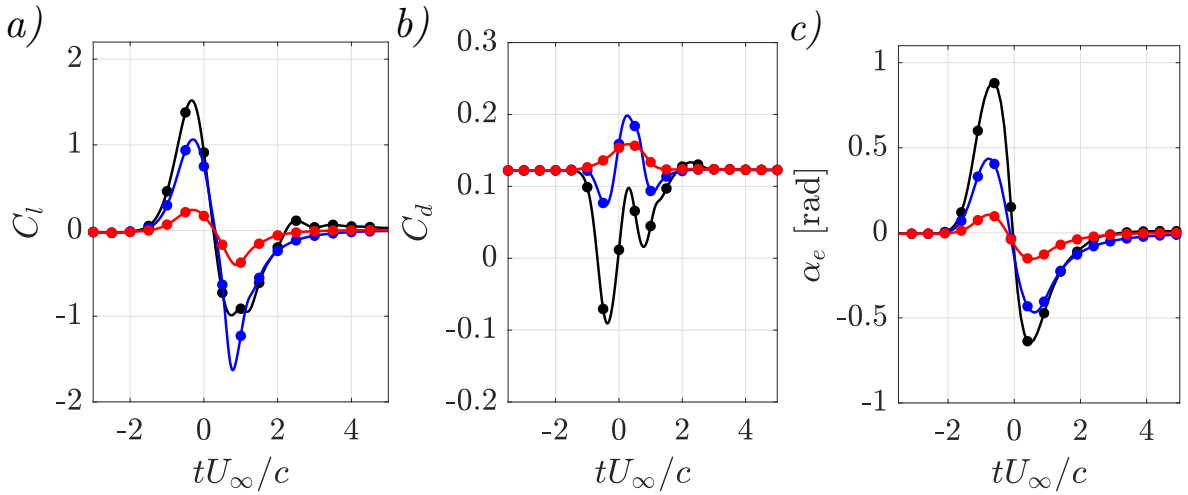

Figure 3.7: Temporal evolution of (*a*) lift and (*b*) drag forces, and (*c*) effective angle of attack for A0D1V1. Line colors correspond to: ——: $h/c = 0.0$. ——: $h/c = 0.5$. ——: $h/c = 1.0$.

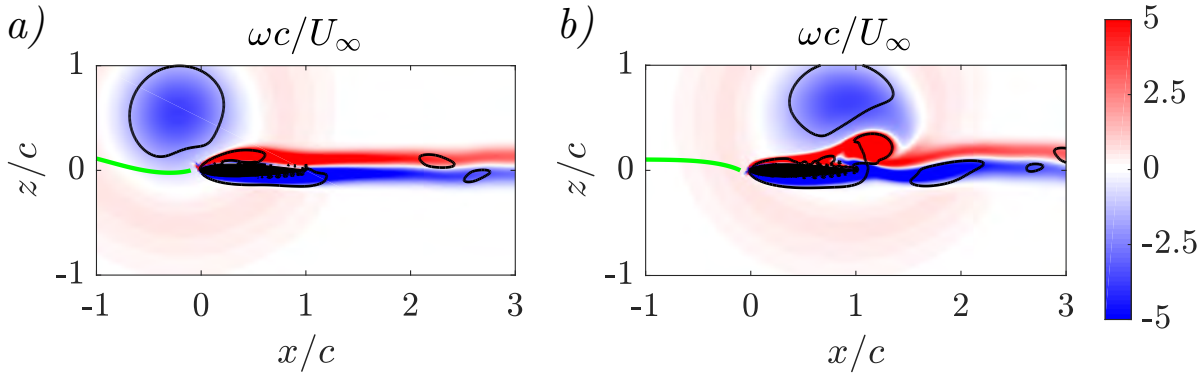

Figure 3.8: Vorticity contours for A0Z05D1V1 at (*a*) $tU_\infty/c = -0.3$, (*b*) $tU_\infty/c = 0.7$. The green line corresponds to the streamline arriving at $(x,z) = (-0.1c, 0)$. The black line corresponds to $\lambda_2 = -0.25U_\infty^2/c^2$.

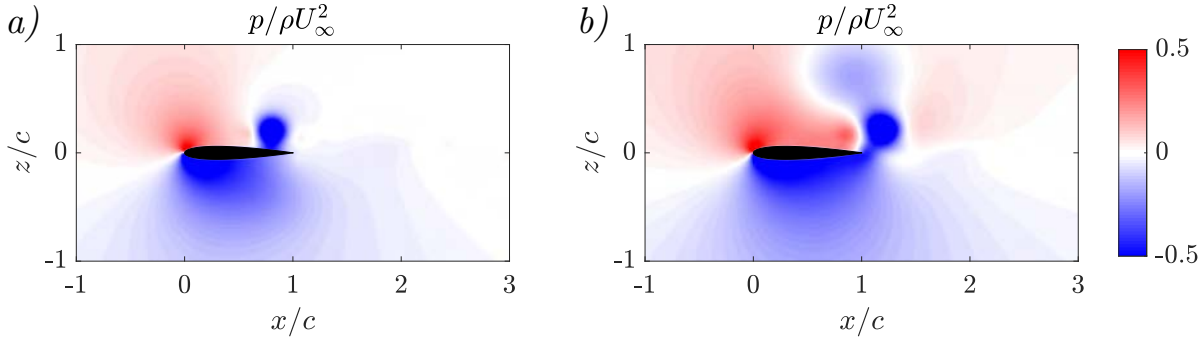

Figure 3.9: Pressure contours at $tU_\infty/c = 0.7$ for (*a*) A0Z0D1V1, (*b*) A0Z05D1V1.

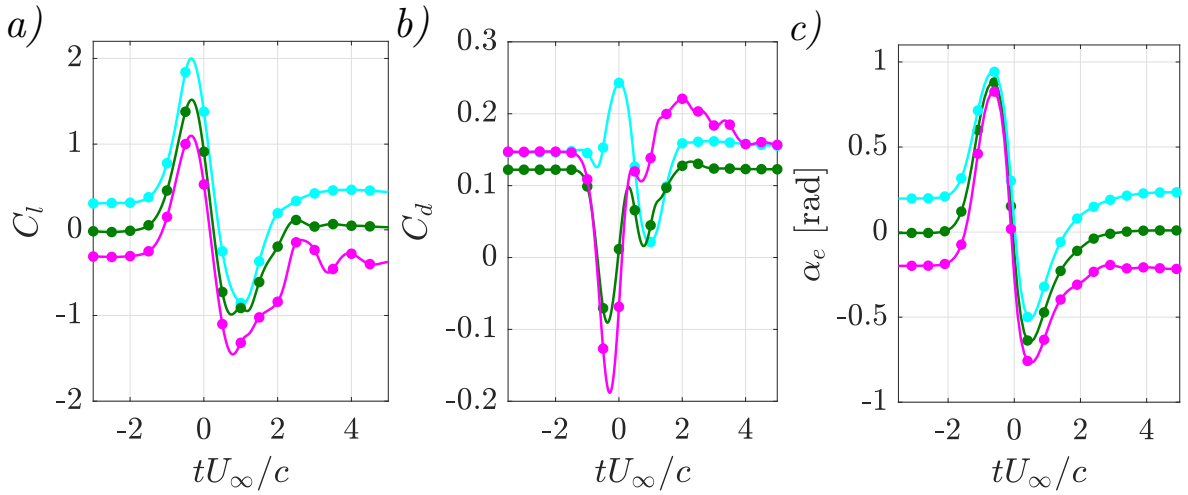

Figure 3.10: Temporal evolution of (*a*) lift and (*b*) drag forces, and (*c*) effective angle of attack for Z0D1V1. Line colors correspond to different angles of attack. ——: $\alpha = -8°$. ——: $\alpha = 0°$. ——: $\alpha = 8°$.

in weaker drag-reduction with respect to static values (i.e., higher values of C_d throughout the gust). Indeed, for $h/c = 1$ drag is increased with respect to the steady state value during the whole interaction with the vortical gust. This effect is probably the result of a decrease of the intensity of the suction peak at the leading edge (due to the reduction in the effective angle of attack) combined with an increase of the skin friction drag in the upper surface of the airfoil (due to the additional horizontal velocity induced by the vortex on the airfoil).

Finally, the effect of the angle of attack on the response of the airfoil to the vortical gust is evaluated in figures 3.10 and 3.11, where cases with $h/c = 0$, $D/c = 1$, $v_{\theta m}/U_\infty = 1$ and different α's are compared. The corresponding vorticity visualizations are provided in the Supplementary Material S8, S1 and S9. In terms of the lift coefficient, figure 3.10(*a*) shows that as α increases, the evolution of $C_l(t)$ is shifted upwards. Indeed, when the difference between the instantaneous C_l and its static value is analyzed (i.e., ΔC_l, plotted in figure 3.11*a*), the effect of α on the absolute value of the maximum and minimum peaks is very small, similar to previous observations in Hufstedler & McKeon (2019) or Biler et al. (2019). The effect of α is more apparent on the evolution of ΔC_l in the recovery phase, with stronger oscillations for $\alpha = -8°$ than for $\alpha = 0°$ or 8°.

In terms of the drag coefficient, α affects both C_d and ΔC_d, as shown in figures 3.10(*b*) and 3.11(*b*). In any case, the effect of α on C_d or ΔC_d is $\lesssim 0.3$, same order of magnitude as the differences in $\Delta C_{l,max}$ that appear in figure 3.11(*a*). Indeed, the changes in ΔC_d due to α can be explained taking into account the projection of the forces induced by the vortical gust along the x-direction. As α increases, the lift force resulting from the generation of the LEV in the upper surface is tilted backwards, resulting in an increased drag. On the contrary, for $\alpha = -8°$ this lift force is tilted forward, yielding a force along the negative x-axis that results in a stronger drag decrease than when $\alpha = 0°$ (where the drag decrease is only due to the suction at the leading edge).

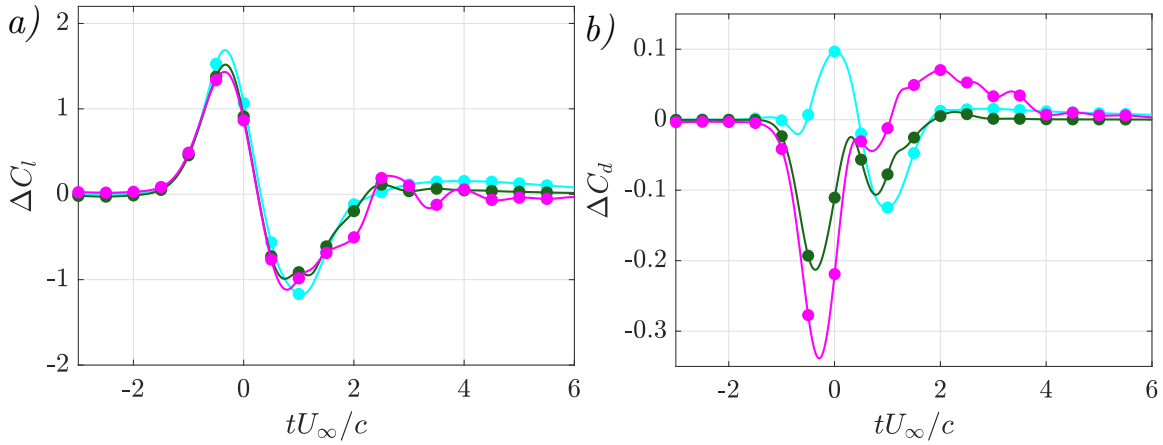

Figure 3.11: Temporal evolution of increments of (a) lift and (b) drag forces with respect to steady state values, for Z0D1V1. Line colors correspond to different angles of attack. ——: $\alpha = -8°$. ——: $\alpha = 0°$. ——: $\alpha = 8°$.

Lastly, the effect of the angle of attack of the airfoil in the effective angle of attack is shown in figure 3.10(c). First, the steady values of the α_e (i.e, for $tU_\infty/c \lesssim -2$ and for $tU_\infty/c \gtrsim 4$) are roughly 45% larger than the value of the angle of attack of the airfoil, emphasizing the fact that α_e characterizes the direction of the flow close to the leading edge, and not the direction of the free-stream with respect to the airfoil's chord. Second, the maximum of α_e is roughly insensitive to α, consistent with the weak effect that α has on the ΔC_l in figure 3.11(a). The same is not true for the minimum of α_e, which varies monotonously with α.

The analysis here presented is in agreement with the trends observed in previous studies at much higher Reynolds numbers (Nguyen et al., 2018; Peng & Gregory, 2017; Barnes & Visbal, 2018a).

3.3.2 Comparison of viscous vortical gusts with potential flow theory.

From the point of view of modeling, it is interesting to evaluate to what extent the potential theory is able to model the forces on the airfoil due to the vortical gust presented in 3.3.1. To that end, the potential model described in Alaminos-Quesada & Fernández-Feria (2017) is applied to the present configuration. This potential model uses Milne-Thomson circle's theorem and conformal mapping, modelling the vortical gust as a point vortex travelling downstream and interacting with a flat plate. The circulation of the vortex remains constant during this interaction, while the bound circulation of the flat plate varies. The trajectory of the vortex is given by a system of ODEs (which must be solved numerically), and forces on the plate (i.e, its bound circulation) can be computed analytically once the instantaneous location of the vortex is known.

It should be noted that the main differences between the assumptions of the potential theory model and the conditions simulated here are the low-Reynolds number ($Re = 1000$ vs a virtually infinite Reynolds number in the potential theory), the viscous nature of the vortex (with the differences in the v_θ profiles shown in figure 3.2), and the finite thickness of the airfoil vs an infinitely thin flat

$v_{\theta m}/U_\infty = 0.1$	▲	$D/c = 0.5$	−·−·	$h/c = 0$	——
$v_{\theta m}/U_\infty = 0.3$	■	$D/c = 1.0$	——	$h/c = 0.5$	——
$v_{\theta m}/U_\infty = 1.0$	•	$D/c = 2.0$	− − −	$h/c = 1$	——

Table 3.1: Linetypes and symbols used for Taylor vortices at $\alpha = 0°$.

plate. Additionally, the radius of the viscous vortex considered here is $r_{vc} \sim O(c)$, while the potential theory relies on $r_{vc}/c \ll 1$.

Figure 3.12(a) shows the time evolution of ΔC_l for Taylor, Lamb-Oseen and potential vortices, for cases with $\alpha = 0°$, $v_{\theta m}/U_\infty = 1$ and $D/c = 1$. Note that ΔC_l is plotted versus the streamwise position of the vortical gust with respect to the leading edge of the airfoil, which for the present viscous vortices (Taylor and Lamb-Oseen) is just $X_l(t) = tU_\infty$. Also, the circulation of the Taylor vortex is estimated at the radius of maximum v_θ (as done in Alaminos-Quesada & Fernández-Feria (2017) when comparing the potential model with the experimental results), resulting in $\Gamma = \Gamma_{v_{\theta\max}} = v_{\theta m} D\pi \exp(-1/2)$. If we focus on the first positive peak in ΔC_l, it can be observed that there is no clear agreement between the viscous and potential cases. However, both Taylor and Lamb-Oseen vortices show similar behavior when the vortex is close to the airfoil, at least in terms of the time to maximum ΔC_l and in the transition from $\Delta C_l > 0$ to $\Delta C_l < 0$. Indeed, the instantaneous vorticity fields of Taylor and Lamb-Oseen vortices for case A0Z0D1V1 (see figure 3.13) show that similar vortical structures are formed during the interaction between the viscous vortices and the airfoil. It is possible to see that both vorticity and the effective angle of attack for Lamb-Oseen cases are lower, justifying the lower value for the peaks in ΔC_l compared with Taylor vortices in figure 3.12(a). Note also that the effect of the Lamb-Oseen and potential vortices on the ΔC_l of the airfoil is evident when the vortices are relatively far from the airfoil, while the effect of the Taylor vortex is only felt at distances of the order of D. Finally, the potential theory predicts a negative peak of ΔC_l that increases in magnitude monotonously with h/c, while in the case of the viscous vortical gust this variation is not monotonous, due to the effect of h/c on the advection velocity of the LEV generated in the upper surface (discussed in section 3.3.1). Similar results are obtained for other values of D and $v_{\theta m}$.

The poor performance of the potential model to predict $\Delta C_{l,\max}$ in the present case contrasts with the relatively good agreement reported in Alaminos-Quesada & Fernández-Feria (2017) between experiments and the potential theory for $h \lesssim c$ and small angles of attack. The comparison between potential, Taylor and Lamb-Oseen vortices suggests that the reason for the present mismatch is related to the differences in the v_θ profile of viscous and potential vortices at small r, i.e. within the viscous core of the vortex. Indeed, the experiments agreeing with the potential model in Alaminos-Quesada & Fernández-Feria (2017) were performed at a larger Reynolds number ($Re \approx 24000$), resulting in smaller viscous cores than those considered here: the reported value of the radius to maximum circumferential velocity in the experiments is $r_{vc} = 0.07c$, while the present vortical gusts have $r_{vc} = D/2 = [0.25 - 1]c$. As a consequence, we conjecture that the viscous cores of the vortices in the experiments of Alaminos-Quesada & Fernández-Feria (2017) are weakly affected by

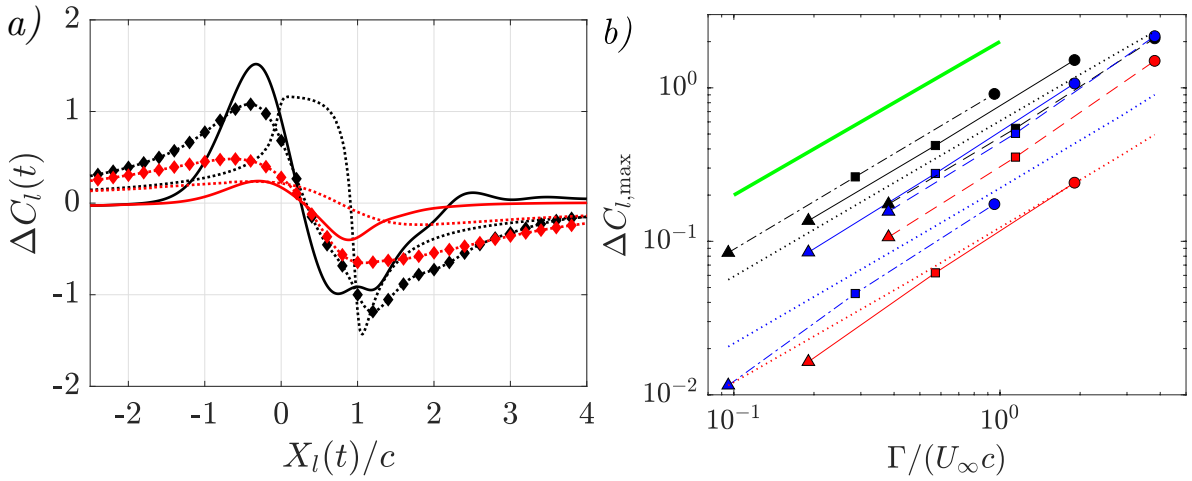

Figure 3.12: (*a*) Evolution of ΔC_l with the streamwise position of the vortical gust ($X_l(t)/c$), for Taylor (——), Lamb-Oseen (⧫), and Potential vortices (·····). All cases have $\alpha = 0°$, $D/c = 1$, $v_{\theta m}/U_\infty = 1$ and $\Gamma = \Gamma_{v_{\theta\max}}$. The line color indicates the value of h/c, as in table 3.1: ——: $h/c = 0.0$. ——: $h/c = 1.0$. (*b*) Variation of $\Delta C_{l,\max}$ with the non-dimensional circulation, at $\alpha = 0°$. Taylor vortices are coded to indicate D/c and h/c, using the linetypes and colors specified in table 3.1. Dotted lines with open circles correspond to results from the potential model, colored with h/c (as in table 3.1). The solid green line on the top is $\Delta C_{l,\max} = \Gamma/(U_\infty c)$.

the interaction with the airfoil, analogous to the constant circulation vortices of the potential model. On the other hand, in the present simulations the vortical gusts are modified in the interaction with the airfoil, provided they are strong enough. This can be observed in the λ_2 contours presented in figures 3.3, 3.8 and 3.13. Weaker vortical gusts seem less affected by the airfoil, like case A0Z0D1V03 (see figure 3.5).

Besides these differences, the DNS results show that $\Delta C_{l,\max}$ is roughly proportional to the circulation of the vortical gust, as predicted by the potential model. This is shown in figure 3.12(*b*), where all cases with $\alpha = 0°$ are presented. The line types and symbols used in the figure for the Taylor vortices are reported in table 3.1. The results of the potential model for $h/c = 0, 0.5$ and 1 are also included in the figure with open symbols. It can be observed that for viscous vortical gusts at given values of $\Gamma/(U_\infty c)$ and $h/c = 0$, the resulting $\Delta C_{l,\max}$ varies up to a factor of 2 when D/c varies from 0.5 to 2. This variability, which is not captured by the potential model, becomes greater as h increases.

3.3.3 A semi-empirical model for lift response to viscous vortical gusts

Based on the results presented in the previous sections, it is clear that for the viscous vortical gusts considered in the present study the resulting $\Delta C_l(t)$ depends on the intensity of the vortical gust (i.e., its circulation), the vertical distance to the airfoil and the size of the vortical gust. Note that the potential model does not include the latter, but assumes that $r_{vc} \ll c$. As a consequence, the potential model is flawed when the radius of the viscous core of the vortex is not much smaller than the airfoil chord.

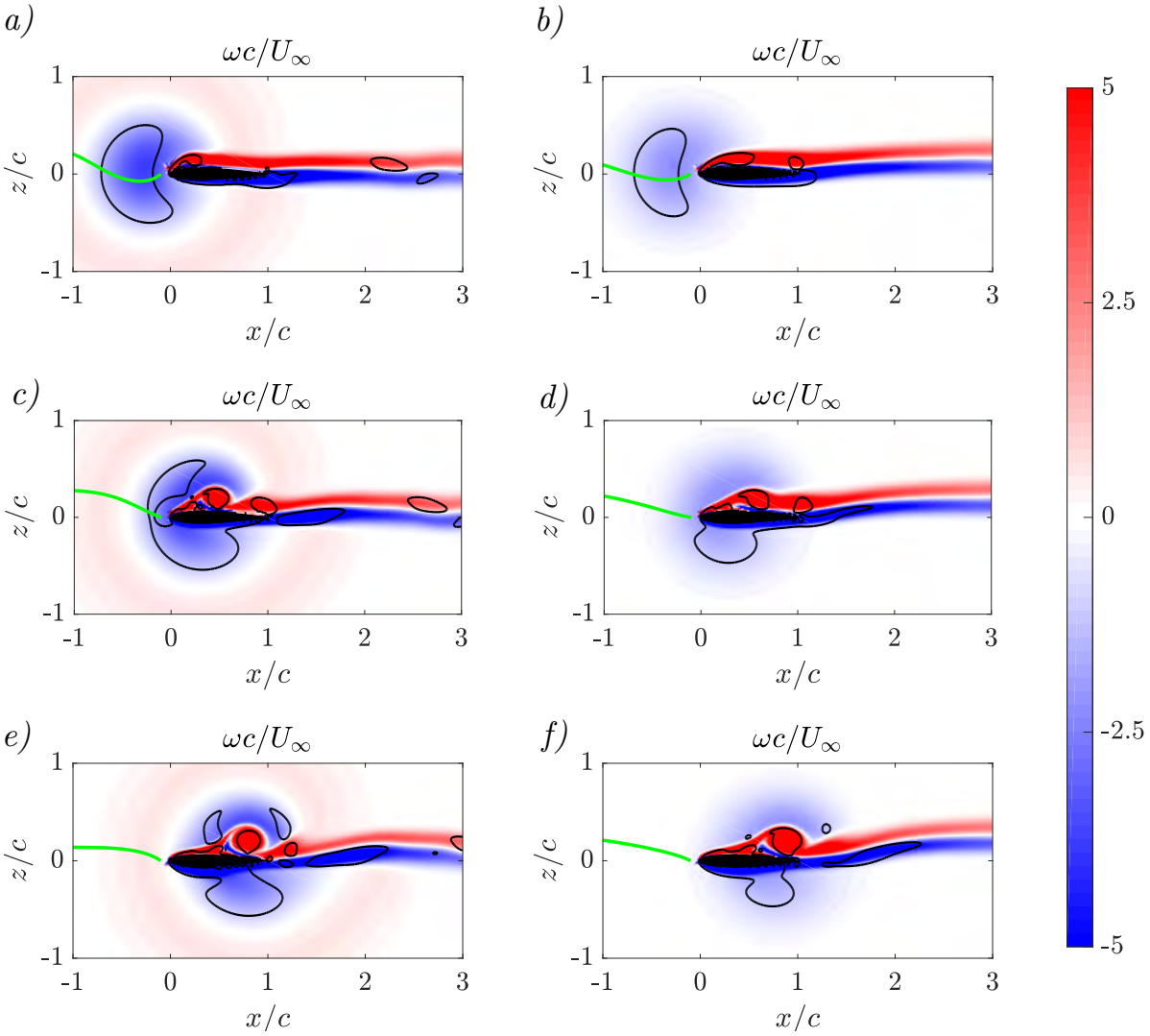

Figure 3.13: Vorticity fields for Taylor Vortex (left) and Lamb-Oseen Vortex (right) with A0Z0D1V1 at $tU_\infty/c = -0.3$ (top), $tU_\infty/c = 0.2$ (mid) and $tU_\infty/c = 0.7$ (bottom). The green line corresponds to the streamline arriving at $(x,z) = (-0.1c, 0)$. The black line corresponds to $\lambda_2 = -0.25U_\infty^2/c^2$.

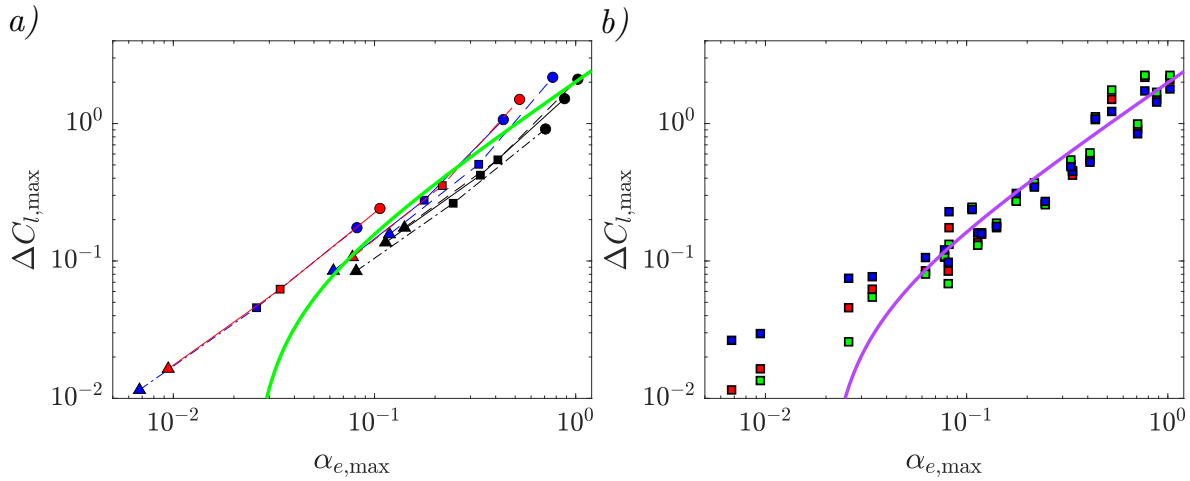

Figure 3.14: Maximum ΔC_l as a function of the maximum effective angle of attack $\alpha_{e,\max}$ induced by the vortex on the airfoil in logarithmic scale. (*a*) Taylor vortices for $\alpha = 0°$. Lines and colors as indicated in table 3.1. (*b*) Taylor vortices for different angles of attack (——: $\alpha = 8°$; ——: $\alpha = 0°$; ——: $\alpha = -8°$). Green (——) and purple (——) lines correspond to fittings (*a*) using only cases with $\alpha = 0°$ and (*b*) using cases with $\alpha = -8°, 0°, 8°$.

Previous works on transverse gusts (Moriche et al., 2019; Perrotta & Jones, 2017) have shown that the peak values of the lift coefficient due to the gust (i.e., $\Delta C_{l,\max}$) are roughly proportional to the maximum effective angle of attack, defined as the ratio between the maximum vertical velocity of the gust over the free-stream velocity. Similar observations where made by Gonzalo et al. (2018) when comparing heaving and flapping wings. Hence, it seems reasonable to test how well does $\alpha_{e,\max}$ characterizes $\Delta C_{l,\max}$ in the present configurations, even if the effective angle of attack in transverse gusts is *global* (i.e, it is felt by the whole airfoil) while the definition of $\alpha_e(t)$ used here is *local* (i.e., only represents the flow direction near the leading edge).

This test is performed in figure 3.14, where $\Delta C_{l,\max}$ is plotted as a function of $\alpha_{e,\max}$. Figure 3.14(*a*) only shows results for $\alpha = 0°$, while figure 3.14(*b*) shows results for $\alpha = -8°, 0°$ and $8°$. The solid lines in both panels correspond to linear fits for $\Delta C_{l,\max}(\alpha_{e,\max})$, with $R^2 = 0.8895$, $R^2_{adjusted} = 0.8851$, and $RMSE = 0.217$ for figure 3.14(*a*) and $R^2 = 0.8871$, $R^2_{adjusted} = 0.8856$, and $RMSE = 0.2097$ for figure 3.14(*b*). Even if the linearity between $\Delta C_{l,\max}$ and $\alpha_{e,\max}$ approximately holds, there is considerable variation at a given $\alpha_{e,\max}$ depending on the values of D/c, h/c and α (i.e., a factor of two or more). Indeed, similar fits can be obtained for $\sin(\alpha_{e,\max})$, without any significant improvement over the results presented in figure 3.14. This variability was already anticipated in section 3.3, and it might be related to the *local* character of $\alpha_{e,\max}$ discussed above. Also, it is important to note that $\alpha_{e,\max}$ is not a parameter that is known *a priori*: it is a result of a (relatively costly) DNS simulation, and hence has a limited value in terms of a predictive model for vortical gusts.

In the remaining of this section we propose an alternative empirical model, that overcomes the limitations of the potential model and the scaling of $\Delta C_{l,\max}$ with $\alpha_{e,\max}$. This empirical model is based on scaling the lift coefficient with an *averaged* effective angle of attack that can be estimated

a priori (i.e., without solving a DNS), and on normalizing the time over which ΔC_l peaks with the size of the vortical gust. These two parameters (averaged effective angle of attack and proper time scale) completely characterize the effect of the vortical gust on the aerodynamic forces on the airfoil, capturing the influence of $v_{\theta m}$, D and h.

First of all, the results presented in section 3.3 suggest that the time at which ΔC_l peaks (namely, $t_{\max}$) depends mostly on the diameter of the viscous vortex (see figure 3.6), with little effect of $v_{\theta m}$ (i.e., figure 3.4), h (i.e., figure 3.7) and α (i.e., figure 3.10). This idea is also supported by the results of the potential model, since the ΔC_l of the potential vortices (with $D \to 0$) peak at $X_l(t)/c = 0$ (i.e., $tU_\infty/c = 0$), as shown in figure 3.12(a). Figure 3.15(a) shows the time to peak as a function of D/c for all the cases in the present database, including Taylor and Lamb-Oseen vortices. Remember that $t = 0$ corresponds to the time at which the center of the viscous vortex would reach the position of the leading edge of the airfoil, if the airfoil were not present. The figure shows that $t_{\max}$ is approximately a linear function of D/c. Indeed, the agreement of the data from Taylor vortices to linear regression lines (computed independently for each value of α) is reasonably good for most of the data. The regression lines for $\alpha = 0°$ and $8°$ coincide (red and green dashed lines), whereas the regression line for $\alpha = -8°$ (in blue dashed line) is slightly different. Most of the outliers at $D/c = 1$ seem to correspond to $\alpha = -8°$. The linear fit between $t_{\max}$ and D/c also seems to work reasonably well for the Lamb-Oseen vortices when $h/c = 0$ and 0.5 (black and blue diamonds in figure 3.15(a) collapsing on top of each other), but not for the Lamb-Oseen vortex at $h/c = 1$ (red diamond on figure 3.15a).

Figure 3.15(b) shows $t_{\max}$ versus the circulation of the vortical gusts for Taylor and Lamb-Oseen vortices with $\alpha = 0°$. The data for the Taylor vortices appear clustered in horizontal lines, each line corresponding to a value of D/c, although with some scatter for cases with $\Gamma/(U_\infty c) \gtrsim 2$. The Lamb-Oseen vortices have $D/c = 1$, and consequently we can observe that they fall close to the Taylor vortices with $D/c = 1$, at least for $h/c = 0$ and 0.5. Again, the Lamb-Oseen vortex with $h/c = 1$ presents a different behaviour, with a value of $t_{\max}$ closer to the largest Taylor vortices ($D/c = 2$).

Figure 3.15(a) also shows a linear regression line to the whole database (black dashed line), which corresponds to

$$t_{\max} U_\infty/c = -0.4033 D/c + 0.06997, \tag{3.8}$$

with $R^2 = 0.9718$, $R^2_{adjusted} = 0.9714$ and $RMSE = 0.0427$.

The second piece of the alternative empirical model proposed here is the *averaged* effective angle of attack. Unlike $\alpha_e(t)$ defined in section 3.3, the idea is to provide an effective angle of attack that can be computed *a priori* and that captures the *global* effect of the vortical gust on the airfoil. Hence, we choose to work with the spatial average of the vertical velocity induced by the vortex over the airfoil chord, namely w_h. This average is computed when the vortical gust is at $x_{\max}$, which corresponds to the the streamwise position where ΔC_l peaks. For the Taylor vortex, this results in

$$w_h = \frac{1}{c}\int_0^c v_{\theta m} \frac{2(x - x_{\max})}{D} \exp\Big(-\frac{2r^2}{D^2}\Big)\, \mathrm{d}x, \tag{3.9}$$

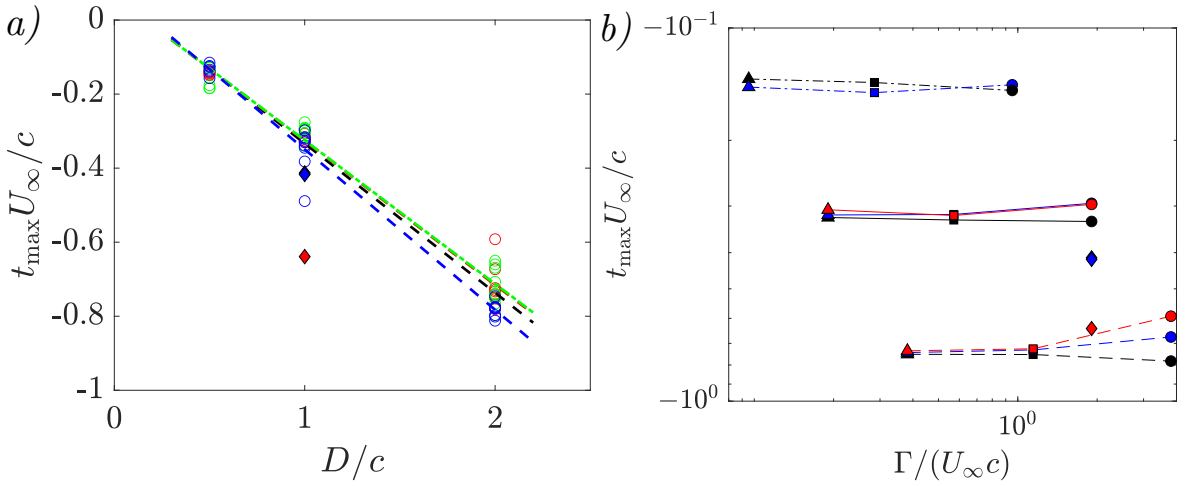

Figure 3.15: (*a*) Time for maximum ΔC_l, as a function of the diameter of the viscous gust. Taylor vortices are represented by empty circles, colors indicating the angle of attack (——: $\alpha = 8°$; ——: $\alpha = 0°$; ——: $\alpha = -8°$). Dashed lines correspond to the linear regressions for each angle of attack. (*b*) Time for maximum ΔC_l, as a function of the circulation of the vortex, for $\alpha = 0°$. Taylor vortices are represented with the lines and symbols reported in table 3.1, and their circulation is defined as $\Gamma = \Gamma_{v_{\theta,\max}}$. In both panels, Lamb-Oseen vortices are represented with diamonds colored with h/c (♦: $h/c = 0.0$; ♦: $h/c = 0.5$; ♦: $h/c = 1.0$).

where $r = \sqrt{(x - x_{\max})^2 + h^2}$ and $x_{\max} \approx U_\infty t_{\max}$. The latter assumes a constant advection velocity of the vortical gust at velocity U_∞, and requires estimating $t_{\max}$ using equation (3.8). Note that w_h depends on the vortex intensity, size and vertical displacement of the vortical gust, and can be estimated *a priori*, without running a simulation or performing an experiment.

Figure 3.16 shows $\Delta C_{l,\max}$ as a function of w_h/U_∞ in logarithmic (a,b) and linear scales (c,d), for $\alpha = 0°$ (a,c) and $\alpha = -8°, 0°, 8°$ (b,d). The figures also include a linear regression curve (in cyan) given by

$$\Delta C_{l_{max}} = 4.076 \cdot w_h/U_\infty - 0.00317. \tag{3.10}$$

This curve has been obtained fitting all Taylor vortices, resulting in a linear regression with $R^2 = 0.9748$, $R^2_{adjusted} = 0.9744$ and RMSE=0.0991, which has a smaller scatter than $\Delta C_{l,\max}$ versus $\alpha_{e,\max}$ in figure 3.14.

Figure 3.16 shows that equation (3.10) adjust the Taylor vortices moderately well at all α. The small deviations observed for $w_h/U_\infty \lesssim 10^{-2}$ correspond to small vortices ($D/c = 0.5$) relatively far from the airfoil ($h/c \geq 0.5$), as it can be observed in 3.16(*a*) for the $\alpha = 0°$ case. On the other hand, the small deviations observed for the largest values of w_h correspond to cases with $v_{\theta m} = U_\infty$, as it can be observed in figure 3.16(*c*) for case $\alpha = 0°$.

It is worth noting that the main trends observed in figure 3.16 are observed for other *a priori* estimations of the effective angle of attack of the airfoil, like the velocity induced by the vortex at $x = c/4$ (not shown). However, the scatter of the results is smaller for the integral definition of w_h given in equation (3.9).

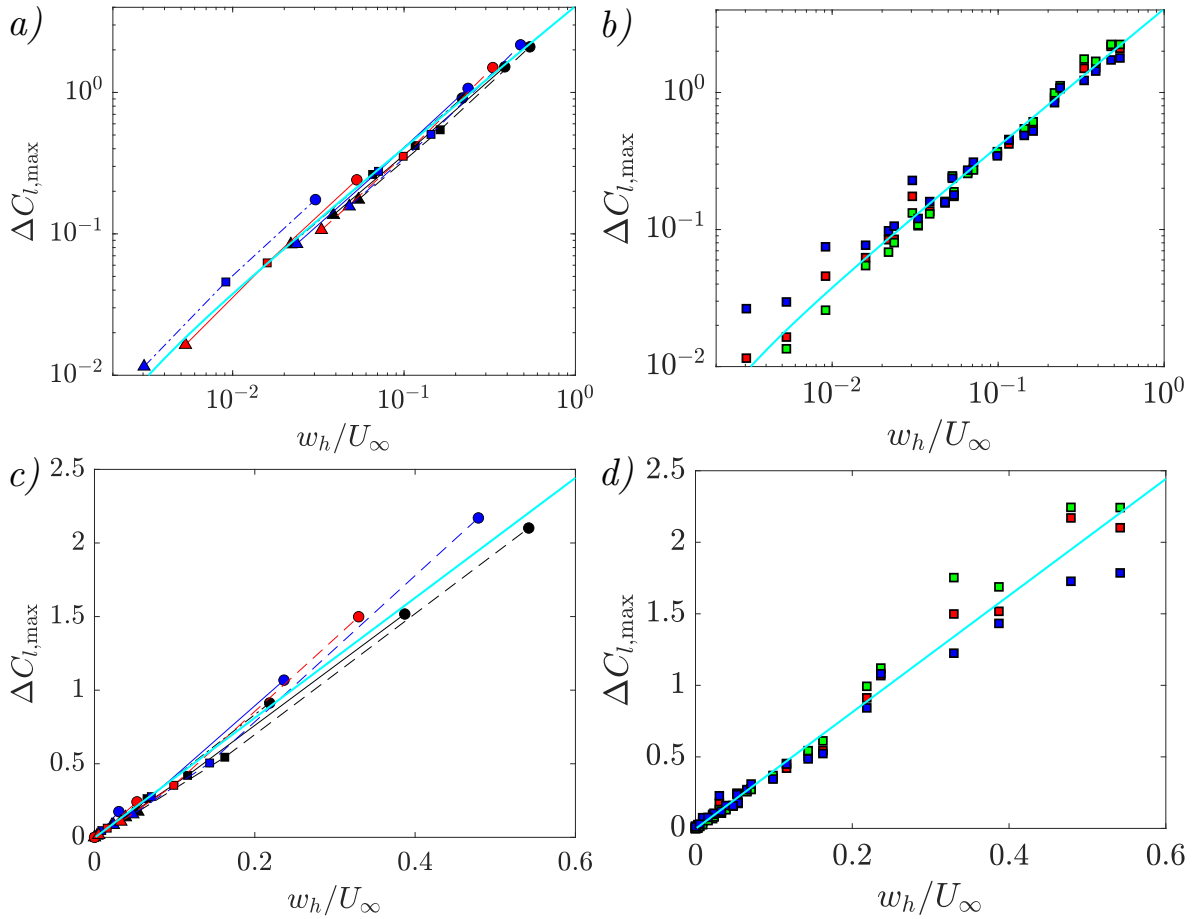

Figure 3.16: Maximum ΔC_l as a function of the averaged vertical velocity induced by the vortex on the airfoil, w_h/U_∞. (a,b) in logarithmic scale, and (c,d) in linear scale. (a,c) Taylor vortices for $\alpha = 0°$. Lines and colors as indicated in table 3.1. (b,d) Taylor vortices for different angles of attack (——: $\alpha = 8°$; ——: $\alpha = 0°$; ——: $\alpha = -8°$). In all panels the cyan line (——) corresponds to equation (3.10).

The relative good fit provided by equations (3.8) and (3.10), together with the similar shapes of the time evolutions of $C_l(t)$ shown in figures 3.4, 3.6, 3.7 and 3.10, raises the question of whether it is possible to obtain a self-similar evolution for ΔC_l. To that end, we compute ensemble averages of $\Delta C_l/(w_h/U_\infty)$ as a function of tU_∞/D[1] for the cases with Taylor vortices and $w_h/U_\infty > 0.01$. These are shown in figure 3.17(a), together with the corresponding medians and the 10% and 90% percentiles, for all Taylor vortices irrespective of the angle of attack.

Inspection of figure 3.17(a) shows that mean and median coincide until the peak in ΔC_l is reached, meaning that the statistical distribution is symmetric. Besides, the 10% and 90% percentile curves remain close to the mean value. In that sense, it is possible to conclude that the initial response of NACA0012 airfoils to Taylor vortices is self-similar. After $\Delta C_{l,\max}$ is reached, mean and median begin to deviate from each other, while the distance between the 10% and 90% percentiles increases. This

[1] Note that this is equivalent to $t/t_{\max}$, since $t_{\max}$ is proportional to D/U_∞.

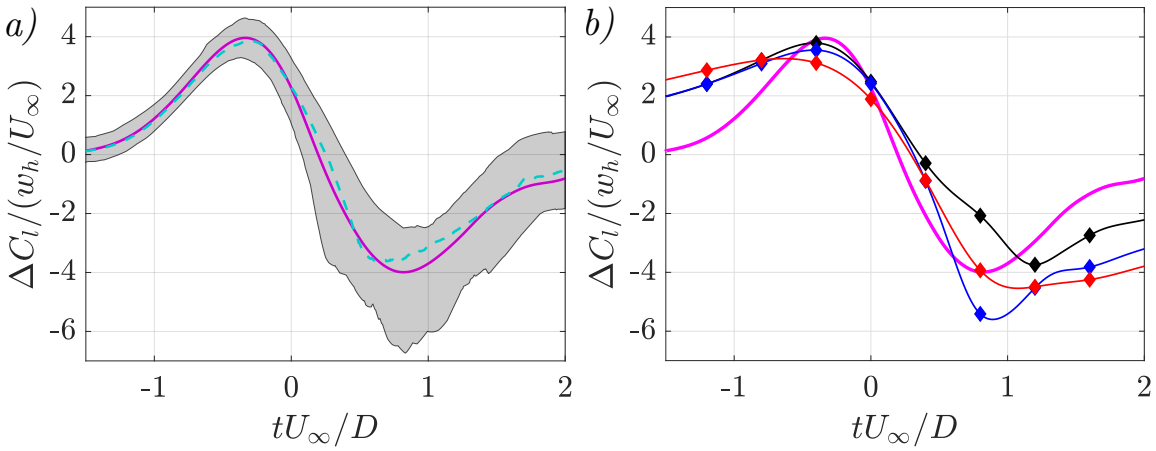

Figure 3.17: Evolution of $\Delta C_l/(w_h/U_\infty)$ as a function of tU_∞/D. (*a*) Mean (——), median (– – –), 10% and 90% percentiles (shaded areas) obtained from all cases with Taylor vortices. (*b*) Mean value for Taylor vortices (——), compared to instantaneous evolutions for Lamb-Oseen vortices (♦: $h/c = 0.0$; ♦: $h/c = 0.5$; ♦: $h/c = 1.0$).

suggest that the self-similar scaling is less valid for $t > 0$, mainly due to the non-linear interactions between Taylor vortex, LEVs and the boundary layers of the airfoil.

Figure 3.17(*b*) compares the self-similar evolution of $\Delta C_l/(w_h/U_\infty)$ of the Taylor vortices (given by its mean value) to the evolutions of $\Delta C_l/(w_h/U_\infty)$ of the three Lamb-Oseen vortices considered in this work. For the latter, w_h is estimated using the velocity profile given in equation (3.3), and the expression for $t_{\max}$ given in equation (3.8). Overall, Taylor and Lamb-Oseen evolutions do not agree, with the latter showing a much slower build up of $\Delta C_l/(w_h/U_\infty)$ for $t < 0$. This is consistent with the slower decay of the circumferential velocity profiles of Lamb-Oseen vortices, which would result in stronger long-distance interactions than in Taylor vortices. Besides these differences, it is worth noting that the peak values of $\Delta C_l/(w_h/U_\infty)$ for Taylor and Lamb-Oseen vortices agree reasonably well (i.e., approximately within the 10% and 90% percentiles of Taylor vortices, as shown in figure 3.17*a*). The Lamb-Oseen vortices with $h/c = 0.5$ and $h/c = 0$ collapse on top of each other during the initial evolution of the gust ($t < 0$), but show significant differences in the evolution for $t > 0$. The Lamb-Oseen vortex with $h/c = 1$ has a significantly different evolution, peaking at earlier times than $h/c = 0.5$ and 0. This suggests that, provided with the necessary DNS data, a self-similar evolution for $\Delta C_l/(w_h/U_\infty)$ could also be computed for Lamb-Oseen vortices, albeit with a different shape as that obtained for Taylor vortices.

3.4 Conclusions

The effect that vortical (viscous) gusts have on the aerodynamic forces of a NACA0012 airfoil has been analyzed using direct numerical simulations at low Reynolds number ($Re = 1000$). The Reynolds number considered here is consistent with the range of vortex diameters chosen for the study ($D/c = 0.5 - 2$), corresponding to viscous cores with sizes comparable to the airfoil chord. A large

database is presented and discussed, with 81 simulations of Taylor vortices (varying the size D, maximum circumferential velocity $v_{\theta m}$, vertical distance of the vortical gust h, and angle of attack of the airfoil α) and 3 additional simulations for Lamb-Oseen vortices.

In agreement with previous works at higher Reynolds numbers, a negative (counter-clockwise) vortical gust produces and initial increase in the lift coefficient as it approaches the airfoil ($t < 0$), followed by a negative perturbation in C_l as it sweeps the airfoil and interacts with the airfoil wake ($t > 0$). The angle of attack seems to have a small effect on the perturbation of the aerodynamic force, so that the change in the lift coefficient ΔC_l remains fairly independent on the angle of attack. The intensity of the initial positive perturbation of ΔC_l increases with the size (D) and intensity of the vortical gust ($v_{\theta m}$), and decreases when the vertical displacement (h) of the vortical gust with respect of the airfoil increases. The behaviour of the negative peak of ΔC_l at $t > 0$ is not monotonous with the vertical displacement of the vortex, due to the interactions between the vortical gust and the Leading Edge Vortex (LEV) developed during the initial interaction of the gust and the airfoil.

The interactions of the airfoil with Taylor and Lamb-Oseen vortices are qualitatively similar. However, due to the slower decay of the velocity profiles induced by the latter, the effect of Lamb-Oseen vortices is felt in the aerodynamic forces of the airfoil at larger distances than for Taylor vortices. As a consequence, head-on Lamb-Oseen vortices ($h/c = 0$) have a progressive effect on the airfoil that results in somewhat weaker LEVs and lower peaks of ΔC_l compared to Taylor vortices. On the other hand, when $h/c \sim 1.0$, Lamb-Oseen vortices have a stronger effect on the aerodynamic response of the airfoil than Taylor vortices.

Special attention has been paid to the characterization of the peak value in the lift coefficient perturbation ($\Delta C_{l,\max}$) with the parameters of the gust. Contrary to potential models, where $\Delta C_{l,\max}$ depends only on the vortex circulation ($\Gamma \propto D v_{\theta m}$) for a fixed vertical displacement (h), the present data show that ΔC_l for a viscous gust at a fixed h is not a linear function of the circulation of the gust (i.e., $v_{\theta m} D$), but has an explicit dependency on D. However, by defining and averaged vertical velocity induced by the vortical gust (w_h), we have been able to show empirically that $\Delta C_{l,\max} \approx 4 w_h / U_\infty$ for all viscous vortices considered here (Taylor and Lamb-Oseen). By definition, w_h depends on the intensity, size, velocity profile and vertical displacement of the gust. Moreover, it can be estimated *a priori*, without having to run a simulation or a experiment: only the velocity profile of the vortical gust is needed.

Finally, the scaling of $\Delta C_{l,\max}$ with w_h can also be applied to the initial development of $\Delta C_l(t)$, resulting in a single function $\Delta C_l / (w_h / U_\infty) = f(t U_\infty / D)$ characterizing the growth of ΔC_l for a given vortical gust velocity profile. Note that in the previous expression, w_h and $t U_\infty / D$ capture the effect of the intensity ($v_{\theta m}$), size (D) and vertical distance (h) on the perturbation of the lift coefficient. The effect of the velocity profile of the viscous vortical gust (i.e., Taylor vortex, Lamb-Oseen vortex, etc.) is captured in the shape of the function $f(t U_\infty / D)$. This result is particularly interesting, and its extension to higher Reynolds numbers, airfoil geometries and to other models for vortical gusts is left for future works.

Acknowledgements

This work was partially supported by grant DPI2016-76151-C2-2-R (AEI/FEDER, UE). We thank Dr. García-Villalba for fruitful discussions.

REFERENCES

Alaminos-Quesada, J. & Fernández-Feria, R. 2017. Effect of the angle of attack on the transient lift during the interaction of a vortex with a at plate. Potential theory and experimental results. *J. Fluid. Struct.* 74:131–141.

Arranz, G. et al. 2018a. A numerical study of the flow around a model winged seed in auto-rotation. *Flow, Turbul. Combust.* 101 (2): 477–497.

Arranz, G. et al. 2018b. Kinematics and dynamics of the auto-rotation of a model winged seed. *Bioinspir. Biomim.* 13 (3): 036011.

Barnes, C.J. & Visbal, M.R. 2018a. Counterclockwise vortical-gust/airfoil interactions at a transitional Reynolds number. *AIAA J.* 56 (7): 2540–2552.

Barnes, C.J. & Visbal, M.R. 2018b. Gust response of rigid and elastically mounted airfoils at a transitional Reynolds number. *Aerosp. Sci. Technol.* 74:112–119.

Biler, H., Badrya, C. & Jones, A.R. 2019. Experimental and computational investigation of transverse gust encounters. *AIAA J.,* 1–15.

Chen, H. & Jaworski, J.W. 2020. Aeroelastic interactions and trajectory selection of vortex gusts impinging upon Joukowski airfoils. *J. Fluid. Struct.* 96:103026.

Corkery, S.J. & Babinsky, H. 2019. An Investigation into Gust Shear Layer Vorticity and the Added Mass Force for a Transverse Wing-Gust Encounter. In *AIAA Scitech 2019 Forum,* 1145.

Corkery, S.J., Babinsky, H. & Harvey, J.K. 2018. On the development and early observations from a towing tank-based transverse wing–gust encounter test rig. *Exp. Fluids* 59 (9): 135.

Gonzalo, A. et al. 2018. From flapping to heaving: A numerical study of wings in forward flight. *J. Fluid. Struct* 83:293–309.

Horlock, J.H. 1968. Fluctuating lift forces on aerofoils moving through transverse and chordwise gusts. *J. Basic. Eng.* 90 (4): 494–500.

Hufstedler, E.A.L. & McKeon, B.J. 2019. Vortical gusts: Experimental generation and interaction with wing. *AIAA J.* 57 (3): 921–931.

Jeong, J. & Hussain, F. 1995. On the identification of a vortex. *J. Fluid Mech.* 285:69–99.

Küssner, H.G. 1936. Zusammenfassender Bericht über den instationären Auftrieb von Flügeln. *Luftfahrtforschung* 13 (12): 410–424.

Leung, J.M., Wong, J.G., Weymouth, G.D. & Rival, D.E. 2018. Modeling transverse gusts using pitching, plunging, and surging airfoil motions. *AIAA J.* 56 (8): 3271–3278.

Moriche, M. 2017. "A numerical study on the aerodynamic forces and the wake stability of flapping flight at low Reynolds number." PhD diss., Universidad Carlos III Madrid.

Moriche, M., Flores, O. & García-Villalba, M. 2016. Three-dimensional instabilities in the wake of a flapping wing at low Reynolds number. *Int. J. Heat. Fluid Fl.* 62:44–55.

Moriche, M., Gonzalo, A., Flores, O. & García-Villalba, M. 2019. Fast transverse maneuvers at low Reynolds numbers. In *AIAA Scitech 2019 Forum,* 0640.

Mueller, T.J. & DeLaurier, J.D. 2003. Aerodynamics of small vehicles. *Annu. Rev. Fluid Mech.* 35 (1): 89–111.

Nguyen, L., Golubev, V. & Visbal, M.R. 2018. Numerical Study of Transitional SD7003 Airfoil Interacting with Canonical Upstream Flow Disturbances. *AIAA J.* 56 (1): 158–181.

Peng, D. & Gregory, J.W. 2015. Vortex dynamics during blade-vortex interactions. *Phys. Fluids* 27 (5): 053104.

Perrotta, G. & Jones, A.R. 2017. Unsteady forcing on a flat-plate wing in large transverse gusts. *Exp. Fluids* 58 (8): 101.

Perrotta, G. & Jones, A.R. 2018. Quasi-steady approximation of forces on flat plate due to large-amplitude plunging maneuvers. *AIAA J.* 56 (11): 4232–4242.

Press, H. & Mazelsky, B. 1954. A study of the application of power-spectral methods of generalized harmonic analysis to gust loads on airplanes.

Raveh, D.E. & Zaide, A. 2006. Numerical simulation and reduced-order modeling of airfoil gust response. *AIAA J.* 44 (8): 1826–1834.

Tang, D. & Dowell, E.H. 2002. Experimental and theoretical study of gust response for high-aspect-ratio wing. *AIAA J.* 40 (3): 419–429.

Uhlmann, M. 2005. An immersed boundary method with direct forcing for the simulation of particulate flows. *J. Comput. Phys.* 209 (2): 448–476.

Zehner, P., Falissard, F. & Gloerfelt, X. 2018. Aeroacoustic study of the interaction of a rotating blade with a Batchelor vortex. *AIAA J.,* 629–647.

CHAPTER 4

LOAD MITIGATION ON HEAVING AIRFOILS USING PASSIVE TRAILING-EDGE FLAPS

Abstract

The load that can be mitigated using a passive-pitching trailing edge flap on NACA0012 airfoils at a Reynolds number Re = 1000 subjected to oscillations in the angle of attack is analysed. For this purpose, Direct Numerical Simulations of the two-dimensional incompressible flow have been performed. The validity of a quasi-steady model to predict the load mitigation using passive pitching flaps, previously proposed in the literature is questioned here. The model predicts a load mitigation proportional to the flap-to-chord length ratio a/c. The results obtained in this study generally deviate from the predictions of the model. The discrepancies cannot be explained only through the sole effect of inertia. Instead, the non-linearities in the aerodynamics or a combination of them and inertia are likely to be the responsibles of these deviations. However, the differences in load mitigation with respect to the model are limited. The results show that the increment in the reduction in fluctuations ΔR_F is proportional to the increment in $\Delta a/c$, which is in line with the predictions of the quasi-steady theory. For a given kinematics, the deviation from the actual value of R_F is a constant, independent of the value of a/c. On the other hand, the quasi-steady model fails in the prediction of the flap deflections obtained in this work. The effect that the inertia of the flap and the preload of the torsional spring have on the load mitigation are analysed for further investigation on the applicability of the passive control device.

4.1 Introduction

Small-scale bioinspired robotic vehicles have attracted the attention of the scientific community over the last decades. For example, flapping-wing micro air vehicles (MAVs), mimicking the flight of natural fliers as birds or insects, have shown potential to outperform the classical fixed-wing configurations in terms of efficiency due to their unconventional force-generating mechanisms (Haider et al., 2021). They fly in unsteady turbulent flows where, contrary to large-scale aircraft, the disturbances in the gusty environment are of the order of magnitude of the incoming velocity (Martínez-Muriel & Flores, 2020). Other small-scale devices, as micro wind turbines inspired in seeds (the maple seed, see Holden et al., 2015, or the *Petrea Volubilis* seed, see Gaitan-Aroca et al., 2020), have shown the feasibility of these devices and the possibility of achieving a more efficient performance.

The disturbances in the gusty environment affect the aerodynamic performance of these bioinspired devices. These disturbances cause cyclic or chaotic loads on the small-scale vehicles and turbines, which are detrimental from the point of view of structural fatigue. This limits the service life of the wind turbines and increases their cost-effectiveness of maintenance (Han et al., 2016). In case the amplitude of these loads is large enough, they can even lead to the complete failure of the structure. Ideally, the design of these devices should be such that they incorporate means to mitigate the unnecessary oscillations around the load required to operate appropriately without modifying it.

Natural fliers and swimmers employ control surfaces to mitigate the effect of unsteadiness in the flow. Kestrels, for example, can hover in strong gusty wind and keep the eyes in a fixed position with respect to an earth-fixed reference system with extreme accuracy (Videler et al., 1983) by activating their musculature. Besides, it is well known that wings and fins are compliant structures, which do not only react actively as shown before, but also passively (Wootton, 1992). In fact, flexibility effects are well known to stabilise or enhance the flight of birds and insects or the swim of fish (Marais et al., 2012; Senda et al., 2012; Addo-Akoto et al., 2021). In striking contrast with this sophisticated use of passive and active control surfaces, our understanding of unsteady load alleviation is still limited.

To mitigate the loads and to control the aeroelastic response of wind turbine blades, Active Flow Control (AFC) techniques can be applied (Johnson et al., 2010). It requires a combination of sensors, actuators and control systems which may go up to local level (Lackner & Kuik, 2010), further increase the complexity of the system, not only in terms of control but also in terms of structure and maintenance perspectives. Solutions based on AFC have been already applied. For example, full span active pitch is a solution used on the majority of (large-scale) horizontal axis wind turbines (HAWTs). However, it has a limited bandwidth in space and time that allows for a reaction only to relatively large and slow turbulent oscillations (Navalkar et al., 2016).

A solution to overcome these limitations is the use of passive devices, based on a simpler implementation. For example, Bottasso et al. (2016a) explored the load alleviation capabilities of an articulated tip device in HAWTs, suggesting that passive solutions can perform nearly as well as the active ones at a reduced complexity. The use of passive flaps located at the trailing edge of the blades

and their effect on load mitigation was also investigated in Bottasso et al. (2016b), showing the ability to attenuate vibrations in a broad frequency range, reducing the fatigue damage, hence increasing the lifetime, without affecting noticeably the power production.

Further progress on passive control strategies has been made by Arredondo-Galeana et al. (2021), proposing a two-dimensional, linear, quasi-steady model to predict the load mitigation that can be achieved by means of a passive-pitching trailing edge flap. The outcome of the model predicts a mitigation that is linearly proportional to the flap-to-chord length ratio a/c, meaning that a fully passive-pitching foil could mitigate completely the loads coming from oscillations in the angle of attack seen by the airfoil. They also perform experiments at Reynolds number $Re = 50,000$ for airfoils with flap located at the 75% of the chord to confirm the validity of the proposed theory.

It is worth mentioning that the typical Reynolds number of HAWTs is $\mathcal{O}(10^6 - 10^7)$. At these values of the Reynolds number, assuming attached inviscid and irrotational flow, and assuming thin airfoil, quasi-steady potential flow theories may apply. However, small-scale devices depart from the hypotheses which the quasi-steady theory is based on. For example, viscous effects are more important, and there is usually massive flow separation, leading to huge deviations from the assumptions of the quasi-steady model. On the other hand, the validity of the theory was only proven for one flap-to-chord length ratio, leaving open the question of whether the results were extensible to larger flaps.

Here, we perform Direct Numerical Simulations of the 2D incompressible flow around airfoils incorporating passive-pitching trailing edge flaps at $Re = 1000$ following a setup similar to the one proposed in Arredondo-Galeana et al. (2021). We analyse the effect of the flap-to-chord length ratio on the load mitigation that is achieved for airfoils undergoing oscillations in the angle of attack. Besides, we extend the parametric space examined in Arredondo-Galeana et al. (2021), considering not only more intense kinematics, but also analysing the effect of other variables as the inertia or the preload of the torsional spring.

The chapter is organised following the next structure: Section 4.2 describes the load mitigation strategy proposed in Arredondo-Galeana et al. (2021) and used in this study. The fluid-structure interaction problem is defined in section 4.3 together with the methodology followed to solve it. In section 4.4, we investigate the validity of the quasi-steady model. The results of the simulations are presented, where the response of the airfoil is characterised in terms of flow, forces and dynamics of the flap. Finally, conclusions are shown in section 4.5.

4.2 Theoretical model

The proposed model is based on the following idea: assuming attached flow, a rigid symmetric airfoil free to rotate (an angle θ') around its leading edge would align with the incoming flow after a change in its direction, as shown in figure 4.1(a), leading to zero lift force. As a certain lift is needed to operate any wind turbine, there must be a moment M_s that opposes the hydrodynamic pitching moment M_h

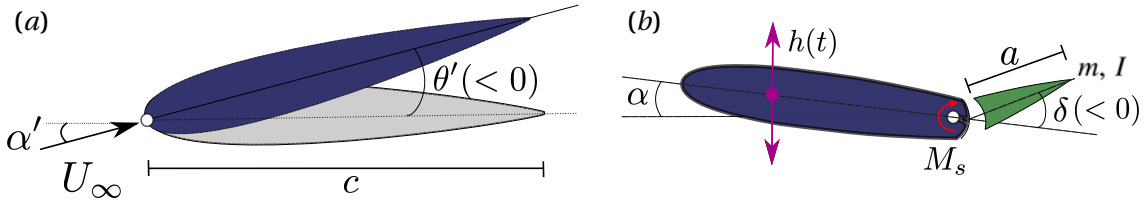

Figure 4.1: (*a*) Sketch of a rigid airfoil pitching around its leading edge, aligning with the incoming flow. (*b*) Sketch of a flapped airfoil to qualitatively describe the problem of load mitigation using a passive-pitching trailing edge flap, together with the main parameters defining it.

acting on the pitching axis of the airfoil, such that the required net lift is obtained when the airfoil is set to a given angle of attack α. This moment M_s can be provided by a highly flexible torsional spring, which, if highly preloaded (i.e. $\theta_p \gg \theta'$), has a virtually constant moment

$$M_s = k_s(\theta_p \pm \theta') \approx k_s\theta_p \tag{4.1}$$

that would ensure $M_s = -M_h$. Consider now the instantaneous change in the angle of attack α'. Using linear thin airfoil theory, this increment in the angle of attack results in a increment in lift $\Delta L_1 = 2\pi\alpha'$ and an increment in the hydrodynamic pitching moment $\Delta M_h = -\Delta L_1 x_{AC}$, where x_{AC} is the position of the aerodynamic center measured from the leading edge. This increase in moment will lead to a counterclockwise (CCW) re-pitch of the airfoil by an angle $\theta' < 0$, which leads to an additional change in lift $\Delta L_2 = 2\pi\theta'$, modifying ΔM_h. As stated in equation (4.1), the moment delivered by the spring is constant, such that

$$M_s = -(M_h + \Delta M_h), \tag{4.2}$$

which leads to $\Delta M_h = 0$, implying that $\alpha' = -\theta'$, and the load of the airfoil remains unchanged.

Let us now address the load mitigation that can be obtained using passive-pitching trailing edge flaps. To predict the load that can be mitigated on a rigid airfoil when is subjected to oscillations in the angle of attack, a linear, quasi-steady (QS) panel method, based on the potential flow hypotheses is used. The load is intended to be mitigated attaching a passive-pitching trailing-edge (TE) flap to the foil, hinged at a position x_p measured from the leading edge, as depicted in figure 4.1(*b*). In the panel method, the rigid foil and the TE flap are considered to be two separate panels, which are characterised by a circulation γ_1 and γ_2 respectively. After an increment in the angle of attack α', the circulation of the first panel becomes $\gamma_1 + \Delta\gamma_1$, while the circulation of the second panel remains γ_2 after a CCW deflection δ_{QS} of the flap. After some algebra, it is found that the flap deflection only depends on the increment in the angle of attack and the position of the hinge following the expression

$$\delta_{QS} = -\alpha'\left(1 - \frac{2x_p}{3c}\right). \tag{4.3}$$

The instantaneous lift coefficient is equal to

$$\Delta C_l^F = 2\pi\alpha'\frac{x_p}{c}, \tag{4.4}$$

where the superscript F refers to the flexible (or flapped) cases. Normalising equation (4.4) by the load increment in the rigid airfoil, i.e. $\Delta C_l^R = 2\pi\alpha'$, it is possible to find the load relative to the rigid case,

$$\Delta C_l^* = x_p/c, \tag{4.5}$$

which leads to the instantaneous load reduction

$$1 - \Delta C_l^* = 1 - x_p/c = a/c. \tag{4.6}$$

Given equation (4.6), the model predicts a linear relationship between the load reduction and the flap-to-chord length ratio. For more details about the load mitigation strategy proposed here, the reader is referred to Arredondo-Galeana et al. (2021).

4.3 Methodology

4.3.1 Problem definition

The problem of the load mitigation on a NACA0012 airfoil of chord c using a passive-pitching TE flap hinged freely at a distance a measured from the trailing edge is considered here. The configuration of the problem is very similar to that followed in the experiments shown in Arredondo-Galeana et al. (2021), and a sketch is provided in figure 4.1(b). The load mitigation will be measured with respect to the load provided by a rigid foil without flap ($a/c = 0$). The airfoils are immersed in an uniform free-stream current of intensity U_∞. The fluid is considered to be incompressible and Newtonian with constant density ρ and dynamic viscosity μ, resulting in a Reynolds number $Re = \rho U_\infty c/\mu = 1000$. The airfoil is initially set at a given angle of attack α. The oscillations in the angle of attack of amplitude α_0' are modelled by imposing a heaving motion that follows the law

$$h(t) = h_0 \cos(2\pi f t), \tag{4.7}$$

where h_0 is the heaving amplitude and f is the frequency of the imposed motion. We also define the angular frequency as $\omega = 2\pi f$, the period of oscillation as $T = 1/f$, and the reduced frequency as $\kappa = \pi f c/U_\infty$.

The flap is characterised by a density ρ_s and a volume V that is a function of the flap length, yielding a total mass $m = \rho_s V$ and a polar moment of inertia with respect to the centroid of the flap I. As mentioned in section 4.2, we model the highly flexible torsional spring through the application of a constant moment M_s at the hinge. This moment is computed such that the deflection of the flap is zero in steady conditions, i.e., $\delta_{eq} = 0$ for $h_0/c = 0$. The constant moment to be applied depends on the flap-to-chord length ratio a/c.

The parametric space covered in Arredondo-Galeana et al. (2021) to prove the validity of the quasi-steady formulation only includes one value of the flap-to-chord length ratio, i.e. $a/c = 0.25$. Here, different values of a/c are covered in order to prove the linear relationship between the load

a/c	ρ^*	h_0/c	α	k
0	1.5	0.05	0°	0.1
0.25	5	0.15	5°	0.3
0.375	25	0.25		0.5
0.5	100	0.5		
0.75				

Table 4.1: Overview of the selected values for the variables defining the parametric space.

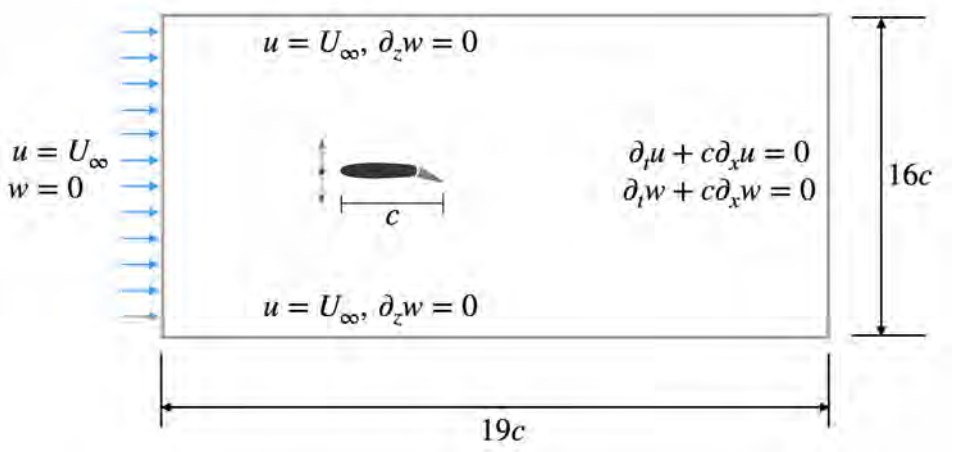

Figure 4.2: Sketch of the computational set-up and selected boundary conditions

reduction and the flap-to-chord length ratio. Besides, we select different reduced frequencies and heaving amplitudes such that the obtained amplitudes of the oscillations in the angle of attack α_0' are both comparable and larger than those considered in Arredondo-Galeana et al. (2021). Finally, different density ratios $\rho^* = \rho_s/\rho$ are considered. The values of the variables considered in this work characterising the kinematics and the material properties of the problem are shown in table 4.1.

4.3.2 Computational Set-up

The FSI problem is solved using TUCANMB, described in chapter 2. Direct numerical simulations (DNS) of the flow are performed in a computational domain with dimensions $19c \times 16c$ in the streamwise and vertical directions respectively. The domain is defined by a uniform grid spacing $\Delta r = c/128$. The time step is selected such that the $CFL = U_{\max}\Delta t/\Delta r$ number is lower than 0.1. The size of the domain and both spatial and temporal resolution are defined based on the grid sensitivity analysis presented in annex A. The origin of the reference system is located at the leading edge of the airfoil. The free-stream inflow is modeled as a Dirichlet boundary condition at the inlet boundary ($x/c = -8$), and the outflow has been modeled with an advective boundary condition ($\partial\mathbf{u}/\partial t + U_\infty \partial\mathbf{u}/\partial x = 0$) at the outlet ($x/c = 11$). Free-slip boundary conditions are set at the lateral boundaries. A sketch of the computational set-up is shown in figure 4.2.

Case	α	κ	h_0/c	ρ^*	$\overline{C_l}$				
					$a/c=0$	$a/c=0.25$	$a/c=0.375$	$a/c=0.5$	$a/c=0.75$
A1	5°	0.3	0.15	1.5	0.216	0.218	0.212	0.214	0.214
A2	5°	0.3	0.25	1.5	0.189	0.178	0.165	0.187	0.209
A3	5°	0.3	0.5	1.5	0.308	0.201	0.162	0.145	0.159
B3	5°	0.5	0.5	1.5	0.413	0.228	0.151	0.147	0.095

Table 4.2: Overview of simulations defining the cases A1, A2, A3, B3.

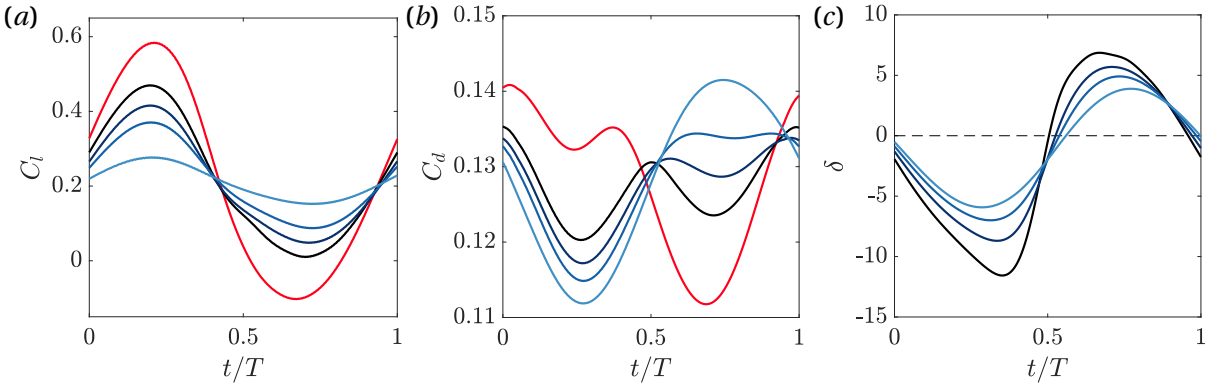

Figure 4.3: Temporal evolution of (a) lift coefficient C_l, (b) drag coefficient C_d and (c) flap deflection δ of cases A1 with $k=0.3$, $h_0/c=0.15$. Line colours correspond to ——: $a/c=0$, ——: $a/c=0.25$, ——: $a/c=0.375$, ——: $a/c=0.5$, ——: $a/c=0.75$.

Simulations are run for 4 cycles to ensure periodicity in both the forces and the flow in the vicinity of the airfoil.

4.4 Results

This section is devoted to evaluate the validity of the load mitigation strategy presented in section 4.2 by analysing the obtained results for the problem stated in section 4.3.1. A large database has been generated from many of the different combinations of the variables representing the parametric space presented in table 4.1.

4.4.1 Effect of flap-to-chord length ratio under different kinematics

To provide a general description of the obtained results, a series of relevant cases, namely A1, A2, A3 and B3, are first introduced. These cases are described in table 4.2. To analyse the effect of the flap-to-chord length ratio, five different values of a/c are considered in each of the cases, namely $a/c=0, 0.25, 0.375, 0.5$ and 0.75. The airfoils are initially set at $\alpha=5°$. Different kinematics are considered, and the density ratio of the flaps is set to $\rho^*=1.5$.

Starting with case A1, we show in figure 4.3(a,b,c) the temporal evolution of lift coefficient, C_l, drag coefficient, C_d, and flap deflection, δ, respectively, for different values of a/c. First, as seen

in figure 4.3(a), the flapped airfoils (i.e. $a/c \neq 0$) present lower peak-to-peak amplitudes of the lift coefficient compared to the rigid case ($a/c = 0$), which is the one yielding the maximum value of C_l. Besides, the amplitude of the lift coefficient is smaller the larger the flap (larger a/c), as predicted by equation (4.4). The temporal evolution of C_l appears to be close to sinusoidal for all a/c, showing values above the mean lift coefficient, $\overline{C_l}$, during most of the downstroke, which spans from $t/T = 0$ to $t/T = 0.5$, and vice versa during upstroke. The mean lift coefficient for all a/c is approximately the same (see table 4.2), and the load mitigation appears to happen similarly during upstroke and downstroke. The time instant at which the maximum value of C_l appears is approximately $t/T \approx 0.25$, i.e., mid-downstroke. The drag coefficient of the flapped cases is reduced during the downstroke when compared to the evolution of the values reported by the rigid case, but increased during upstroke, as shown in figure 4.3(b), leading to similar values in $\overline{C_d}$. Please note that, while $\overline{C_l}$ approximately ranges from -0.1 to 0.6, the values seen in $\overline{C_d}$ go from 0.11 to 0.14. The higher the value of a/c, the larger the reduction of C_d is found during downstroke, contrary to what is seen during upstroke, where the drag coefficient increases substantially. The subcase with $a/c = 0.75$ is the one showing the largest value of drag coefficient. The temporal evolution of flap deflections for the flapped airfoils are shown in figure 4.3(c). Negative values of δ correspond to CCW instantaneous deflections, which are mainly found during downstroke, while all flaps report positive –clockwise (CW)– deflections during most of the upstroke. The evolution of all flaps is qualitatively similar, with smaller amplitudes for larger flaps, following a temporal evolution resembling a sinusoidal one. Cases with shorter flaps deviate from this sinusoidal shape, where the maximum absolute deflection is obtained during downstroke and is larger than the maximum deflection obtained during upstroke for all cases. Besides, the time at which the absolute value of the maximum flap deflection changes with a/c. This maximum absolute flap deflection $|\delta|_{\max}$ is found at $t/T \approx 0.35$ for the $a/c = 0.25$ case, but $t/T \approx 0.285$ for $a/c = 0.75$. The value of the maximum flap deflection is $|\delta|_{\max} \approx 11.5°$, found for the $a/c = 0.25$ subcase. This can be compared to the value predicted by the QS model, where for the $a/c = 0.25$ subcase, the maximum flap deflection is given by $|\delta_{QS}|_{\max} = \alpha_0'/2 = 2.57°$.

Importantly, we see a difference when flap deflections are compared to the QS model: Looking at equation (4.3), the lower the value of x_p/c (i.e. larger a/c), the larger the value of δ_{QS}. Here, we see the opposite trend –larger flaps oscillate with lower amplitude–. We will come back to this fact later in section 4.4.2.

Consider now case A2, where the amplitude of the heaving motion has been increased with respect to case A1 to $h_0/c = 0.25$. Looking at the temporal evolution of C_l, C_d and δ in figures 4.4(a, b, c), a qualitative description similar to the one used to report case A1 can be provided here. However, several differences between cases A1 and A2 can be spotted. On the first hand, the temporal evolution of C_l is no longer symmetric, presenting oscillations during the upstroke, as seen in figure 4.4(a). These oscillations are stronger for the $a/c = 0$ case than for the rest of the subcases. The evolution of the C_d is reasonably similar to that of the A1 cases, as shown in figure 4.4(b), reaching the maximum value at $t/T \approx 0.4$ in the $a/c = 0$ subcase, rather than at the beginning of the downstroke

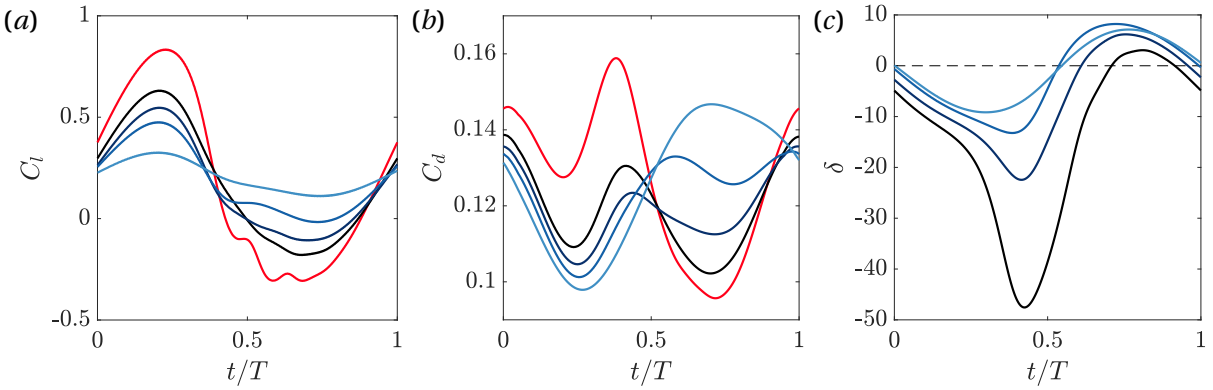

Figure 4.4: Temporal evolution of (a) lift coefficient C_l, (b) drag coefficient C_d and (c) flap deflection δ of cases A2 with $k = 0.3$, $h_0/c = 0.25$. Line colours correspond to ——: $a/c = 0$, ——: $a/c = 0.25$, ——: $a/c = 0.375$, ——: $a/c = 0.5$, ——: $a/c = 0.75$.

as it happened in case A1. Flap deflections are asymmetric ($\overline{\delta} < 0°$) in all cases, see figure 4.4(c), with noticeable negative peaks for subcases with $a/c = 0.25$ and 0.375. In fact, the maximum absolute flap deflection $|\delta|_{\max}$ is found to be close to 48° and is given by the subcase with $a/c = 0.25$.

The asymmetry in flap deflections is probably due to the interaction between the flap and the separated boundary layers, as shown in figure 4.5. Vortical structures are identified using the λ_2 criterion (Jeong & Hussain, 1995). Green lines added in figure 4.5 are the contours given by $\lambda_2 = -5U_\infty^2/c$. While the boundary layer is attached on both surfaces of the foil at the beginning of the downstroke, see figure 4.5(a), it starts to separate during early downstroke (figure 4.5b, $t/T = 0.125$). Apparently due to a combination between the inertia of the flap and the separation of the boundary layer, the flap pitches CCW. Maximum separation of the boundary layer is reached at a time instant close to the end of the downstroke (figure 4.5d), very close to the instant when $|\delta|_{\max}$ is found. During upstroke, the boundary layer gets closer to the top surface progressively, reattaching at $t/T \approx 0.7$, see figure 4.5(f, g), while the boundary layer along the bottom surface remains attached. Oscillations in the lift coefficient could also be attributed to this separation and subsequent reattachment during the upstroke. Again, increasing the size of the flap make them be less prone to suffer larger and asymmetric deflections, despite the fact that the density ratio is small in this case, $\rho^* = 1.5$. This way, inertia appears to have an impact on the response of the flap that should not be negligible.

Moving to case A3, i.e. increasing the amplitude to $h_0/c = 0.5$, temporal evolutions of C_l, C_d and δ qualitatively resemble those of case A2, see figure 4.6. However, it is possible to see in figure 4.6(a) that the evolution of C_l is clearly not sinusoidal any longer. In fact, all subcases show a increase in the lift coefficient with a slope dC_l/dt approximately constant from $t/T = 0$ to a time instant between $t/T = 0.15$ and 0.2. This is probably due to the larger vorticity production around the leading edge of the foils caused by the increase in the heaving velocity. This constant slope dC_l/dt is a function of a/c, being larger for lower values of a/c. On the other hand, the value of the mean lift coefficient changes with a/c, see table 4.2.

Consider now an increase in the reduced frequency to $\kappa = 0.5$, i.e. case B3, keeping $h_0/c = 0.5$. The

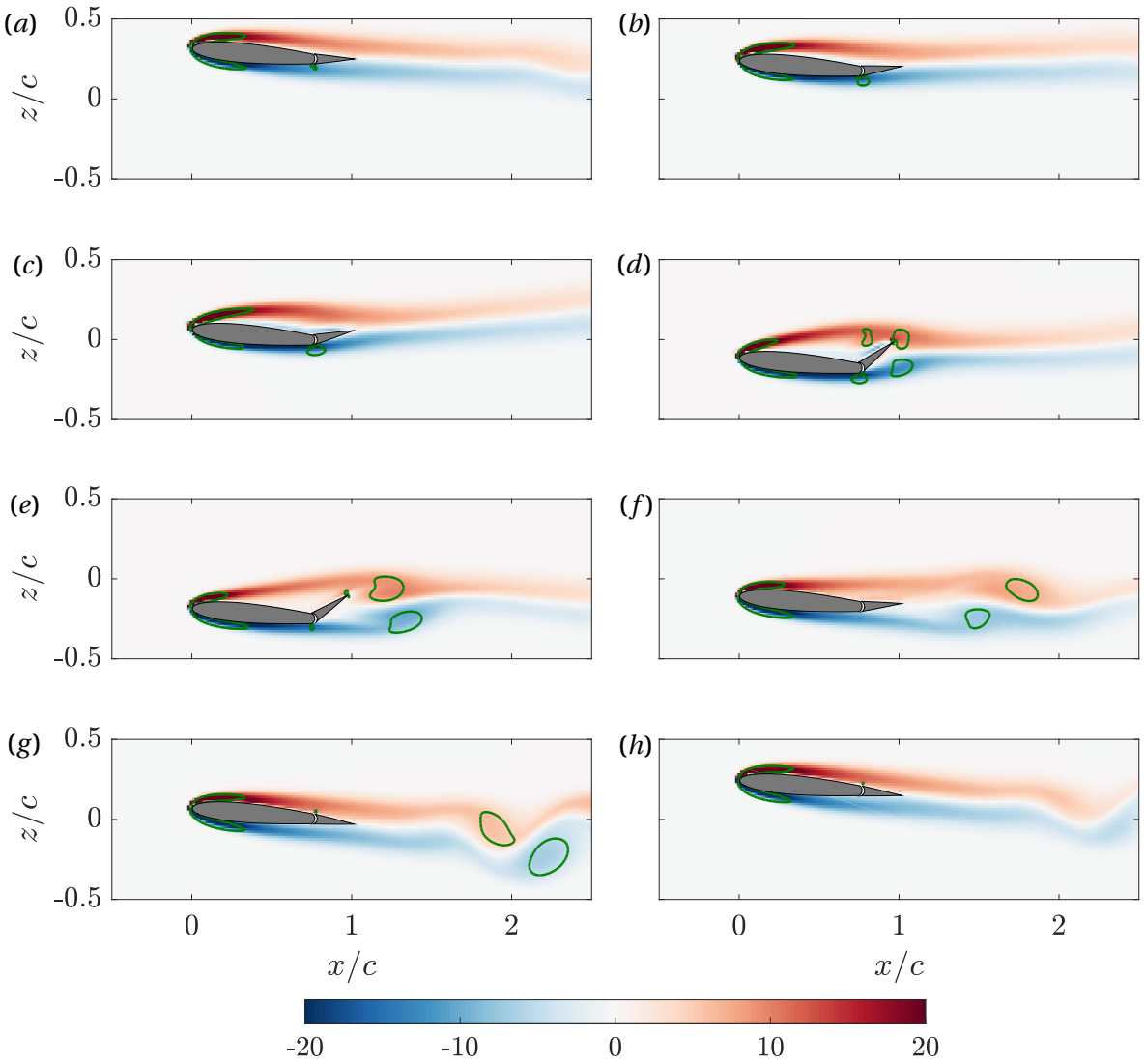

Figure 4.5: Vorticity, $\omega_y c/U_\infty$, contours for case A2, $a/c = 0.25$. Time instants correspond to (a) $t/T = 0$, (b) $t/T = 0.125$, (c) $t/T = 0.25$, (d) $t/T = 0.375$, (e) $t/T = 0.5$, (f) $t/T = 0.625$, (g) $t/T = 0.75$, (h) $t/T = 0.875$. The green line corresponds to $\lambda_2 = -5U_\infty^2/c^2$.

lift coefficient increases during downstroke for cases with $a/c \leq 0.5$, as seen in figure 4.7(a). However, it remains approximately constant for the case with $a/c = 0.75$ up to $t/T \approx 0.3$. The maximum value of C_l is reached again for all cases approximately at mid-downstroke, and the largest value is yielded by the rigid case as it happened for all cases with lower reduced frequency. Differently to cases with $\kappa = 0.3$, the drag coefficient reports two clear peaks for most of the cases, see figure 4.7(b). This goes accompanied by negative values of C_d during upstroke in all cases but $a/c = 0.75$. Besides, several peaks appear in the temporal evolution of the flap deflection, rather than the only one that was seen in cases with $\kappa = 0.3$. In these cases, a LEV is also developed and shed during upstroke. These LEVs developed during the upstroke induce velocities on the flap, explaining the peaks appearing at $t/T \approx 0.05$. The peaks at $t/T = 0.5$ are due to the interaction with the LEV developed during the

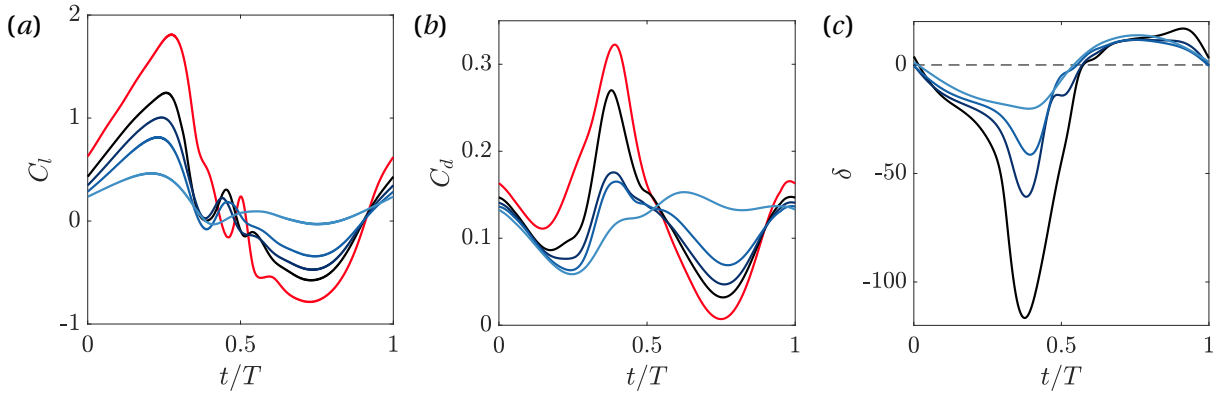

Figure 4.6: Temporal evolution of (a) lift coefficient C_l, (b) drag coefficient C_d and (c) flap deflection δ of cases A3 with $k = 0.3$, $h_0/c = 0.5$. Line colours correspond to ——: $a/c = 0$, ——: $a/c = 0.25$, ——: $a/c = 0.375$, ——: $a/c = 0.5$, ——: $a/c = 0.75$.

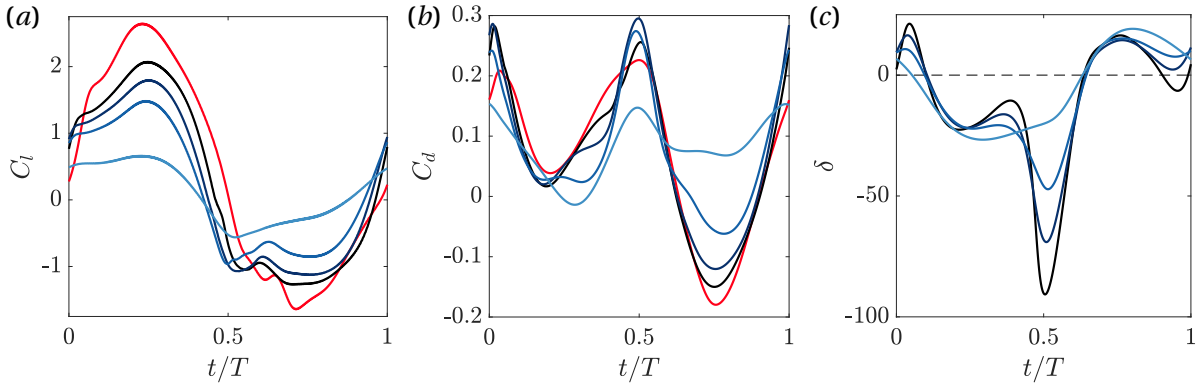

Figure 4.7: Temporal evolution of (a) lift coefficient C_l, (b) drag coefficient C_d and (c) flap deflection δ of cases B3 with $k = 0.5$, $h_0/c = 0.5$. Line colours correspond to ——: $a/c = 0$, ——: $a/c = 0.25$, ——: $a/c = 0.375$, ——: $a/c = 0.5$, ——: $a/c = 0.75$.

downstroke. This can be clearly seen in figure 4.8, which shows the evolution of the LEV developed during the upstroke (in blue) at different time instants.

Hence, depending on the kinematics, the behaviour of force generation and flap deflections is clearly influenced by the generation of vortical structures. At the same time and in a coupled way, the flaps might also influence this generation of vortical structures. In order to clarify this statement, vorticity fields for selected subcases at $t/T = 0.25$ shown in figure 4.9 at midstroke, i.e. $t/T = 0.25$. The comparison between the LEV generated in the $a/c = 0.75$ subcase (see figure 4.9d) with those generated in the rest of subcases (figure 4.9a, b, c), suggests that the passive flap, if large enough, modifies the development of vortical structures around the foil. However, vortical structures are not drastically modified for cases with short flaps.

Although the results for $\alpha = 0°$ are not shown here, similar comments apply to those cases, with symmetric temporal evolutions of C_l and δ for all cases, and symmetric flow fields during downstroke and upstroke.

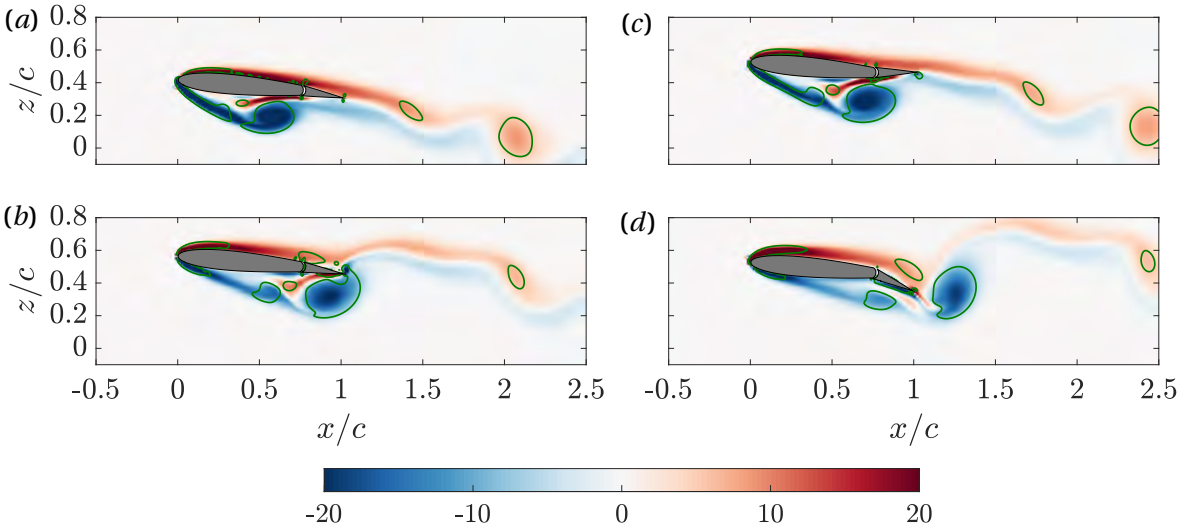

Figure 4.8: Vorticity, $\omega_y c/U_\infty$, contours for case B3, $a/c = 0.25$, at time instants (*a*) $t/T = 0.875$, (*b*) $t/T = 0.9375$, (*c*) $t/T = 1$, (*d*) $t/T = 0.0625$. The green line corresponds to $\lambda_2 = -5U_\infty^2/c^2$.

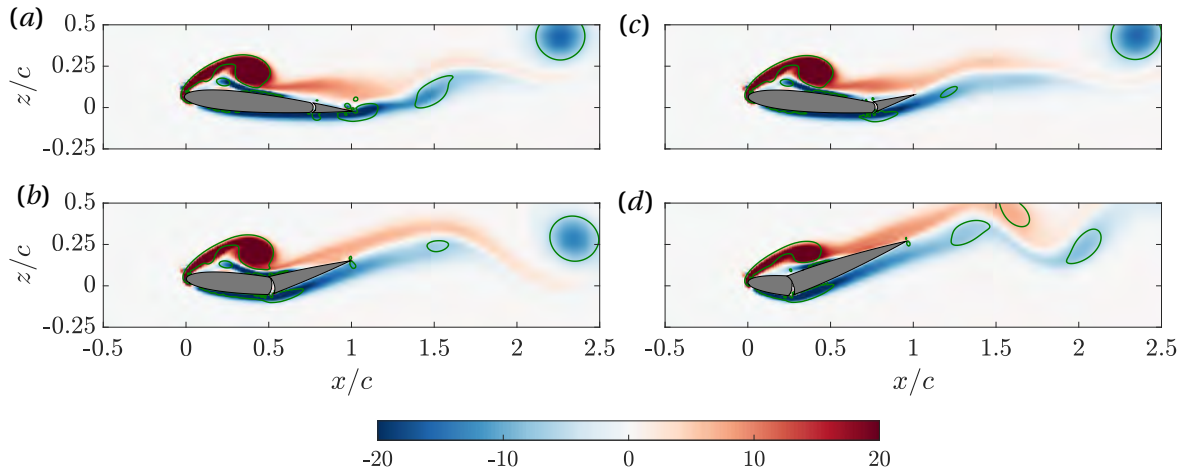

Figure 4.9: Vorticity, $\omega_y c/U_\infty$, contours at $t/T = 0.25$ for case B3 with flap-to-chord length ratios (*a*) $a/c = 0$, (*b*) $a/c = 0.25$, (*c*) $a/c = 0.5$, (*d*) $a/c = 0.75$. The green line corresponds to $\lambda_2 = -5U_\infty^2/c^2$.

To understand the mechanism by which the passive pitching flaps reduce the generation of forces, we compare in figure 4.10 the chordwise distribution of pressure difference $\Delta C_p = C_p^- - C_p^+$ between lower and upper surfaces of the airfoil of cases with $\alpha = 5°$, $a/c = 0.25$, $\kappa = 0.3$, at heaving amplitudes $h_0/c = 0.15, 0.25, 0.5$. C_p^+ and C_p^- are, respectively, the pressure coefficients (i.e. $C_p = 2(p - p_\infty)/\rho U_\infty^2$) of the top and bottom surfaces of the airfoil. Besides, we include for comparison cases where the flap is fixed, allowing to compare with the rigid cases. The chordwise ΔC_p distributions are shown for two instants of the period, namely $t/T = 0$ and 0.25, which correspond to the beginning of downstroke and mid-downstroke, respectively. Similar comments can be made for both time instants. The flap modifies the pressure distributions along the entire airfoil, such that the force generation changes. The changes in the distributions of ΔC_p of the flapped cases with respect to those reported by the

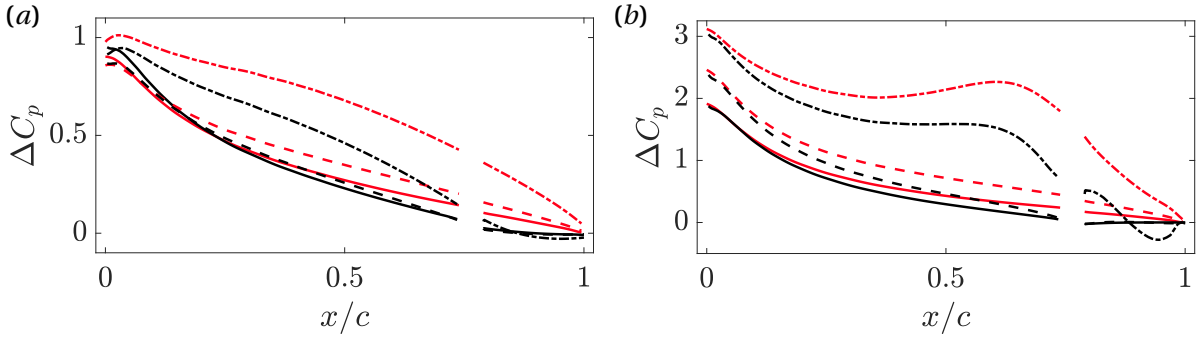

Figure 4.10: Instantaneous chordwise distributions of pressure coefficient difference ΔC_p along the chord of the foil and flap at (*a*) $t/T = 0$ and (*b*) $t/T = 0.25$. heaving amplitudes $h_0/c = 0.15, 0.25, 0.5$. Line colours correspond to ——: fixed flap, ——: free flap. Line types correspond to ——: $h_0/c =$ 0.15, — — —: $h_0/c = 0.25$, —·—·: $h_0/c = 0.5$.

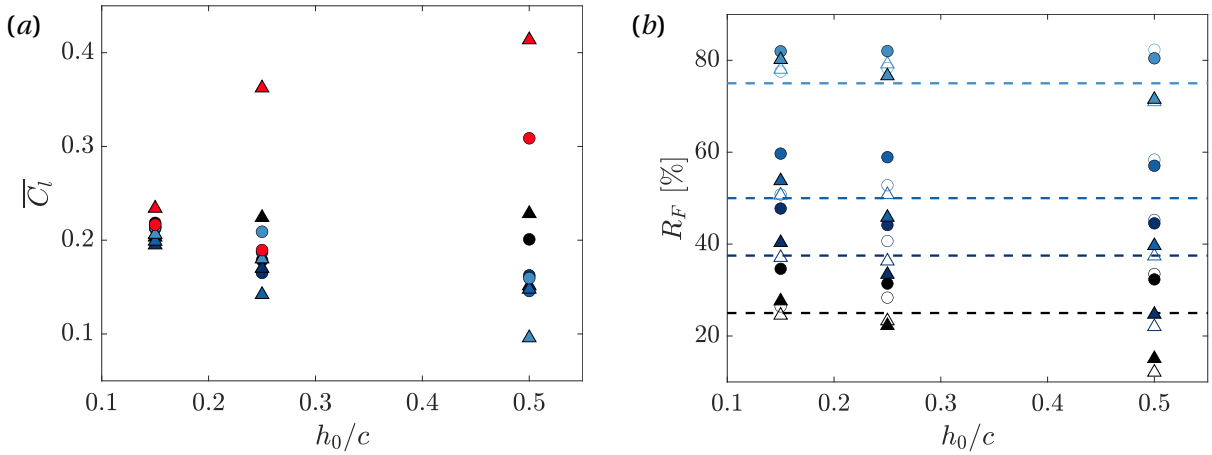

Figure 4.11: (*a*) Mean lift coefficient $\overline{C_l}$ for $\alpha = 5°$ cases and (*b*) reduction in fluctuations R_F for all cases. Circles and triangles correspond to $k = 0.3$ and $k = 0.5$, respectively. Colours correspond to ——: $a/c = 0$, ——: $a/c = 0.25$, ——: $a/c = 0.375$, ——: $a/c = 0.5$, ——: $a/c = 0.75$. Empty and filled markers correspond to $\alpha = 0°$ and $\alpha = 5°$.

rigid cases seen in figure 4.10(*a*, *b*) can be linked to a reduction of the effective angle of attack, as suggested in Arredondo-Galeana et al. (2021). On the other hand, the values of ΔC_p found at chordwise locations corresponding to those of the flap remain very close to 0 for freely-flapped cases with $h_0 = 0.15$ and 0.25.

After analysing the cases described in table 4.2, i.e. cases A1, A2, A3 and B3, two main observations can be made. First, the load that is mitigated is higher the larger the value of a/c. Second, the load mitigation is not always symmetric in both downstroke and upstroke: there are some cases yielding a mean lift coefficient that is not the same as that reported by the rigid case (see table 4.2). In fact, $\overline{C_l}$ is a function of both a/c and kinematics $(\kappa, h_0/c)$. The previous two comments can also be made for the rest of the cases in the database. The dependence of the mean lift coefficient on the kinematics and flap length for all cases in the database with $\alpha = 5°$, $\rho^* = 1.5$, $\kappa \geq 0.3$, $h_0/c \geq 0.15$, is shown in figure 4.11(*a*). While for low heaving amplitudes, all cases report very similar values of $\overline{C_l}$ disregarding the

reduced frequency, the values yielded by flapped foils clearly deviate from those given by rigid foils in cases with $\kappa = 0.3$, $h_0/c = 0.5$ and $\kappa = 0.5$, $h_0/c \geq 0.25$. In fact, these cases are those showing a clear LEV development and shedding.

The load reduction for the experiments performed in Arredondo-Galeana et al. (2021) is defined as $R_L = 1 - \tilde{C}_l^F / \tilde{C}_l^R$, where $\tilde{C}_l$ is the measured lift amplitude, and where the superscripts F, R refer to flexible and rigid cases, respectively. $\tilde{C}_l$ is obtained in Arredondo-Galeana et al. (2021) computing the Fourier coefficients of the first mode of the temporal evolution of C_l. In this work, due to the fact that the obtained temporal evolution of the lift coefficient is not sinusoidal, and is asymmetric during both upstroke and downstroke in many of the cases, computing the $\tilde{C}_l$ only in terms of the first Fourier mode might not be accurate. Moreover, a definition of the load reduction only in terms of the lift amplitudes appears to be insufficient in this work, due to the fact that the mean lift coefficient is not the same for rigid and flexible cases. Hence, instead of considering the load reduction, we define the reduction in fluctuations as

$$R_F = 1 - \frac{\mathrm{RMS}\left(\hat{C}_l^F\right)}{\mathrm{RMS}\left(\hat{C}_l^R\right)}, \tag{4.8}$$

where $\hat{C}_l$ is computed as $\hat{C}_l(t) = C_l(t) - \overline{C_l}$ and is a function of time. This way, only fluctuations of the lift coefficient around its mean value are considered. Despite the fact that the reduction in fluctuations were also computed using the first Fourier mode and the results were found to be similar, we find this definition of the reduction of fluctuations to be more suitable. Results for R_F are shown in figure 4.11(b). It is possible to see that the majority of the cases report reduction in the fluctuations larger than the values predicted by the QS model (horizontal dashed lines, one for each value of a/c considered here). This happens in contrast to what is found for experiments in Arredondo-Galeana et al. (2021) at $Re = 50000$, where the obtained results match the QS model for low amplitudes of the oscillations in the angle of attack (also modeled with a heaving motion), while failing for cases with $\kappa = 0.3$, $h_0/c \geq 0.15$ or $\kappa \geq 0.5$. Here, the cases yielding values of R_F lower than the predicted ones are, in general terms, those with the most extreme kinematics, given by $\kappa = 0.5$, $h_0 = 0.5$, which are the cases where a clear LEV is generated. Arredondo-Galeana et al. (2021) linked the validity of the quasi-steady model to predict the load mitigation to the formation of the LEV. Here, it is impossible to claim validity of the model to predict the actual value of the reduction in fluctuations in any of the cases, disregarding the kinematics and the possible subsequent development of a LEV. The maximum difference found in the results when compared to the predictions of the QS model is seen for the subcase with $a/c = 0.375$, $\alpha = 0$, $\kappa = 0.5$, $h_0/c = 0.5$, where the predicted value of the reduction of the fluctuations is 0.375 but only a value of 0.22 is found. Not only that, if the focus is put on case A1, which is the one with the least intense kinematics within the cases considered in section 4.4.1, and where the model is supposed to work better based on the results shown in Arredondo-Galeana et al. (2021), the errors are still large. Namely, A1 cases with $a/c = 0.25, 0.375$ and 0.5 report an absolute difference in R_F equal to 0.1 with respect to the predictions of the QS model.

Nevertheless, and despite the fact that the QS model is not able to predict accurately the value

of R_F, we do see a trend of this variable with a/c that resembles the proportionality proposed in the model. Focusing on this particular A1 case, it is possible to see that subcase $a/c = 0.25$ reports a reduction in fluctuations equal to $R_F = 0.345$, which deviates almost 0.1 from the predictions. However, moving from $a/c = 0.25$ to $a/c = 0.5$, the reduction in fluctuations is now $R_F = 0.597$, keeping this difference constant. Analogously, this happens generally for all cases considered in this work, claiming that a variation in the flap-to-chord length ratio $\Delta a/c$ leads to an equal variation in the reduction of fluctuations ΔR_F, which allows to propose a modification of equation (4.6) in the form

$$R_F = a/c + K \tag{4.9}$$

where K is a coefficient that depends only on kinematics and not on a/c, setting the difference between the expected value and the actual one. In order to set K, only a simulation with an intermediate value of a/c should be needed to predict the value of R_F for any value of a/c. This way, it is possible to reduce the discrepancies with respect to the previously proposed model.

4.4.2 Flap dynamics

Based on the results shown in section 4.4.1, a tendency that was observed in all cases is that flaps do not deflect as predicted by the quasi-steady model, with larger flap deflections for smaller flaps, contrary to what was predicted by equation (4.3). This can be shown in figure 4.12(*a*), where the maximum negative deflection (maximum CW deviation) δ_{mn} of the A1 cases is plotted as a function of the location of the pivoting axis of the flap, x_p/c, together with the values predicted by the QS model (black line). Although not shown here, alternative models where the inertia of the flap is considered, and based on linear quasi-steady aerodynamics, have been also explored to predict the flap deflection. The results suggest that the sole effect of inertia is not responsible of these deviations. This fact was also the result of the unsteady alternative model proposed in Arredondo-Galeana et al. (2021). Hence, the changes in the dynamics of the flap could be attributed to the non-linearities in the flow (i.e., thickness of boundary layer, separation or development and shedding of LEVs), which are not considered in the QS models but known to be important in flows at low Reynolds numbers. Additionally, results shown in section 4.4 for a given kinematics suggest that inertia effects might still be relevant and cannot be completely discarded. Further exploration is needed to confirm this hypothesis.

On the other hand, focusing on $a/c = 0.25$ subcases, the maximum deflections were found to be larger than those predicted by equation (4.3), in contrast to the results provided by Arredondo-Galeana et al. (2021) for $Re = 50,000$, where deviations are found for cases where the amplitude in the oscillations of the angle of attack due to heaving are larger than approximately 9°, and the rest of the cases match the results predicted by the QS model. These discrepancies are attributed again to a combination of non-linearities in the flow and inertia effects.

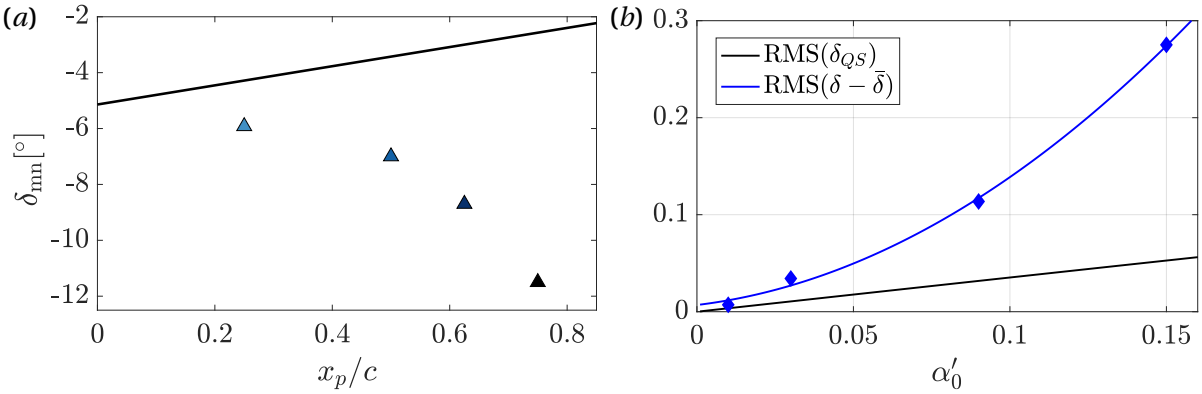

Figure 4.12: (*a*) Maximum negative deflection δ_{mn} as a function of the pivoting axis of the flap x_p/c. Symbols refer to the values of case A1. In black, δ_{QS}. (*b*) In black, expected fluctuations of the flap deflections given by the QS model, $D_{QS} = \mathrm{RMS}(\delta_{QS})$. Blue symbols refer to the obtained fluctuations around the mean values of the flap deflections $D = \mathrm{RMS}(\delta - \overline{\delta})$, and the blue line is the fitting $D_f = 9.25\alpha_0'^2 + 0.39\alpha_0' + 0.007$.

However, in the limit of $\kappa \to 0$, $h_0/c \to 0$, the results at $Re = 1000$ should match the predictions of the QS model, δ_{QS}. For a given kinematics, i.e., for a given pair of $h_0/c, k$, we obtain a temporal evolution of the oscillations in the angle of attack with amplitude α_0'. As the behaviour of the flap becomes chaotic for large reduced frequencies and heaving amplitudes, we select to analyse the behaviour of four cases with $a/c = 0.25$, namely $\kappa = 0.1$, $h_0/c = 0.05$ and $\kappa = 0.3$, $h_0/c = 0.05, 0.15$ and 0.25. For each of these points in the parametric space, we compute the fluctuations in flap deflection around their mean value $D = \mathrm{RMS}(\delta - \overline{\delta})$. The values of the pairs $\alpha_0' - D$ obtained for the four cases are plotted in blue symbols in figure 4.12(*b*). We also show the predicted values of δ_{QS} in black for the range in α_0' considered. Bear in mind that these values have been computed considering $a/c = 0.25$. It is clear that, contrary to the linear growth of D_{QS}, the quantity D increases non-linearly with α_0'. We compute a parabolic fit (blue line in figure 4.12b) in the form $D_f(\alpha_0') = 9.25\alpha_0'^2 + 0.39\alpha_0' + 0.007$, with a value of $R^2 = 0.998$, $R^2_{adj} = 0.994$ and $RMSE = 0.009$, where the subscript f denotes the fit. To claim asymptotic convergence to the QS model, the slope of the fitting must coincide with that of the QS model for $\alpha_0' \to 0$, which for cases with $a/c = 0.25$ is

$$\lim_{\alpha_0' \to 0} \frac{\partial D_{QS}}{\partial \alpha_0'} = 0.356. \tag{4.10}$$

The value of the coefficient of the fit that goes with the linear term is 0.39, very close to the expected value of 0.356, and the independent term c is very close to 0, asymptotically tending to the quasi-steady behaviour when $\alpha_0' \to 0$. This way, it is found that flaps follow a quadratic evolution with the amplitude of the oscillations in the angle of attack α_0' instead of a linear one.

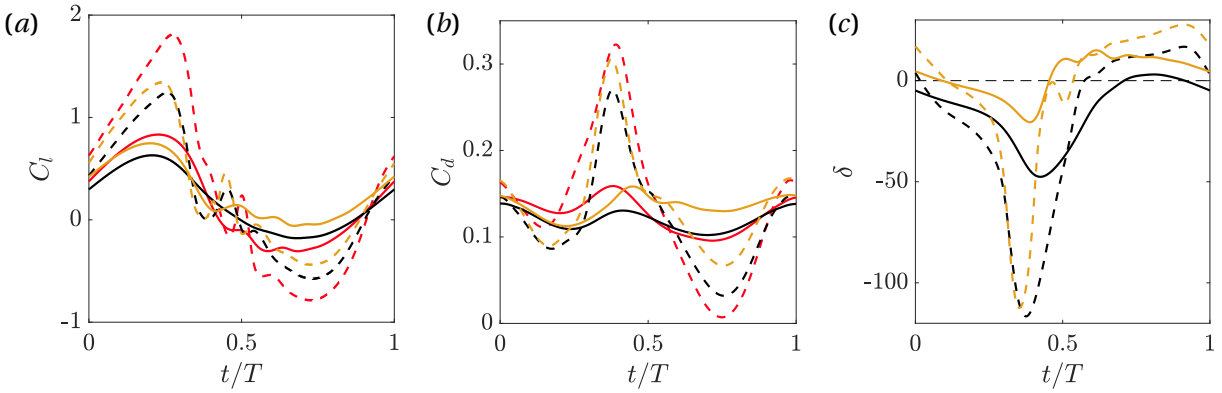

Figure 4.13: Effect of the constant moment of the hinge on the temporal evolution of (*a*) lift coefficient C_l, (*b*) drag coefficient C_d and (*c*) flap deflection δ of cases with $k = 0.3$. Line colours correspond to ——: $a/c = 0$, ——: $a/c = 0.25, \delta_{eq}$, ——: $a/c = 0.25, \delta_0$. Line types correspond to ——: $h_0/c = 0.25$, – – –: $h_0/c = 0.5$.

4.4.3 Effect of constant moment

In terms of applicability, a reduction in the mean lift coefficient may lead to deviations from the design requirements of the device, despite the fact that the fluctuations in loads are mitigated. In order to try to overcome this issue, we analyse the effect of the constant moment applied at the hinge, which will lead to a change in the flap deflections.

Consider the subcases with $a/c = 0.25$ of A2 and A3, characterised by asymmetric flap deflections ($\bar{\delta} \neq 0$). The mean lift coefficient $\overline{C_l}$ of the subcase of A2 is very close to the one given by the rigid foil as shown in figure 4.11(*a*), despite the asymmetric flap deflections. On the other hand, the case of A3 reports a $\overline{C_l} \approx 0.2$, differing from that of the rigid one, which is $\overline{C_l} \approx 0.31$. The moment applied at the hinge, while still constant, is now modified for these two cases such that the flap deflection averaged over a cycle is approximately zero ($\bar{\delta} = 0$). These cases are denoted as δ_0. The temporal evolution of C_l, C_d and δ of the cases $a/c = 0.25$ of A2 and A3, for both δ_{eq} and δ_0 alternatives, are shown in figure 4.13. Besides, rigid cases of A2 and A3 are also added for reference. After the change in the moment applied at the hinge, the value of the three variables under consideration in the δ_0 subcases are shifted upwards compared to the values given by the δ_{eq} subcases. The effect of the change in the moment applied at the hinge is negligible in terms of the reduction of fluctuations, finding the same value of R_F in both δ_0 and δ_{eq} scenarios. While the difference in $\overline{C_l}$ for the A3 case ($h_0/c = 0.5$) between rigid and flapped cases is now negligible due to this shift, the A2 flapped case also sees an increment in $\overline{C_l}$, leading it to be $\overline{C_l} = 0.275$, compared to the mean lift coefficient obtained by the rigid foil, $\overline{C_l} \approx 0.19$. This way, the value of the mean lift coefficient $\overline{C_l}$ changes with a change in the constant moment applied. Hence, this analysis shows the impossibility to keep $\overline{C_l^F} = \overline{C_l^R}$ for each of the kinematics considered in this work using a single value of the constant moment applied at the hinge. If needed, other alternatives should be looked into in order to satisfy this condition.

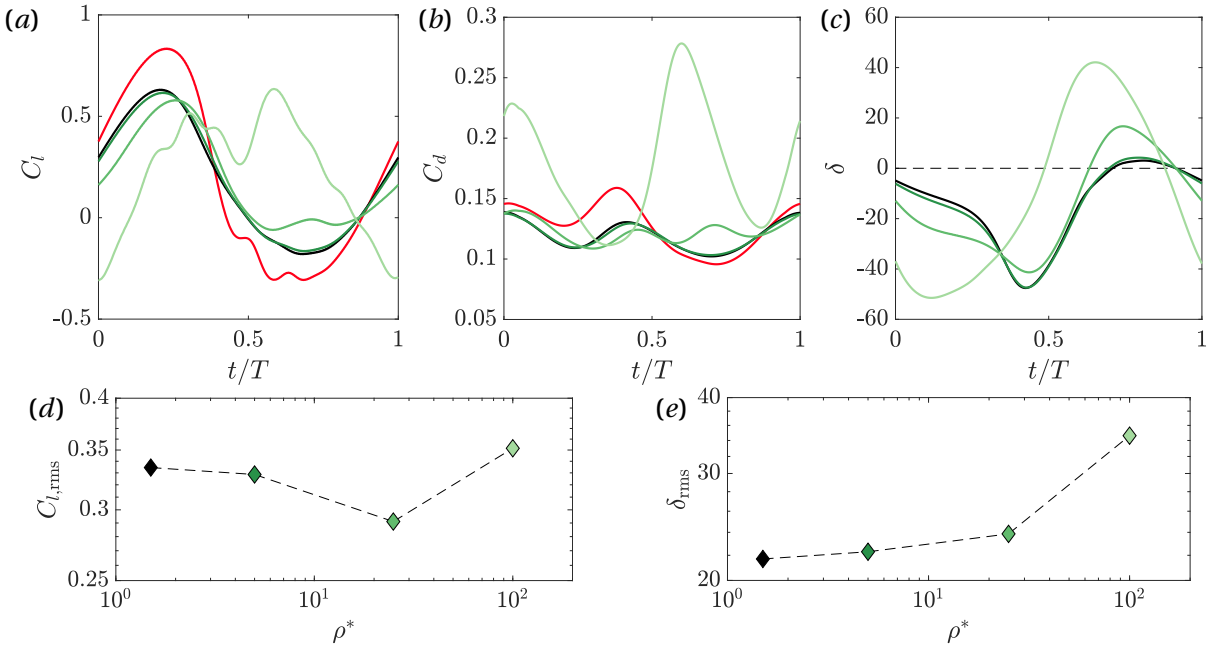

Figure 4.14: Temporal evolution of (a) lift coefficient C_l, (b) drag coefficient C_d and (c) flap deflection δ of cases with $k = 0.3$, $h_0/c = 0.25$. Colours correspond to ——: $a/c = 0$, ——: $\rho^* = 1.5$, ——: $\rho^* = 5$, ——: $\rho^* = 25$, ——: $\rho^* = 100$.

4.4.4 Effect of inertia

We analyse now the effect of the inertia of the flap on its dynamics and the aerodynamic response of the airfoil by modifying the density ratio. Consider now cases with same kinematics as A2 ($\kappa = 0.3$, $h_0/c = 0.25$) and $a/c = 0.25$, with flaps characterised by density ratios equal to $\rho^* = 1.5, 5, 25$ and 100. The temporal evolution of C_l, C_d, and δ for these cases is shown in figure 4.14(a, b, c). The $a/c = 0$ case is also included in red. There are no relevant changes in any of the measured quantities when comparing the flaps with $\rho^* = 1.5$ with $\rho^* = 5$. When looking at the case with $\rho^* = 25$, the evolution of the lift coefficient is lagged during the first instants of the period with respect to $\rho^* \leq 5$ cases. Moreover, a larger value of $\overline{C_l}$ is obtained when compared to $\rho^* \leq 5$ due to an increase in C_l within the interval $t/T \approx 0.6 - 0.8$. This is mainly due to the positive flap deflections that are found at the same time interval. In fact, despite that the absolute value of the maximum flap deflection $|\delta|_{\mathrm{max}}$ is reduced, the fluctuations of the flap deflection are increased. When the value of the density ratio is increased to $\rho^* = 100$, the temporal evolution of all variables changes substantially. The lift coefficient presents two positive peaks compared to the only one seen for the rest of the cases. The two peaks are the product of a positive balance between the oscillations in the angle of attack due to heaving and the instantaneous shape of the airfoil that changes with the flap deflection. In fact, the second peak in mainly caused by the large positive deflection of the flap during the first part of the upstroke. The mean drag coefficient is a 65% larger than the one yielded by the rigid case.

Figures 4.14(d, e) show the RMS values of the lift coefficient, $C_{l,\mathrm{rms}}$ and the flap deflections, δ_{rms},

respectively. While the value of the RMS of the lift coefficient is reduced when increasing the density ratio up to $\rho^* = 25$, it peaks up when the density ratio is further increased to $\rho^* = 100$. This non-monotonic evolution of $C_{l,\mathrm{rms}}$ with the density ratio contrasts with the monotonic evolution of δ_{rms}. This highlights the relevance in the selection of the inertia of the flap in its response and dynamics. On the other hand, as the effect of ρ^* is negligible when the density ratio is increased or decreased in the range of $\rho^* \sim \mathcal{O}(10^1)$, this further suggests that the discrepancies with the QS model and the experiments at larger Reynolds numbers cannot be explained only in terms of inertia.

4.5 Conclusions

The load that can be mitigated in airfoils at $Re = 1000$ by using a passive-pitching trailing-edge flap has been analysed performing direct numerical simulations of the fluid-structure interaction problem. In particular, we analyse the validity of the quasi-steady model proposed in Arredondo-Galeana et al. (2021), where it is predicted that the load that can be mitigated is proportional to the flap-to-chord length ratio a/c.

The Reynolds number considered in the study is consistent with that found for micro-air vehicles and micro wind turbines. Different values of a/c were tested at different kinematics, varying other quantities in the parametric space as the solid-to-fluid density ratio ρ^*, yielding a large database.

Depending on the amplitude of the oscillations in the angle of attack given by the different kinematics, the temporal evolution of the forces and the flap deflections vary significantly when a/c is modified. The lift coefficient fluctuations are reduced when increasing a/c, as well as the flap deflections. The load mitigation that is obtained for the majority of the cases is close to the values predicted by the quasi-steady model proposed in Arredondo-Galeana et al. (2021). Many of the cases report a mitigation larger than the expected one, while the only ones showing a decrease in the mitigation are those with the most intense kinematics, i.e. $\kappa = 0.5$, $h_0/c = 0.5$, disregarding the value of a/c. However, despite the deviations of the results with respect to the predicted values, an increment in the flap-to-chord length ratio $\Delta a/c$ leads to an equal increment in the reduction of fluctuations ΔR_F, in line with the quasi-steady model.

The quasi-steady model is unable to predict the flap deflections obtained in this work. In fact, the quasi-steady model predicts larger deflections for larger flaps (larger a/c, smaller x_p/c) under a given kinematics, while the flap deflections shown in section 4.4 behave in the opposite sense, growing with x_p/c under the same kinematics. On the other hand, for fixed values of a/c, it is seen that the fluctuations of the flap deflections around their mean value increases quadratically with the amplitude of the oscillations in the angle of attack, instead of the linear relationship found in the QS model. We hypothesise that this fact is linked to the non-linearities in the flow, rather than inertia effects, although they might play a non-negligible role.

Finally, both the effect of the inertia through a change in the density ratio, and that of the constant moment at the hinge, on the dynamics of the airfoil have been investigated, showing the relevance of

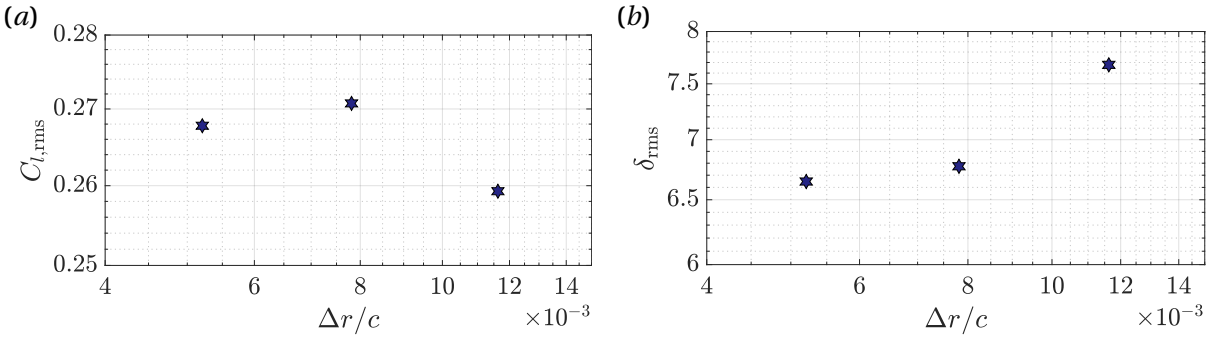

Figure 4.15: Temporal evolution of (a) lift coefficient C_l and (b) flap deflection δ of cases with $k = 0.3$, $h_0/c = 0.15$.

the selection of both quantities in terms of the required performance.

Acknowledgements

Part of this work was carried out during a research visit at the VOILAb, (Institute of Energy Systems, University of Edinburgh), under the supervision of Prof. Ignazio Maria Viola.

A.1 Grid and domain sensitivity analysis

A grid sensitivity study is performed to select the spatial and temporal resolution to be employed in the simulations. The case A1 in table 4.2 with $a/c = 0.25$ is selected as the benchmark case. Three different spatial resolutions Δr are considered, $c/86$, $c/128$, $c/156$, and will be specified using superscripts R, S and T, respectively. The bodies are discretised using the same eulerian resolution. The temporal resolution is also modified such that the $CFL = U_{\max}\Delta t/\Delta r$ number is always below 0.1. The grid sensitivity on the root mean square of the lift coefficient C_l and flap deflection δ, namely $C_{l,\mathrm{rms}}$ and δ_{rms} is shown in figure 4.15. The relative changes in $C_{l,\mathrm{rms}}$ when going from $c/86$ to $c/128$ are about 4%. When going from $c/128$ to $c/196$, relative changes become smaller than a 1%. Similar relative changes are obtained for δ_{rms}. Besides, as the evolution of δ_{rms} is monotonic, it is possible to compute a ground truth (GT) using Richardson extrapolation, which is

$$\delta^{GT}_{\mathrm{rms}} = \delta^{\mathrm{T}}_{\mathrm{rms}} - \frac{\delta^{\mathrm{S}}_{\mathrm{rms}} - \delta^{\mathrm{T}}_{\mathrm{rms}}}{r^p - 1} = 6.62^\circ, \quad \text{with } p = \log\left(\frac{\delta^{\mathrm{R}}_{\mathrm{rms}} - \delta^{\mathrm{S}}_{\mathrm{rms}}}{\delta^{\mathrm{S}}_{\mathrm{rms}} - \delta^{\mathrm{T}}_{\mathrm{rms}}}\right)/\log(r), \tag{4.11}$$

where $r = \Delta r^R/\Delta r^S = 1.5$. Given the ground truth, it is possible to compute the relative errors on δ_{rms} with respect to this ground truth using the different resolutions, computed as

$$\epsilon^i_\delta = \frac{|\delta^i_{\mathrm{rms}} - \delta^{GT}_{\mathrm{rms}}|}{\delta^{GT}_{\mathrm{rms}}}, \tag{4.12}$$

and the values of the relative error are $\epsilon_\delta = 0.15, 0.02$ and 0.003. Based on the obtained results, the simulations are performed with a spatial resolution $\Delta r = c/128$. The numerical uncertainty in the flap deflection, computed as in Viola et al. (2013), is $U_\delta = 0.1833^\circ$.

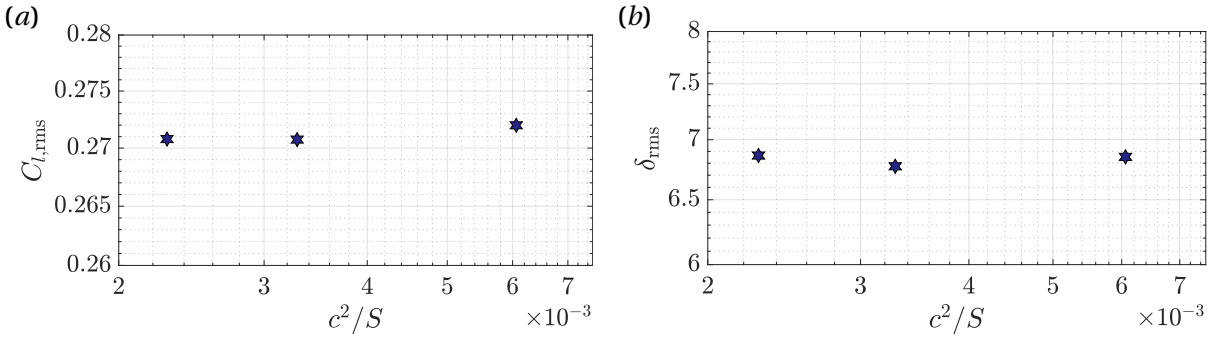

Figure 4.16: Temporal evolution of (*a*) lift coefficient C_l and (*b*) flap deflection δ of cases with $k = 0.3$, $h_0/c = 0.15$.

Besides, the effect of the domain size on the same quantities is also characterised. Three different sizes are considered here: $(15c \times 12c)$, $(19c \times 16c)$, $(23c \times 20c)$. The results obtained for each of the domain sizes are shown in figure 4.16. It is possible to see that the effect of the domain size is almost negligible. As the analysis of the effect of resolution has been performed with a domain size $(19c \times 16c)$, the simulations are also performed using this domain.

REFERENCES

Addo-Akoto, R., Han, J. S. & Han, J. H. 2021. Roles of wing flexibility and kinematics in flapping wing aerodynamics. *J. Fluids Struct.* 104:103317.

Arranz, G., Flores, O. & García-Villalba, M. 2022a. Flow interaction of three-dimensional self-propelled flexible plates in tandem. *J. Fluid Mech.* 931.

Arranz, G., Martínez-Muriel, C., Flores, O. & García-Villalba, M. 2022b. Fluid-structure interaction of multi-body systems: Methodology and applications. *J. Fluid Struct.* 110:103519.

Arredondo-Galeana, A., Young, A. M., Smyth, A. S. M. & Viola, I. M. 2021. Unsteady load mitigation through a passive trailing-edge flap. *J. Fluids Struct.* 106:103352.

Bottasso, C. L. et al. 2016a. Articulated blade tip devices for load alleviation on wind turbines. *Wind Energ. Sci.* 1 (2): 297–310.

Bottasso, C. L., Croce, A., Gualdoni, F. & Montinari, P. 2016b. Load mitigation for wind turbines by a passive aeroelastic device. *J. Wind Eng. Ind. Aerodyn.* 148:57–69.

Felis, M. L. 2017. RBDL: an efficient rigid-body dynamics library using recursive algorithms. *Auton. Robots* 41 (2): 495–511.

Gaitan-Aroca, J., Sierra, F. & Castellanos Contreras, J. U. 2020. Bio-inspired rotor design characterization of a horizontal axis wind turbine. *Energies* 13 (14): 3515.

García-Villalba, M. et al. 2021. Demonstration of patient-specific simulations to assess left atrial appendage thrombogenesis risk. *Frontiers Physiol.* 12:596596.

Haider, N., Shahzad, A., Mumtaz Q., Muhammad N. & A. S., Syed I. 2021. Recent progress in flapping wings for micro aerial vehicle applications. *Proc. Inst. Mech. Eng., Part C* 235 (2): 245–264.

Han, B., Zhou, L., Yang, F. & Xiang, Z. 2016. Individual pitch controller based on fuzzy logic control for wind turbine load mitigation. *IET Renew. Power Gener.* 10 (5): 687–693.

Holden, J. R., Caley, T. M. & Turner, M. G. 2015. Maple seed performance as a wind turbine. In *53rd AIAA Aerospace Sciences Meeting*, 1304.

Jeong, J. & Hussain, F. 1995. On the identification of a vortex. *J. Fluid Mech.* 285:69–99.

Johnson, S. J., Baker, J. P., Van Dam, C.P. & Berg, D. 2010. An overview of active load control techniques for wind turbines with an emphasis on microtabs. *Wind Energy* 13 (2-3): 239–253.

Jurado, R., Arranz, G., Flores, O. & García-Villalba, M. 2022. Numerical simulation of flow over flapping wings in tandem: Wingspan effects. *Phys. Fluids* 34 (1): 017114.

Marais, C., Thiria, B., Wesfreid, J. E. & Godoy-Diana, R. 2012. Stabilizing effect of flexibility in the wake of a flapping foil. *J. Fluid Mech.* 710:659–669.

Martínez-Muriel, C. & Flores, O. 2020. Analysis of vortical gust impact on airfoils at low Reynolds number. *J. Fluids Struct.* 99:103138.

Moriche, M. 2017. "A numerical study on the aerodynamic forces and the wake stability of flapping flight at low Reynolds number." PhD diss., Universidad Carlos III Madrid.

Moriche, M., Flores, O. & García-Villalba, M. 2016. Three-dimensional instabilities in the wake of a flapping wing at low Reynolds number. *Int. J. Heat. Fluid Fl.* 62:44–55.

Navalkar, S. T. et al. 2016. Wind tunnel tests with combined pitch and free-floating flap control: data-driven iterative feedforward controller tuning. *Wind Energy Sci.* 1 (2): 205–220.

Sane, S. P. 2003. The aerodynamics of insect flight. *J. Exp. Biol.* 206 (23): 4191–4208.

Senda, K. et al. 2012. Effects of structural flexibility of wings in flapping flight of butterfly. *Bioinspir. Biomim.* 7 (2): 025002.

van Oorschot, B. K., Choroszucha, R. & Tobalske, B. W. 2020. Passive aeroelastic deflection of avian primary feathers. *Bioinsp. & Biomim.* 15 (5): 056008.

Videler, J. J., Weihs, D. & Daan, S. 1983. Intermittent gliding in the hunting flight of the kestrel, Falco tinnunculus. *J. exp. Biol* 102:1–12.

Viola, I. M., Bot, P. & Riotte, M. 2013. On the uncertainty of CFD in sail aerodynamics. *Int. J. Numer. Methods Fluids* 72 (11): 1146–1164.

Wootton, R. J. 1992. Functional morphology of insect wings. *Annual review of entomology* 37 (1): 113–140.

CHAPTER 5

FLUID-STRUCTURE RESONANCE IN SPANWISE-FLEXIBLE FLAPPING WINGS

The contents of this chapter are currently under review in:
Journal of Fluid Mechanics

Abstract

We report direct numerical simulations of the flow around a spanwise-flexible wing in forward flight. The simulations were performed at $Re = 1000$ for wings of aspect ratio 2 and 4 undergoing a heaving and pitching motion at a Strouhal number $St_c \approx 0.5$. We have varied the effective stiffness of the wing Π_1 while keeping the effective inertia constant, $\Pi_0 = 0.1$. It has been found that there is an optimal aerodynamic performance of the wing linked to a damped resonance phenomenon, that occurs when the imposed frequency of oscillation approaches the first natural frequency of the structure in the fluid, $\omega_{n,f}/\omega \approx 1$. In that situation, the time-averaged thrust is maximum, increasing by a factor of 2 with respect to the rigid case with an increase in propulsive efficiency of about 15%. This enhanced aerodynamic performance results from the combination of larger effective angles of attack of the outboard wing sections and a delayed development of the leading edge vortex. With increasing flexibility beyond the resonant frequency the aerodynamic performance drops significantly, both in terms of thrust production and propulsive efficiency. The cause of this drop lies in the increasing phase lag between the deflection of the wing and the heaving/pitching motion, which results in weaker leading edge vortices, negative effective angles of attack in the outboard sections of the wing, and drag generation in the first half of the stroke. Our results also show that flexible wings with the same $\omega_{n,f}/\omega$ but different aspect ratio have the same aerodynamic performance, emphasizing the importance of the structural properties of the wing on its aerodynamic performance.

5.1 Introduction

Micro-air vehicles (MAVs) are becoming increasingly important in society, being demanded for security services, protection, surveillance, etc. Among the different configurations being explored for those vehicles, the greatest potential in terms of maneuverability and versatility is perhaps offered by bioinspired configurations with flapping wings, similar to insects or small birds (Haider et al., 2021; Shyy et al., 2013). These configurations are also the most complex from a technical point of view, involving unsteady aerodynamic mechanisms (i.e., leading edge vortex (LEV), rotational lift, wake capture and clap-and-fling) that have been described in the literature (Ellington, 1999; Dickinson et al., 1999; Sane, 2003; Wang, 2005; Platzer et al., 2008). However, one aspect which is not yet properly understood is the effect of wing flexibility, despite significant progress in recent years. The current understanding is that the aerodynamic performance can be enhanced, provided that the wing kinematics and the structural properties are adequately selected. Indeed, it has been shown that there exists an optimal range of flexibility for propulsion (Shyy et al., 2010), and that wing flexibility can reduce the energetic cost of flight for natural flyers (Reid et al., 2019).

Other effects have also been studied, like the influence of flexibility on the development and evolution of coherent structures surrounding the wings (Gordnier et al., 2013). However, the accumulated knowledge is not yet sufficient to significantly influence current MAV designs. In fact, Haider et al. (2021) recently emphasized that the development of MAVs with flexible flapping wings has not yet reached capabilities similar to those of natural flyers.

The main problem that hinders further progress is the complexity of the interactions between flexible, flapping wings and the surrounding fluid. There are some studies that have tackled this problem considering isotropic homogeneous wings (Hamamoto et al., 2007; Nakata & Liu, 2012; Shahzad et al., 2018). Other authors have tried to make progress by simplifying the problem, considering chordwise or spanwise flexibility in a separate way. In fact, most of the available studies consider chordwise flexibility only, like Alben (2012), Moored et al. (2012), Quinn et al. (2014), Olivier & Dumas (2016), Yeh & Alexeev (2016), Hoover et al. (2018), Arora et al. (2018), and K. Liu et al. (2022). The literature is vast and additional references can be found in recent reviews (Quinn & Lauder, 2022; Wang et al., 2022).

The two key questions addressed in the literature of chordwise-flexible wings/airfoils are whether there is a flexibility (or a range of flexibilities) that leads to optimal propulsive performance, and what are the mechanisms that explain that optimal performance. While there is broad agreement on an affirmative answer for the first question, the literature proposes two non-exclusive mechanisms contributing to the answer to the second question. The first mechanism is a fluid-structure resonance, which results in maximum deflections of the trailing edge of the chordwise-flexible wing (Michelin & Llewellyn Smith, 2009; Paraz et al., 2016; Floryan & Rowley, 2018). The second mechanism is related to the phase lag between actuation and deformation. When properly tuned, it can lead to an optimal bending of the wing that projects the aerodynamic loads on the wing into the forward direction, hence maximizing thrust (Ramananarivo et al., 2011; Zhu et al., 2014b). In this regard, it is important

to recall that in damped harmonic oscillators, both structural and damping non-linearities affect the phase lag between forcing and response at all frequencies (Nayfeh & Mook, 2008), resulting in phase lags at resonance different from the 90° phase lag obtained in linear oscillators. Indeed, Ramananarivo et al. (2011) attributed the enhanced propulsive performance of chordwise-flexible wings to non-linear damping effects.

Obviously, the two mechanisms are not exclusive, and the optimal bending of a particular wing/kinematic might occur at the resonant frequency. An example reconciling these two mechanisms is Goza et al. (2020), who observed resonant behavior leading to optimal performance in numerical simulations of chordwise-flexible 2D airfoils over a wide range of flexibilities. For large amplitudes of excitation, they reported that both resonance and non-linear effects played a role. In particular, they observed that the peak in the structural response weakened and broadened in frequency, a behavior that they attributed to added mass and non-linear effects, like flow separation and non-linear vortex interaction. They also noted that this broader and weaker frequency response for large amplitude oscillations is consistent with the non-linear damping effects of a non-linear oscillator, linking in this form their results to those of Ramananarivo et al. (2011).

Comparatively, there are less studies analyzing the effect of spanwise flexibility, which are briefly reviewed below. One of the first studies available in the literature was performed using a panel method by Liu & Bose (1997). They showed that the propulsive efficiency of the planforms can be optimized by controlling the tip-to-root relative motion. In a similar fashion, also using a potential flow model, Zhu (2007) reported simulations studying the effect of spanwise flexibility on fluid-driven wings with low effective inertia ($\Pi_0 \approx \mathcal{O}(10^{-4})$) and inertia-driven wings with a typical effective inertia of insects ($\Pi_0 \approx \mathcal{O}(10^{-1})$). While fluid-driven flexible wings exhibited no enhancement in performance with respect to rigid wings whichever the flexibility, thrust was greatly increased for inertia-driven wings when increasing the flexibility up to an optimal value. A corresponding increase in propulsive efficiency was not observed. This was followed by an influential experiment reported by Heathcote et al. (2008). These authors studied spanwise flexible wings in heaving motion immersed on a free stream in the range $Re = 10000 - 30000$, based on the incoming velocity. They found an increase in thrust for a limited degree of flexibility, with little influence of the Reynolds number in the range considered. The experiment of Heathcote et al. (2008) has been the subject of several numerical simulations with various methods. For example Chimakurthi et al. (2009), Aono et al. (2009) and Kang et al. (2011) employed Reynolds-Averaged Navier-Stokes (RANS) simulations with a non-linear beam structural model, while Gordnier et al. (2013) used a high-order implicit Large Eddy Simulation (LES) to model the flow. These numerical studies have shown a non-monotonic response of the mean thrust with respect to the wing flexibility and a sudden loss of performance for very flexible wings. Shyy et al. (2010) suggest that the poor aerodynamic performance of the very flexible wings is related to the cumulative effect of the effective angle of attack and to the role of the tip to root relative motion, with large phase lags for the very flexible wings. Gordnier et al. (2013) reported a detailed analysis of the phenomena that drive the fluid-structure interaction, for a configuration corresponding to

Heathcote et al. experiments. They showed that for the moderately flexible wings, higher effective angles of attack result in the development of a stronger LEV. Due to the more rapid effective bend up and down motion towards the tip of the wing the convection of the LEV is inhibited leading to a superior aerodynamics performance. This further supports the idea that the phase lag between tip and root motions is a key parameter in the fluid-structure interaction of spanwise flexible wings.

To the best of our knowledge, Kodali et al. (2017) is the first work that explicitly linked the enhancement in aerodynamic performance with a resonance phenomenon when spanwise flexibility is considered. However, this fluid-structure resonance can also be inferred from previous works, like in Zhu (2007) and Qi et al. (2010). Kodali et al. (2017) reported a two-way coupled aeroelastic model of a heaving, spanwise-flexible wing in forward flight. The aerodynamics was modelled using 2D, unsteady potential flow, evaluated at each spanwise location, so that this represents a high Reynolds number approximation. The structure was modelled using an Euler-Bernoulli beam equation. The analysis was performed by changing the wing aspect-ratio while keeping constant the remaining structural parameters, thus varying the natural frequency of the wing. They found the optimal aerodynamic performance (defined in terms of energy requirements, not thrust production) when the natural frequency matched the oscillation frequency, i.e. a resonance was observed as already mentioned. They also found that the relative motion between the tip and root sections lagged by roughly 90° for the optimal flexibility. A final observation was that the structural response was governed by the first natural mode of the structure, with the remaining modes being barely excited.

Note, however, that the use of linear models for aerodynamics (i.e., potential aerodynamics) and structure (i.e., Euler-Bernoulli beam eq.) somewhat limits the scope of the work of Kodali et al. (2017), especially taking into account the aforementioned role of non-linearities in the aerodynamic performance of chordwise-flexible airfoils/wings. These limitations are not present in other studies. For instance, Zhu (2007) uses a potential aerodynamic model in combination with a non-linear structural model, and Qi et al. (2010) uses a lattice Boltzmann flexible particle method (i.e., non-linear aerodynamic and structural models) at very a low Reynolds numbers ($Re = \mathcal{O}(10^2)$). Interestingly, while these three studies found optimal values for flexibility in the inertia-driven range ($\Pi_0 \approx \mathcal{O}(10^{-1})$) consistent with a fluid-structural resonance, they show important differences in terms of mean thrust coefficients, propulsive efficiencies, and phase lag between excitation and structural response (i.e., wing tip displacement). The reasons for these discrepancies are not completely clear, given the differences in the wing kinematics, flight conditions (forward flight vs hover flight), Reynolds number, structural non-linearities, and fluid damping (linear vs non-linear, leading edge vortex effects, viscous vs inviscid).

In view of the above, we aim to characterize the role of fluid-structure resonance in the enhancement of aerodynamic performance of spanwise flexible wings. In particular, we perform direct numerical simulations of the incompressible flow around heaving and pitching flexible wings in forward flight at $Re = 1000$. We consider rectangular wings with two different aspect ratios, and several values of the effective stiffness. This will allow us to explore if the aspect ratio is important

only as a structural parameter (i.e., changing the natural frequency of the structure, as in the study of Kodali et al., 2017), or if it is also relevant in terms of the generation of aerodynamic loads. Our study analyses a Reynolds number that is intermediate to those available in the literature, which are either much lower (Qi et al., 2010) or much higher (Liu & Bose, 1997; Heathcote et al., 2008; Chimakurthi et al., 2009; Aono et al., 2009; Kang et al., 2011; Gordnier et al., 2013). Contrary to previous works, direct numerical simulations of the flow allow to represent in detail the surrounding fluid, allowing a proper description of the non-linear and viscous character of the fluid damping at intermediate Reynolds numbers.

The paper is structured as follows: Section 5.2 presents the problem definition, followed by the numerical details of the algorithms used to solve the fluid-structure interaction problem. Section 5.3 shows the results of the simulations, characterizing the aerodynamic forces, the structural response of the wing, and the mechanisms that explain the changes in the aerodynamic forces with the wing's flexibility. Finally, conclusions are presented in section 5.4.

5.2 Methodology

5.2.1 Problem definition

A finite wing in forward flight immersed in a uniform and steady free-stream of magnitude U_∞ is considered. The fluid has constant density and viscosity (ρ_f and μ), resulting in a Reynolds number based on the chord of the wing, c, and the free-stream velocity equal to $Re = \rho_f U_\infty c/\mu = 1000$. The wing is a rectangular flat plate with finite aspect ratio $\mathcal{AR} = b/c$, where b is the span of the wing and the dimensionless thickness is $h_s^* = h_s/c = 0.02$. The wing is rigid in the chordwise direction and flexible in the spanwise direction. To study the effect of the wing span, two aspect ratios are considered, $\mathcal{AR} = 2$ and 4.

A heaving and pitching motion is imposed on the mid-span section of the wing. The rest of the wing deforms passively. The kinematics is described by the following laws

$$h(t) = h_0 \cos\left(\frac{2\pi t}{T}\right), \tag{5.1a}$$

$$\theta(t) = \theta_0 \cos\left(\frac{2\pi t}{T} + \phi_{hp}\right), \tag{5.1b}$$

where h_0 is the heaving amplitude, θ_0 the pitching amplitude, ϕ_{hp} the phase difference between heaving and pitching motions, and T the oscillation period. We also define the frequency of the imposed motion as $f = 1/T$, the angular frequency as $\omega = 2\pi f$, and the reduced frequency as $k = \pi f c/U_\infty$. The Strouhal number based on the chord of the wing is defined as $St_c = fc/U_\infty$. The pivoting axis for pitching is placed at the mid-chord, $x/c = 0.5$. The kinematic parameters shown in table 5.1 have been selected to ensure positive thrust and relatively strong LEVs, with flapping amplitude large enough to ensure non negligible non-linear effects. Incidentally, these parameters yield optimal propulsive efficiency for a system of two airfoils arranged in horizontal tandem (see

h_0/c	θ_0	St_c	k	ϕ_{hp}
$0.388c$	$26.19°$	0.496	1.558	$\pi/2$

Table 5.1: Parameters of the kinematics imposed at the midsection of the wing

Ortega-Casanova & Fernández-Feria, 2019; Martínez-López, 2019 and Martínez-Muriel, 2023 for details), which will be the subject of a follow-up study.

The material properties of the wing are varied to study the effect of spanwise flexibility. As discussed in the following subsection, this is done by adjusting the first natural frequency of the wing in vacuum,

$$\frac{\omega_n c}{U_\infty} = \beta_n^2 \sqrt{\frac{E^* h_s^{*2}}{12\rho^*}}, \tag{5.2}$$

where β_n is the first eigenvalue of the transcendental equation

$$\cos(\beta_i \mathcal{AR}/2)\cosh(\beta_i \mathcal{AR}/2) + 1 = 0, \tag{5.3}$$

as described in Kodali et al., 2017. In equation (5.2), $E^* = E/\rho_f U_\infty^2$ is the normalized Young's modulus and $\rho^* = \rho_s/\rho_f$, is the solid to fluid density ratio. Following Shyy et al., 2010, we define the effective inertia and effective stiffness of the wings, respectively as

$$\Pi_0 = \rho^* h_s^* \left(\frac{k}{\pi}\right)^2, \quad \Pi_1 = \frac{E^* h_s^{*3}}{12}. \tag{5.4}$$

These two parameters, Π_0 and Π_1, serve to characterize the structural and inertia properties of the wing.

In the present study, Π_0 is kept constant while Π_1 is varied to cover a wide range of frequency ratios, ω_n/ω, as shown in table 5.2. A density ratio $\rho^* = 20$ is selected such that $\rho^* h_s^* = 0.4$ and a value of $\Pi_0 = 0.0984$ are obtained. This value is of the same order of magnitude of the effective inertia of insects (Shyy et al., 2013; Jongerius & Lentink, 2010; Hamamoto et al., 2007; Ren et al., 2013) and birds (Kodali et al., 2017). The range of the effective stiffness considered here, $\Pi_1 \sim [\mathcal{O}(10^{-1}) - \mathcal{O}(10^2)]$, is comparable to that considered in previous studies (Fu et al., 2018). In addition, a rigid wing ($\Pi_1 \to \infty$) is also included in the study to provide a baseline for comparison.

5.2.2 Structural model

A lumped-torsional flexibility model is used to simulate the spanwise flexibility of the wing. The wing is discretized into $N_B = 5\mathcal{AR} + 1$ rigid segments connected by torsional springs, as depicted in figure 5.1(a). To avoid overlapping when the segments rotate relative to each other, the segments are separated a distance $e = h_s$ when placed horizontally. Note that a similar approach was employed by Arranz et al. (2022a) to simulate the chordwise flexibility of self-propelling plates.

Under this model, the wing can be considered as a multi-body system (MBS) of N_B bodies with $1 + N_B$ degrees of freedom; namely, the vertical displacement (h), the pitching angle (θ), and the relative rotation angles between each segment, $\phi_i, i = 1, \ldots, N_B - 1$ (see figure 5.1b).

Id	$\mathcal{AR}$	ω_n/ω	$\omega_{n,f}/\omega$	Π_1	$\Pi_1(2/\mathcal{AR})^4$	Nomenclature	$c/\Delta r$	$\overline{C_T}$	C_L^{rms}	η_p
1	4	∞	∞	∞	∞	**Rigid**	96	0.416	2.331	0.217
2	4	3.6	2.22	66.3	4.14	**Intermediate**	96	0.552	2.618	0.235
3	4	1.8	1.11	16.6	1.04	**Optimal**	96	0.844	3.272	0.248
4	4	1.2	0.74	7.4	0.46	**Sub-optimal**	96	0.129	1.707	0.066
5	4	0.7	0.44	2.7	0.17	Sub-optimal 2	56	-0.02	0.668	-0.024
6	2	∞	∞	∞	∞	**Rigid**	96	0.330	2.183	0.178
7	2	17.5	10.75	96.25	96.25	-	56	0.348	2.195	0.181
8	2	9.3	5.7	27.2	27.2	-	56	0.366	2.213	0.186
9	2	4.6	2.82	6.7	6.7	Intermediate	56	0.471	2.458	0.212
10	2	3.25	2	3.3	3.3	-	56	0.621	2.674	0.234
11	2	2.3	1.41	1.7	1.7	**Optimal**	96	0.734	2.995	0.237
12	2	1.6	0.99	0.83	0.83	Sub-optimal	56	0.216	2.086	0.099
13	2	0.65	0.4	0.13	0.13	-	56	-0.05	0.507	-0.065

Table 5.2: Overview of problem parameters and simulation results. $\mathcal{AR}$ is the aspect ratio. ω_n/ω and $\omega_{n,f}/\omega$ are the ratios of natural frequency in vacuum and in fluid, respectively, to the angular frequency of the flapping motion. Π_1 is the effective stiffness. $c/\Delta r$ is the grid resolution used in the refined zone of the domain. $\overline{C_T}$, $C_L{}^{\text{rms}}$ and η_p are the time-averaged thrust coefficient, the RMS of the lift coefficient, and the propulsive efficiency, respectively.

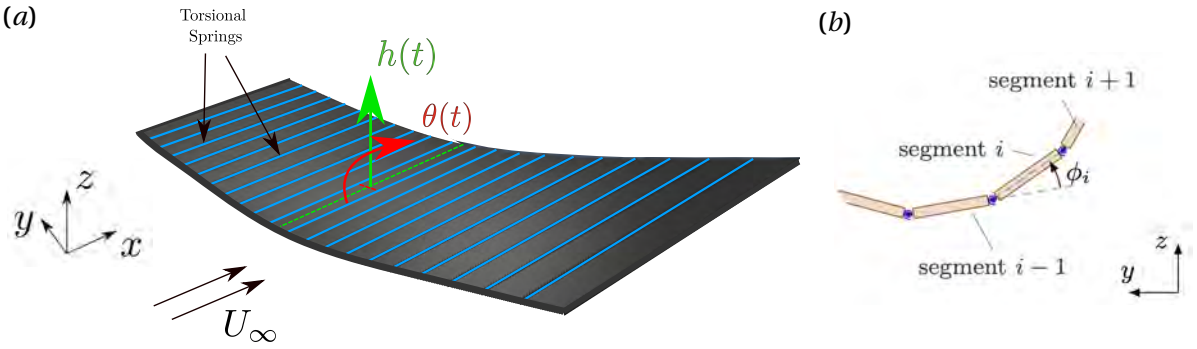

Figure 5.1: (*a*) Sketch of the multibody model to qualitatively describe the spanwise flexibility of a wing, where the system of bodies is connected via torsional springs. (*b*) Sketch of the degree of freedom (ϕ_i) between two consecutive segments.

For the sake of brevity, only a summary of the most representative aspects of the method are presented here, further details can be found in Arranz et al. (2022b). The governing equations for the MBS can be cast in the form:

$$H(\mathbf{q})\ddot{\mathbf{q}} + C(\mathbf{q},\dot{\mathbf{q}}) = \boldsymbol{\xi} + \boldsymbol{\xi}_h, \tag{5.5}$$

where $\mathbf{q} = [h, \theta, \phi_1, \ldots, \phi_{N_B-1}]$ is the vector of generalized coordinates, H is the generalized inertia matrix, C is the generalized bias force vector, which include Coriolis and centrifugal accelerations, $\boldsymbol{\xi} = [0, 0, -K\phi_1, \ldots, -K\phi_{N_B-1}]$, where K is the torsional spring constant, and $\boldsymbol{\xi}_h$ is the vector of hydrodynamic forces acting on the wing. In order to compute the generalized inertia matrix, H, and the generalized bias force, C, the open-source Rigid Body Dynamics Library (RBDL) developed by Felis (2017) is used. The H matrix is computed through the Composite Rigid-Body algorithm (CRBA), and

the C vector is computed through the Recursive Newton-Euler algorithm (RNEA). The stiffness of the torsional springs, K is adjusted solving an eigenvalue problem as done by Arora et al. (2018), so that the first natural frequency of the MBS matches the first natural frequency of the corresponding flexible structure in vacuum, ω_n.

5.2.3 Flow Solver

The fluid solver employed in this work is TUCAN, a constant-density fluid solver that uses the Immersed Boundary Method (IBM) proposed by Uhlmann (2005) to model the presence of the wing in the flow. The three-dimensional Navier-Stokes equations for an incompressible flow modified for the IBM are used to describe the fluid dynamics,

$$\nabla \cdot \mathbf{u} = 0, \tag{5.6a}$$

$$\frac{\partial \mathbf{u}}{\partial t} + (\mathbf{u} \cdot \nabla)\mathbf{u} = -\nabla p + \nu \nabla^2 \mathbf{u} + \mathbf{f}_{IBM}, \tag{5.6b}$$

$$\mathbf{u}(\mathbf{x}) = \mathbf{U}_{\partial\Gamma} \quad \forall \mathbf{x} \in \partial\Gamma, \tag{5.6c}$$

where $\mathbf{u}$ is the velocity field, p is the kinematic pressure (i.e., pressure over the fluid density ρ_f), $\nu = \mu/\rho_f$ is the kinematic viscosity, and $\mathbf{f}_{IBM}$ is the IBM forcing term that models the presence of the wing. This forcing term ensures that the no-slip boundary condition (equation 5.6*c*) is satisfied at the solid boundaries (i.e., on the surface of the wing segments), where $\mathbf{U}_{\partial\Gamma}$ is the velocity at the segments' surface. To compute the velocity at the wing surface, equation (5.5) is solved together with equation (5.6). In particular, at every time step, the hydrodynamic forces are computed and used to update the position and velocity of the segments according to equation (5.5). Then, the new hydrodynamic forces are computed from equation (5.6), leading to a weak coupling between both systems of equations. This might result in a small incompatibility between the flow field at the wing surface and the wing's velocity at the end of the time step, which in any case remains bounded and negligible over the simulation time. The weak coupling between the equations is also known to lead to stability problems for density ratios below 1.2 (Uhlmann, 2005). However, in the range of parameters considered in this study no stability issues have been observed (Arranz et al., 2022b).

Two different meshes are required. First, a staggered Cartesian grid is used to discretize the fluid variables, referred to as the Eulerian mesh. The spatial derivatives appearing in figure (5.6) are approximated by centered finite differences in the staggered grid defined by the Eulerian mesh. Second, the surface of the wing's segments ($\partial\Gamma$) is discretized with a Lagrangian mesh, that follows the active/passive motion of the solid body within the fluid. The boundary condition on the wing surface (i.e., equation 5.6c) is imposed on this Lagrangian mesh, which requires the use of discrete delta functions to interpolate velocities and the IBM forcing term back and forth between the Lagrangian and Eulerian meshes. A complete description of the fluid solver implemented in TUCAN can be found in Moriche (2017).

TUCAN has already been successfully employed, both for 2D (Moriche et al., 2017; Martínez-Muriel & Flores, 2020) and 3D aerodynamics problems (Moriche et al., 2016; Arranz et al., 2018b;

Arranz et al., 2020; Moriche et al., 2021) and also for cardiac flows (García-Villalba et al., 2021; Gonzalo et al., 2022).

5.2.4 Computational Set-up

Direct Numerical Simulations (DNS) of the problem described in section 5.2.1 are performed using TUCAN. The time step is selected such that the CFL number is lower than 0.3. The simulations are performed in a computational domain with dimensions $14c \times 11c \times 7c$ in the streamwise, spanwise and vertical directions, respectively. A refined zone is defined roughly at the middle of the domain with a uniform grid spacing in all directions, Δr. Outside this refined region, a constant stretching of 1% is applied to the grid in all directions. The wings are located in the refined zone, which has a size of $(2c \times L_{y,r} \times 3c)$ where $L_{y,r} = (\mathcal{AR}+1)c$ depends on the aspect ratio of the wing, leaving enough space to the boundaries not to have spurious effects on this refined zone, and enough space downstream to properly develop the wake. The origin of the reference system is located at the leading edge of the mid-span section of the wing. The free stream condition is modeled with an inflow velocity at the inlet boundary ($x/c = -4.75$), while the outflow has been modeled with an advective boundary condition ($\partial \mathbf{u}/\partial t + U_\infty \partial \mathbf{u}/\partial x = 0$) at the outlet ($x/c = 9.25$). Free slip boundary conditions are imposed in the lateral boundaries.

The simulations are started in a grid that uses a lower resolution of $\Delta r = c/56$ in the refined zone, which captures qualitatively the dynamics of the problem as shown in the Appendix B.2. These simulations are run for 4 cycles. Then, for selected configurations (see table 5.2), two additional cycles are run at a higher resolution, $\Delta r = c/96$. This higher resolution is chosen based on the grid refinement study performed by Arranz et al. (2020) for a similar problem at the same Reynolds number. We have checked that the number of cycles run in all simulations are enough to ensure that aerodynamic forces and the flow in the vicinity of the wing are periodic. The rigid segments that represent the Lagrangian mesh are discretized using $\Delta_l = c/96$ irrespective of the resolution used for the Eulerian grid.

Finally, note that the space between the segments, e, is larger than the Eulerian grid spacing, allowing fluid to pass through these gaps. The effect of the gaps is negligible to the global evolution of forces, as shown in Appendix B.1, although they leave a visible footprint in the flow structures as will be shown below.

5.3 Results

5.3.1 Force coefficients

First, thrust and lift coefficients, C_T and C_L, respectively, for cases with $\mathcal{AR} = 4$, are presented as a function of time in figure 5.2. These coefficients are defined as

$$C_T = \frac{-2\mathbf{F}\cdot\mathbf{e}_x}{\rho_f U_\infty^2 S}, \quad C_L = \frac{2\mathbf{F}\cdot\mathbf{e}_z}{\rho_f U_\infty^2 S}, \tag{5.7}$$

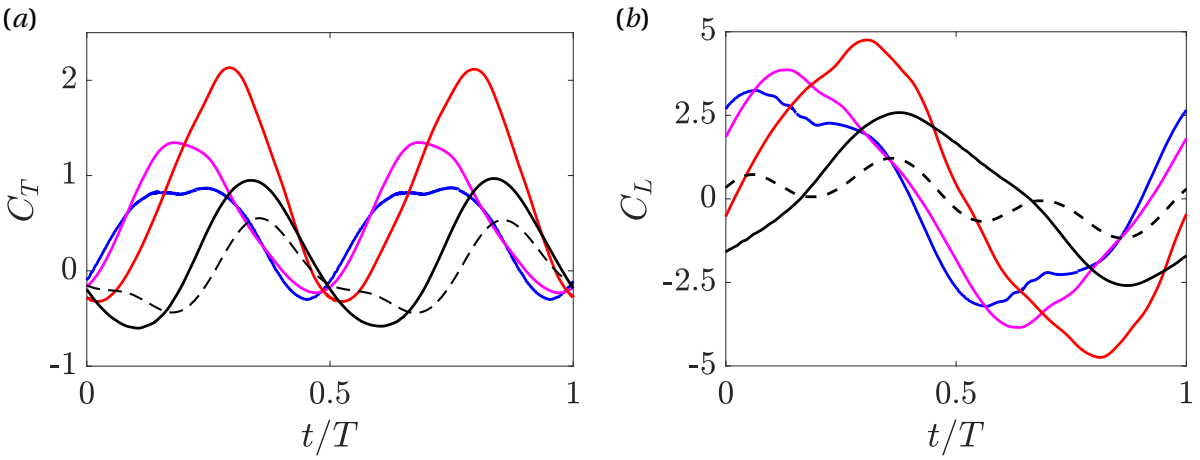

Figure 5.2: Temporal evolution of (a) thrust coefficient, C_T, and (b) lift coefficient, C_L, of $\mathcal{AR} = 4$ wings. Line colors correspond to: ——: 1 (Rigid). ——: 2 (Intermediate). ——: 3 (Optimal). ——: 4 (Sub-optimal). – – –: 5 (Sub-optimal 2).

where $\mathbf{F}$ is the total aerodynamic force and $\mathbf{e}_k$ is the unitary vector in the k-axis direction. Due to the symmetry of upstroke and downstroke motions, the time-averaged value of the thrust coefficient is different from 0 in general, while the mean value of the lift coefficient is 0. As expected, there is a clear influence of the wing flexibility on the evolution of the forces. When moving from rigid to more flexible wings (i.e. decreasing Π_1), a non-monotonic behaviour of the maximum values of both C_T and C_L is observed, in accordance with previous studies of heaving wings in forward flight (Heathcote et al., 2008) and hovering wings (Qi et al., 2010). Focusing on C_T, figure 5.2(a) shows that its maximum value during the downstroke increases with the flexibility for cases 1, 2 and 3. Increasing flexibility beyond case 3 results in a sudden drop in C_T, as shown by cases 4 and 5. Moreover, the time instant at which the peak in both force coefficients is produced depends on the flexibility. For the rigid case C_T peaks at $t/T \approx 0.15$, prior to mid-downstroke. For case 3, the maximum occurs at $t/T \approx 0.3$, after the mid-downstroke. A similar behaviour can be observed in figure 5.2(b) for C_L in terms of maximum values and times. The temporal evolution of C_T and C_L for the cases with $\mathcal{AR} = 2$, and their variation with the wing flexibility, are qualitatively similar to those shown in figure 5.2 for $\mathcal{AR} = 4$, and are provided as the Supplementary Material.

Given the temporal evolution of the forces, we choose to characterize the aerodynamic performance of the wings in terms of the mean thrust coefficient, $\overline{C_T}$, and the root-mean square (RMS) of the lift coefficient, ${C_L}^{\text{rms}}$. Note that we choose ${C_L}^{\text{rms}}$ instead of $\overline{C_L}$, since the latter is zero for the wing kinematics considered here. Figure 5.3 shows the variation of $\overline{C_T}$ and ${C_L}^{\text{rms}}$ with the effective stiffness of the wing. The effect of the aspect ratio of the wing in $\overline{C_T}$ and ${C_L}^{\text{rms}}$ is captured by re-scaling the effective stiffness (horizontal axis on the top) with the factor $(2/\mathcal{AR})^4$, as proposed by Kang et al. (2011). Figure 5.3 suggests that this re-scaling is able to collapse into a single curve the force coefficients of the flexible cases with $\mathcal{AR} = 4$ and 2, at least for values of $\Pi_1 (2/\mathcal{AR})^4 \lesssim 10$.

Overall, figure 5.3 shows that the variability of $\overline{C_T}$ and ${C_L}^{\text{rms}}$ with the wing's effective stiffness

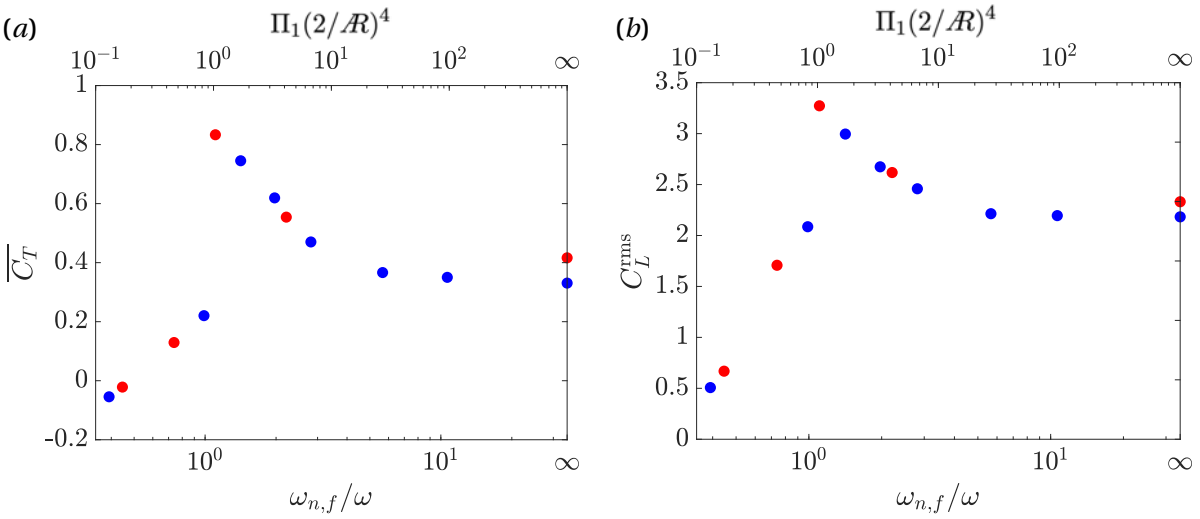

Figure 5.3: (*a*) Mean thrust coefficient $\overline{C_T}$ and (*b*) RMS of lift coefficient ${C_L}^{\mathrm{rms}}$. Blue symbols, $\mathcal{R} = 2$. Red symbols, $\mathcal{R} = 4$.

is qualitatively similar, presenting a monotonic increase from stiffer to more flexible cases (i.e. decreasing Π_1) until a peak is reached. Decreasing the effective stiffness beyond this point results in a sudden drop of $\overline{C_T}$ and ${C_L}^{\mathrm{rms}}$, as already anticipated when discussing the temporal evolution of the coefficients.

Figure 5.3(*a*) also allows to analyze the effect of $\mathcal{R}$ on the mean thrust coefficient. For the rigid wings there is a factor of 1.25 between the $\overline{C_T}$ of $\mathcal{R} = 2$ and $\mathcal{R} = 4$. For the flexible wings, changing the $\mathcal{R}$ implies changing the rescaled effective stiffness, i.e. moving along the top horizontal axis of figure 5.3(*a*). In particular, a change of $\mathcal{R}$ from 2 to 4 results in a shift of more than a decade (a factor of 1/16). For the range of flexibilities near the peak, this yields a factor of up to 2.25 in $\overline{C_T}$. This suggests that the effect of $\mathcal{R}$ on the structural properties of flexible wings is dominant over its direct effect on the generation of aerodynamic forces.

In the following, we loosely denote *optimal* cases for each aspect ratio those that correspond to the peak in the aerodynamic performance. We denote *sub-optimal* cases those which are beyond the sudden drop in performance (i.e. for smaller Π_1 than the optimal cases). We denote *intermediate* cases those between the rigid and the optimal cases. For reference, this terminology is included in table 5.2. The stereotypical cases selected (somewhat arbitrarily) for analysis are: cases with id [1, 2, 3, 4] for $\mathcal{R} = 4$ and [6, 9, 11, 12] for $\mathcal{R} = 2$, denoting them as *rigid*, *intermediate*, *optimal* and *sub-optimal*, respectively.

The aerodynamic force coefficients in figure 5.3 are also plotted as a function of the ratio of natural frequency in fluid over the frequency of the motion, $\omega_{n,f}/\omega$ (see horizontal axis on the bottom). The natural frequency in fluid is computed as in Moore (2015) and Arora et al. (2018),

$$\frac{\omega_{n,f}}{\omega} = \frac{\omega_n/\omega}{\sqrt{1+I_a}} = \frac{\beta_n^2}{2\pi}\sqrt{\frac{\Pi_1}{\Pi_0(1+I_a)}} = \frac{a}{2\pi}\sqrt{\frac{\Pi_1(2/\mathcal{R})^4}{\Pi_0(1+I_a)}}, \tag{5.8}$$

where the dimensionless parameter I_a represents the additional moment of inertia of the wing due to the added mass term (Arora et al., 2018), and the solution to equation (5.3) has been expressed as $\beta_n^2 = a(2/\mathcal{AR})^2$, with a equal to a positive constant. Since in the present study, Π_0 and I_a are held constant for all cases, equation (5.8) yields a linear relationship between $\log_{10}(\omega_{n,f}/\omega)$ and $\log_{10}(\Pi_1(2/\mathcal{AR})^4)$, allowing the use of two horizontal axes in figure 5.3. Indeed, given the straightforward physical interpretation of $\omega_{n,f}/\omega$, in the following we will use this quantity to characterize the wing's flexibility, instead of $\Pi_1(2/\mathcal{AR})^4$. Finally, the natural frequency in fluid given by eq. (5.8) approximates well that obtained from a linear stability analysis of the coupled fluid-structure system (Goza et al., 2020). For example, the value of $\omega_{n,f}$ using eq. (5.8) for the cases with $\Pi_1 = 20$ in Goza et al. (2020) is $\omega_{n,f} \approx 6.1\pi U_\infty/c$ while the one obtained from the linear stability analysis is $\omega_{n,f} \approx 6.2\pi U_\infty/c$.

The results in figure 5.3 show that the optimal flexibility is found for values of $\omega_{n,f}/\omega$ slightly above 1 (see also table 5.2 for the precise values). For $\omega_{n,f}/\omega < 1$ the drop in performance is observed, for both wing aspect-ratios. Similar observations can be inferred from the works of Zhu et al. (2014b) and Qi et al. (2010), although for different kinematics and Reynolds number.

We also analyze the effect of flexibility on the power requirements and the propulsive efficiency of the wings. The propulsive efficiency of the wing is computed as

$$\eta_p = \frac{\overline{C_T}}{\overline{P}}, \tag{5.9}$$

where $\overline{P}$ is the time-averaged non-dimensional input power of the wing. The instantaneous non-dimensional input power is computed similarly as in Arranz et al. (2022a), by using the reaction forces and moments on the segment whose motion is imposed. The reaction force on the vertical direction is denoted R_z and the reaction pitching moment is denoted R_θ. Then, the instantaneous non-dimensional power for the flexible wings is computed as

$$P(t) = \frac{2}{\rho_f U_\infty^3 S}\left(\max(R_z(t)\dot{h}(t),0) + \max(R_\theta(t)\dot{\theta}(t),0)\right). \tag{5.10}$$

Note that the definition for the power is such that no extraction of energy from the fluid is considered (Berman & Wang, 2007; Vejdani et al., 2018; Jurado et al., 2022).

Figure 5.4(a) shows the temporal evolution of the required input power for the four stereotypical cases with $\mathcal{AR} = 4$. The peak power input for the intermediate and optimal cases with $\mathcal{AR} = 4$ is roughly twice that for the rigid case. Thus, not surprisingly, producing more thrust requires more power to move the wing. When comparing the intermediate and the rigid cases, the increase in power input for the intermediate case occurs only during the first half of each stroke. For the optimal case, whose thrust peak is delayed (see figure 5.2a), the increase in required power extends to 80% of each half cycle. Note that although the peak thrust of the optimal case is about 50% higher than the peak thrust of the intermediate case (see figure 5.2a), the peak power input for these two cases is not that different. For the sub-optimal case, the power input drops significantly, reaching a level similar to the rigid case.

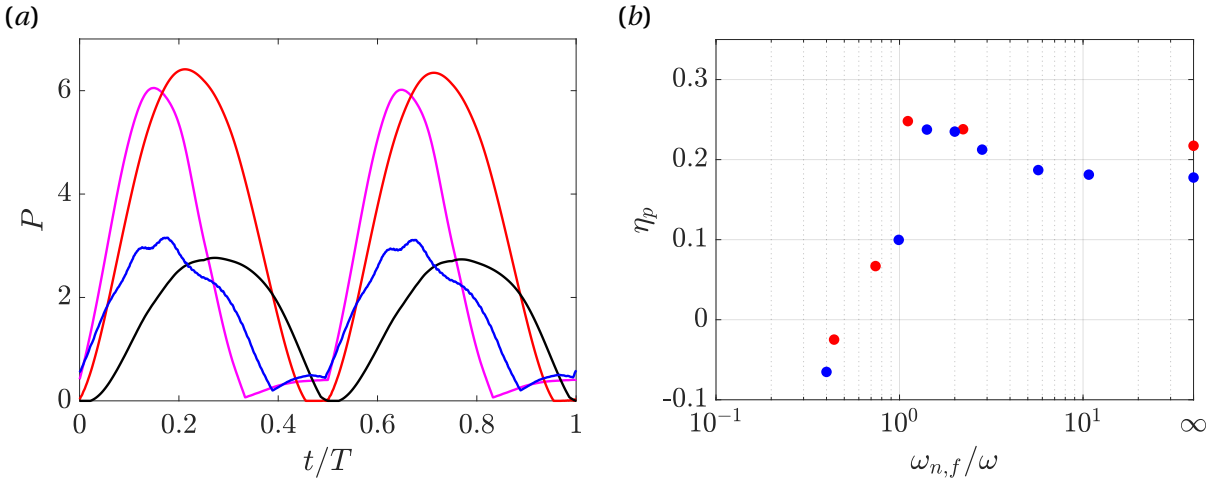

Figure 5.4: (*a*) Power requirements for $\mathcal{AR} = 4$ cases. Line colors correspond to: ——: Rigid. ——: Intermediate. ——: Optimal. ——: Sub-optimal. (*b*) Propulsive efficiency η_p for rigid, intermediate, optimal and sub-optimal cases for both aspect ratios.

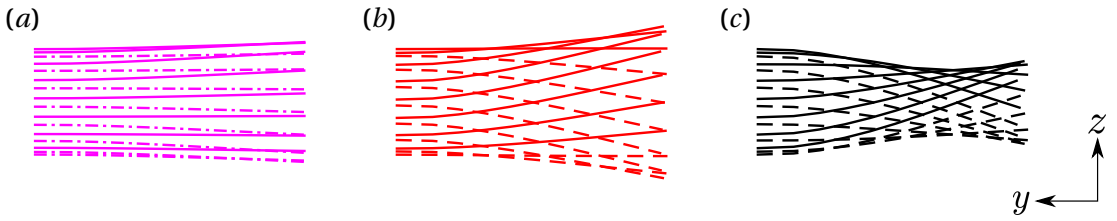

Figure 5.5: Deflection of the mid-chord line of the wing during the cycle. Only half wing is shown from root (left) to tip (right). Solid (dashed) lines correspond to the downstroke (upstroke). The following cases for $\mathcal{AR} = 4$ are shown: (*a*) Intermediate (——). (*b*) Optimal (——). (*c*) Sub-optimal (——).

Figure 5.4(*b*) shows the propulsive efficiency for all cases considered (including both aspect ratios) as a function of the frequency ratio. When comparing the optimal case with the rigid case we observe a small increase in the efficiency (for $\mathcal{AR} = 4$, from $\eta = 0.217$ to 0.248, and for $AR = 2$, from $\eta = 0.177$ to 0.237). The propulsive efficiency of intermediate and optimal cases are very similar, even if the optimal cases has a net thrust coefficient that is approx. 45% larger in the optimal cases. Beyond the optimal case the drop in efficiency is noticeable, analogous to the behaviour observed for $\overline{C_T}$ and ${C_L}^{\text{rms}}$ in figure 5.3. The differences between the propulsive efficiency of flexible wings with $\mathcal{AR} = 2$ and 4 are small, and only become significant in the limit of a rigid wing.

5.3.2 Structural response

As seen in the previous section, the optimal aerodynamic performance of the wings is reached when the frequency of the imposed motion, ω, approaches the first natural frequency of the structure in the fluid, $\omega_{n,f}$. This hints to the occurrence of a resonance phenomenon, which we try to characterize now, starting with the analysis of the structural response. We first provide a qualitative view of the wing deformation for three of the cases with $\mathcal{AR} = 4$. Figure 5.5 compares the deflection patterns of the intermediate, optimal and sub-optimal cases. Each line in the figure corresponds to the projection of

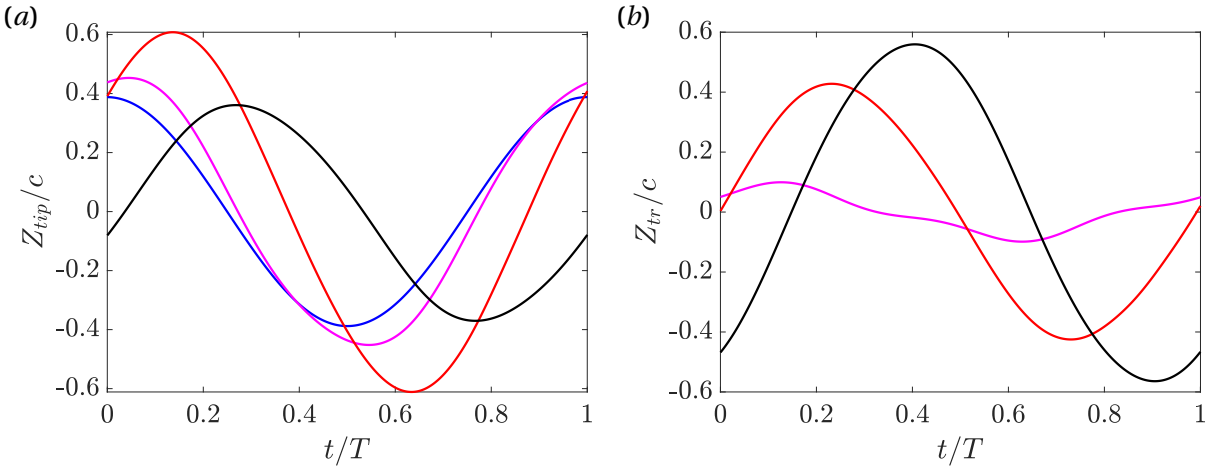

Figure 5.6: Time evolution of (a) the mid-chord vertical position of the tip Z_{tip} and (b) the tip to root vertical relative position Z_{tr}, for $\mathcal{AR} = 4$. Rigid case, ——. Intermediate case, ——. Optimal case, ——. Sub-optimal case, ——.

the instantaneous mid-chord line of the wing (i.e. the pivoting axis of the wing) in the (y,z) plane of the inertial reference system displayed in figure 5.1. The networks of lines form envelopes, which illustrate the differences among the cases. In the intermediate case the deviations with respect to the rigid motion (i.e., horizontal lines) are small, resulting in an envelope with a mildly diverging pattern from root to tip (figure 5.5a). With increasing flexibility, the tip-to-root deflections are more pronounced and consequently the diverging pattern is accentuated (see figure 5.5b for the optimal case). Note that the diverging pattern implies that the heaving amplitude of any section along the span increases with respect to the heaving amplitude of the rigid case. In contrast, a further increase of flexibility beyond the optimal case leads to even larger tip-to-root deflections, however the various deflection lines form a convergent-divergent pattern (see figure 5.5c for the sub-optimal case). Thus, for the sub-optimal case, despite a larger tip-to-root deflection, the heaving amplitude of any section along the span decreases with respect to the heaving amplitude of the rigid case.

This effect can be seen in a more quantitative way in figure 5.6, that shows the temporal evolution of the vertical position (i.e., displacement) of the mid-chord tip, $Z_{tip}(t)$, (figure 5.6a), and the temporal evolution of the mid-chord tip-to-root deflection, $Z_{tr} = Z_{tip} - h$ (figure 5.6b). As discussed above, the tip displacement increases when the wing is made more flexible up to the optimal case. A further increase in flexibility leads to a lower amplitude of Z_{tip} for the sub-optimal cases (figure 5.6a) although the tip-to-root deflection is larger (figure 5.6b). Furthermore, the time at which the maximum tip displacement is found for flexible cases is delayed with respect to the rigid case. This phase lag increases monotonically with the flexibility, in agreement with previous studies, as Heathcote et al. (2008), Kang et al. (2011), and Kodali et al. (2017) among many others. Following Kodali et al. (2017), we may simplify the description assuming that Z_{tip} follows approximately a sinusoidal law with amplitude, h_{tip}, and a phase lag with respect to the imposed heaving motion, ϕ_{tip}, i.e.

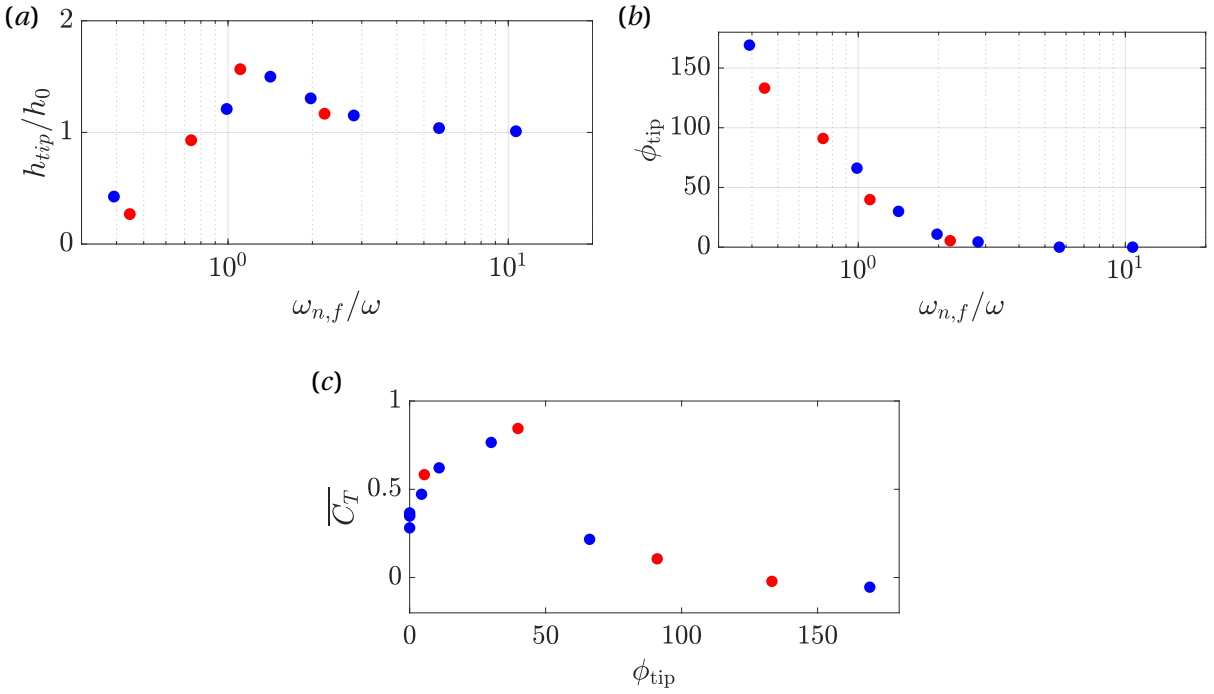

Figure 5.7: (*a*) Semi-amplitude of the vertical position of the tip normalized with the heaving amplitude, h_{tip}/h_0, as a function of the frequency ratio in fluid, $\omega_{n,f}/\omega$. (*b*) Phase lag of the tip displacement relative to the wing root ϕ_{tip}, as a function of the frequency ratio in fluid, $\omega_{n,f}/\omega$. (*c*) Time-averaged thrust coefficient $\overline{C_T}$ as a function of the phase lag ϕ_{tip}. $\mathcal{AR} = 2$, blue symbols. $\mathcal{AR} = 4$, red symbols.

$Z_{tip}(t/T) \approx h_{tip}\cos(2\pi t/T - \phi_{\text{tip}})$. With this definition, the phase lag can be computed as

$$\phi_{\text{tip}} = -\tan^{-1}\left(\frac{Z_{tip}(0.25)}{Z_{tip}(0.5)}\right). \tag{5.11}$$

Note that similar values of ϕ_{tip} are obtained with more sophisticated definitions of the phase lag, like for instance using Fourier transform of $Z_{tip}(t)$.

We analyze now these two quantities: the semi-amplitude of the mid-chord vertical position of the tip, $h_{tip} = \max(Z_{tip}(t/T))$, and the corresponding phase lag, ϕ_{tip}, as a function of the frequency ratio in fluid, $\omega_{n,f}/\omega$, for all cases in table 5.2. These quantities are shown in figures 5.7(*a*) and 5.7(*b*). First, the amplitude increases as the frequency of oscillation approaches the resonant frequency, reaching a ratio of tip-to-root amplitudes $h_{tip}/h_0 \approx 1.5$. This amplification factor is not very large. For comparison, Kodali et al. (2017) report values of $h_{tip}/h_0 \approx 10$. Note that the values of h_0/c considered by Kodali et al. (2017) are significantly smaller than the present one, so that an amplification of 10 is not realizable in our configuration. The maximum amplitude in figure 5.7(*a*) is found for a value of $\omega_{n,f}/\omega$ slightly beyond 1. Second, the shape of the phase lag plot is also rather standard with a gradual transition from 0 to 180° occurring near the resonant frequency. For the optimal cases (i.e., maximum $\overline{C_T}$ as shown in figure 5.7*c*) a phase lag slightly less than 45° is found. This result is consistent with the behavior reported by Qi et al. (2010) at lower Reynolds numbers, but not with

Kodali et al. (2017) who found a phase lag of approximately 90° at resonance. These discrepancies in amplification and phase lag are probably related to the linear/non-linear character of the system. Kodali et al. (2017) uses a linear Euler-Bernoulli beam and a potential aerodynamic model, and their results are consistent with a weakly-damped linear oscillator (with large amplification and a phase shift of 90°). Our results and Qi et al. (2010), based on a non-linear structure and non-linear aerodynamics, are consistent with a non-linear damped oscillator, which exhibit phase shifts at resonance different than 90°.

Summarizing, the results presented in this section show that the optimum in propulsive performance ($\overline{C_T}$ and η_p) reported in section 5.3.1 is linked to a fluid-structure resonance. However, as discussed in the introduction, the resonant mechanism is not incompatible with a second mechanism based on non-linearities tuning the phase lag between actuation and deformation to maximize aerodynamic forces (i.e., as in Ramananarivo et al., 2011). In the next section, we will discuss the role of this second mechanism, by analyzing how the wing deformation affects flow structures and force generation.

5.3.3 Flow analysis

The optimal aerodynamic performance of the resonant wings with $\omega_{n,f}/\omega \approx 1$ is linked to their larger heaving amplitudes of the wing tip, shown in figure 5.5. Then, since the heaving amplitude varies along the span, we analyze the sectional thrust coefficient at selected locations along the span to assess this effect. The sectional force coefficient is defined as

$$c_t(y,t) = \frac{-2\mathbf{f}(y,t)\cdot\mathbf{e}_x}{\rho_f U_\infty^2 c}, \tag{5.12}$$

where $\mathbf{f}(y,t)$ is the sectional aerodynamic force. Figure 5.8 shows the time evolution of c_t at selected spanwise locations, $2y/b = [0,\ 0.2,\ 0.6,\ 0.8]$. The figure includes the rigid, intermediate, optimal and sub-optimal cases with $\mathcal{AR} = 4$. Compared to the rigid case, the flexible wings with $\omega_{n,f}/\omega \geq 1$ show larger peak values of c_t at all spanwise sections. For the intermediate case, c_t only departs from the rigid case values at around the mid-strokes. In the optimal case, c_t shows more marked differences with respect to the rigid case, with a delayed maximum with higher peak values. The closer to the tip, the stronger this effect becomes (i.e. compare figures 5.8*c* and *d*, for $2y/b = 0.6$ and 0.8, respectively). The sub-optimal case presents two markedly different regions, the central part and the outboard part. In the central part ($2y/b = 0$ and 0.2 in figures 5.8*a* and *b*), c_t of the sub-optimal wing presents a similar trend as the rest of the cases, although with somewhat lower values. In the outboard part ($2y/b = 0.6$ and 0.8 in figures 5.8*c* and *d*), c_t displays an out-of-phase behaviour, with negative values of c_t (i.e., drag) during the first half of the stroke. This behaviour occurs because the combined effect of the bending deformation of the wing and the pitching motion are out of phase (see figures 5.6 and 5.7*c*), resulting in a counter-productive interaction and a reduced aerodynamic performance.

Indeed, it is important to note that when the total force is decomposed into contributions normal and tangential to the wing surface, the normal contribution is dominant (not shown here). This

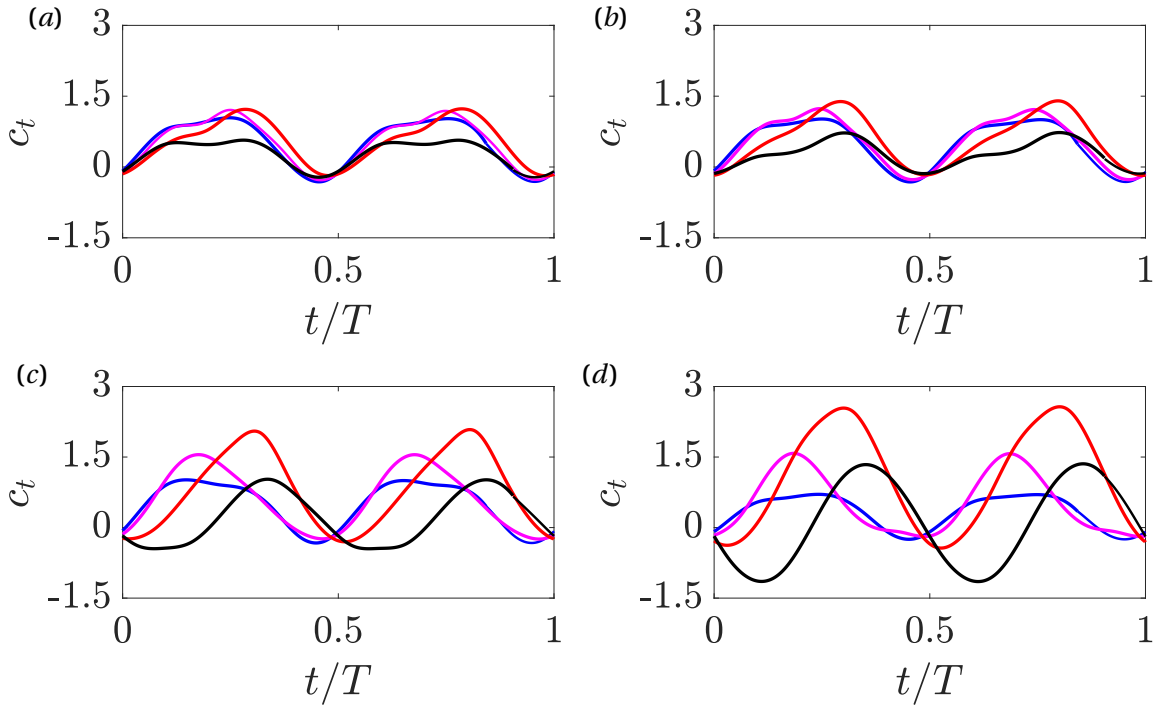

Figure 5.8: Time evolution of sectional thrust coefficient c_t for $\mathit{AR} = 4$ wings. (*a*) $2y/b = 0$. (*b*) $2y/b = 0.2$. (*c*) $2y/b = 0.6$. (*d*) $2y/b = 0.8$. Rigid case, ——. Intermediate case, ——. Optimal case, ——. Sub-optimal case, ——.

implies that the aerodynamic forces are mostly produced by pressure forces, and consequently the pitching angle of the wing controls whether a given pressure difference between the upper and lower surfaces of the wings produces thrust or drag. For the kinematics of the present study, suction in the upper surface of the wing can only produce thrust during the downstroke, i.e. when the pitching angle is negative.

In order to try to explain the larger sectional forces of the optimal case, we turn our attention to the effective angle of attack of the wing, defined as

$$\alpha_e(y,t) = \theta(t) - \tan^{-1}\Big(\frac{U_{z,p}(y)}{U_\infty - U_{x,p}(y)}\Big), \tag{5.13}$$

where $U_{x,p}(y)$ and $U_{z,p}(y)$ are the streamwise and vertical velocities of the mid-chord line, respectively. Figure 5.9 shows α_e as a function of the spanwise coordinate and time for the four cases of $\mathit{AR} = 4$. It is possible to see how larger values of the effective angles of attack are reached near the tips as the wings become more flexible. The peak values near the tips appear delayed with respect to the peak values at the mid-span. For the sub-optimal case (figure 5.9*d*), α_e has opposite signs near the wing tips than at the mid-span during most of the stroke, which explains the drag generation (i.e. $c_t < 0$) in figures 5.8(*c*) and (*d*).

As in previous works (Gordnier et al., 2013; Gonzalo et al., 2018), the effective angle of attack helps explaining some of the features associated to the aerodynamic forces generated by the rigid

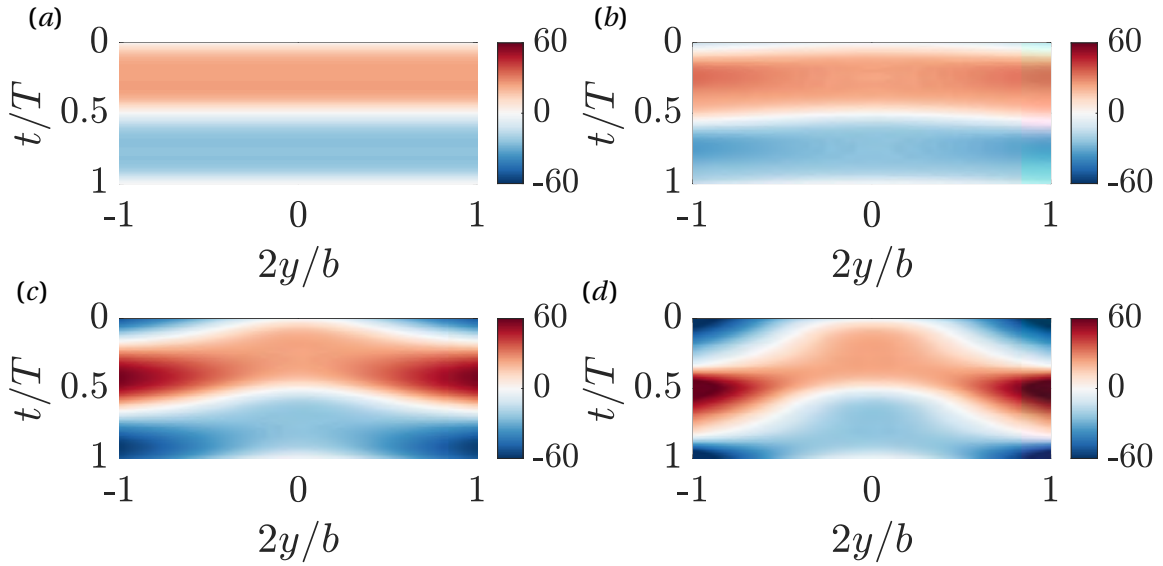

Figure 5.9: Effective angle of attack, α_e, as a function of the spanwise coordinate, $2y/b$, and time, t/T, for cases with $\mathcal{AR} = 4$. (*a*) Rigid. (*b*) Intermediate. (*c*) Optimal. (*d*) Sub-optimal.

and flexible wings. However, it does not provide a complete picture. For example, in figure 5.8(*d*), the peak value of c_t for the optimal case occurs at $t/T \approx 0.3$, while the peak value of α_e in figure 5.9(*c*) occurs at later times, closer to $t/T \approx 0.4$. Moreover, by definition, α_e of all cases is the same at the mid-section ($y = 0$), yet figure 5.8(*a*) shows significant differences between the cases. The missing piece is related to development of the leading edge vortex (LEV) on the suction surface of flapping wings, and its role in the development of unsteady aerodynamic forces (Eldredge & Jones, 2019).

In order to characterize the effect of the wing flexibility on the development of the LEV, figure 5.10 provides flow visualizations of the rigid, optimal and sub-optimal cases with $\mathcal{AR} = 4$. Vortical structures are visualized by iso-contours of Q, the second invariant of the velocity gradient tensor. Three time instants during the wing's downstroke are shown, namely during the initial phase of downstroke, $t/T = 1/8$, the mid-downstroke, $t/T = 2/8$, and the end of the downstroke, $t/T = 4/8$. For additional information, the Supplementary Material contains videos with the complete evolution of the vortical structures of the four selected cases with $AR = 4$. Qualitatively similar evolutions are observed for the wings with $AR = 2$.

At the beginning of the downstroke ($t/T = 1/8$), figure 5.10(*a*) shows that the three wings start to develop an LEV. For the rigid wing, the LEV is uniform along the spanwise direction, covering the whole span of the wing. For the wing with optimal flexibility the LEV is stronger near the mid-section than near the wing tips, while for the sub-optimal case the LEV is only apparent in the central part of the wing. As the wing moves down, the intensity of the LEVs grows while the LEV is advected downstream (figure 5.10*b*). At the end of the downstroke (figure 5.10*c*), the LEVs generated by the rigid, optimal and sub-optimal wings are very different. In the rigid case, the LEV is a quasi 2D structure aligned with the spanwise direction, with a clear pattern of braid vortices. The spacing of these braids coincides with the spacing of the gaps between the wing panels, although the effect

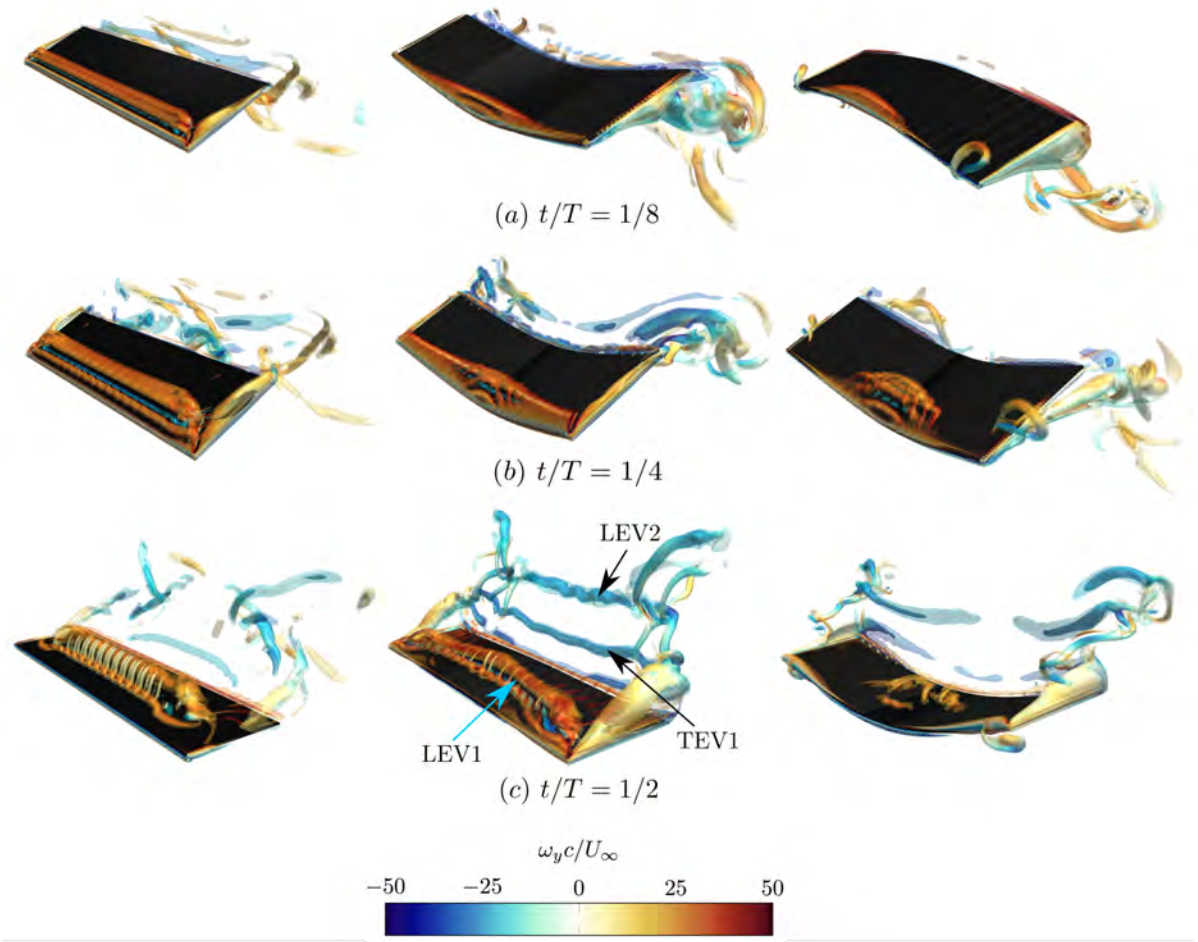

Figure 5.10: Flow visualization using iso-surfaces of the second invariant of the velocity gradient tensor, Q, for cases with $\mathit{AR} = 4$. Left column, rigid case. Mid column, optimal case. Right column, sub-optimal case. Top row (*a*), $t/T = 1/8$. Mid row (*b*), $t/T = 2/8$. Bottom row (*c*), $t/T = 4/8$. Transparent iso-surfaces correspond to $Q = 6\omega^2$, where $\omega = 2\pi f$. Filled iso-surfaces correspond to $Q = 15\omega^2$. Iso-surfaces are coloured with the spanwise vorticity ω_y. The arrows in panel (*c*) highlight the LEV and TEV formed during the downstroke of the wing (LEV1 and TEV1), and the LEV formed during the previous upstroke of the wing (LEV2).

of the gaps on the aerodynamic performance of the wing is rather small (see Appendix B.1). For the optimal case, the LEV is inclined with respect to the spanwise direction, having moved further downstream at the mid-span section than near the wing tips. The braids are also present, although they seem to be less intense than over the rigid wing. For the sub-optimal case, the LEV generated in the central part of the wing is mostly broken, and two new LEVs are starting to develop near the wing tips. These tip LEVs are developing when the α_e in figure 5.9(*d*) is beginning to grow, and just before the pitching angle changes sign, which may explain the relatively large drag contributions near the wing tips of the sub-optimal cases at the beginning of each stroke.

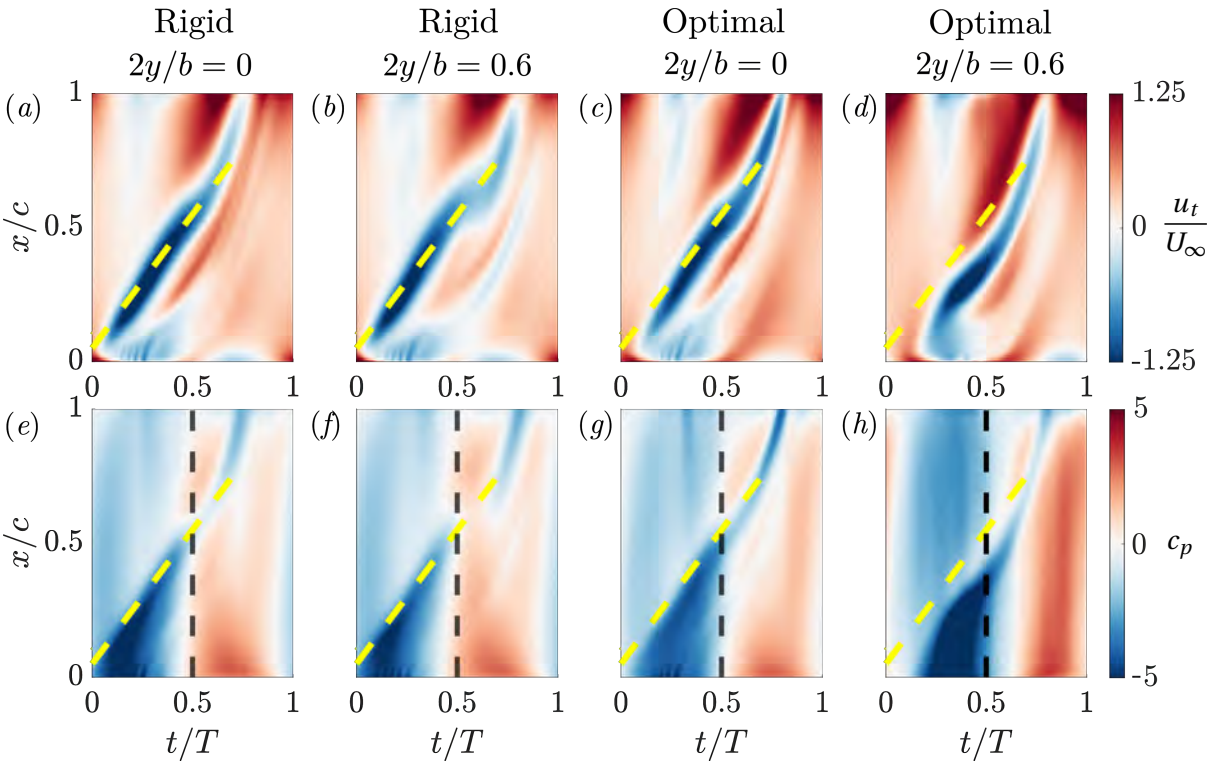

Figure 5.11: (a, b, c, d) Velocity tangent to the wing computed as $u_t = u_x \cos(\theta) - u_z \sin(\theta)$. (e, f, g, h) Pressure coefficient $c_p = 2(p - p_\infty)/(\rho U_\infty^2)$. Blue means suction. (a, c, e, g) correspond to the spanwise mid section, $2y/b = 0$. (b, d, f, h) correspond to the spanwise section at $2y/b = 0.6$. Vertical black line represents end of downstroke. The yellow dashed line is $x/c = 0.1 + t/T$.

Overall, we can extract two important ideas from figure 5.10 that help understand the aerodynamic performance of these three cases. First, in the sub-optimal case the out-of-phase motion of the tips prevents the development of coherent LEV vortices over the wing, resulting in lower aerodynamic loads at all spanwise sections. Second, the LEV of the optimal case seems to have a delayed development when compared to the LEV of the rigid wing. This fact is apparent when looking in figure 5.10(c) at the coherence of the vortex LEV2 (i.e., the LEV shed in the previous upstroke of the wing), which is only clearly visible for the optimal wing.

The differences in LEV development between optimal and rigid cases that have been shown qualitatively in figure 5.10 are further explored now in a more quantitative manner. Figure 5.11 shows the chordwise velocity component, u_t, and the pressure coefficient, $c_p = 2(p - p_\infty)/(\rho U_\infty^2)$, both measured at a distance $3\Delta r$ from the upper surface of the wing. Both variables are plotted as a function of the chordwise coordinate (x/c) and time, at two spanwise positions (i.e., mid-span and $2y/b = 0.6$).

We first focus on the plots of $u_t(x, t)$ (figure 5.11a-d). The oblique bands of negative (blue) $u_t(x, t)$ correspond to the regions of counterflow generated below the LEV, and serve as an indication of the chordwise position of the LEV. These bands have been highlighted in the figure with a yellow dashed

line. The slope of this line represents the advection speed of the LEV, which is approximately equal to $c/T = 0.496U_\infty$. The alternative positive/negative bands upstream of the LEV correspond to the secondary vortices that form near the leading edge of the wing (Li et al., 2020). Figures 5.11(*a*) and (*b*) show that the LEV of the rigid case moves downstream at roughly the same velocity at both spanwise positions, $2y/b = 0$ and 0.6. The LEV of the optimal case seems to form later than in the rigid case (i.e., u_t at $t/T = 0$ is less intense for the optimal case than for the rigid case). Moreover, the LEV of the optimal case moves downstream more slowly during the downstroke at $2y/b = 0.6$ (figure 5.11*d*) than at the mid-span section (figure 5.11*c*), in agreement with the flow visualizations provided in figure 5.10. Interestingly, the LEV of the rigid and optimal case roughly move at the same speed at the mid-span section of the wing.

The delayed evolution of the LEV has an effect on the pressure distribution on the surface of the flexible wings. For the rigid cases, the separation of the LEV occurs at about $t/T \approx 0.33$ at all spanwise locations, indicated in figures 5.11(*e*) and (*f*) by the change of the sign of c_p in the region between the leading edge of the wing and the LEV (i.e. below the yellow line). For the optimal case, the LEV separation occurs at $t/T \approx 0.4$ at the mid-span section (figure 5.11*g*) and at $t/T \approx 0.46$ at $2y/b = 0.6$ (figure 5.11*f*). The pressure distribution of the rigid and optimal cases also differs downstream of the LEV, although it is difficult to say if these differences are due to the evolution of the LEV itself, or to the generation of a stronger trailing edge vortex in the optimal case (i.e., vortex TEV1 in figure 5.10*c*). In summary, the delayed development of the LEV in the optimal case most likely explains the delayed peaks and higher maximum values of c_t for the optimal case compared to the rigid case (see figure 5.8), and the overall better aerodynamic performance of the optimal case.

5.4 Conclusions

We have presented direct numerical simulations of the flow around a spanwise-flexible wing in forward flight. The simulations were performed at $Re = 1000$ for a wing undergoing a heaving and pitching motion at a Strouhal number $St_c \approx 0.5$. We have considered wings of two aspect ratios, $\mathcal{AR} = 2$ and 4. For both cases we have varied the material properties of the wing, keeping constant the effective inertia, $\Pi_0 = 0.1$, and varying the effective stiffness Π_1 in a broad range, including a rigid wing for comparison ($\Pi_1 \to \infty$). The structural model of the wing consisted of a series of rigid segments joined by torsional springs whose stiffness was adjusted to match the natural frequencies in vacuum of a corresponding Euler-Bernoulli beam.

It has been found that there is an optimal aerodynamic performance of the wing linked to a fluid-structure resonance phenomenon, that occurs when the imposed frequency of oscillation approaches the first natural frequency of the structure in the fluid, $\omega_{n,f}/\omega \approx 1$. In that situation, the time-averaged thrust is maximum, increasing by a factor of 2 with respect to the rigid case. The associated increase in propulsive efficiency is milder, about 3-6% in absolute terms, since the increase in thrust production is also linked to an increase in the required power to maintain the wing motion.

With increasing flexibility beyond the optimal case, $\omega_{n,f}/\omega < 1$, the aerodynamic performance drops significantly, both in terms of thrust production and propulsive efficiency.

The effect of the aspect ratio in the aerodynamic performance of the flexible wings seems to be limited to its effect on determining the natural frequency of the wing. Flexible wings with the same $\omega_{n,f}/\omega$ but different $\mathcal{AR}$ have very similar aerodynamic performances in terms of averaged thrust coefficients and propulsive efficiencies, suggesting that the aerodynamic benefits of the resonance are dominant over the aerodynamic benefits associated to larger $\mathcal{AR}$. This does not preclude some (weak) $\mathcal{AR}$ effects on the amplitude and phase lag of the structural response.

In order to characterize the resonance phenomenon we have started by analyzing the structural response of the wing. It has been found that for all cases considered, the mid-chord line of the wing presents a bending pattern corresponding to the first bending mode of an Euler-Bernoulli beam. This is not surprising, since there is a factor of about 10 between the natural frequencies of the first and second modes of the wings considered in this study. Hence, the frequency ratios considered in this work are still relatively far from the second mode. Thus, the drop in aerodynamic performance cannot be attributed to the excitation of a second bending mode. Instead, the analysis of the wing tip motion compared to the root motion has shown a pattern consistent with the response to periodic forcing of a non-linear damped harmonic oscillator. Increasing the flexibility from $\omega_{n,f}/\omega > 1$ to $\omega_{n,f}/\omega < 1$ results in increased tip-to-root deflections, with a sharp transition of the amplitudes around $\omega_{n,f}/\omega \approx 1$ and a gradual transition in the phase lag between the tip and root motions from 0 to 180°. The fluid damping seems to be significant, since the amplitude of the tip displacement is only ≈ 1.5 times larger than the amplitude of the heaving motion. The phase lag at the resonance is $\phi_{\text{tip}} \approx 45°$, far from the expected value for linear oscillators (i.e. $\phi_{\text{tip}} \approx 90°$).

The reason why the structural resonance results in an enhanced aerodynamic performance is twofold. First, the increased amplitude of motion of the outboard wing sections leads to larger effective angles of attack. Second, the motion of the outboard wing sections is delayed with respect to the motion of the mid-span section of the wing. This results in a delayed development of the leading edge vortex, which together with the larger effective angles of attack explains the larger aerodynamic load in the outboard sections of the optimal wing. This beneficial fluid-structure interaction holds while the bending deformation and the pitching motion of the wing are synchronized. Indeed, the outboard wing sections of the sub-optimal cases are out-of-phase, leading to drag generation during the first half of each stroke. Overall, the coupling among deformation, force generation and wing orientation (i.e., pitching angle) in our results is reminiscent of the streamlining arguments of Ramananarivo et al. (2011) for chordwise-flexible wings, albeit the fundamental differences between both configurations.

Compared to the existing literature on spanwise-flexible wings, our results suggest that the differences between Kodali et al. (2017) and Zhu (2007) and Qi et al. (2010) can be explained by the linear/non-linear character of the structural model. Our results are consistent with Qi et al. (2010), even if the Reynolds number and flow configuration (forward flight vs hover) are different. This,

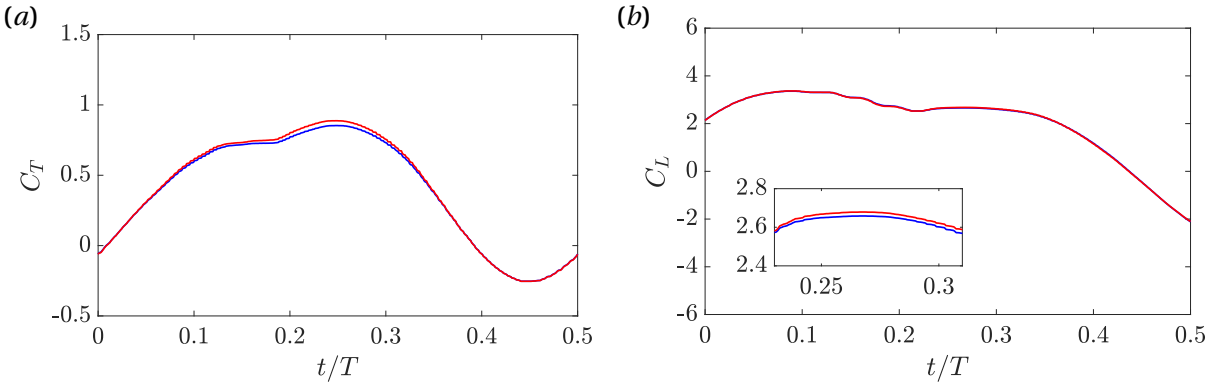

Figure 5.12: Time evolution of (*a*) thrust coefficient C_T and (*b*) lift coefficient C_L, for the $\mathcal{AR} = 4$ rigid wing case. Model with gaps, ——. Model without gaps, ——.

together with the similarities with Zhu (2007) (non-linear structure, and linear aerodynamics) seem to suggest a dominant role of structural non-linearities in determining the amplitude and phase shift at resonance.

Acknowledgements

This work was partially supported by grant DPI2016-76151-C2-2-R (AEI/FEDER, UE). The authors thankfully acknowledge the computer resources at MareNostrum and the technical support provided by Barcelona Supercomputing Center (RES-IM-2020-2-0006), as well as at LUSITANIA III and the technical support provided by Centro Extremeño de Investigación, Innovación Tecnológica y Supercomputación (CénitS) (RES-IM-2020-3-0024).

B.1. Effect of gaps on aerodynamic performance

The flexible-wing model consists of several rigid segments joined with torsional springs. The segments are separated by small gaps to avoid overlapping when the segments rotate with respect to each other. In the rigid case there is no risk of overlapping so that the rigid case can be used to assess the influence of the gaps on the aerodynamic performance of the wing. To this aim, we have performed an additional simulation of a rigid wing without gaps, consisting of a a single segment of chord c and aspect ratio $\mathcal{AR} = 4$.

Figure 5.12 shows the time evolution of thrust and lift coefficients during half a cycle for both cases (i.e. rigid wing with gaps and rigid wing without gaps). It is possible to see that the gaps do not significantly affect the temporal evolution of the force coefficients, where changes in C_T are not higher than 3%, while changes in C_L are not higher than 0.7%.

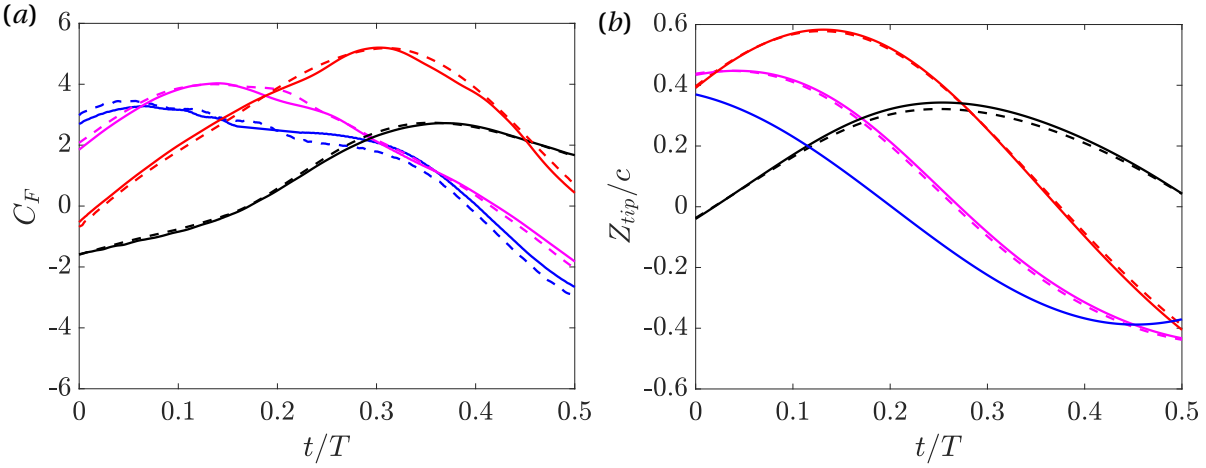

Figure 5.13: Time evolution of (a) total force coefficient C_F and (b) mid-chord vertical position of the tip Z_{tip}. Solid lines, $c/\Delta r = 96$. Dashed lines, $c/\Delta r = 56$. Rigid case, ——. Intermediate case, ——. Optimal case, ——. Sub-optimal case, ——.

B.2. Analysis of grid resolution

The nominal grid resolution used in the present work, $c/\Delta r = 96$, was selected based on a grid refinement study performed in a previous study for a similar problem at the same Reynolds number (Arranz et al., 2020). In order to generate additional data points at a lower computational cost, some additional simulations were performed at a coarser grid resolution, $c/\Delta r = 56$, as reported in Table 5.2. In this appendix we quantify the differences between the results obtained with both grid resolutions for the rigid, intermediate, optimal and sub-optimal cases for $\mathcal{AR} = 4$. We proceed as in Gonzalo et al. (2018, appendix A), analyzing the total force coefficient

$$C_F = \frac{2|\mathbf{F}|}{\rho_f U_\infty^2 S}. \tag{5.14}$$

Figure 5.13 shows the time evolution of C_F and Z_{tip} during the downstroke for the four cases considered. Overall, the results obtained with the lower resolution grid compare reasonably well with the results obtained with the nominal grid resolution. In order to provide a more quantitative comparison, for both quantities (C_F and Z_{tip}) we compute the root mean square of the fluctuations with respect to the mean for both grid resolutions and define the normalized differences

$$\epsilon_F = \frac{\left|C_{F,56}^{\text{rms}} - C_{F,96}^{\text{rms}}\right|}{C_{F,96}^{\text{rms}}}, \quad \epsilon_Z = \frac{\left|Z_{tip,56}^{\text{rms}} - Z_{tip,96}^{\text{rms}}\right|}{Z_{tip,96}^{\text{rms}}}, \tag{5.15}$$

where the subscripts 56 and 96 indicate the corresponding grid resolution. The maximum value of ϵ_F is found for the intermediate case, and it is smaller than 3%. The maximum value of ϵ_Z is found for the sub-optimal case and is approximately equal to 5%. Since these differences are relatively small, we conclude that it is reasonable to include the results obtained with the low resolution grid in Table 5.2 and Figures 5.3, 5.4b and 5.7.

REFERENCES

Alben, S. 2012. Flapping propulsion using a fin ray. *J. Fluid Mech.* 705:149–164.

Aono, H. et al. 2009. Computational modeling of spanwise flexibility effects on flapping wing aerodynamics. In *47th AIAA aerospace sciences meeting including the new horizons forum and aerospace exposition,* 1270.

Arora, N., Kang, C.-K., Shyy, W. & Gupta, A. 2018. Analysis of passive flexion in propelling a plunging plate using a torsion spring model. *J. Fluid Mech.* 857:562–604.

Arranz, G., Flores, O. & García-Villalba, M. 2020. Three-dimensional effects on the aerodynamic performance of flapping wings in tandem configuration. *J. Fluids Struct.* 94:102893.

Arranz, G., Flores, O. & García-Villalba, M. 2022a. Flow interaction of three-dimensional self-propelled flexible plates in tandem. *J. Fluid Mech.* 931.

Arranz, G., Martínez-Muriel, C., Flores, O. & García-Villalba, M. 2022b. Fluid-structure interaction of multi-body systems: Methodology and applications. *J. Fluid Struct.* 110:103519.

Arranz, G. et al. 2018b. Kinematics and dynamics of the auto-rotation of a model winged seed. *Bioinspir. Biomim.* 13 (3): 036011.

Berman, G. J. & Wang, Z. J. 2007. Energy-minimizing kinematics in hovering insect flight. *J. Fluid Mech.* 582:153–168.

Chimakurthi, S. K. et al. 2009. Computational aeroelasticity framework for analyzing flapping wing micro air vehicles. *AIAA J.* 47 (8): 1865–1878.

Dickinson, M. H., Lehmann, F.O. & Sane, S. P. 1999. Wing rotation and the aerodynamic basis of insect flight. *Science* 284 (5422): 1954–1960.

Eldredge, J. D. & Jones, A. R. 2019. Leading-edge vortices: mechanics and modeling. *Annu. Rev. Fluid Mech.* 51:75–104.

Ellington, C. P. 1999. The novel aerodynamics of insect flight: applications to micro-air vehicles. *J. Exp. Biol.* 202 (23): 3439–3448.

Felis, M. L. 2017. RBDL: an efficient rigid-body dynamics library using recursive algorithms. *Auton. Robots* 41 (2): 495–511.

Floryan, D. & Rowley, C. W. 2018. Clarifying the relationship between efficiency and resonance for flexible inertial swimmers. *J. Fluid Mech.* 853:271–300.

Fu, J., Liu, X., Shyy, W. & Qiu, H. 2018. Effects of flexibility and aspect ratio on the aerodynamic performance of flapping wings. *Bioinspir. Biomim.* 13 (3): 036001.

García-Villalba, M. et al. 2021. Demonstration of patient-specific simulations to assess left atrial appendage thrombogenesis risk. *Frontiers Physiol.* 12:596596.

Gonzalo, A. et al. 2018. From flapping to heaving: A numerical study of wings in forward flight. *J. Fluid. Struct* 83:293–309.

Gonzalo, A. et al. 2022. Non-Newtonian blood rheology impacts left atrial stasis in patient-specific simulations. *Int. J. Numer. Meth. Biomed. Eng.* e3597.

Gordnier, R.E., Chimakurthi, S.K., Cesnik, C. & Attar, P.J. 2013. High-fidelity aeroelastic computations of a flapping wing with spanwise flexibility. *Journal of Fluids and Structures* 40:86–104.

Goza, A., Floryan, D. & Rowley, C. 2020. Connections between resonance and nonlinearity in swimming performance of a flexible heaving plate. *J. Fluid Mech.* 888.

Haider, N., Shahzad, A., Mumtaz Q., Muhammad N. & A. S., Syed I. 2021. Recent progress in flapping wings for micro aerial vehicle applications. *Proc. Inst. Mech. Eng., Part C* 235 (2): 245–264.

Hamamoto, M., Ohta, Y., Hara, K. & Hisada, T. 2007. Application of fluid–structure interaction analysis to flapping flight of insects with deformable wings. *Adv. Robotics* 21 (1-2): 1–21.

Heathcote, S., Wang, Z. & Gursul, I. 2008. Effect of spanwise flexibility on flapping wing propulsion. *J. Fluids Struct.* 24 (2): 183–199.

Hoover, A. P., Cortez, R., Tytell, E. D. & Fauci, L. J. 2018. Swimming performance, resonance and shape evolution in heaving flexible panels. *J. Fluid Mech.* 847:386–416.

Jongerius, S. R. & Lentink, D. 2010. Structural analysis of a dragonfly wing. *Exp. Mech.* 50 (9): 1323–1334.

Jurado, R., Arranz, G., Flores, O. & García-Villalba, M. 2022. Numerical simulation of flow over flapping wings in tandem: Wingspan effects. *Phys. Fluids* 34 (1): 017114.

Kang, C.-K., Aono, H., Cesnik, C. E. S. & Shyy, W. 2011. Effects of flexibility on the aerodynamic performance of flapping wings. *J. Fluid Mech.* 689:32–74.

Kodali, D., Medina, C., Kang, C.-K. & Aono, H. 2017. Effects of spanwise flexibility on the performance of flapping flyers in forward flight. *J. Royal Soc. Interface* 14 (136): 20170725.

Li, Z.Y. et al. 2020. Experimental investigation on the leading-edge vortex formation and detachment mechanism of a pitching and plunging plate. *J. Fluid Mech.* 901.

Liu, K., Liu, X. & Huang, H. 2022. Scaling the self-propulsive performance of pitching and heaving flexible plates. *J. Fluid Mech.* 936.

Liu, P. & Bose, N. 1997. Propulsive performance from oscillating propulsors with spanwise flexibility. *Proc. Royal Soc. A Math. Phys. Eng. Sci.* 453 (1963): 1763–1770.

Martínez-López, C. 2019. *Aerodynamic performance optimization of two wings in tandem configuration.* BSc thesis, Universidad Carlos III de Madrid, http://hdl.handle.net/10016/30239.

Martínez-Muriel, C. 2023. "Bioinspired fluid-structure interaction problems: gusts, load mitigation and resonance." PhD diss., Universidad Carlos III Madrid.

Martínez-Muriel, C. & Flores, O. 2020. Analysis of vortical gust impact on airfoils at low Reynolds number. *J. Fluids Struct.* 99:103138.

Michelin, S. & Llewellyn Smith, S. G. 2009. Resonance and propulsion performance of a heaving flexible wing. *Phys. Fluids* 21 (7): 071902.

Moore, M. N. J. 2015. Torsional spring is the optimal flexibility arrangement for thrust production of a flapping wing. *Phys. Fluids* 27 (9): 091701.

Moored, K.W., Dewey, P.A., A.J. Smits, AJ & Haj-Hariri, H. 2012. Hydrodynamic wake resonance as an underlying principle of efficient unsteady propulsion. *J. Fluid Mech.* 708:329–348.

Moriche, M. 2017. "A numerical study on the aerodynamic forces and the wake stability of flapping flight at low Reynolds number." PhD diss., Universidad Carlos III Madrid.

Moriche, M., Flores, O. & García-Villalba, M. 2016. Three-dimensional instabilities in the wake of a flapping wing at low Reynolds number. *Int. J. Heat. Fluid Fl.* 62:44–55.

Moriche, M., Flores, O. & García-Villalba, M. 2017. On the aerodynamic forces on heaving and pitching airfoils at low Reynolds number. *J. Fluid Mech.* 828:395–423.

Moriche, M. et al. 2021. Characterization of aerodynamic forces on wings in plunge maneuvers. *AIAA J.* 59 (2): 751–762.

Nakata, T. & Liu, H. 2012. A fluid–structure interaction model of insect flight with flexible wings. *J. Comp. Phys.* 231 (4): 1822–1847.

Nayfeh, A. H. & Mook, D. T. 2008. *Nonlinear oscillations.* John Wiley & Sons.

Olivier, M. & Dumas, G. 2016. A parametric investigation of the propulsion of 2D chordwise-flexible flapping wings at low Reynolds number using numerical simulations. *J. Fluids Struct.* 63:210–237.

Ortega-Casanova, J. & Fernández-Feria, R. 2019. Maximum propulsive efficiency of two pitching and plunging plates in tandem at low Reynolds number: A numerical analysis. *Int. J. Numer. Meth. Heat Fluid Flow* 29 (11): 4013–4033.

Paraz, F., Schouveiler, L. & Eloy, C. 2016. Thrust generation by a heaving flexible foil: Resonance, nonlinearities, and optimality. *Phys. Fluids* 28 (1): 011903.

Platzer, M. F., Jones, K. D., Young, J. & Lai, J. C. S. 2008. Flapping wing aerodynamics: progress and challenges. *AIAA J.* 46 (9): 2136–2149.

Qi, D., Liu, Y., Shyy, W. & Aono, H. 2010. Simulations of dynamics of plunge and pitch of a three-dimensional flexible wing in a low Reynolds number flow. *Phys. Fluids* 22 (9): 091901.

Quinn, D. & Lauder, G. 2022. Tunable stiffness in fish robotics: mechanisms and advantages. *Bioinspir. Biomim.* 17 (1): 011002.

Quinn, D. B., Lauder, G. V. & Smits, A. J. 2014. Scaling the propulsive performance of heaving flexible panels. *J. Fluid Mech.* 738:250–267.

Ramananarivo, S., Godoy-Diana, R. & Thiria, B. 2011. Rather than resonance, flapping wing flyers may play on aerodynamics to improve performance. *Proc. Natl Acad. Sci.* 108 (15): 5964–5969.

Reid, H. E. et al. 2019. Wing flexibility reduces the energetic requirements of insect flight. *Bioinspir. Biomim.* 14 (5): 056007.

Ren, H., Wang, X., Li, X. & Chen, Y. 2013. Effects of dragonfly wing structure on the dynamic performances. *J. Bionic Eng.* 10 (1): 28–38.

Sane, S. P. 2003. The aerodynamics of insect flight. *J. Exp. Biol.* 206 (23): 4191–4208.

Shahzad, A., Tian, F. B., Young, J. & Lai, J. C. S. 2018. Effects of flexibility on the hovering performance of flapping wings with different shapes and aspect ratios. *J. Fluids Struct.* 81:69–96.

Shyy, W., Aono, H., Kang, C. K. & Liu, H. 2013. *An introduction to flapping wing aerodynamics.* Vol. 37. Cambridge University Press.

Shyy, W. et al. 2010. Recent progress in flapping wing aerodynamics and aeroelasticity. *Prog. Aerosp. Sci.* 46 (7): 284–327.

Uhlmann, M. 2005. An immersed boundary method with direct forcing for the simulation of particulate flows. *J. Comput. Phys.* 209 (2): 448–476.

Vejdani, H. R., Boerma, D. B., Swartz, S. M. & Breuer, K. S. 2018. The dynamics of hovering flight in hummingbirds, insects and bats with implications for aerial robotics. *Bioinspir. Biomim.* 14 (1): 016003.

Wang, C., Tang, H. & Zhang, X. 2022. Fluid-structure interaction of bio-inspired flexible slender structures: a review of selected topics. *Bioinspir. Biomim.*

Wang, Z. J. 2005. Dissecting insect flight. *Annu. Rev. Fluid Mech.* 37:183–210.

Yeh, P. D. & Alexeev, A. 2016. Effect of aspect ratio in free-swimming plunging flexible plates. *Comput. Fluids* 124:220–225.

Zhu, Q. 2007. Numerical simulation of a flapping foil with chordwise or spanwise flexibility. *AIAA J.* 45 (10): 2448–2457.

Zhu, X., He, G. & Zhang, X. 2014b. How flexibility affects the wake symmetry properties of a self-propelled plunging foil. *Journal of fluid mechanics* 751:164–183.

CHAPTER 6

ON THE ROLE OF WAKE-CAPTURE AND RESONANCE IN SPANWISE-FLEXIBLE FLAPPING WINGS IN TANDEM

The contents of this chapter have been submitted to:
Journal of Fluid Mechanics

Abstract

Direct numerical simulations of the flow around spanwise-flexible flapping wings in tandem are reported. Wings of aspect ratio 2 and 4 in forward flight undergo heaving and pitching motion following optimal 2D kinematics. The Reynolds number of the simulations is $Re = 1000$. The effect of flexibility is explored by varying the effective stiffness of the wings, while the effective inertia is kept constant. It is found that the aerodynamic performance and structural behavior of forewings are dominated by a fluid-structural resonance. The maximum propulsive performance for the forewings is obtained when the driving frequency approaches the first natural frequency of the structure, $\omega_{n,f}/\omega \approx 1$, similarly to what is observed in isolated wings undergoing the same kinematics. On the other hand, hindwings show optimal performance in a broad region near $\omega_{n,f}/\omega \approx 2$, and their aerodynamic performance seems to be dominated by wake capture and aerodynamic tailoring effects. These effects are qualitatively analyzed by estimating the effective angle of attack of the hindwings, which only requires information about the wake shed by the forewings. The aerodynamic performance of the hindwings is dependent on the flexibility of the forewing, which impacts the intensity of the vortices shed into the wake and the resulting effective angle of attack. The timing between the effective angle of attack and the pitching motion of the hindwing controls the generation of thrust (or drag) of each spanwise section of the hindwing. A preliminary study on the aerodynamic

performance of systems made of wings with different flexibility suggests that they could outperform tandem systems with equally flexible wings.

6.1 Introduction

The excellent aero-hydrodynamic performance achieved by flying and swimming animals has always attracted the attention of the scientific community. In recent years, it has become possible to design small, bioinspired robotic devices (De Croon et al., 2009; Raj & Thakur, 2016), such as flapping-wing micro-air vehicles, resembling the flight of insects and small birds (Wood, 2008; Keennon et al., 2012). However, the performance of these devices is still far from that of their natural counterparts (Haider et al., 2021).

Among the latter, of particular interest for the present investigation are dragonflies and damselflies, which are able to fly efficiently in many different flight modes, performing very rapid maneuvers with large accelerations and small turning radius, exceeding the average capabilities of other insects (Bomphrey et al., 2016; Sun et al., 2017). Dragonflies and damselflies have two pairs of flexible wings arranged in horizontal tandem, and depending on the flight mode, each pair of wings may be actuated differently (Sun et al., 2017). Around the wings and due to their motion, vortical structures are often developed, leading to complex vortex-structure interactions (Salami et al., 2019). The development of the vortical structures, their interaction with the wings, and the deformation and force generated by the latter are all coupled, resulting in a highly complex fluid-structure interaction (FSI) problem where the mechanisms driving the efficient flight are not well understood.

There is a vast literature on the aerodynamic performance of dragonflies (Salami et al., 2019). Several authors have tried to capture and characterize the kinematics of dragonfly wings in controlled environments (Wakeling & Ellington, 1997; Chen et al., 2013). Other authors have performed numerical computations (Li & Dong, 2017; Bode-Oke et al., 2018; Zou et al., 2019; Lai et al., 2020; Shumway et al., 2020), or experiments (Zheng et al., 2015, 2016a; Hefler et al., 2018), in order to understand better and characterize the different flight modes of dragonflies, looking at the surrounding fluid flow and determining the aerodynamic forces. These studies are generally useful since they illustrate the different ways in which the flexible wings interact with the flow to enhance the performance in terms of force generation and/or propulsive efficiency. However, from these works, it is difficult to extract general rules for design since it is usually not possible to identify the mechanisms driving the optimal fluid-structure interaction.

Progress has also been made by studying simplified configurations, often not taking into account flexibility effects. Many studies have been carried out considering 2D foils (Broering & Lian, 2012; Lua et al., 2016; Shanmugam & Sohn, 2019; Bie & Li, 2022) or 3D rigid wings (Zheng et al., 2016b; Nagai et al., 2019; Arranz et al., 2020; L. Peng et al., 2021; Jurado et al., 2022; Lagopoulos et al., 2023) in horizontal tandem arrangement. These studies have shown that the aerodynamic performance of the tandem system may be enhanced by selecting the proper wing kinematics. It has

been observed that increased propulsive efficiency is achieved when the hindfoil benefits from hydrodynamic interactions with the vortices shed by the forefoil (Ortega-Casanova & Fernández-Feria, 2019; Martínez-López, 2019). The two key parameters which dictate this interaction are the distance between the wings and the phase lag between their corresponding motions. However, the role of wing flexibility in such interactions has been scarcely studied in the literature (Alaminos-Quesada & Fernandez-Feria, 2021).

In fact, it is well known that wing flexibility may have a large influence on the aerodynamic performance of isolated wings. Many studies have shown the benefits of flexibility on propulsion (Shyy et al., 2010), also reducing the energetic requirements (Reid et al., 2019). Relevant works are those of Alben (2012), Moored et al. (2012), Quinn et al. (2014), Moore (2015), and K. Liu et al. (2022) among others. Two main mechanisms have been proposed in the literature to explain the optimal performance of isolated airfoils and wings in different scenarios (chordwise and spanwise flexible wings). The first mechanism is a fluid-structure resonance that results in maximum deflections when the structure is excited at the natural frequency of the fluid-structure system (see, for example, Floryan & Rowley (2018)). The second one is a streamlining/tailoring argument in which the phase lag between actuation and deformation is properly tuned, leading to optimal bending and projection of the aerodynamic forces into the direction of motion, maximizing thrust, as suggested in Ramananarivo et al. (2011). These mechanisms are non-exclusive and have been reconciled in the literature (Goza et al., 2020; Quinn & Lauder, 2022), suggesting that in some cases the optimal bending may occur at the resonant frequency of the fluid-structure system. In fact, it has been shown recently that the optimal propulsive performance of isolated spanwise-flexible flapping wings is driven by a fluid-structure resonance (Martínez-Muriel et al., 2023), where the coupling between deformation, force generation, and wing orientation is beneficial while the bending motion and the pitching motion are synchronized.

The mechanisms discussed above are starting to be clarified for isolated wings. It is then unsurprising that the effects of wing flexibility on tandem systems are not yet understood. For example, questions that remain unanswered are, among others: i) what is the role of fluid-structure resonance in tandem systems; ii) to what extent the aerodynamic performance is modified/enhanced by hydrodynamic interactions between the wake of the forewing and the hindwing, iii) what is the interplay between fluid-structure resonance and the wake-hindwing hydrodynamic interactions, iv) how different is then the aeroelastic response of the hindwing compared to the aeroelastic response of the forewing. These are questions that go beyond what can be answered in a single study. Our aim in the present work is, therefore, to contribute to the knowledge on the topic by studying a simplified configuration that retains most of the ingredients that play a significant role. We simulate numerically the forward flight of a pair of spanwise-flexible flapping wings in horizontal tandem configuration. We vary the flexibility of the wings and this allows to study the aeroelastic response and the aerodynamic performance of the wings both near and far away from resonance. Note that it will also be possible to understand the differences with respect to the isolated case, since the latter

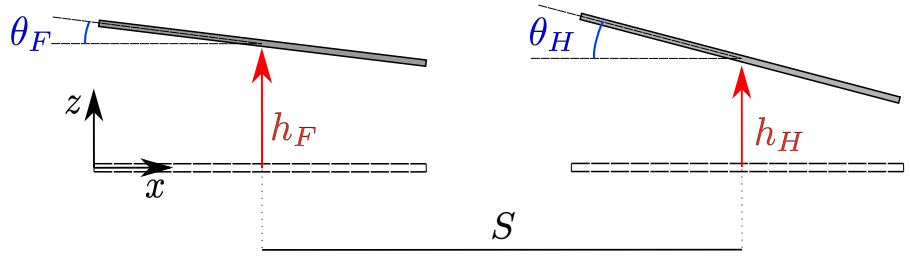

Figure 6.1: Sketch of the kinematics followed by the midsection of the wings composing the tandem system, which also corresponds to the kinematics followed by forefoil and hindfoil in the 2D problem.

has been previously studied for the same kinematics as the one considered here (Martínez-Muriel et al., 2023).

The paper is structured as follows: the problem under consideration is introduced in section 6.2, together with the methodology followed to solve it. The results of the 2D configuration which are relevant for the discussion to follow are reported in section 6.3. In section 6.4, the main results of the paper are reported. First, an overview of the performance of the tandem system is given. This is followed by separate descriptions of the aeroelastic behavior of the forewing and the hindwing. To finish the paper we explore the performance of systems made of wings with different flexibilities. Conclusions are presented in section 6.5.

6.2 Methodology

6.2.1 Problem definition

We consider two equal wings in horizontal tandem configuration flying at a velocity U_∞. The wings are modeled as rectangular flat plates of chord c and span b with aspect ratio $\mathcal{AR} = b/c$ and thickness $h_s^* = h_s/c = 0.02$. The wings are rigid in the chordwise direction, but flexible in the spanwise direction. The flow is considered to be incompressible, and the Reynolds number based on the chord of the wings and the free-stream velocity is $Re = U_\infty c/\nu = 1000$. Two different aspect ratios are studied in this analysis, $\mathcal{AR} = 2$ and 4.

A heaving and pitching motion is imposed on the mid-span section of each of the wings, while the rest of the wing deforms passively. A sketch of the arrangement and kinematics of the wings is shown in figure 6.1. The kinematics at the mid-span section is described by the laws

$$h_i(t) = h_0 \cos(2\pi t/T + \phi_{fh,i}), \tag{6.1a}$$

$$\theta_i(t) = \theta_0 \cos(2\pi t/T + \phi_{fh,i} + \phi_{hp,i}), \tag{6.1b}$$

where h_0 is the heaving amplitude, θ_0 the pitching amplitude, ϕ_{fh} the phase difference between the forewing and the hindwing, ϕ_{hp} the phase difference between heaving and pitching motions, and T the oscillation period. We also define the frequency of the imposed motion as $f = 1/T$, the angular frequency as $\omega = 2\pi f$, the reduced frequency as $k = \pi f c/U_\infty$, and the Strouhal number

i	h_0	θ_0	St_c	ϕ_{fh}	ϕ_{hp}
F (Forewing)	0.388	26.19°	0.496	0	$\pi/2$
H (Hindwing)				347.1°	$\pi/2$

Table 6.1: Kinematic parameters of the imposed motion on the forewing ($i = F$) and the hindwing ($i = H$) of the 3D problem.

as $St_c = fc/U_\infty$. The subindex i refers to forewings ($i = F$) or hindwings ($i = H$). The pivoting axis for the pitching motion is placed at the mid-chord of each wing. The horizontal distance between the pivoting axes of the wings is $S = 1.5c$. The value of the parameters defining the kinematics are shown in table 6.1. These are the result of the optimization problem for maximum propulsive efficiency of a system of horizontal tandem foils, performed in a similar way as in Ortega-Casanova & Fernández-Feria (2019). The optimization is carried out using a conjugate direction method with a Powell optimizer (see Martínez-López, 2019 for details).

To analyze the role of spanwise flexibility in tandem wings, we vary the material properties of the wings, characterized by the first natural frequency of the spanwise bending of the wing, ω_n. We account for the added mass effect of the fluid as in Moore (2015), Arora et al. (2018), and Martínez-Muriel et al. (2023), defining the natural frequency in fluid as

$$\omega_{n,f} = \frac{\omega_n}{\sqrt{1+I_a}}, \tag{6.2}$$

where $I_a = 27\pi/128\rho^* h_s^*$. Hence, the ratio of natural frequency in fluid, $\omega_{n,f}$ over the frequency of the imposed motion is

$$\frac{\omega_{n,f}}{\omega} = \frac{\omega_n/\omega}{\sqrt{1+I_a}} = \frac{\beta_n^2}{2\pi}\sqrt{\frac{\Pi_1}{\Pi_0(1+I_a)}}, \tag{6.3}$$

where β_n is the first eigenvalue of the transcendental equation

$$\cos(\beta_k \mathcal{AR}/2)\cosh(\beta_k \mathcal{AR}/2) + 1 = 0, \tag{6.4}$$

as described in Kodali et al., 2017.The frequency ratio depends on the effective inertia and the effective stiffness of the wings, defined respectively as

$$\Pi_0 = \rho^* h_s^* \left(\frac{k}{\pi}\right)^2, \quad \Pi_1 = \frac{E^* h_s^{*3}}{12}, \tag{6.5}$$

following Shyy et al., 2010. In these expressions, $E^* = E/\rho_f U_\infty^2$ is the normalized Young's modulus and $\rho^* = \rho_s/\rho_f$ is the solid to fluid density ratio. A density ratio $\rho^* = 20$ is selected such that the resulting effective inertia ($\Pi_0 = 0.1$) is of the same order of magnitude as such observed for dragonflies and other insects (Hamamoto et al., 2007; Jongerius & Lentink, 2010; Shyy et al., 2010; Ren et al., 2013). We choose to cover a range of $\Pi_1 \sim [\mathcal{O}(10^{-1}) - \mathcal{O}(10^2)]$ comparable to those analysed in previous works (Fu et al., 2018). We also consider rigid wings ($\Pi_1 \to \infty$), yielding the range of $\omega_{n,f}/\omega$ reported in table 6.2.

Id	$\mathcal{AR}$	Tandem	ω_n/ω	$\omega_{n,f}/\omega$	Π_1	$\Pi_1(2/\mathcal{AR})^4$	Nomenclature	$c/\Delta r^{\text{iso}}$	$c/\Delta r^{\text{tand}}$
1	4	Yes	∞	∞	∞	∞	**Rigid**	96	96
2	4	Yes	3.6	2.22	66.3	4.14	**Intermediate**	96	96
3	4	Yes	1.8	1.11	16.6	1.04	**Resonant**	96	96
4	4	Yes	1.2	0.74	7.4	0.46	**Sub-optimal**	96	56
6	2	Yes	∞	∞	∞	∞	**Rigid**	96	96
7	2	No	17.5	10.75	96.25	96.25	-	56	-
8	2	No	9.3	5.7	27.2	27.2	-	56	-
9	2	Yes	4.6	2.82	6.7	6.7	Intermediate	56	56
10	2	Yes	3.25	2	3.3	3.3	-	56	96
11	2	Yes	2.3	1.41	1.7	1.7	**Resonant**	96	96
12	2	Yes	1.6	0.99	0.83	0.83	Sub-optimal	56	56

Table 6.2: Overview of problem parameters. $\mathcal{AR}$ is the aspect ratio. ω_n/ω and $\omega_{n,f}/\omega$ are the ratios of natural frequency in vacuum and in fluid, respectively, to the angular frequency of the flapping motion. Π_1 is the effective stiffness. $c/\Delta r^{\text{iso}}$ and $c/\Delta r^{\text{tand}}$ are the grid resolutions used in the refined zone of the domain for isolated and tandem cases, respectively. For all cases, simulations of the isolated wing are available, as reported in Martínez-Muriel et al. (2023). The column Tandem indicates the cases for which simulations of the tandem system have been performed.

6.2.2 Structural model

A lumped-torsional flexibility model is used to model the spanwise flexibility of the pair of wings (Arora et al., 2018; Arranz et al., 2022b), as described in Martínez-Muriel et al. (2023) for isolated wings. Each wing is discretized into $N_B = 5\mathcal{AR}+1$ rigid segments, which are connected by torsional springs, as depicted in figure 6.2(a). The distance between a rigid segment and the torsional spring is $e = h_s/2$ as it is shown in figure 6.2(b), such that there is no overlapping between the segments as they move. The effect of the gaps on the aerodynamic performance of the wings is found to be negligible, although they leave a footprint in the flow structures, as shown by Martínez-Muriel et al. (2023). The rigidity of the torsional springs is set to match the desired natural frequency of the wing. The resulting structural model for each wing is a system of N_B connected rigid bodies with $1+N_B$ degrees of freedom, namely the vertical displacement, h_i, the pitching angle, θ_i, and the relative rotation angles between each segment, $\phi_{i,j},\ j = 1,\ldots,N_B-1$ (see figure 6.2b), where the index i represents the wing.

6.2.3 Fluid-structure interaction solver

A summary of the most representative features of the Fluid-Structure Interaction (FSI) solver is briefly described hereafter. For further details, the reader is referred to Arranz et al. (2022b).

The governing equations for the multi-body system (MBS) can be cast in the form:

$$H(\mathbf{q})\ddot{\mathbf{q}} + C(\mathbf{q},\dot{\mathbf{q}}) = \boldsymbol{\xi} + \boldsymbol{\xi}_h, \tag{6.6}$$

where $\mathbf{q}$ is the vector of generalized coordinates, H is the generalized inertia matrix, C is the generalized bias force vector, which includes Coriolis and centrifugal accelerations, $\boldsymbol{\xi}$ is the vector of internal forces/accelerations, and $\boldsymbol{\xi}_h$ is the vector of hydrodynamic forces acting on the wing.

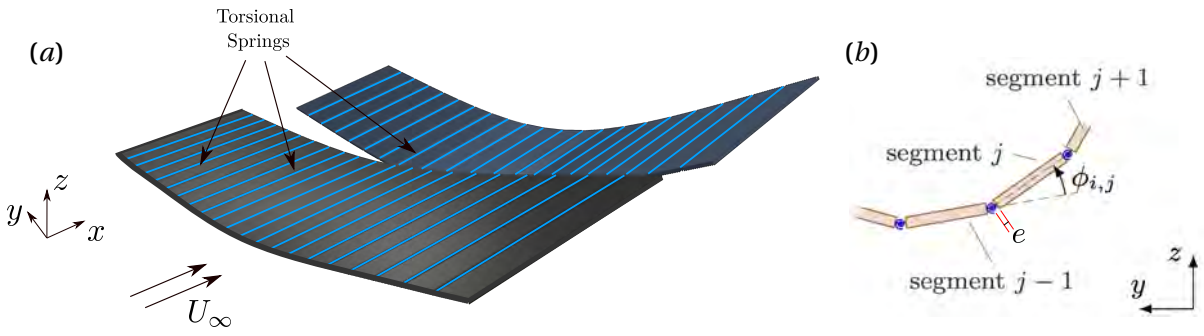

Figure 6.2: (*a*) Sketch of the disposition of the wings and the multibody model to qualitatively describe the spanwise flexibility of a wing, where the segments of the MBS are connected using torsional springs. (*b*) Sketch of the degree of freedom ($\phi_{i,j}$) between two consecutive segments.

For this particular problem, $\mathbf{q} = [h_1, \theta_1, \phi_{1,1}, \ldots, \phi_{1,N_B-1}, h_2, \theta_2, \phi_{2,1}, \ldots, \phi_{2,N_B-1}]$, and $\boldsymbol{\xi} = [0, 0, -K\phi_{1,1}, \ldots, -K\phi_{1,N_B-1}, 0, 0, -K\phi_{2,1}, \ldots, -K\phi_{2,N_B-1}]$, where K is the torsional spring constant. The generalized inertia matrix, H, and the generalized bias force, C, are computed using the Composite Rigid-Body algorithm (CRBA) and the Recursive Newton-Euler algorithm (RNEA), respectively. This is done using the open-source Rigid Body Dynamics Library (RBDL) developed by Felis (2017).

The in-house code TUCAN is employed in this work. It is a solver that uses the Immersed Boundary Method (IBM) proposed by Uhlmann (2005) to model the presence of the wings in the flow. The 3D Navier-Stokes equations for an incompressible flow, accounting for the modifications of the IBM, are used to describe the fluid dynamics,

$$\nabla \cdot \mathbf{u} = 0, \tag{6.7a}$$

$$\frac{\partial \mathbf{u}}{\partial t} + (\mathbf{u} \cdot \nabla)\mathbf{u} = -\nabla p + \nu \nabla^2 \mathbf{u} + \mathbf{f}_{IBM}, \tag{6.7b}$$

$$\mathbf{u}(\mathbf{x}) = \mathbf{U}_{\partial\Gamma} \quad \forall \mathbf{x} \in \partial\Gamma, \tag{6.7c}$$

where $\mathbf{u}$ is the velocity field, p is the kinematic pressure (i.e., pressure over the fluid density ρ_f), and $\nu = \mu/\rho_f$ is the kinematic viscosity. The equations are discretized using second-order central differences on a staggered grid. Time integration is performed with a low-storage semi-implicit 3-stage Runge-Kutta scheme. The forcing term $\mathbf{f}_{IBM}$ is added to ensure that the no-slip boundary condition (equation 6.7c) is satisfied at the boundaries of the bodies (i.e., on the surface of the wing segments), where $\mathbf{U}_{\partial\Gamma}$ is the velocity at the surface of those segments. The system of equations (6.6) is weakly coupled to the system of equations (6.7). It is well known that weakly-coupled systems of equations might be prone to stability issues. However, in the parametric range considered in this study, no stability problems have been observed (Arranz et al., 2022b).

A complete description of the fluid solver implemented in TUCAN together with an extensive validation can be found elsewhere (Moriche, 2017; Moriche et al., 2017). The multibody version has

also been successfully employed in previous works (Arranz et al., 2022a; Martínez-Muriel et al., 2023).

6.2.4 Computational Set-up

The computational setup is very similar to the one described in Martínez-Muriel et al. (2023) for isolated wings. The size of the computational domain is $14c \times 11c \times 7c$ in the streamwise, spanwise, and vertical directions, respectively. The wings are located in the central part of the computational domain, inside of a refined zone with a uniform grid spacing, Δr, in all directions. The size of the refined zone is $(3.5c \times L_{y,r} \times 3c)$, with $L_{y,r} = (\mathcal{AR}+1)c$ depending on the aspect ratio of the wing. Outside of this refined region, a constant stretching of 1% is applied to the grid in all directions. The origin of the reference system is located at the leading edge of the mid-span section of the wing. The time step is chosen such that the CFL number is lower than 0.3. At the inlet ($x/c = -4.75$), a constant uniform velocity is imposed while at the outlet ($x/c = 9.25$) an advective boundary condition is used ($\partial\mathbf{u}/\partial t + U_\infty \partial\mathbf{u}/\partial x = 0$). Free slip boundary conditions are imposed at the lateral boundaries.

All simulations are first run for four cycles with a grid resolution of $\Delta r = c/56$ (in the refined zone). Then, for all relevant cases (see table 6.2), three additional cycles are run at the higher resolution, $\Delta r = c/96$. This higher resolution is chosen based on the grid refinement study performed by Arranz et al. (2020) for a similar problem at the same Reynolds number. In order to have more data points for analysis and to save computational resources, a few less relevant cases are run with the coarse grid resolution only, as indicated in table 6.2. As shown by Martínez-Muriel et al. (2023) for an isolated wing, with this relatively coarse resolution the force coefficients present a difference of about 3% with respect to the finer grid resolution of $\Delta r = c/96$. The number of cycles run in all simulations are enough to ensure that both aerodynamic forces and the flow near the wings are periodic.

6.2.5 Definition of aerodynamic coefficients

The aerodynamic performance of the wings can be measured in terms of the thrust and lift coefficients, which are defined as

$$C_{T,i} = \frac{-2\mathbf{F}_i \cdot \mathbf{e}_x}{\rho_f U_\infty^2 S}, \quad C_{L,i} = \frac{2\mathbf{F}_i \cdot \mathbf{e}_z}{\rho_f U_\infty^2 S}, \tag{6.8}$$

where $\mathbf{F}_i$ is the total aerodynamic force of the ith wing and $\mathbf{e}_k$ is the unitary vector in the k-axis direction. Values of thrust and lift coefficients averaged over a cycle are denoted by $\overline{C_{T,i}}$ and $\overline{C_{L,i}}$, respectively. On the other hand, the propulsive efficiency of each wing is defined as

$$\eta_i = \frac{\overline{C_{T,i}}}{\overline{P_i}}, \tag{6.9}$$

where $\overline{P_i}$ is the non-dimensional input power of the ith wing averaged over a cycle. The instantaneous non-dimensional input power coefficient, P_i, defined as

$$P_i(t) = \frac{2}{\rho_f U_\infty^3 S}\left(\max(R_{z,i}(t)\dot{h}_i(t),0) + \max(R_{\theta,i}(t)\dot{\theta}_i(t),0)\right), \tag{6.10}$$

is computed as in Martínez-Muriel et al. (2023), by using the reaction forces and moments on the segment whose motion is imposed. The reaction force in the vertical direction is denoted R_z and the reaction pitching moment is denoted R_θ. This definition is such that no energy extraction from the fluid is allowed (Berman & Wang, 2007; Vejdani et al., 2018; Jurado et al., 2022). For rigid wings, the reactions are simply $R_z = F_z$, $R_\theta = M_y$, where M_y is the aerodynamic moment about the pivoting axis of the wing.

We will also discuss sectional force coefficients c_t and c_l, together with the sectional normal force coefficient c_n, which are defined as

$$c_{t,i} = \frac{-2\mathbf{f}_i \cdot \mathbf{e}_x}{\rho_f U_\infty^2 c}, \quad c_{l,i} = \frac{2\mathbf{f}_i \cdot \mathbf{e}_z}{\rho_f U_\infty^2 c}, \quad c_{n,i} = c_{l,i}\cos(\theta_i) - c_{t,i}\sin(\theta_i), \tag{6.11}$$

where $\mathbf{f}$ is the sectional aerodynamic force. This definition is also valid for two-dimensional foils. In a similar fashion to 3D, the propulsive efficiency for foils is defined as

$$\eta_i^{2D} = \overline{c_{t,i}} / \overline{P_i^{2D}} \tag{6.12}$$

where $\overline{P_i^{2D}}$ is the non-dimensional input power coefficient of the ith wing averaged over a cycle, where the instantaneous value is computed as

$$P_i^{2D}(t) = \frac{2}{\rho_f U_\infty^3 c}\left(\max(f_{z,i}(t)\dot{h}_i(t), 0) + \max(m_{y,i}(t)\dot{\theta}_i(t), 0)\right). \tag{6.13}$$

Finally, we define the pressure coefficient c_p as

$$c_p = \frac{p - p_\infty}{\frac{1}{2}\rho_f U_\infty^2}, \tag{6.14}$$

where p_∞ is the pressure of the free stream.

6.3 Two-dimensional problem and selection of kinematics

Arranging wings in horizontal tandem may be beneficial, as mentioned in section 1, if the kinematics are properly selected. To provide a basis for the analysis of flexible wings in tandem, in this section we analyze the aerodynamic performance of a system of two-dimensional foils in tandem, that move with the same kinematics as the mid-span sections of the flexible wings. To highlight the benefits of the tandem configuration, the results obtained for the 2D tandem system are compared to those yielded by an isolated foil.

First, vorticity contours at $t/T \approx 0.25$ for both the isolated foil and the system of foils in tandem are shown in figure 6.3. The isolated foil sheds leading edge vortices on both downstroke (labeled LEV1 and LEV3 in figure 6.3*a*) and upstroke (labeled LEV2 and LEV4) that are equal due to the mirror-symmetry of the kinematics. These vortices are located in the wake following a staggered disposition, in such a way that each pair induces a jet-like motion (indicated with yellow arrows in the figure) that favors propulsion, even if it is misaligned with the direction of the incoming free stream. Vorticity leaving the trailing edge forms a shear layer, that is engulfed by the traveling LEVs.

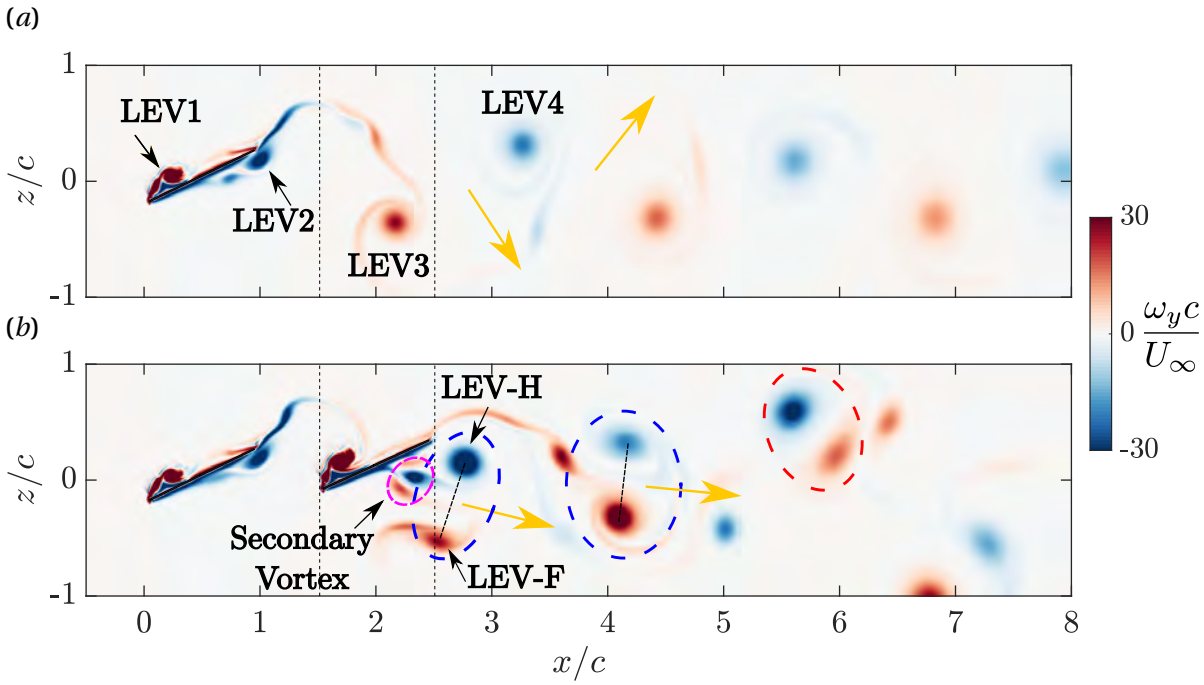

Figure 6.3: Spanwise vorticity, $\omega_y c/U_\infty$, fields for (a) isolated foil and (b) tandem system at $t/T \approx 0.25$. Red means clockwise rotation.

When looking at the tandem foils, figure 6.3(b), the vortical structures near the forefoil are very similar to those of the isolated foil, suggesting that the aerodynamic performance of the forefoil is similar to the aerodynamic performance of the isolated foil. On the other hand, due to the interaction with the LEVs shed by the forefoil (labeled LEV-F in the figure), the LEV developed by the hindfoil is stronger (labeled LEV-H). In addition, a secondary vortex is also shed from the pressure surface of the hindfoil. This secondary vortex travels with the dipole (circled in dashed blue in figure 6.3b), formed by LEVs from fore- and hindfoil. The dipole is asymmetric from the beginning, as the LEV-H is stronger than the LEV-F, and due to this asymmetry, the dipole rotates. For $x/c \leq 4$, the dipole is roughly vertical, exerting a horizontal jet and leading to an increase in the thrust coefficient. For $x/c > 4$, the dipole starts to drift in the vertical direction, and the direction of rotation is determined by the most intense vortex forming the dipole.

The temporal evolution of lift, c_l, and thrust, c_t, coefficients for both forefoil and hindfoil are compared with those provided by the isolated foil in figure 6.4. The forces of the hindfoil are significantly larger than those of the isolated foil, consistent with the flow visualization. A propulsive efficiency of $\eta^{2D}_{iso} = 0.237$ is obtained for the isolated foil. This value can be compared with the efficiency of both foils in tandem, which are increased to $\eta^{2D}_F = 0.289, \eta^{2D}_H = 0.358$.

The larger force generation on the hindfoil can be attributed to the hydrodynamic interaction between the hindfoil and the wake of the forefoil, denoted in the following *wake capture*, for the sake of brevity. In this wake capture phenomenon, the velocity induced by the forefoil goes in phase with the imposed motion of the hindfoil during long intervals of the cycle, i.e., positive vertical velocity

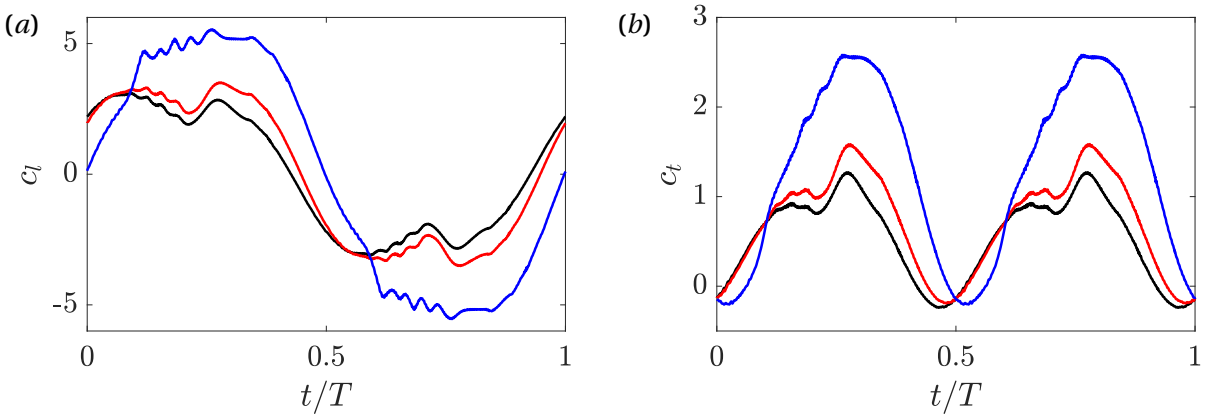

Figure 6.4: Temporal evolution of (*a*) lift and (*b*) thrust coefficient. Line colors correspond to: ——: Isolated. ——: Forefoil. ——: Hindfoil.

induced by the forefoil when the hindfoil is heaving down, and vice versa. This leads to an increase in the effective angle of attack of the hindfoil. In order to quantify the effect of the wake capture (and hence to understand the change in the force generation of the hindfoil) we compute the effective angle of attack of the hindfoil and compare it with that of the forefoil, which depends only on the imposed kinematics.

The effective angle of attack of the hindfoil has contributions from the velocity induced by the forefoil, and contributions from the kinematics of the hindfoil. To characterize the former, we follow the approach proposed by Zhu et al. (2014a), Z. R. Peng et al. (2018) and Arranz et al. (2022a), who use the velocity field in the wake of an isolated forefoil (i.e, $u_z(x,z,t)$) to estimate the velocities induced by the forefoil on the hindfoil. Following Martínez-Muriel & Flores (2020), we define a locally-averaged vertical velocity,

$$\overline{u_z}(z,t) = \frac{1}{c}\int_{x_{LE}^H}^{x_{TE}^H} u_z(x_0,z,t)\,dx_0, \tag{6.15}$$

where $u_z(x,z,t)$ is the velocity in the wake of the isolated forefoil, and the average is taken from the leading edge to the trailing edge of the hindfoil (i.e., $x_{LE}^H = 1.5c$, $x_{TE}^H = 2.5c$, see figure 6.3). Figure 6.5(*a*) shows contours of $\overline{u_z}$ as a function of time and the vertical coordinate. The trajectory of the mid-chord point of the hindfoil is shown in blue. The values of $\overline{u_z}$ along this trajectory are employed to estimate the vertical velocity induced by the forefoil on the hindfoil, $u_{z,MC}$. These values will be used for the computation of the effective angle of attack. Note that the induced velocity is positive from $t/T \approx 0.2$ to 0.7, and negative during the remaining part of the cycle, resulting in positive contributions to the effective angle of attack of the foil during most of the up/down stroke.

In order to define the effective angle of attack of the hindfoil, we combine the geometric angle of attack of the leading edge of the hindfoil with the velocity induced by the forefoil,

$$\alpha_e = \theta + \arg\tan\left(\frac{u_{z,MC} - \dot{h} - c\dot{\theta}/2}{U_\infty}\right). \tag{6.16}$$

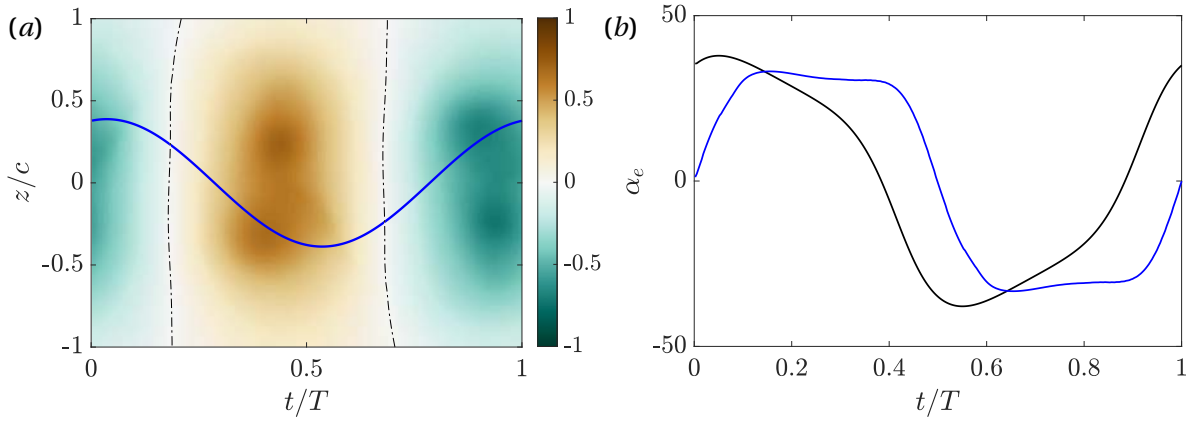

Figure 6.5: (*a*) Contours of locally-averaged vertical velocity, $\overline{u_z}/U_\infty$, as a function of time and the vertical coordinate. Dashed black lines correspond to $\overline{u_z}/U_\infty = 0$. The blue line corresponds to the trajectory of the mid-chord of the hindfoil. (*b*) Time evolution of the geometric angle of attack, α_g (——), and the estimate of the effective angle of attack, α_e (——).

We also define the geometric angle of attack,

$$\alpha_g = \theta + \arg\tan\left(\frac{-\dot{h} - c\dot{\theta}/2}{U_\infty}\right), \tag{6.17}$$

which is equal to the effective angle of attack seen by the isolated foil and the forefoil. These two angles are presented in figure 6.5(*b*), showing a clear effect of the forefoils wake on the hindfoil: the effective angle of attack of the hindfoil is lagged with respect to the isolated foil's, with a smaller peak value and a broader maximum.

It is illustrative to compare the time evolution of the effective angles of attack for the isolated foil and the hindfoil, figure 6.5(*b*), with the time evolution of the corresponding lift coefficients, figure 6.4(*a*). It is apparent that the time instants where the effective angles of attack of the hindfoil are larger than those of the isolated foil match the instants when the force generation is also larger. In particular, for the hindfoil, the shape of the lift coefficient curve is rather similar to the shape of the estimated effective angle of attack curve.

Thus, it is possible to qualitatively estimate the lift coefficient of the hindfoil by using the estimation of its effective angle of attack. However, this approximation does not account for the contribution of the LEVs shed by the hindfoil, which is rather complex and difficult to incorporate into the definition of α_e.

Finally, the effect that the hindfoil has on the forefoil is analyzed. Figure 6.6 shows the pressure field around the isolated foil (figure 6.6*a*) and the tandem system (figure 6.6*b*). The presence of the hindfoil in the tandem system modifies the pressure distribution around the forefoil. This effect seems to be related to a blockage effect in the region between the foils (note the strong pressure gradient in figure 6.6*b*), resulting in a larger pressure difference between the pressure and suction sides of the forefoil, and larger aerodynamic forces. On the other hand, the pressure field around the

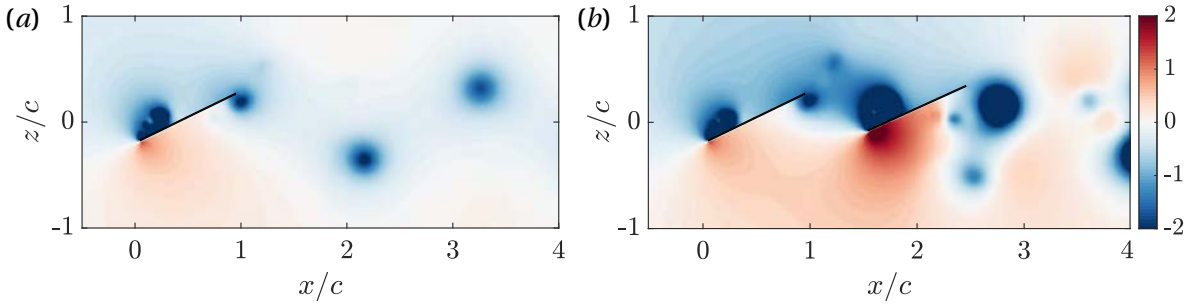

Figure 6.6: Pressure coefficient, c_p, contours for (a) isolated and (b) tandem system at mid downstroke of the trajectory, $t/T \approx 0.25$.

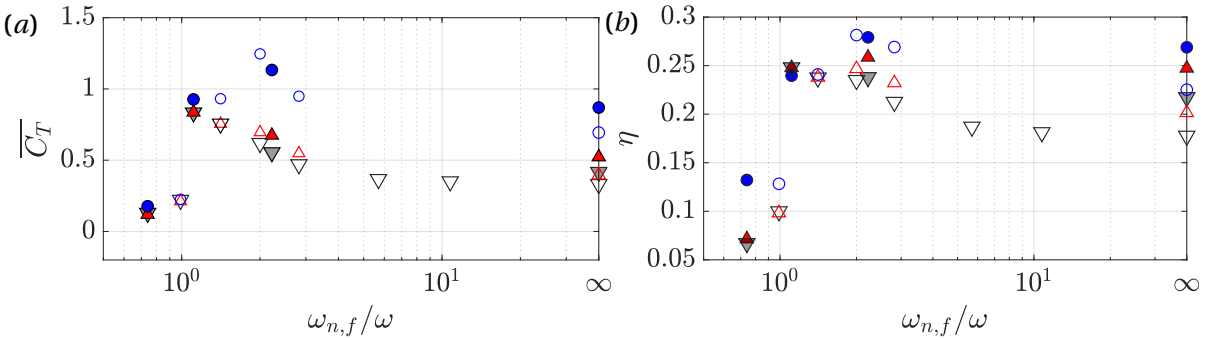

Figure 6.7: (a) Mean C_T and (b) propulsive efficiency averaged over a cycle for wings with $\mathcal{AR} = 2$ (open symbols) and $\mathcal{AR} = 4$ (closed symbols). ▼: isolated wings. ▲: forewings. •: hindwings.

hindfoil shows stronger pressure peaks at the leading edge, consistent with a larger effective angle of attack and a stronger LEV, in line with the discussion presented in the previous paragraphs.

6.4 Three-dimensional spanwise-flexible wings arranged in horizontal tandem

6.4.1 Overview of the aerodynamic performance of tandem systems

Following the observations for the two-dimensional problem, we analyse now the performance of a pair of three-dimensional spanwise-flexible wings arranged in horizontal tandem.

The propulsive performance of the tandem systems and isolated wings can be measured in terms of the mean thrust coefficient $\overline{C_{T,i}}$ and propulsive efficiency η_i, where the subindex $i = F, H$ and I for forewings, hindwings and isolated wings, respectively. They are shown in figure 6.7 as a function of the natural frequency in fluid over the angular frequency of the flapping motion, $\omega_{n,f}/\omega$. The effect of $\omega_{n,f}/\omega$ on the performance of the tandem system is very similar for $\mathcal{AR} = 4$ and 2. Overall, the values of $\overline{C_{T,F}}$ and η_F are similar to $\overline{C_{T,I}}$ and η_I, although the former are somewhat higher than the latter for $\omega_{n,f}/\omega \geq 2$. The maximum values of $\overline{C_T}$ and η for forewings and isolated wings are reached at $\omega_{n,f}/\omega \approx 1$. In the following, we denote these cases as *resonant* cases. For $\omega_{n,f}/\omega < 1$, both

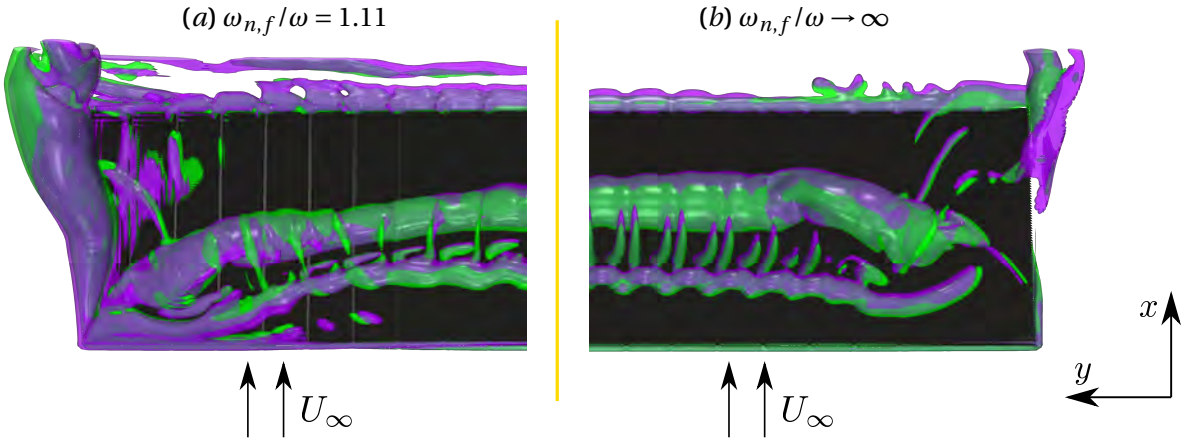

Figure 6.8: Flow visualization using iso-surfaces of the second invariant of the velocity gradient tensor, $Q = 7.5\omega^2$, colored in purple (forewings) and green (isolated wings). The yellow line denotes the location of the midsection of the wings, separating (*a*) resonant wings ($\omega_{n,f}/\omega = 1.11$) and (*b*) rigid wings ($\omega_{n,f}/\omega \to \infty$) of $\mathcal{AR} = 4$. Time instant correspond to $t/T = 0.5$.

the mean thrust coefficient and the propulsive efficiency drop sharply. Cases that are beyond this drop in performance (i.e., $\omega_{n,f}/\omega < 1$) are denoted as *sub-optimal*. We denote *rigid* cases those with $\omega_{n,f}/\omega \to \infty$, and *intermediate* cases those between the rigid and the resonant cases. For reference, this terminology is included in table 6.2.

The effect of $\omega_{n,f}/\omega$ on the performance of the hindwings is slightly different. Both $\overline{C_{T,H}}$ and η_H exhibit a broad maximum at $\omega_{n,f}/\omega \approx 2$, with a moderate increase in performance with respect to the rigid hindwings (30% and 4% for $\mathcal{AR} = 4$ wings, somewhat larger for $\mathcal{AR} = 2$ wings). Increasing the flexibility beyond $\omega_{n,f}/\omega < 2$ results in a slow decrease in $\overline{C_{T,H}}$ and η_H up to $\omega_{n,f}/\omega \approx 1$, followed by a steeper drop on performance for $\omega_{n,f}/\omega < 1$. When the tandem system is considered as a whole, the best performance is achieved at $\omega_{n,f}/\omega \approx 2$ as well. In the following, we denote this case as the "optimal" tandem case.

The differences in the performances of forewings and hindwings observed in figure 6.7 suggest that the underlying mechanisms at play in each wing are different. Hence, we proceed to analyze the fluid-structure interaction of each wing separately.

6.4.2 Aeroelastic behaviour of forewings

The results presented in figure 6.7 suggest that the aeroelastic response of forewings and isolated wings is very similar. This similarity is further analyzed in figure 6.8, where we compare instantaneous flow fields around forewings and isolated wings, for two different values of $\omega_{n,f}/\omega$. The figure shows the developing LEV on the suction side of the wings during the downstroke, using iso-surfaces of the second invariant of the velocity gradient tensor, Q. Four cases are represented in figure 6.8: green for isolated wings and purple for forewings, left for resonant wings ($\omega_{n,f}/\omega = 1.11$) and right for rigid wings. It is possible to see that the structure of the vortices over forewings and isolated wings are

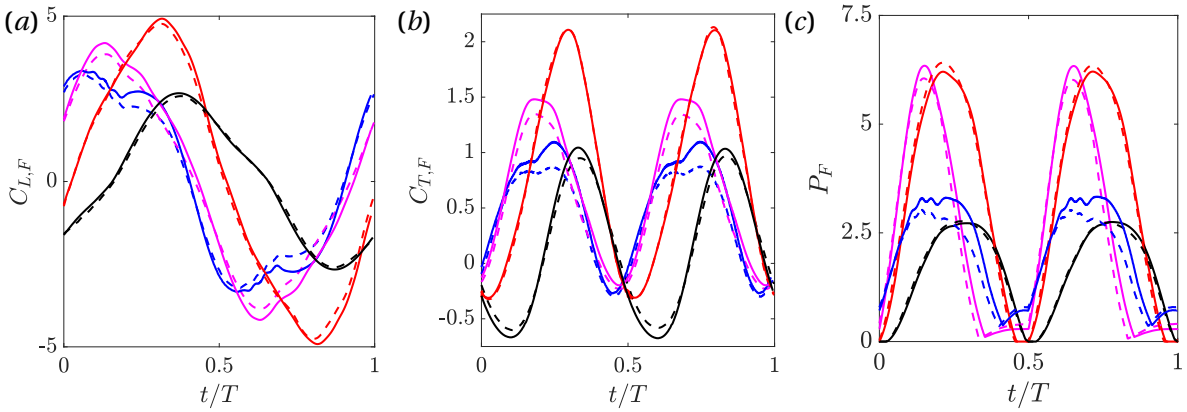

Figure 6.9: Temporal evolution of (a) lift coefficient, $C_{L,F}$, (b) thrust coefficient, $C_{T,F}$, and (c) input power coefficient, P_F. Solid (——) and dashed (– – –) lines correspond to forewings and isolated wings, respectively. Line colors correspond to: ——: Rigid. ——: Intermediate. ——: Resonant. ——: Sub-optimal.

very similar, suggesting that the mechanism governing their aeroelastic behavior is the same. This mechanism has been thoroughly described by Martínez-Muriel et al. (2023) for isolated wings. In the following, we provide a brief description of the mechanism for completeness.

The temporal evolution of lift, $C_{L,i}$, thrust, $C_{T,i}$, and input power, P_i, coefficients of forewings and isolated wings with $\mathcal{AR} = 4$ is presented in figure 6.9. The differences between forewings and isolated wings are small, consistent with the results presented in figures 6.7 and 6.8. The maximum instantaneous values of $C_{L,F}$ and $C_{T,F}$ increase with flexibility up to the resonant case, decreasing suddenly for the sub-optimal case. These maximum values are obtained at later times as flexibility increases, consistent with an increasing lag between the excitation (motion of the root of the wing) and the response (motion of the rest of the wing). Rigid and intermediate forewings seem to have larger values of lift and thrust coefficients than isolated wings, especially around mid-stroke (i.e., $t/T \approx 0.1 - 0.3$). This is probably caused by the same blocking effect discussed in section 6.3 for 2D foils, see figure 6.6. On the other hand, forewings with resonant and sub-optimal flexibility do not seem to benefit from the tandem configuration.

Figure 6.9(c) shows that the power required to drive rigid and intermediate forewings is slightly larger than for the corresponding isolated wings. The increase in P_F over P_I for these cases is smaller than the increase in $C_{T,F}$ over $C_{T,I}$, which explains the larger propulsive efficiency of forewings compared to isolated wings in figure 6.7(b). Resonant forewings have slightly lower power requirements than resonant isolated wings, while the power requirements of suboptimal forewings are virtually the same as for suboptimal isolated wings. In order to characterize the structural response of forewings and isolated wings, figure 6.10 shows the amplitude and phase of the wing tip displacement, as a function of their natural frequency. Overall, the structural response is consistent with that of a non-linear damped harmonic oscillator. Figure 6.10(a) shows moderate values of the maximum amplification (i.e, $h_{tip}/h_0 \approx 1.4$) at the resonant frequency ($\omega_{n,f}/\omega \approx 1$), with a sharp transition from

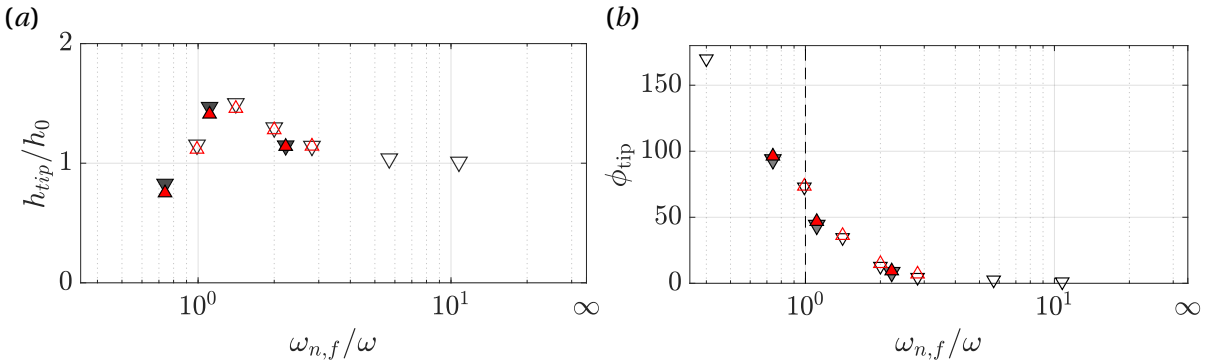

Figure 6.10: (*a*) Amplitude of the vertical position of the tip normalized with the heaving amplitude, h_{tip}/h_0, as a function of the frequency ratio in fluid, $\omega_{n,f}/\omega$. (*b*) Phase lag of the tip displacement relative to the wing root ϕ_{tip}, as a function of the frequency ratio in fluid, $\omega_{n,f}/\omega$. In both figures, (▼): isolated wings, (▲): forewings. $\mathcal{AR} = 2$, open symbols. $\mathcal{AR} = 4$, closed symbols.

the resonant response to the suboptimal responses. Due to the non-linearity of the system (both fluid and structural), the phase lag between the motion of the root (excitation) and the tip (response) at resonance is $\phi_{tip} \approx 45°$, in agreement with previous works (Qi et al., 2010; Martínez-Muriel et al., 2023). Note that this phase lag is important, since it allows the synchronization of the effective angle of attack of the wings and their pitching motion, maximizing the aerodynamic loads generated by the wing and their projection in the horizontal direction (aerodynamic tailoring, see Ramananarivo et al., 2011).

6.4.3 Aeroelastic behaviour of hindwings

As shown in section 6.4.1, the effect of $\omega_{n,f}/\omega$ in the propulsive performance of hindwings is different than in forewings and isolated wings. In particular, the optimal performance for hindwings is not found at the fluid-structural resonance, suggesting a significant role of the wake capture mechanism described for 2D foils in section 6.3. Consequently, in this section we will analyze the interplay among wing kinematics, structural response, and wake capture that determines the aerodynamic performance of the hindwing.

To assess the aeroelastic response of the hindwing, figure 6.11 shows the sectional thrust coefficient $c_t(y,t)$ at the mid-span ($2y/b = 0$) and near the wing tip ($2y/b = 0.8$), for $\mathcal{AR} = 4$ hindwings with different flexibility. For reference, the sectional thrust coefficient of the isolated, rigid wing is also included in the figure (blue dashed line). At the mid-span (figure 6.11*a*), all hindwings present an increase in c_t with respect to the rigid isolated wings, with the exception of the sub-optimal hindwing whose c_t is similar to the isolated case. The increase in c_t is also present when comparing the flexible hindwings with their isolated flexible counterparts (not shown), suggesting a relevant contribution from the wake capture phenomenon (compare figures 6.11*a* and 6.4*b*). Note that the conditions of the mid-span section of wings with $\mathcal{AR} = 4$ are relatively close to the 2D foils discussed in section 6.3, due to negligible wing tip effects (see Arranz et al., 2020) and the prescribed kinematics of the root (i.e., smaller effect of flexibility).

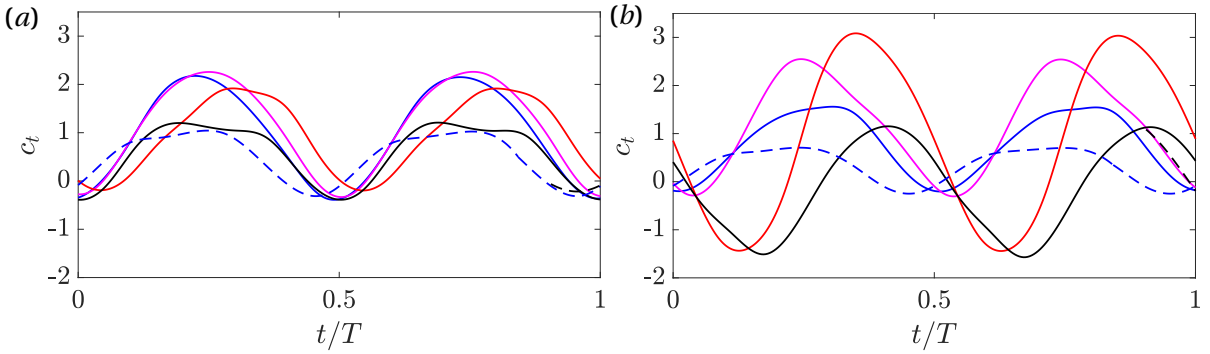

Figure 6.11: Sectional thrust coefficients, c_t, for hindwings at (a) $2y/b = 0$, (b) $2y/b = 0.8$. Line colors correspond to: ——: Rigid. ——: Intermediate. ——: Resonant. ——: Sub-optimal. The blue dashed line corresponds to the isolated rigid case.

When moving from the mid-span section to the outboard sections of the hindwing, the full complexity of the problem becomes apparent: 3D effects become more relevant due to the proximity of the wing tips, and the kinematics of the wing section are determined by the structural response, which is fully coupled with the wake capture and the generation of aerodynamic loads. For the rigid case, where only wake capture and 3D effects are at play, c_t decreases from the mid-span to the wing tips. This can be observed comparing the blue solid lines in figures 6.11a and 6.11b. For the intermediate and resonant cases, the maximum values of $c_t(y,t)$ are larger near the wing tips than at the mid-span section. Indeed, figure 6.11(b) shows that increasing flexibility results in larger maximum values for c_t near the wing tips ($2y/b = 0.8$), except for the sub-optimal case. However, the resonant case also shows large negative values of c_t (i.e, sectional drag) near the wing tips during a considerable portion of the cycle. This explains the lower values of $\overline{C_{T,H}}$ for resonant wings than for intermediate wings in figure 6.7(a). The generation of drag near the wing tip becomes more acute for the sub-optimal case, as shown by the black line in figure 6.11(b).

To further explore this observation, we proceed to estimate the effective angles of attack of the wing section at $2y/b = 0.8$, following the procedure described for the 2D tandem foils in §6.3. We estimate the vertical velocity in the wake of the forewing as

$$\overline{u_z}(y,z,t) = \frac{1}{c}\int_{x_{LE}^H}^{x_{TE}^H} u_z(x_0,y,z,t)\,dx_0, \tag{6.18}$$

where $u_z(x,y,z,t)$ is the vertical velocity in the wake of the corresponding isolated wing, the integral is taken from the leading edge to the trailing edge of the hindwing. Figure 6.12 presents $\overline{u_z}$ at $2y/b = 0.8$ for the rigid, intermediate, and resonant cases. The spatio-temporal distribution of the wake velocities is very similar for the three cases, with larger velocity magnitude (i.e., stronger vortices) with increasing flexibility. Figure 6.12 also includes the trajectory of the mid-chord of the hindwings at the wing section $2y/b = 0.8$. Overall, the upwash (i.e., positive $\overline{u_z}$) regions roughly correspond with the downstroke of the hindwing for the three cases, increasing the aerodynamic loads generated by the hindwing compared to the isolated rigid wing. The figure also shows that the synchronization of

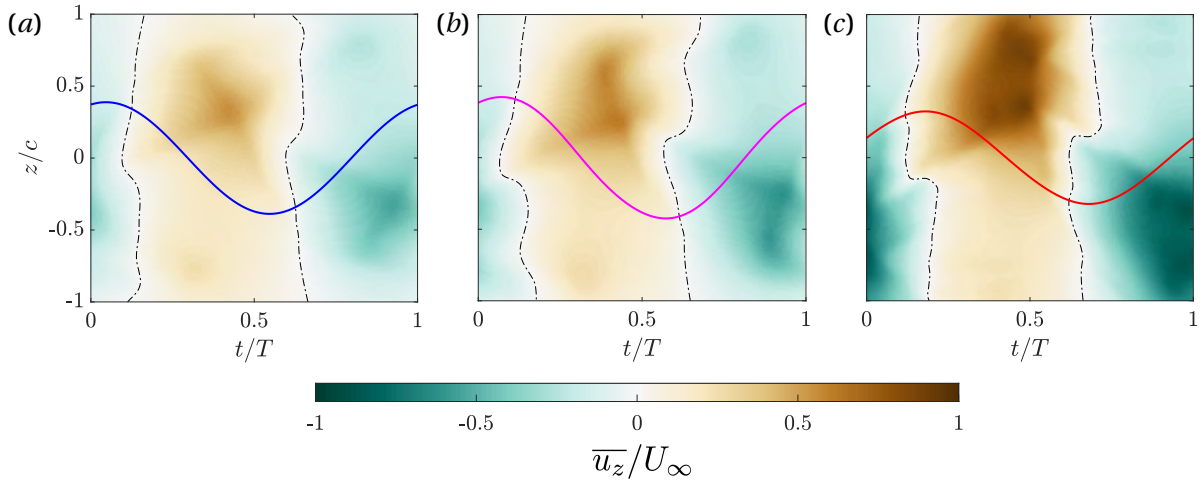

Figure 6.12: Contours of locally-averaged vertical velocity, $\overline{u_z}/U_\infty$, at $2y/b = 0.8$, as a function of time and the vertical coordinate. Dashed black lines correspond to $\overline{u_z}/U_\infty = 0$. The solid lines corresponds to the trajectories of the mid-chord of the corresponding section of the hindwing. (*a*) Rigid case. (*b*) Intermediate case. (*c*) Resonant case.

the upwash and the downstroke of the hindwing is better for the intermediate case, as evidenced by the close proximity of the dash-dotted lines with $\overline{u_z} = 0$ and the maximum and minimum of the trajectory in figure 6.12(*b*). For the resonant case this synchronization is worse, which might contribute to its lower propulsive performance (even with a stronger upwash).

In order to quantify this effect and its interaction with the pitching angle of the wing, we compute the effective angle of attack as defined in equation (6.16). The vertical velocity perceived by the hindwing, $u_{z,MC}$, is taken along the trajectories shown in figure 6.12, and $\dot{h}$ is the vertical velocity of the mid-chord point at $2y/b = 0.8$. The temporal evolution of the α_e's of the hindwings is shown in figure 6.13(*a*) in solid lines. For comparison, the α_e's of the forewings are included in dashed lines. We can observe that the α_e of hindwings are delayed with respect to the α_e of the forewings. Also, the α_e of rigid cases are delayed with respect to intermediates, and α_e of intermediates are slightly delayed with respect to rigid, both for forewings and hindwings. These time lags have implications for the generation of aerodynamic forces. First, the delay in α_e results in a delay in the development and detachment of the LEV (Martínez-Muriel et al., 2023), which results in stronger peaks in the sectional normal force coefficients, as shown in figure 6.13(*b*). Second, the production of thrust depends on the synchronization of the time evolution of the normal forces and the pitching angle, since the latter determines the projection of the forces in the horizontal direction (aerodynamic tailoring). Recall that the phase lag of the kinematics of the forewing and hindwing is small ($\phi_{fh} = -13°$), resulting in a time lag $\approx 0.03T$ between the pitching motions of forewing and hindwing. Consequently, the pitching angle of both wings changes sign at $t/T \approx 0$ and $t/T \approx 0.5$. For the hindwings, the synchronization of the zero-crossing of α_e and pitching angles explains the superior propulsive performance of the intermediate case (even if the normal forces generated by the resonant case are larger, as shown in

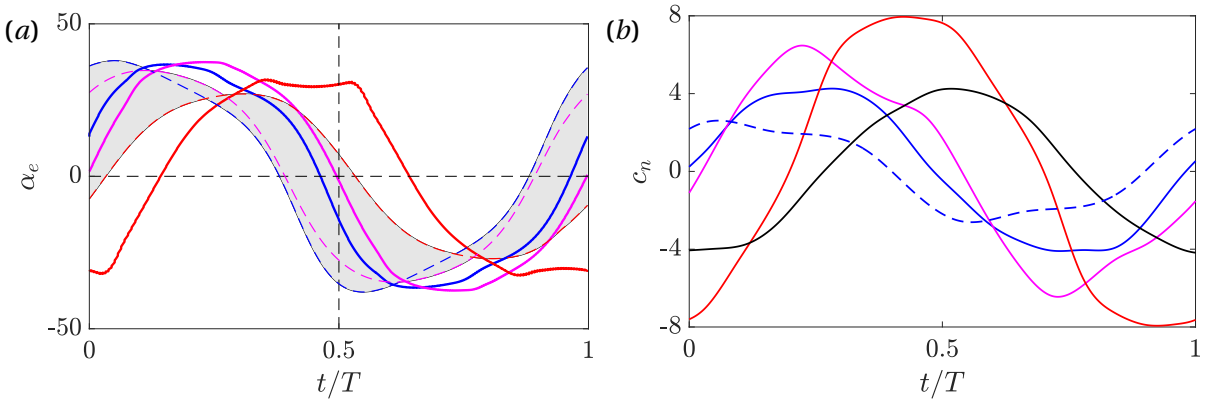

Figure 6.13: Temporal evolution of (a) the estimate of the effective angles of attack α_e and (b) the sectional normal force coefficient c_n at a spanwise section $2y/b = 0.8$. Line colors correspond to: ——: rigid, ——: intermediate, and ——: resonant hindwings. The area shaded in gray represents the envelope of effective angles of attack seen by the rigid-to-resonant forewings at the same spanwise $2y/b = 0.8$ section. The dashed blue line in panel (b) refers to the rigid forewing.

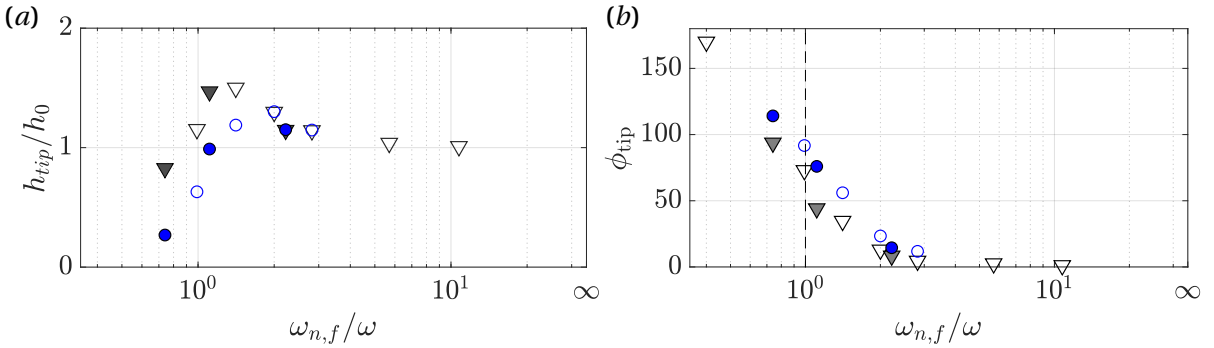

Figure 6.14: (a) Amplitude of the vertical position of the tip normalized with the heaving amplitude, h_{tip}/h_0, as a function of the frequency ratio in fluid, $\omega_{n,f}/\omega$. (b) Phase lag of the tip displacement relative to the wing root ϕ_{tip}, as a function of the frequency ratio in fluid, $\omega_{n,f}/\omega$. In both figures, (▼): isolated wings, (•): hindwings. $\mathcal{AR} = 2$, open symbols. $\mathcal{AR} = 4$, closed symbols.

figure 6.13b), and the appearance of sectional drag for the resonant case (as discussed in figure 6.11).

The change in the aerodynamic performance of the hindwings comes together with a change in the structural response, which is presented in figure 6.14. Recall that the structural response of the forewings is very similar to the structural response of the isolated wings (see figure 6.10). The values of the amplitude of the vertical displacement of the hindwing tip as a function of $\omega_{n,f}/\omega$ are presented in figure 6.14(a). They are qualitatively similar when compared to the isolated wings, presenting a maximum in h_{tip}/h_0 and a sharp drop for $\omega_{n,f}/\omega < 1$. However, the value of the frequency ratio at which the hindwings present a maximum is $\omega_{n,f}/\omega \approx 2$, same as $\overline{C_{T,H}}$ in figure 6.7(a), further supporting the idea that the optimal performance of the hindwings is not dominated by a fluid-structure resonance. Moreover, the maximum tip displacement of the hindwing is smaller than forewings and isolated wings at resonance, and the phase lags for the optimal hindwing (i.e., $\omega_{n,f}/\omega \approx 2$) are small (see figure 6.14b). These two observations draw a picture where the benefits of

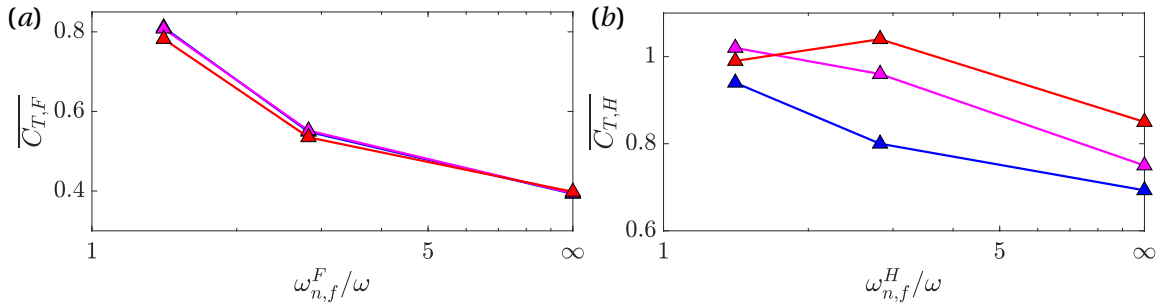

Figure 6.15: Mean thrust coefficient $\overline{C_T}$ as a function of the flexibility of the wing, $\omega_{n,f}/\omega$, for (a) forewings and (b) hindwings. Colored lines connect cases where the opposite wing has the same flexibility, namely: ——: Rigid. ——: Intermediate. ——: Resonant.

the hindwing flexibility are related to the synchronization of wing deformation with the incoming wake (i.e, to maximize the wake capture) and with the pitching angle (i.e., aerodynamic tailoring), with a smaller role associated to the increased amplitude of the wing tip displacement (i.e., fluid-structure resonance).

6.4.4 Mixed tandem systems

The results shown in the previous sections indicate that the optimal performance of forewings is found at resonance, while the optimal performance of hindwings is found at $\omega_{n,f}/\omega \approx 2$. This observation suggests that a system made of wings with different flexibilities could outperform a system where the wings have the same flexibility. We denote in the following such systems as mixed tandem systems.

In order to explore this idea we have performed a proof-of-concept study, running numerical simulations of a series of mixed tandem systems. Due to the available computational resources, we have only considered $\mathcal{AR} = 2$ wings (the required computational domain is smaller) and the simulations are conducted with the moderate grid resolution $\Delta r = c/56$. The latter has been shown to be good enough to represent accurately the trends in the forces (Martínez-Muriel et al., 2023). We have considered all possible combinations with rigid ($\omega_{n,f}/\omega = \infty$), intermediate ($\omega_{n,f}/\omega = 2.82$) and resonant ($\omega_{n,f}/\omega = 1.41$) flexibilities for $\mathcal{AR} = 2$. This leads to 9 systems, 6 of which are mixed tandem systems, and the other 3 are systems with equal flexibility already included in Table 6.2. For the mixed systems, we need to distinguish between the natural frequency in the fluid of each wing. We do so by introducing the superscript F for forewing and H for hindwing.

Figure 6.15(a) shows the value of the mean thrust coefficient of the forewings, $\overline{C_{T,F}}$, as a function of $\omega^F_{n,f}/\omega$. Each line corresponds to a different value of $\omega^H_{n,f}/\omega$. As expected, the $\overline{C_{T,F}}$ of the forewings do not depend on the stiffness of the hindwing, with resonant forewings providing the largest thrust in all cases.

The results for the thrust coefficient of hindwings are shown in figure 6.15(b). We first analyze the rigid hindwings ($\omega^H_{n,f}/\omega = \infty$), when the flexibility of the forewing is varied. What we observe is that

$\overline{C_{T,H}}$ increases with the flexibility of the forewing, at least for $\omega^F_{n,f}/\omega \geq 1$. This enhanced aerodynamic performance of the hindwings can be linked to the larger velocities induced by the forewings on the wake (see figure 6.12), which increases the effective angle of attack of the hindwings and their thrust. Recall that, as these hindwings are rigid, the trajectory of all the sections is the same independent of the flexibility of the forewing, and no aerodynamic tailoring is involved.

We now analyse the response of the different hindwings while maintaining the same flexibility of the forewing. Hindwings of cases where the forewing is either rigid (blue line) or intermediately flexible (magenta line) have increasing values of $\overline{C_{T,H}}$ as the wing is made more flexible, with maximum values at the resonance. However, when the forewing is resonant (and the wake velocities are stronger), the maximum $\overline{C_{T,H}}$ is obtained for the intermediate hindwing, consistent with an increasing relevance of the wake capture and aerodynamic tailoring mechanisms as the wake of the forewing becomes stronger.

Overall, our proof-of-concept study shows that the largest $\overline{C_{T,F}} + \overline{C_{T,H}}$ is provided by the system with a resonant forewing and an intermediate hindwing, confirming the hypothesis that mixed tandem systems can outperform systems with equally-flexible wings. The implication for the design of systems of flexible flapping wings in tandem is that while the flexibility of the forewing can be prescribed to ensure a resonance at the driving frequency, the flexibility of the hindwing needs to be tuned together with the kinematic parameters (i.e., driving frequency, heaving and pitching amplitudes, phase shifts and distance between forewing and hindwing) to ensure optimal performance of the system.

6.5 Conclusions

In this work, the effect of spanwise-flexibility on the propulsive performance of tandem flapping wings is analyzed using Direct Numerical Simulations. Different flexibilities (i.e., effective stiffness $\Pi_1 \approx [1-100, \infty]$) and two aspect ratios ($\mathcal{AR} = 2$ and 4) are considered in a simple configuration: a pair of rectangular wings in forward flight at $Re = 1000$, with a prescribed heaving and pitching motion at the mid-span section of the wing, while the rest of the wing deforms passively. The selected kinematics are optimal, in the sense of maximizing the propulsive efficiency in a 2D configuration.

The results show that the aerodynamic performance and structural behavior of forewings are similar to that found for isolated wings, with a small influence of the hindwing. In particular, the maximum propulsive performance of the forewings is obtained at excitation frequencies close to the natural frequency, $\omega_{n,f}/\omega \approx 1$. This implies that the fluid-structure resonance mechanism is dominant in explaining the enhanced propulsive performance of forewings, same as in isolated wings (Martínez-Muriel et al., 2023).

Conversely, the optimal performance of the hindwing is found at $\omega_{n,f}/\omega \approx 2$ (i.e., more rigid than the optimal forewing), suggesting that the performance of the hindwing is not dominated by the same fluid-structure resonance that dominates the forewing's performance. The analysis of the

results of the simulations has shown that the hindwing performance is dominated by two additional mechanisms, namely wake capture and aerodynamic tailoring. These mechanisms are well described in the literature. The wake capture mechanism is the basic mechanism at play in tandem rigid wings: the hindwing takes advantage of the vortices shed by the forewing to increase thrust and reduce the power required to sustain its flapping motion (Broering & Lian, 2012). The aerodynamic tailoring consists on synchronizing the aerodynamic forces with the pitching angle of the wing, maximizing thrust generation during the cycle (Ramananarivo et al., 2011).

Our results show that the hindwing flexibility introduces a lag between the motion of the root (which in our study is chosen to have an optimal wake capture) and the motion of the tips. The magnitude of this lag affects both the intensity of the wake capture and the timing between forces and pitching angle, which in turn affects the wing deformation (both amplitude and phase lag). To quantify these effects we have defined an effective angle of attack, which qualitatively correlates with the aerodynamic forces produced by the hindwing. This quantity only requires information from the wake of the forewing, meaning that it can be computed from simulations of isolated wings. Note that the performance of the hindwing is dependent on the flexibility of the forewing, since the latter impacts the strength of the vortices in the wake, and hence the maximum propulsive performance of the hindwing.

The observation that the mechanisms resulting in optimally performing forewings and hindwings are different has motivated a proof-of-concept study of tandem systems with mixed flexibilities (i.e., different flexibilities for forewing and hindwing). Our preliminary results show that mixed flexibility systems can outperform systems with the same flexibility in forewing and hindwing. Indeed, the maximum propulsive efficiency is obtained for mixed system with a forewing with $\omega^F_{n,f}/\omega \approx 1$ and a hindwing with $\omega^H_{n,f}/\omega \approx 2$.

The results of this work have implications for the optimization process of tandem systems with spanwise flexible wings. Our results suggest that the flexibility of the forewing can be chosen to ensure a fluid-structure resonance at the driving frequency. This will maximize the forewing propulsive performance and the wake intensity. On the other hand, the hindwing flexibility needs to be optimized together with the kinematic parameters, to ensure an optimal interaction of the hindwing with the incoming wake (wake capture) and an optimal synchronization of the forces generated by the hindwing and its pitching angle (aerodynamic tailoring).

Acknowledgements

This work was partially supported by grant DPI2016-76151-C2-2-R (AEI/FEDER, UE). The authors thankfully acknowledge the computer resources at MareNostrum and the technical support provided by Barcelona Supercomputing Center (RES-IM-2020-2-0006), as well as at LUSITANIA III and the technical support provided by Centro Extremeño de Investigación, Innovación Tecnológica y Supercomputación (CénitS) (RES-IM-2020-3-0024).

REFERENCES

Alaminos-Quesada, J. & Fernandez-Feria, R. 2021. Propulsion performance of tandem flapping foils with chordwise prescribed deflection from linear potential theory. *Phys. Rev. Fluids* 6 (1): 013102.

Alben, S. 2012. Flapping propulsion using a fin ray. *J. Fluid Mech.* 705:149–164.

Arora, N., Kang, C.-K., Shyy, W. & Gupta, A. 2018. Analysis of passive flexion in propelling a plunging plate using a torsion spring model. *J. Fluid Mech.* 857:562–604.

Arranz, G., Flores, O. & García-Villalba, M. 2020. Three-dimensional effects on the aerodynamic performance of flapping wings in tandem configuration. *J. Fluids Struct.* 94:102893.

Arranz, G., Flores, O. & García-Villalba, M. 2022a. Flow interaction of three-dimensional self-propelled flexible plates in tandem. *J. Fluid Mech.* 931.

Arranz, G., Martínez-Muriel, C., Flores, O. & García-Villalba, M. 2022b. Fluid-structure interaction of multi-body systems: Methodology and applications. *J. Fluid Struct.* 110:103519.

Berman, G. J. & Wang, Z. J. 2007. Energy-minimizing kinematics in hovering insect flight. *J. Fluid Mech.* 582:153–168.

Bie, D. & Li, D. 2022. Numerical analysis of the wing–wake interaction of tandem flapping wings in forward flight. *Aerospace Science and Technology* 121:107389.

Bode-Oke, A. T., Zeyghami, S. & Dong, H. 2018. Flying in reverse: kinematics and aerodynamics of a dragonfly in backward free flight. *J. Royal Soc. Interface* 15 (143): 20180102.

Bomphrey, R. J., Nakata, T., Henningsson, P. & Lin, H. T. 2016. Flight of the dragonflies and damselflies. *Philosophical Transactions of the Royal Society B: Biological Sciences* 371 (1704): 20150389.

Broering, T. M. & Lian, Y. S. 2012. The effect of phase angle and wing spacing on tandem flapping wings. *Acta Mechanica Sinica* 28 (6): 1557–1571.

Chen, Y. H., Skote, M., Zhao, Y. & Huang, W. M. 2013. Dragonfly (Sympetrum flaveolum) flight: Kinematic measurement and modelling. *J. Fluids Struct.* 40:115–126.

De Croon, G. C. H. E. et al. 2009. Design, aerodynamics, and vision-based control of the DelFly. *Int. J. Micro Air Veh.* 1 (2): 71–97.

Felis, M. L. 2017. RBDL: an efficient rigid-body dynamics library using recursive algorithms. *Auton. Robots* 41 (2): 495–511.

Floryan, D. & Rowley, C. W. 2018. Clarifying the relationship between efficiency and resonance for flexible inertial swimmers. *J. Fluid Mech.* 853:271–300.

Fu, J., Liu, X., Shyy, W. & Qiu, H. 2018. Effects of flexibility and aspect ratio on the aerodynamic performance of flapping wings. *Bioinspir. Biomim.* 13 (3): 036001.

Goza, A., Floryan, D. & Rowley, C. 2020. Connections between resonance and nonlinearity in swimming performance of a flexible heaving plate. *J. Fluid Mech.* 888.

Haider, N., Shahzad, A., Mumtaz Q., Muhammad N. & A. S., Syed I. 2021. Recent progress in flapping wings for micro aerial vehicle applications. *Proc. Inst. Mech. Eng., Part C* 235 (2): 245–264.

Hamamoto, M., Ohta, Y., Hara, K. & Hisada, T. 2007. Application of fluid–structure interaction analysis to flapping flight of insects with deformable wings. *Adv. Robotics* 21 (1-2): 1–21.

Hefler, C., Qiu, H. & Shyy, W. 2018. Aerodynamic characteristics along the wing span of a dragonfly Pantala flavescens. *J. Exp. Biol.* 221 (19): jeb171199.

Jongerius, S. R. & Lentink, D. 2010. Structural analysis of a dragonfly wing. *Exp. Mech.* 50 (9): 1323–1334.

Jurado, R., Arranz, G., Flores, O. & García-Villalba, M. 2022. Numerical simulation of flow over flapping wings in tandem: Wingspan effects. *Phys. Fluids* 34 (1): 017114.

Keennon, M., Klingebiel, K. & Won, H. 2012. Development of the nano hummingbird: A tailless flapping wing micro air vehicle. In *50th AIAA aerospace sciences meeting including the new horizons forum and aerospace exposition,* 588.

Kodali, D., Medina, C., Kang, C.-K. & Aono, H. 2017. Effects of spanwise flexibility on the performance of flapping flyers in forward flight. *J. Royal Soc. Interface* 14 (136): 20170725.

Lagopoulos, N. S., Weymouth, G. D. & Ganapathisubramani, B. 2023. Effect of aspect ratio on the propulsive performance of tandem flapping foils. *Flow* 3:E1.

Lai, Y. H., Lin, Y. J., Chang, S. K. & Yang, J. T. 2020. Effect of wing–wing interaction coupled with morphology and kinematic features of damselflies. *Bioinspir. Biomim.* 16 (1): 016017.

Li, C. & Dong, H. 2017. Wing kinematics measurement and aerodynamics of a dragonfly in turning flight. *Bioinspir. Biomim.* 12 (2): 026001.

Liu, K., Liu, X. & Huang, H. 2022. Scaling the self-propulsive performance of pitching and heaving flexible plates. *J. Fluid Mech.* 936.

Lua, K. B. et al. 2016. Aerodynamics of two-dimensional flapping wings in tandem configuration. *Phys. Fluids* 28 (12): 121901.

Martínez-López, C. 2019. *Aerodynamic performance optimization of two wings in tandem configuration*. BSc thesis, Universidad Carlos III de Madrid, http://hdl.handle.net/10016/30239.

Martínez-Muriel, C., Arranz, G., García-Villalba, M. & Flores, O. 2023. Fluid-structure resonance in spanwise-flexible flapping wings. *Currently under review in J. Fluid Mech.*

Martínez-Muriel, C. & Flores, O. 2020. Analysis of vortical gust impact on airfoils at low Reynolds number. *J. Fluids Struct.* 99:103138.

Moore, M. N. J. 2015. Torsional spring is the optimal flexibility arrangement for thrust production of a flapping wing. *Phys. Fluids* 27 (9): 091701.

Moored, K.W., Dewey, P.A., A.J. Smits, AJ & Haj-Hariri, H. 2012. Hydrodynamic wake resonance as an underlying principle of efficient unsteady propulsion. *J. Fluid Mech.* 708:329–348.

Moriche, M. 2017. "A numerical study on the aerodynamic forces and the wake stability of flapping flight at low Reynolds number." PhD diss., Universidad Carlos III Madrid.

Moriche, M., Flores, O. & García-Villalba, M. 2017. On the aerodynamic forces on heaving and pitching airfoils at low Reynolds number. *J. Fluid Mech.* 828:395–423.

Nagai, H., Fujita, K. & Murozono, M. 2019. Experimental study on forewing–hindwing phasing in hovering and forward flapping flight. *AIAA journal* 57 (9): 3779–3790.

Ortega-Casanova, J. & Fernández-Feria, R. 2019. Maximum propulsive efficiency of two pitching and plunging plates in tandem at low Reynolds number: A numerical analysis. *Int. J. Numer. Meth. Heat Fluid Flow* 29 (11): 4013–4033.

Peng, L. et al. 2021. Tandem-wing interactions on aerodynamic performance inspired by dragonfly hovering. *Royal Society open science* 8 (8): 202275.

Peng, Z. R., Huang, H. & Lu, X. Y. 2018. Collective locomotion of two self-propelled flapping plates with different propulsive capacities. *Phys. Fluids* 30 (11): 111901.

Qi, D., Liu, Y., Shyy, W. & Aono, H. 2010. Simulations of dynamics of plunge and pitch of a three-dimensional flexible wing in a low Reynolds number flow. *Phys. Fluids* 22 (9): 091901.

Quinn, D. & Lauder, G. 2022. Tunable stiffness in fish robotics: mechanisms and advantages. *Bioinspir. Biomim.* 17 (1): 011002.

Quinn, D. B., Lauder, G. V. & Smits, A. J. 2014. Scaling the propulsive performance of heaving flexible panels. *J. Fluid Mech.* 738:250–267.

Raj, A. & Thakur, A. 2016. Fish-inspired robots: design, sensing, actuation, and autonomya review of research. *Bioinspir. Biomim.* 11 (3): 031001.

Ramananarivo, S., Godoy-Diana, R. & Thiria, B. 2011. Rather than resonance, flapping wing flyers may play on aerodynamics to improve performance. *Proc. Natl Acad. Sci.* 108 (15): 5964–5969.

Reid, H. E. et al. 2019. Wing flexibility reduces the energetic requirements of insect flight. *Bioinspir. Biomim.* 14 (5): 056007.

Ren, H., Wang, X., Li, X. & Chen, Y. 2013. Effects of dragonfly wing structure on the dynamic performances. *J. Bionic Eng.* 10 (1): 28–38.

Salami, E., Ward, T. A., Montazer, El. & Ghazali, N. N. N. 2019. A review of aerodynamic studies on dragonfly flight. *Proceedings of the Institution of Mechanical Engineers, Part C: Journal of Mechanical Engineering Science* 233 (18): 6519–6537.

Shanmugam, A. R. & Sohn, C. H. 2019. Numerical investigation of the aerodynamic benefits of wing-wing interactions in a dragonfly-like flapping wing. *Journal of Mechanical Science and Technology* 33 (6): 2725–2735.

Shumway, N., Gabryszuk, M. & Laurence, S. 2020. The impact of dragonfly wing deformations on aerodynamic performance during forward flight. *Bioinspir. Biomim.* 15 (2): 026005.

Shyy, W. et al. 2010. Recent progress in flapping wing aerodynamics and aeroelasticity. *Prog. Aerosp. Sci.* 46 (7): 284–327.

Sun, X., Gong, X. & Huang, D. 2017. A review on studies of the aerodynamics of different types of maneuvers in dragonflies. *Archive of Applied Mechanics* 87 (3): 521–554.

Uhlmann, M. 2005. An immersed boundary method with direct forcing for the simulation of particulate flows. *J. Comput. Phys.* 209 (2): 448–476.

Vejdani, H. R., Boerma, D. B., Swartz, S. M. & Breuer, K. S. 2018. The dynamics of hovering flight in hummingbirds, insects and bats with implications for aerial robotics. *Bioinspir. Biomim.* 14 (1): 016003.

Wakeling, J. M. & Ellington, C. P. 1997. Dragonfly flight. II. Velocities, accelerations and kinematics of flapping flight. *J. Exp. Biol.* 200 (3): 557–582.

Wood, R. J. 2008. The first takeoff of a biologically inspired at-scale robotic insect. *IEEE transactions on robotics* 24 (2): 341–347.

Zheng, Y., Wu, Y. & Tang, H. 2015. Force measurements of flexible tandem wings in hovering and forward flights. *Bioinspir. Biomim.* 10 (1): 016021.

Zheng, Y., Wu, Y. & Tang, H. 2016a. A time-resolved PIV study on the force dynamics of flexible tandem wings in hovering flight. *J. Fluids Struct.* 62:65–85.

Zheng, Y., Wu, Y. & Tang, H. 2016b. An experimental study on the forewing–hindwing interactions in hovering and forward flights. *International Journal of Heat and Fluid Flow* 59:62–73.

Zhu, X., He, G. & Zhang, X. 2014a. Flow-mediated interactions between two self-propelled flapping filaments in tandem configuration. *Phys. Rev. Lett.* 113 (23): 238105.

Zou, P. Y., Lai, Y. H. & Yang, J. T. 2019. Effects of phase lag on the hovering flight of damselfly and dragonfly. *Physical Review E* 100 (6): 063102.

CHAPTER 7

MAIN CONTRIBUTIONS AND CONCLUSIONS

Bioinspired locomotion has attracted the scientific community during the last decades. Still, there is lack of knowledge and many open questions to be addressed in order to achieve human-developed designs with performance and efficiency comparable to that found in natural locomotion. The main contribution of this thesis is the exploration and analysis of the physics underlying different simplified bioinspired problems, with the hope that they serve to pave the way for future research and eventual design of more efficient and sustainable small-scale robotic vehicles. For a detailed discussion and a deeper understanding of the results, the reader is referred to the studies that can be found in chapters 3 to 6.

Four different problems have been treated in this thesis, which can be split in two main blocks. The two first problems can be grouped in the block of flight in gusty environments. The effect of perturbations on large-scale aerodynamic problems has been widely addressed in the past, where it has been possible to propose reduced order models in order to characterise the aerodynamic response of aircraft. However, the hypotheses which those studies rely on do not apply for small-scale problems, being necessary to extract new models describing the aerodynamic behaviour of small-scale bodies immersed in gusty environments. Chapter 3, although in a simplified configuration, analyses the hydro-aerodynamic response of two-dimensional airfoils to isolated vortical gusts, exemplifying the interaction between flying or swimming vehicles with the disturbances found in nature. On the other hand, vehicles are designed not only focusing on their aerodynamic response but also many other different considerations must be taken into account. Among them, there are requirements in terms of the structural integrity of the vehicle, which will determine at least part of their lifespan. One of the main well-known issues with structures subjected to cyclic/unsteady loads is fatigue. Chapter 4 addresses the load that can be mitigated using passive-pitching trailing edges on airfoils undergoing oscillations in the angle of attack, in order to evaluate their aerodynamic

response. The results are compared to a quasi-steady potential flow theory, where the hypothesis which it is based on are no longer valid in the current situation.

The two last problems focus on the coupling between unsteady and aeroelastic effects on wings in forward flight. In particular, chapters 5 and 6 analyse the effects of spanwise flexibility on the aerodynamic performance of wings undergoing flapping motions. While the wings in chapter 5 are isolated, those considered in chapter 6 are arranged in horizontal tandem configuration, resembling how they are disposed in dragonflies. The analysis of isolated wings helps to elucidate the role of spanwise flexibility on their aerodynamic performance, while the study of wings in tandem arrangement allows to gather information on the combined effect of kinematics, flexibility and wing-wake interaction.

7.1 Highlights of scientific contributions

Chapter 3. Analysis of vortical gust impact on airfoils at low Reynolds number:

- The impact of vortical gusts with different intensity, size, location and vorticity distribution on airfoils flying at Reynolds number $Re = 1000$ is analysed in this work. A large database covering the parametric space has been generated.
- The aerodynamic response of the airfoil has been reproduced in terms of forces and fluid flow, identifying the dependence of each of variable on them. It has been found that the temporal evolution of the change in lift coefficient with respect to the steady state value is barely dependent on the angle of attack.
- A linear dependence of the time instant when the maximum lift is achieved and the diameter of the gust and the free stream velocity is found. Besides, this maximum lift is roughly proportional to the circulation of the gust, but varies non-linearly with the vertical separation between gust and airfoil.
- A semi-empirical model is proposed to compute the temporal evolution of the change in lift coefficient due to the gust based on an integral definition of the vortex velocity induced along the chord of the airfoil.

Chapter 4. Load mitigation on heaving airfoils using passive trailing-edge flaps:

- The load mitigation that can be achieved on airfoils undergoing heaving motion at $Re = 1000$ using passive-pitching trailing edge flaps is studied performing direct numerical simulations.
- The obtained results are compared with quasi-steady linear models. While these quasi-steady models are not able to predict the exact value of the reduction of fluctuations, it has been

proved that, under the parametric space covered in this work, an increment in the flap-to-chord length ratio leads to an equal increment in the reduction of fluctuations, in line with the predictions of the model. The quasi-steady model is unable to predict the flap deflections.

- The effect of different parameters describing the dynamics of the flap and the aerodynamic performance of the foil has been assessed. In particular, the effects of inertia and the preload of the torsional spring on the load mitigation have been explored to analyse the applicability of passive-pitching trailing edge flaps.

Chapter 5. Fluid-structure resonance in spanwise-flexible flapping wings:

- Direct numerical simulations are performed to assess the role of flexibility in the spanwise direction of wings undergoing flapping motion.
- Different values of the effective stiffness, Π_1, are selected, while the effective inertia of the wing, Π_0 is held constant. The effect of the aspect ratio is also analysed considering wings of aspect ratio 2 and 4. The results show that, while this effect is relevant for rigid wings, it becomes almost negligible for the flexible wings considered in this study.
- The optimal propulsive performance and efficiency is linked to a fluid-structure resonance, occurring when the natural frequency of the wings in fluid, $\omega_{n,f}$, matches the excitation frequency, ω. At this point, maximum thrust is obtained, being 2 times larger than that of rigid wings. On the other hand, the propulsive efficiency increases by a 3-6% in absolute terms.
- The aeroelastic response is characterised in terms of amplitudes and phase lags, the former showing peaks also at $\omega_{n,f}/\omega \approx 1$, and the latter having a value of approximately 45° at that frequency ratio. It is seen that this leads to an optimal distribution of effective angles of attack that maximize force generation, suggesting streamlining arguments similar to those found in the literature.

Chapter 6. On the role of wake-capture and resonance in tandem flapping wings:

- The propulsive performance of spanwise-flexible wings arranged in horizontal tandem configuration has been analysed. While the mid sections of the wings follow optimal 2D kinematics, the rest of the wings deform passively. Their deformation is now a result of the coupling between unsteady aerodynamics and structure in the case of forewings, while hindwings also combine those effects with a wake capture, i.e., the interaction with the vortices shed by the forewing.
- The optimal aerodynamic performance of forewings can be explained through the same mechanisms that are used to explain that of isolated spanwise flexible wings, i.e., a fluid-structure resonance combined with a proper projection of the generated forces.

- The force generation and efficiency of hindwings can be drastically improved if the flexibility is properly selected. Optimal aerodynamic performance of hindwings cannot be explained through a resonance phenomenon. Instead, due to wake capture effects and an aerodynamic tailoring, the natural frequency of hindwings such that the efficiency and force coefficients are maximum is shifted towards larger values. The performance of the hindwings can be qualitatively analysed estimating the effective angle of attack using the information about the velocity induced by the forewing on the hindwing.

- Based on the results seen for systems with equally flexible wings, a proof-of-concept study has been conducted analysing tandem systems with mixed flexibility, suggesting that they could outperform those with equally flexible wings.

7.2 Future work

The present work has intended to gather information about the unsteady and aeroelastic response of different bioinspired fluid-structure interaction problems. Nevertheless, as clearly stated in the previous section and chapters, the goal of the work has always been to pave the way for future studies such that eventually we obtain enough knowledge in the field in order to design devices whose efficiency is close to that achieved in the animal kingdom. In order to achieve this ultimate goal, more steps must be done. Here we propose some future work lines.

First, it would be interesting to extend the problems of chapters 3 and 4 to three dimensions. The assumptions that have been made allow to study the physics in simple configurations to isolate the effects under the scope of the analysis. However, finite wing/blade effects are obviously relevant on both their interaction with vortices and load mitigation. Regarding this second problem, the spanwise load distribution typically found in finite wings/blades is not constant. Hence, the assumption of an infinitely long trailing-edge flap is also strong for design purposes, and its extensions to three-dimensions is key.

On the other hand, effects of flexibility have been restricted in chapters 5 and 6 to flexibility in the spanwise direction of wings. However, although it is the one mainly governing the structural response of different lifting surfaces found in insects, these surfaces usually combine membranes and veins leading to a non-uniform distribution of flexibility. Studies of chapters 5 and 6 should be extended for non-uniformly flexible structures. Finally, the parametric space the problems considered in this dissertation is so vast that a huge part of them remains unexplored. Further exploration, combined with the aim of extracting accurate reduced-order models, are ideas to keep in mind.